

A BI-DOMAIN MODEL FOR DESCRIBING ISCHEMIC MYOCARDIAL D-C POTENTIALS

by

Leslie Tung

S.B., Massachusetts Institute of Technology  
(1972)

S.M., Massachusetts Institute of Technology  
(1972)

SUBMITTED IN PARTIAL FULFILLMENT  
OF THE REQUIREMENTS  
FOR THE DEGREE OF

DOCTOR OF PHILOSOPHY

at the

MASSACHUSETTS INSTITUTE OF TECHNOLOGY

June, 1978

© 1978 by Leslie Tung

Signature of Author .....  
Department of Electrical Engineering and Computer Science, May 19, 1978

Certified by .....  
Thesis Supervisor

.....  
Reader

.....  
Reader

.....  
Reader

Accepted by .....  
Chairman, Departmental Committee on Graduate Students

ARCHIVES

MASSACHUSETTS INSTITUTE  
OF TECHNOLOGY

OCT 26 1978

LIBRARIES

"A Bi-Domain Model for Describing Ischemic Myocardial  
D-C Potentials"

by

Leslie Tung

Submitted to the Department of Electrical Engineering and  
Computer Science on May 19, 1978 in partial fulfillment  
of the requirements for the Degree of Doctor of Philosophy

ABSTRACT

With an abrupt termination of the blood supply (acute ischemia) to heart muscle (myocardium), electrical d-c potentials will arise and appear as shifts in the baseline of the electrocardiogram (ECG). These potentials are important because they contain information regarding the extent of the ischemic myocardium, and thus can be used to evaluate the effectiveness of various interventions intended to improve the state of ischemic myocardial cells. The purpose of this thesis is to develop a model to describe the the d-c baseline shift, measured on the heart surface, as it arises from a given ischemic source distribution.

One difficulty for modeling potentials measured on the heart is that the distance scales involved are very large compared to the length of a single cell. Consequently, branching tree networks, which have been developed to describe cell-to-cell interactions, are not very practical for describing the large population of cells comprising the heart, because of the enormous numerical complexity. At the same time, because the potentials are measured on the heart surface, "far-field" (e.g. dipole) models are inadequate. Consequently, a model in the intermediate region is needed.

We develop the concept that myocardium is a member of a class of tissue systems whose electrical properties can be appropriately described in terms of a "bi-domain structure". Bi-domain, volume-conductive structures differ from classical volume conductors (mono-domain structures) in that a distinction is made between current flow in the extracellular space and current flow in the intracellular space. This distinction is justified by the physical presence of a high resistance membrane separating the two spaces, together with the fact that the intracellular spaces are electrically coupled through low resistance, intercellular connections. With a bi-domain structure, Ohm's law and charge conservation can be modified to account for the presence of the other

domain, and boundary conditions must then altered.

Classical mono-domain structures can be considered to be a degenerate case of bi-domain structures. This is a natural consequence of the fact that the equations governing a bi-domain structure permit solutions corresponding to those of a mono-domain structure. The general solutions for the extracellular or intracellular potential in a bi-domain structure are composed of two terms -- one shared by mono-domain structures (a solution to Laplace's equation), and the other unique to bi-domain structures (a solution to the Helmholtz equation). The first term represents a "common-mode" interpretation for the current density, while the second represents a "differential-mode" interpretation. The relative magnitude of these two terms determines the appropriate model for a given tissue system. We use the bi-domain model here to describe the ischemic myocardial d-c potential.

We compare the results of the bi-domain model for ischemic myocardium to those of the "solid angle model". This model is the only quantitative model now in use for describing ischemic potentials. We show that the solid angle model can be derived from the bi-domain model only under a number of limiting assumptions which are not generally satisfied by the experimental situation.

Finally, we study a number of cases involving a variety of ischemic source distributions, in the hope of obtaining some insight into the effect of various physical parameters (such as bulk resistivity or width of the ischemic/healthy border) on the shape of the potential distribution at the heart surface. We then use our theoretical results to interpret a number of experimental findings.

Thesis supervisor: Roger G. Mark  
Title: Matsushita Associate Professor of Electrical  
Engineering in Medicine

Reader: Richard B. Adler  
Title: Professor of Electrical Engineering and Computer  
Science

Reader: Thomas F. Weiss  
Title: Associate Professor of Electrical Engineering and  
Computer Science

Reader: Alan J. Grodzinsky  
Title: Associate Professor of Electrical and Bioengineering

## ACKNOWLEDGMENTS

First I would like to thank my thesis committee collectively, who undertook a difficult job of jointly supervising the work for my thesis. I feel extremely privileged to have been able to associate with each member of the committee. Out of necessity, many hours were spent together in committee meetings to discuss the progress of the work, not to mention the additional hours spent in private conversations. Yet the benefits far outweighed the inconveniences. Because of their widely differing backgrounds, each committee member provided his own special insight, which I found to be most invaluable.

I am deeply grateful to Dr. Roger Mark, my thesis supervisor, for his interest in my work over the years. He helped to guide me to the thesis topic through numerous discussions and sharpened my thinking concerning electrocardiologic experiments and measurements. I would like to express my deepest appreciation to Prof. Richard Adler, who, of all the committee members, spent by far the greatest amount of time discussing with me the theoretical aspects of the thesis. With his continual help, I was able to get a glimmering of many of the subtle issues involved, and to be able to express them on paper. Then I would like to thank Prof. Thomas Weiss for his constant encouragement over the years, and I especially appreciate his guidance for the direction of the thesis as it developed. Thanks to his many comments regarding the writing of the thesis, the document may stand a chance of being read. Last, but not at all least, I would like to thank Prof. Alan Grodzinsky for his many interesting discussions regarding matters not only in my research work but in related fields as well.

In addition, I must thank the several cardiologists whose work in the laboratory I have had the privilege of observing. In particular, I am deeply indebted to Dr. Peter Maroko, who freely gave me his time and generously spent countless hours educating me in the field of experimental electrocardiology. I would also like to thank Dr. James Muller and Dr. Lair Ribeiro for spending their time at the operating table explaining the simplest procedures to a rather ignorant graduate student, and for allowing me to step into their experiments to make my own recordings.

Then I would like to thank the directors and staff of the Biomedical Engineering Center for Clinical Instrumentation for providing me with workspace and facilities. In particular, I would like to thank the



technical director, Dr. Stephen Burns, and also Mr. Edward Sadowski and Ms. Gloria McAvenia for their support. In addition, I would like to thank Paul Schluter, Neal Dowling, and especially Joe Walters, whose RUNOFF program arranged the format of this document, for helping me with the nitty-gritty details of using the computer facility at the Center. Credit must also go to Jonathan Sachs, for writing many of the plotting programs used to present the results of this work.

The work described in this document was supported primarily by training grants from the National Institutes of Health, and by a fellowship from the Whitaker Health Sciences Fund. I am particularly grateful to Prof. William Siebert for making this support available to me.

Finally, I would like to dedicate this thesis to my wife, Sze-Ping. Her continual support, cheerful encouragement, endless patience, and invaluable assistance at the very end helped carry me through to the completion of this document.

Leslie Tung

Cambridge, Massachusetts  
May 19, 1978

TABLE OF CONTENTS

	Page
Abstract	2
Acknowledgments	4
Table of Contents	6
List of Illustrations	9
Introduction	14
Chapter 1: The Ischemic Myocardial Potential	19
A. Time line	20
B. Deviations in the d-c baseline of the ECG as the ischemic myocardial potential	24
Chapter 2: Previous Analytical Models	42
A. Cable models	42
B. Branching networks	44
C. Biologically microscopic field models	44
D. Biologically macroscopic field models	45
Chapter 3: Use of the "Solid Angle" Model	47
A. Historical development	47
B. Recent applications	51
C. Difficulties with the solid angle model	53
Chapter 4: The Bi-Domain Model	59
A. Electrically coupled cells and interpenetrating domains	59
B. Membrane current flow	68
C. General equations	73

D. General solutions	77
E. Boundary conditions	82
F. "Differential" and "common" modes	85
G. The mono-domain and the bi-domain	93
H. Summary	94
Chapter 5: Case Studies Using the Bi-Domain Model	103
A. Rectangular, transmural ischemic zone with abrupt borders	104
B. Rectangular, transmural ischemic zone with lateral diffuse borders	111
C. Rectangular ischemic zone with both lateral and transverse diffuse borders	112
D. Sensitivity analysis	115
Chapter 6: The Solid Angle Model, Derived from the Bi-Domain Model	136
A. Assumptions of the solid angle model	136
B. Equivalence relationships between solid angle and bi-domain sources	143
C. Boundary conditions	146
D. Applicability of the solid angle model	149
Chapter 7: Case Studies Comparing The Bi-Domain and Solid Angle Models	154
A. Subepicardial ischemic zone	156
B. Subendocardial ischemic zone	163
C. Transmural ischemic zone	165
D. Intramural ischemic zone	168
Chapter 8: Issues of Experimental Interest	181
A. ST-TQ spatial maps and the "inverse" problem	182
B. Biologically microscopic vs. macroscopic	192

measurements

C. Magnetocardiograms 194

Chapter 9: Future Experiments 196

A. D-C spatial maps 196

B. Changes in potential distribution with altered boundary conditions 196

C. Measurements of electrical parameters during ischemia 197

D. In vitro experiments 198

Summary 200

Appendix A: Uniqueness 205

Appendix B: Experimental Values for the Parameters of the Bi-Domain Model 212

Appendix C: The Integral Form of the Bi-Domain Model 219

Appendix D: Anisotropy 224

Appendix E: Microscopic to Macroscopic Description 227

Appendix F: The FFT, Fourier Cosine Integral, and Fourier Cosine Series 236

Appendix G: Legendre Polynomials and Fourier Cosine Series 241

Appendix H: Computer Programs 246

References 266

Biographical Note 277

LIST OF ILLUSTRATIONS

Figure	Page
1.1 - The ischemic epicardial electrogram	29
1.2 - Diagram of normal and ischemic cardiac waveforms	30
1.3 - Historical highlights of the solid angle model and ischemic ST-TQ <sub>segment</sub>	31
1.4 - Polarities observed for the ST-TQ segment	32
1.5 - Monotonic spatial distribution for the ischemic ST-TQ segment	33
1.6 - ST, TQ combinations	34
1.7 - "Mild" and "severe" ischemia: changes in the cardiac waveforms	35
1.8 - Epicardial ST-TQ mapping	36
1.9 - Continuous a-c sweep recording of the epicardial electrogram during ischemia	37
1.10 - Early evidence for d-c baseline currents during ischemia	38
1.11 - Continuous d-c sweep recording of the epicardial electrogram during ischemia	39
1.12 - Ischemic magnetocardiogram	40
1.13 - Temporal development of shift in the TQ and ST segments of the epicardial electrogram following an acute coronary occlusion	41
3.1 - The mathematical definition of the solid angle model	55
3.2 - The ischemic zones of interest	56
3.3 - The theory for the ischemic ST-TQ segment in 1962	57
3.4 - Predicted precordial (chest) and epicardial	58

surface distributions for the ischemic ST-TQ segment for various types of ischemic zones.

4.1 -	Current flow in the intracellular and extracellular spaces	96
4.2 -	Relationship between the macroscopic and microscopic intracellular current densities for parallel cells	97
4.3 -	Equivalent "large-signal" model for the cell membrane separating the intracellular and extracellular spaces	98
4.4 -	Equivalent "small-signal" model for the cell membrane separating the intracellular and extracellular spaces	98
4.5 -	Complementary monopole source pair, representing the flow of membrane current between domains	99
4.6 -	Equivalent "small-signal" model for the cell membrane separating the intracellular and extracellular domains	100
4.7 -	Example illustrating the "differential-mode" of the bi-domain structure	101
4.8 -	Example illustrating the "common-mode" of the bi-domain structure	102
5.1 -	The rectangular myocardial strip (asymmetrical case)	119
5.2 -	The rectangular myocardial strip (symmetrical case)	119
5.3 -	The rectangular source distribution, U	120
5.4a -	Equipotential lines for the extracellular potential for the case of an abrupt ischemic border	121
5.4b -	Extracellular surface potential plots for the case of an abrupt ischemic border	122
5.4c -	Intracellular surface potential plots for the case of an abrupt ischemic border	123

5.5a - Equipotential lines for the extracellular potential for the case of a lateral diffuse ischemic border	124
5.5b - Extracellular surface potential plots for the case of a lateral diffuse ischemic border	125
5.6a - Equipotential lines for the extracellular potential for the case of lateral and transverse diffuse ischemic borders	126
5.6b - Extracellular surface potential plots for the case of lateral and transverse diffuse ischemic borders	127
5.7 - Effect of changes in the extracellular bulk resistivity on the exposed surface potential distribution	128
5.8 - Effect of changes in the intracellular bulk resistivity on the exposed surface potential distribution	129
5.9 - Effect of changes in the myocardial bulk resistivity on the exposed surface potential distribution	130
5.10 - Effect of changes in the ratio of the intracellular and extracellular bulk resistivities, holding the composite myocardial bulk resistivity fixed, on the exposed surface potential distribution	131
5.11 - Effect of changes in the space constant on the exposed surface potential distribution arising from an ischemic zone with abrupt borders	132
5.12 - Effect of changes in the space constant on the exposed surface potential distribution arising from an ischemic zone with lateral diffuse borders	133
5.13 - Effect of changes in the width of the lateral border of the ischemic zone on the exposed surface potential distribution	134
5.14 - Effect of changes in the width of the transverse border of the ischemic zone on the exposed surface potential distribution	135

6.1 -	The derivation of the solid angle model from the bi-domain Helmholtz model	151
6.2 -	Open and closed ischemic border surfaces	152
6.3 -	Boundary conditions for the bi-domain Poisson model	153
7.1 -	Ischemic zones lying in the spherical myocardial wall	169
7.2 -	Extracellular surface potential plots for the case of a subepicardial ischemic zone, using the bi-domain Poisson model	170
7.3a -	Equipotential lines for the extracellular potential for the case of a subepicardial ischemic zone, using the solid angle model	171
7.3b -	Extracellular surface potential plots for the case of a subepicardial ischemic zone, using the solid angle model	172
7.4a -	Equipotential lines for the extracellular potential for the case of a subendocardial ischemic zone, using the bi-domain Poisson model	173
7.4b -	Extracellular surface potential plots for the case of a subendocardial ischemic zone, using the bi-domain Poisson model	174
7.5a -	Equipotential lines for the extracellular potential for the case of a subendocardial ischemic zone, using the solid angle model	175
7.5b -	Extracellular surface potential plots for the case of a subendocardial ischemic zone, using the solid angle model	176
7.6a -	Equipotential lines for the extracellular potential for the case of a transmural ischemic zone, using the bi-domain model	177
7.6b -	Extracellular surface potential plots for the case of a transmural ischemic zone, using the bi-domain model	178
7.7a -	Equipotential lines for the extracellular potential for the case of a transmural	179



	ischemic zone, using the solid angle model	
7.7b	- Extracellular surface potential plots for the case of a transmural ischemic zone, using the solid angle model	180
A1	- Simply connected surface enclosing a bi-domain structure	211
A2	- Simply connected surface enclosing a bi-domain in contact with a mono-domain structure	211
A3	- Multiply connected surfaces enclosing a bi-domain structure	211
C1	- The microscopic structure of a bi-domain system	223
E1	- Extracellular potential arising from a single cell	234
E2	- Replacing the surface density by a volume density	235
F1	- Sampling of the analog waveform	240
G1	- Table of values for $p(j,k)$	245

## INTRODUCTION

The potentials which arise when heart muscle (myocardium) loses its blood supply (i.e. becomes ischemic) are of experimental interest, as it may be possible to use these potentials as an index of the extent and severity of ischemic myocardial injury. A popular candidate has been deviations in that portion of the electrocardiogram (ECG) commonly referred to as the "ST segment", which has long been associated with sudden (acute) myocardial ischemia. In the last decade there has been a renewed interest in mapping the ST segment directly on the heart surface of open-chest animals in the hope of providing information regarding changes in the extent and severity of the ischemic injury, particularly when a pharmacologic, metabolic, or hemodynamic intervention has been applied.

Over the years, the theory for myocardial ischemic potentials has evolved into a "solid angle" model by the extrapolation of results from one science (electrostatic field theory) to another (cardiac electrophysiology). No identification has been made between the parameters and sources of the solid angle model on the one hand, and the physical structure of the myocardium on the other. In addition, the assumptions underlying the model have never been tested, nor have the predictions of the model been verified. However, investigators currently use the model in

a quantitative fashion to interpret their experimental findings.

If we search the literature for other models which describe the electrical activity of heart muscle (not necessarily applied to ischemic conditions), we find that many of the models typically describe the "far-field" behavior -- that is, they describe the electrocardiogram on the chest wall at locations well removed from the myocardial electrical source. The equivalent sources for these models are represented by a dipole, multipole, or dipole sheet description. The solid angle model described earlier is basically a member of this class of "far-field" models, although it has been applied to describe potentials close to the heart (in fact, directly on the heart surface).

In addition to the class of "far-field" models, there exist several classes of models at the opposite end of the spatial scale which describe the electrical activity of myocardial cells on a cell by cell basis. One class of models takes a field-theoretic approach to describe the extracellular potential of a single cell, lying in a homogeneous volume conductor, in terms of the electrical behavior at the cell membrane. By assuming that the cells in the myocardium do not interact, superposition can be used to arrive at the composite potential. Unfortunately, since these models are inherently microscopic in nature, they require a detailed description of the position of each cell

and its membrane. Another class of models takes a network approach and describes the geometry of the tissue structure as a closed, branching tree network, with each cell forming a branch of the network. Because of their numerical complexity, these models are useful only in describing potentials over distances which are at most on the order of several hundred cell lengths. In practice, these models are incapable of describing potentials in myocardial tissue, consisting of several million cells in a volume of several cubic centimeters.

However, the experimental situation under consideration is the exposed heart in the open-chest, a preparation which is typically used in the study of the local electrical changes which accompany myocardial ischemia. Signals on the heart surface are directly measured with gross electrodes, having dimensions which are typically on the order of several hundred cell lengths. These multicellular, or "macroscopic", surface potentials arise from a very large population of cells and are not suitably described by any of the classes of models previously mentioned. The "bi-domain model" described in this work has been created to fill this need, and approaches the problem by averaging the cellular sources to obtain an equivalent macroscopic source from which the macroscopic potential can be derived. It utilizes the fact that cardiac cells are a member of a class of tissue systems whose cellular components are electrically interconnected.

In addition, it attempts to account for the physical structure of the myocardium in the definition of its parameters and sources.

We will begin by providing background information regarding the changes in the ECG which arise from myocardial ischemia, and we will define the ischemic potential of interest (Chapter 1). We will then summarize the various classes of electrical models which have been formulated to describe the electrical activity of myocardium (Chapter 2) and focus specifically on the solid angle model (Chapter 3). Following a discussion of the present day use and limitations of the solid angle model, we will proceed to formulate the bi-domain model, taking the physical structure of the myocardium into account (Chapter 4). The parameters of the model will correspond to macroscopic, measurable quantities. Using the bi-domain model, we will study several cases in which the various parameters of the model are varied, in order to determine the effect they have on the shape of the surface potential distribution (Chapter 5). Next, we will turn back to the solid angle model and show that under a number of limiting assumptions, the solid angle model can be derived from the bi-domain model (Chapter 6). Various cases will be considered in which the two models are compared (Chapter 7). Then, we will compare the theoretical results of Chapters 5 and 7 to the experimental results reported in the literature (Chapter 8). Finally, we will conclude by

suggesting a number of topics for future research (Chapter 9).

CHAPTER 1: The Ischemic Myocardial Potential

In this chapter we provide a general background regarding the electrical potentials which arise following the sudden onset of myocardial ischemia, which is a loss of the blood supply for heart muscle. We shall be discussing spatial distributions of changes in the electrocardiogram (ECG), measured on the outer surface of the heart (epicardium), as opposed to the inner surface of the heart (endocardium), illustrated in Fig. 1.1 [Netter (1969)]. In particular, we focus on the changes in the height of the portion of the ECG known as the "ST segment". The magnitude of the ST segment has usually been measured with respect to the baseline (the "TQ segment"). This relative difference will hereafter be referred to as the "ST-TQ segment", and is the quantity measured by (a-c coupled) clinical ECG recorders. In Fig. 1.2 we illustrate the normal and ischemic epicardial surface electrogram (SEG), measured in open-chest animals. Changes in the height of the ST-TQ segment have been recorded quite extensively. In summarizing the data, we would like to direct the reader's attention to the polarity (positive or negative) and concavity (location of relative maximum or minimum) of the spatial distribution of the ST-TQ segment shift, since these will be the features of interest in the theoretical calculations performed later in Chapters 5 and 7. We shall conclude this chapter by

designating shifts in the baseline (TQ) component of the ST-TQ shift, rather than the total ST-TQ segment, as the "ischemic potential". A model which is suitable for describing the spatial distribution of the ischemic potential, and which takes into account the physical structure of the myocardium, is the subject of this work.

#### 1-A. Time line

Studies of changes in the ST-TQ segment following the sudden onset of (acute) ischemia date back to 1918 when Smith recorded ST-TQ segment elevation in dogs, and to 1920 when Pardee recorded similar potentials in humans. Today, these studies continue in the form of spatial ST-TQ segment maps, both on the surface of exposed animal hearts and on the chest of human patients [Maroko et al (1972), Nielsen (1973), Madias and Hood (1974), Reid et al (1974), Muller et al (1975,1977), Flaherty (1976)]. In this section we summarize the various historical highlights regarding the ischemic ST-TQ segment, illustrated in Fig. 1.3. Also shown in Fig. 1.3 are the highlights regarding the development of the "solid angle" theory, currently used to describe the spatial distribution of the ST-TQ segment. We will return to a discussion of these theoretical highlights in Chapter 3.

In 1945 Wolferth et al observed ST-TQ elevation at epicardial sites over a region of ischemic injury, and a simultaneous ST-TQ depression at epicardial sites on the wall



of the heart opposite to the wall containing the ischemic region, in the manner illustrated in Fig. 1.1. They described the ST-TQ depression as a "reciprocal" phenomenon which was somehow related to the occurrence of the "primary" ST-TQ elevation. Hellerstein and Katz (1948) also reported reciprocal ST depression not only on the epicardial and endocardial surfaces of the wall of the heart opposite to the wall containing the ischemic zone, but also on the surface of the same wall of the heart subjacent to the ischemic region - i.e. on the endocardium for a subepicardial ischemic zone, and on the epicardium for a subendocardial ischemic zone (Fig. 1.4). However in 1954 Rakita et al reported that single polarity, monotonic, spatial distributions of ST-TQ segment elevation generally resulted from acute ischemia, without reciprocal ST-TQ depression (Fig. 1.5). Occasionally, however, islands of ST-TQ segment depression were observed at the ischemic border, but their magnitude fluctuated with time and apparently bore no relationship to the amount of ST-TQ elevation.

In 1960 Katcher et al and Samson and Scher used d-c coupled amplifiers to record the d-c components of ST-TQ segment shifts arising from ischemia. They observed that the ST-TQ shift, as measured by clinical a-c coupled amplifiers, was composed of both baseline (TQ) and ST shifts. Fig. 1.6 summarizes the various combinations of TQ and ST shifts which were observed by Katcher et al.

In 1961 Prinzmetal et al advanced the notion of two forms of ischemia - a "mild" form, exhibited primarily by TQ segment elevation and a "severe" form, exhibited primarily by TQ depression (Fig. 1.7). This notion lends a different interpretation to cases where ST-TQ depression is observed in the vicinity of the ischemic zone.

In 1971-2 Maroko et al developed the technique of epicardial or precordial ST-TQ segment mapping at a discrete number of sites as a means for predicting changes in the extent and severity of the ischemic zone. The technique is illustrated in Fig. 1.3, taken from Braunwald and Maroko (1974). The intent was to identify those regions of myocardium which were potentially salvageable and to test the effectiveness of various pharmacologic or hemodynamic interventions [for a review, see Hillis and Braunwald (1977a,1977b,1977c)]. Ischemia was induced by the ligation (tying off or clamping) of a coronary artery, and the behavior of the ST-TQ segment was then monitored in both the ischemic and non-ischemic regions. The ligation was then removed, and the intervention was administered. Again, the coronary artery was ligated. Changes in the total number of sites having an ST-TQ shift, and changes in the sum of the magnitudes of the ST-TQ shifts taken over all the sites, were then used as electrical indices to predict changes in the amount of eventually dead (necrotic) myocardium.

Since then much effort has been devoted to test the

validity of the ST-TQ index by studying the relationship between epicardial ST-TQ segment maps and other indices of myocardial ischemia measured simultaneously, indices such as metabolic or histologic changes, or changes in the regional myocardial blood flow [Kjekshus et al (1972), Karlsson et al (1973), Smith et al (1975), Lekven et al (1975), Bodenheimer et al (1976), Irvin and Cobb (1977)]. However, to the present time an indisputable correlation has yet to be obtained. One reason for this, as we shall discuss in more detail in Chapter 8, is that the two components of the ST-TQ segment (the TQ baseline and ST segment) are sensitive to different factors, and therefore can act independently. Hence, it may be the case that in the experiments mentioned above, sufficient control of the various factors was not achieved. Other studies have also been made to examine the relationship between precordial ST-TQ segment maps and other myocardial ischemic indices [Muller et al (1975), Selwyn et al (1977)].

Finally, the use of the ST-TQ segment as an index of the extent and severity of the ischemic zone now appears to be controversial [Braunwald and Maroko (1976), Fozzard and DasGupta (1976), Holland and Brooks (1977a), Surawicz (1977), Muller et al (1978)]. A focal point for the controversy is illustrated in Fig. 1.9, taken from Muller et al (1975). Although it is generally the case (as in panel A) that the ST-TQ segment shift is maximal at the center of the ischemic

zone (suggesting a correlation to the degree of ischemia), occasionally the maximal ST-TQ shift occurs instead at the border of the ischemic zone (as in panel B), particularly in cases of local conduction block. Consequently, there is apparently a limitation to the usefulness of the ST-TQ segment as an ischemic index.

1-B. Deviations in the d-c baseline of the ECG as the ischemic myocardial potential

There has long been an interest in the relative importance of the d-c baseline component compared to the total ST-TQ shift. In 1897 Burdon-Sanderson and Page demonstrated the existence of an "injury potential", a d-c shift in the extracellular potential of exposed frog ventricular muscle, following mechanically induced or chemically induced injury to the muscle. Using a capillary electrometer, they found that injured areas became electrically negative with respect to uninjured areas. In 1943 Nahum et al performed a clever experiment to determine during which portion of the cardiac cycle significant ischemic current occurred. They alternately connected and disconnected an electrical pathway between the ischemic myocardium and the body, and observed the resulting changes in the precordial electrocardiogram (Fig. 1.10). A significant change resulted during the baseline interval ("electrical diastole"), whereas the potential during the interval of the ST segment ("electrical systole") remained

isoelectric. Consequently they were among the first to conclude that the baseline shift might be the predominant component of the ST-TQ shift.

In 1960 Katcher et al and Samson and Scher used d-c coupled amplifiers to measure both the baseline and ST components of the ST-TQ segment accompanying acute myocardial ischemia (Fig. 1.11). Samson and Scher reported a greater contribution to the ST-TQ segment due to the ST segment, while Katcher et al reported the opposite, a greater contribution due to the TQ segment. However, the most recent evidence regarding the relative importance of the TQ vs. ST segment identifies the TQ segment as the predominant component in acute ischemia. Experiments by Cohen and Kaufman (1975), using magnetocardiograms to detect d-c currents, have concluded that the most consistent component of the ischemic shift in the ST-TQ segment is baseline depression (Fig. 1.12). Vincent et al (1977) focused their efforts to specifically obtain quantitative d-c measurements of the TQ and ST segment shifts. They found that shifts in the ST segment were absent in early ischemia, in contrast to a significant amount of TQ shift (Fig. 1.13). Wittig and Williams (1977) and Janse et al (1977) have reported similar observations of a baseline shift in the initial stages of ischemia, preceding an ST shift.

It is fortunate that the evidence in the literature suggests that the shift in the d-c baseline, rather than the

total ST-TQ shift, is the predominant "ischemic potential", since there are a number of practical advantages in using this electrical index. First, it is much more easily defined than the ST segment, and is therefore subject to less measurement error. Second, the time course of the TQ shift following a coronary occlusion appears to be consistent and predictable, whereas the appearance of the ST shift occurs at variable time intervals [Katcher et al (1960), Samson and Scher (1960)]. Third, the magnitude of the ST shift is sensitive to local conduction block, which affects the sequence of cellular activation, and this block often arises if the ischemic region is very large [Muller et al (1975)]. Fourth, since the baseline is at a d-c frequency, we can use a simple, resistive model to represent the passive cell membrane behavior, and we can impose a static condition on the parameters of the system. And fifth, more information is available regarding the membrane properties during the resting phase (electrical diastole) than during the active phase (electrical systole), so that the membrane behavior can be better described during the TQ interval. Consequently, in this work we shall consider shifts in the TQ baseline of the ECG, to be the "ischemic potential." The theories to be discussed are directed at this quantity.

Finally, we view the problem of the genesis of the ischemic potential in terms of two sub-problems. The first sub-problem is to relate the electrical activity on the

multicellular, or tissue, level (recorded as epicardial electrograms) to the electrical activity on the cellular level. The other sub-problem is sequential to the first and consists of relating the deviations from the normal electrical state of single, ischemic myocardial cells to the biochemistry of ischemia. We will deal with only the first aspect of the overall problem in this work. There exists some direct evidence which links changes in the transmembrane resting potential (TRP) and transmembrane action potential (TAP) to shifts in the TQ and ST segments respectively [Samson and Scher (1960), Prinzmetal et al (1961), Prinzmetal et al (1962), Prinzmetal et al (1968), Johnson (1976)], as illustrated in Fig. 1.2. Using flexibly mounted microelectrodes, Samson and Scher (1960) observed that under ischemic conditions, a reduction in the magnitude of the transmembrane resting potential (TRP), and a reduction and shortening of the plateau of the action potential, occurred. These changes were correlated with changes in the TQ and ST segments respectively. In 1961, contrary to conventional assumptions, Prinzmetal et al suggested that ischemic cells are not always hypopolarized during diastole but rather may sometimes be hyperpolarized in states of "mild" ischemia. A hyperpolarized condition was associated with TQ elevation, while a hypopolarized condition was associated with TQ depression (Fig. 1.7). Prinzmetal et al (1962) also made simultaneous intracellular and extracellular d-c recordings,

which showed that at all recording sites with ST-TQ elevation, a reduction was seen in the TRP of individual cells. Furthermore, TQ depression accounted for at least 80% of the total ST-TQ elevation, and there was a consistent correlation between TQ depression and decreased TRP. The magnitude of TQ depression was approximately 1/4 of the reduction in the TRP.

Other indirect evidence exists for the relationship between baseline and TRP. Studies have shown that factors altering the cellular resting potential, such as changes in electrolyte concentrations [Prinzmetal et al (1959)], result in electrocardiograms with ST-TQ shifts. Infusion of myocardium with hypertonic potassium or hypotonic sodium solutions (decreasing the TRP) results in ST-TQ elevation, while infusion with hypotonic potassium or hypertonic sodium solutions (increasing the TRP) results in ST-TQ depression.

Therefore, in this work we will consider factors which alter the transmembrane resting potential to be the "input" variables to the ischemic myocardial system, and the shift in the baseline (TQ segment) to be the "output" variable. The subject of this work, the "bi-domain model", attempts to link electrical potentials on a macroscopic, multicellular level to the electrical activity of the membrane on a cellular level.



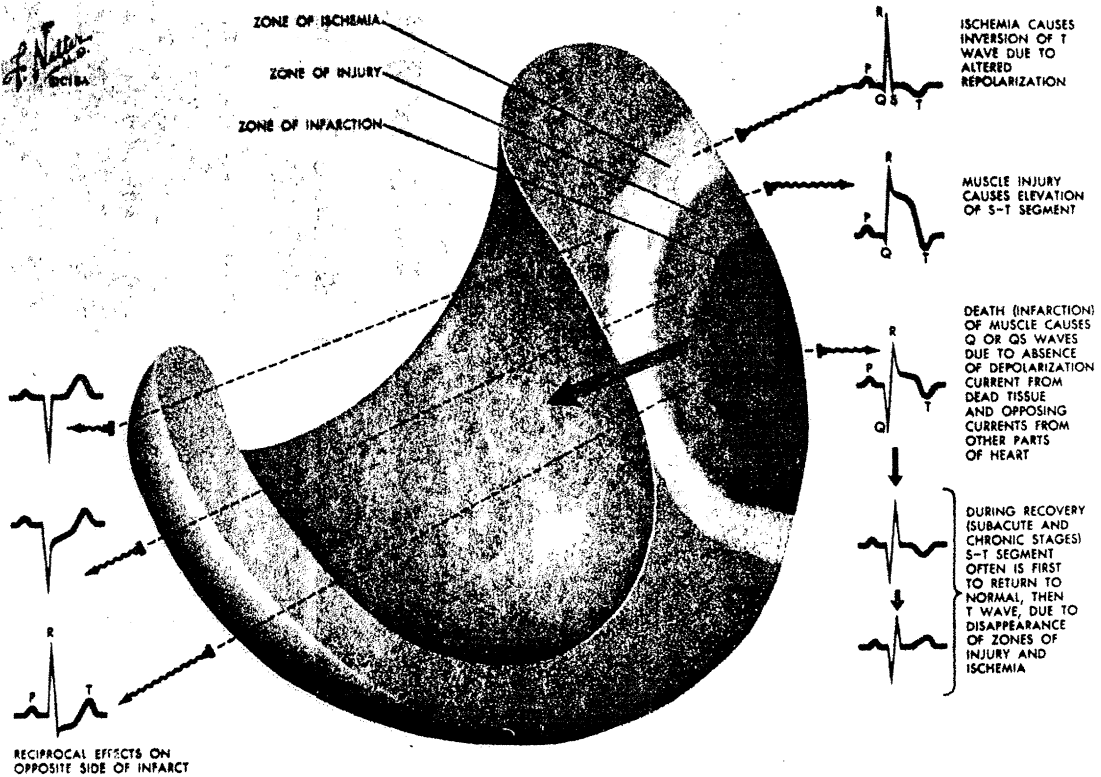
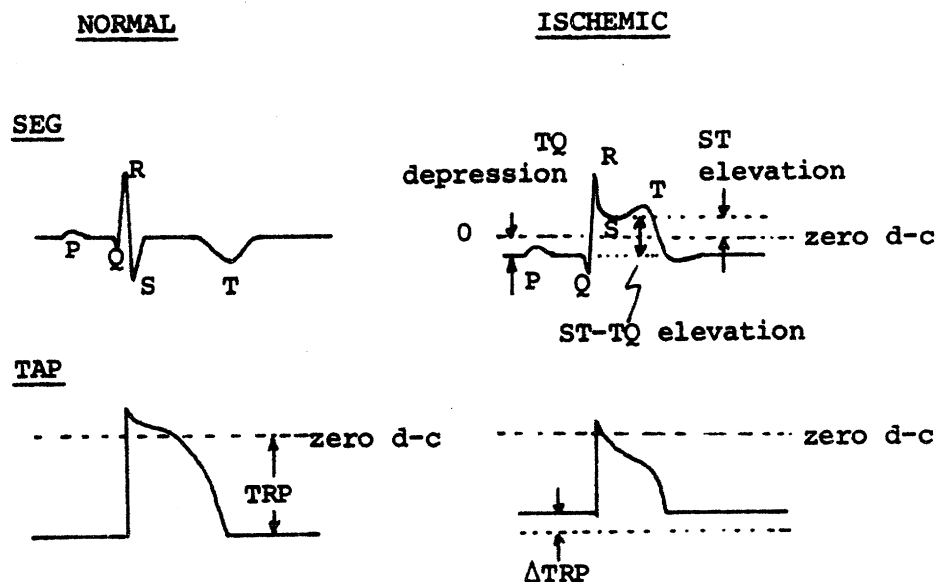


FIGURE 1.1 - The ischemic epicardial electrogram [Netter (1969)]. Note: The figure illustrates an advanced stage of myocardial ischemia, in which the center of the ischemic zone has died (become infarcted). In this work we are concerned only with the early stage of ischemia, before any cells have died. Our definition for ischemia is broader than the one used by Netter (simply defined on a morphological basis as an inversion of the T wave), and includes all electrocardiographic changes due to a loss of the blood supply. Thus, we would refer to Netter's "zone of ischemia" combined with his "zone of injury" as our "zone of ischemia".



- SEG = unipolar epicardial surface electrogram
- TAP = cellular transmembrane action potential
- TRP = cellular transmembrane resting potential
- ST shift = absolute measurement of the height of the ST segment with respect to zero d-c
- TQ shift = absolute measurement of the height of the TQ segment with respect to zero d-c
- ST-TQ shift = relative measurement of the height of the ST segment with respect to the TQ segment

FIGURE 1.2 - Diagram of normal and ischemic cardiac waveforms

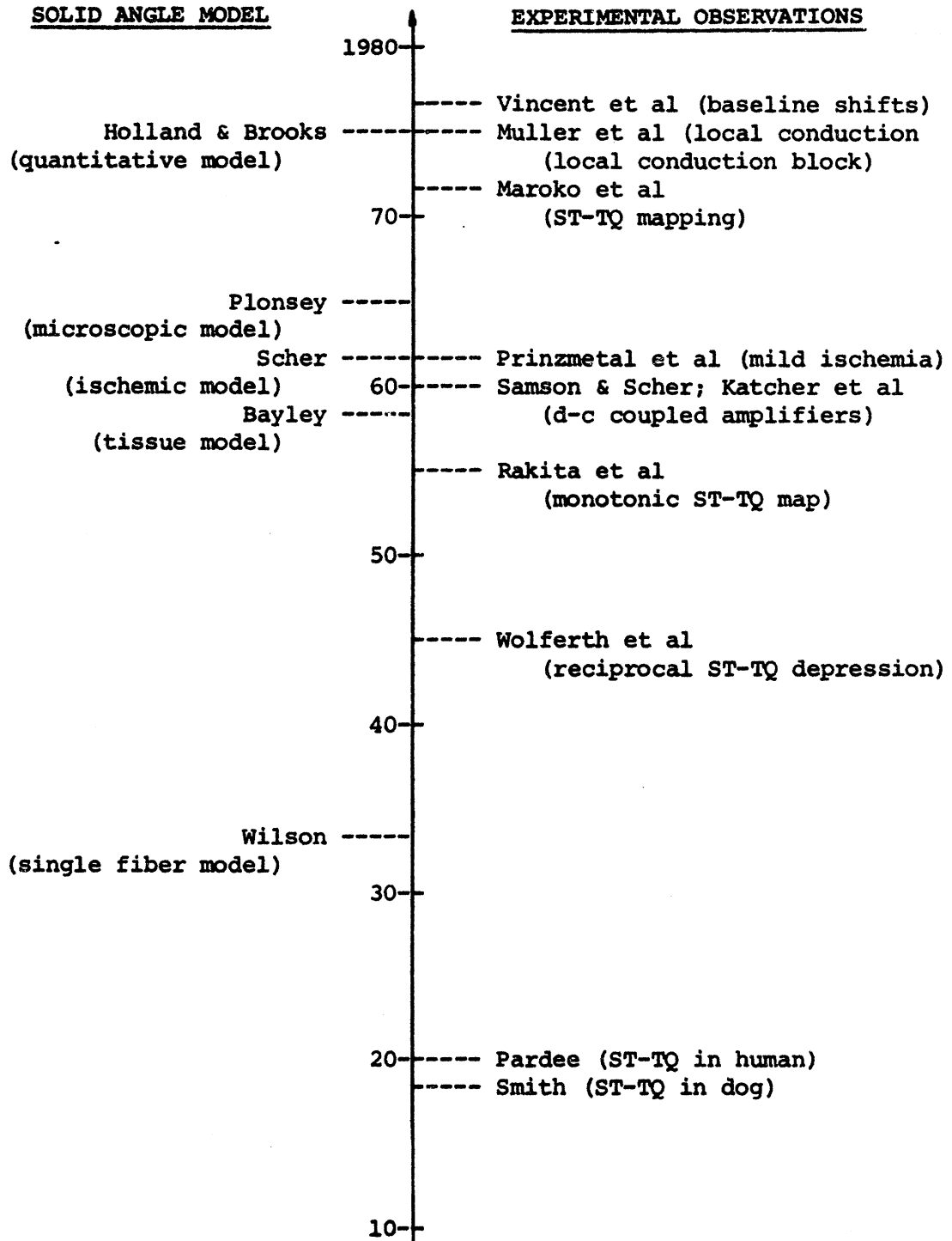


FIGURE 1.3 - Historical highlights of the solid angle model and ischemic ST-TQ segment

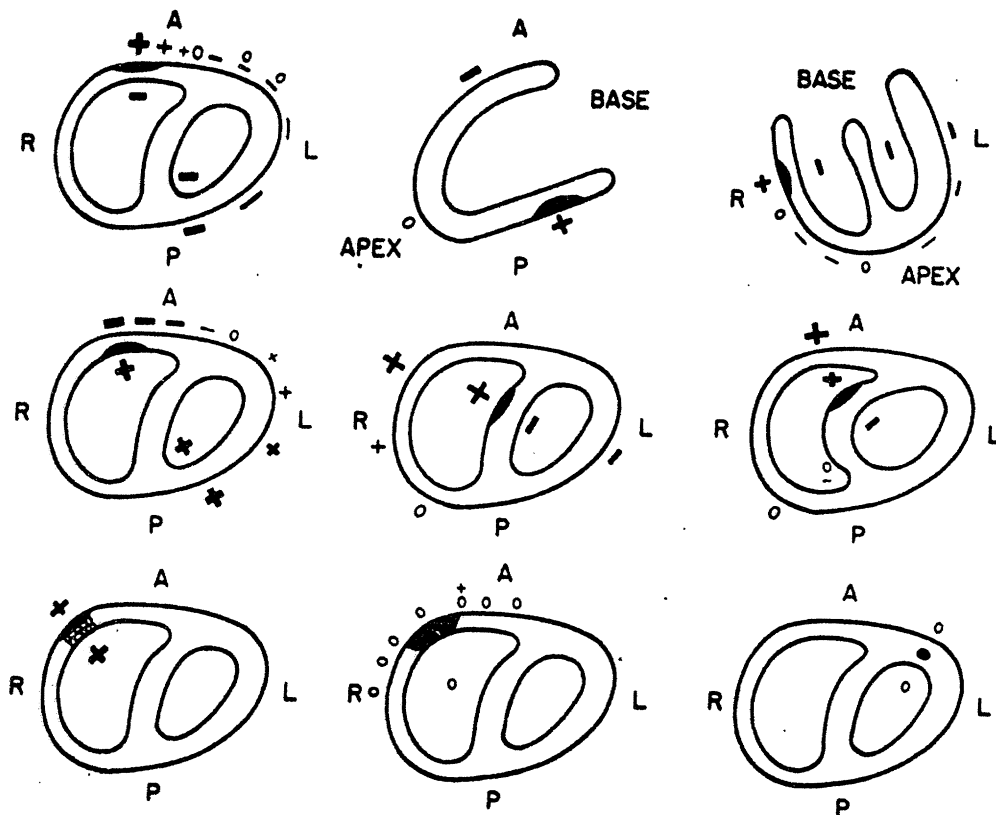


Fig. 17. Diagrammatic representation of the effect of injury in various locations on the S-T displacement. The blackened area in each of the nine figures locates the injured area. Stippling indicates regions of injury intermingled with uninjured regions. Network indicates extension of hemorrhagic regions beyond injury. Plus (+) means S-T elevation; zero (0), isoelectric S-T; minus (-), S-T depression; the thickness of plus and minus signs gives an index of the relative magnitudes of the S-T deviations. A is anterior; P, posterior; R, right; and L, left. Discussed in text.

FIGURE 1.4 - Polarities observed for the ST-TQ segment [Hellerstein and Katz (1948)]. Note that "S-T" in the description refers to the relative ST-TQ segment.

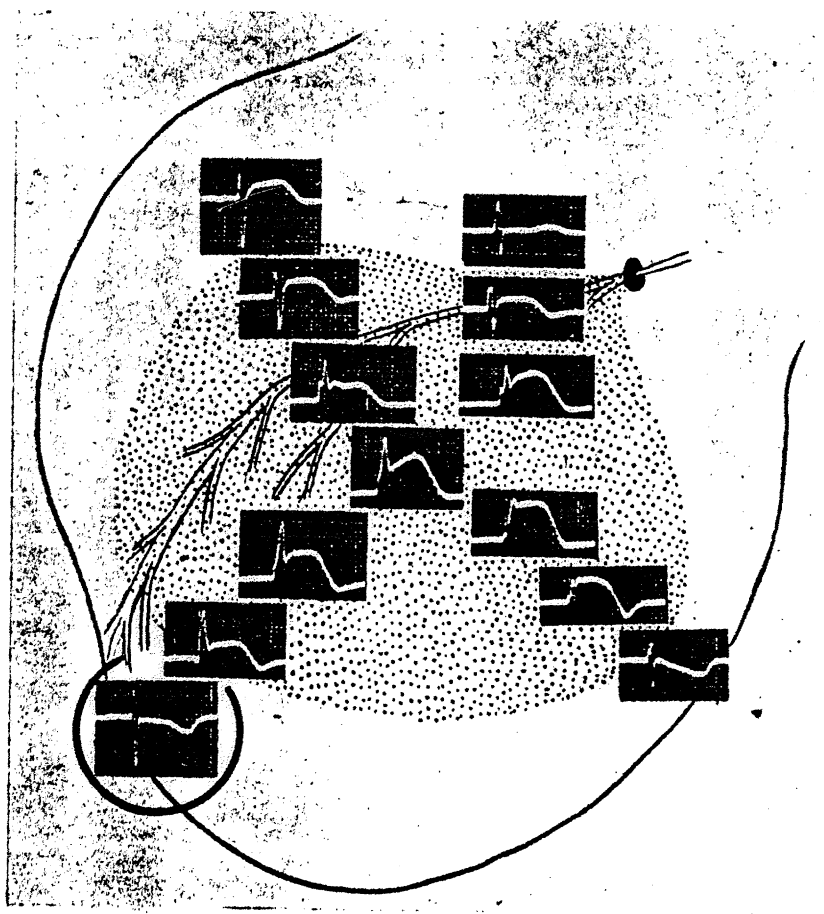


Fig. 6.—Epicardial leads from injured area and adjacent normal-appearing muscle. Black circle in diagram of coronary shows location of ligature. Stippling represents cyanosis which developed after ligation, delineating injured epicardial area. S-T segment elevation is most marked in leads from center of injury and decreases gradually toward the margins. Isoelectric S-T segments are recorded from normal-appearing epicardium outside the margins of injury. The circled complex in the lower left-hand corner is recorded from the posterior surface and illustrates reciprocal S-T segment depression.

FIGURE 1.5 - Monotonic spatial distribution for the ischemic ST-TQ segment [Rakita et al (1954)]

**Table 1**  
**Qualitatively Different Patterns of RS-T Segment Shift and Baseline Shift Obtainable with Capacitance-Coupled as Compared with Direct-Coupled Amplifier Systems.\***

Capacitance-coupled (AC) Amplifier: RS-T segment	DC Amplifier		Circumstances of Observation
	RS-T Segment	Base- line	
Elevation	+	-- ( 1 )	early ischemia trauma center of ischemic areas
	+	0 ( 2 )	borders of ischemic areas late in ischemia at center of ischemic area
	+	> + ( 3 )	release of prolonged occlusion
	0	-- ( 4 )	trauma immediately after occlusion
	-	< - ( 5 )	transiently immediately after occlusion
Isometric Depression	--	+ ( 6 )	about margins of ischemic areas (pink muscle)** centers or borders after release of short occlusion
	--	0 ( 7 )	norepinephrine injections islands beyond margins of ischemic areas (pink muscle)** centers or borders after release of short occlusion
	0	+ ( 8 )	posterior surface of heart during ischemic period
	-	> - ( 9 )	not observed
	+	< + ( 10 )	not observed
		+ = + ( 11 )	release of prolonged occlusion
	- = - ( 12 )	transiently immediately after occlusion	
	( 0 0 )	(many normals)	

\*Circumstances under which these patterns were obtained experimentally. Ten of the possible twelve patterns were observed, resulting in a greater than threefold gain in precision over the AC amplifier.

\*\*RS-T depression may increase transiently after release.

**FIGURE 1.6 - ST, TQ combinations**  
**[Katcher et al (1960)]**

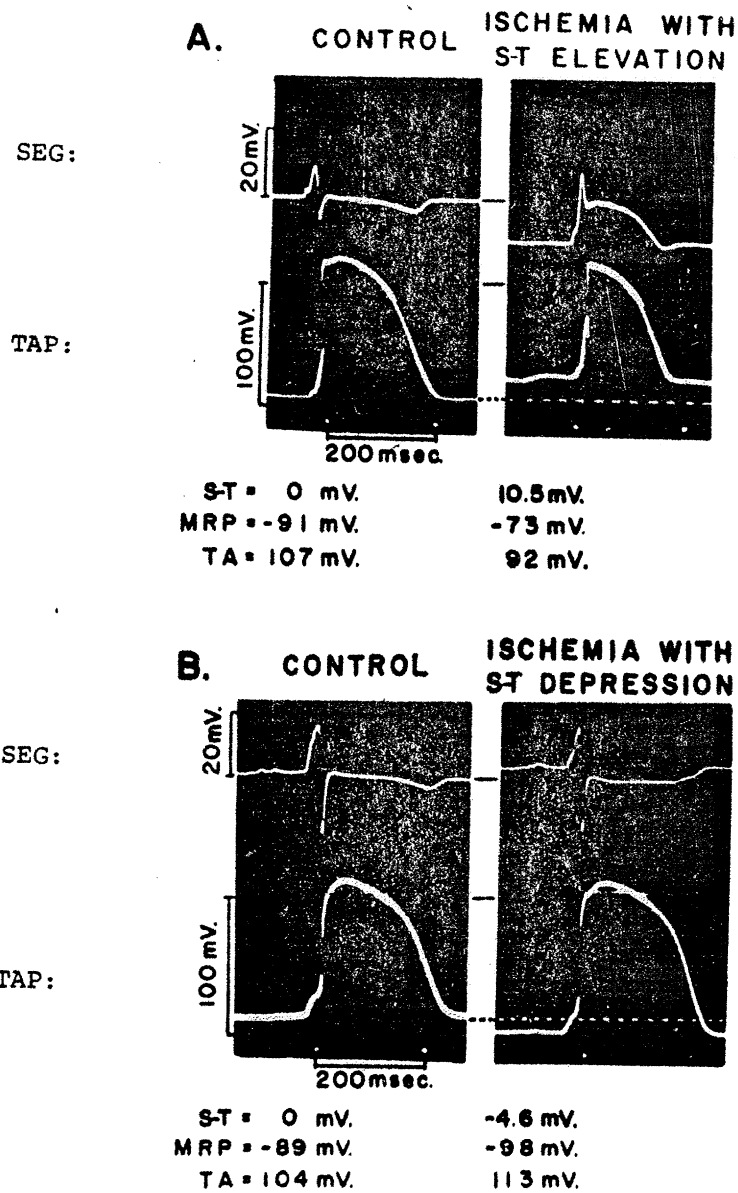
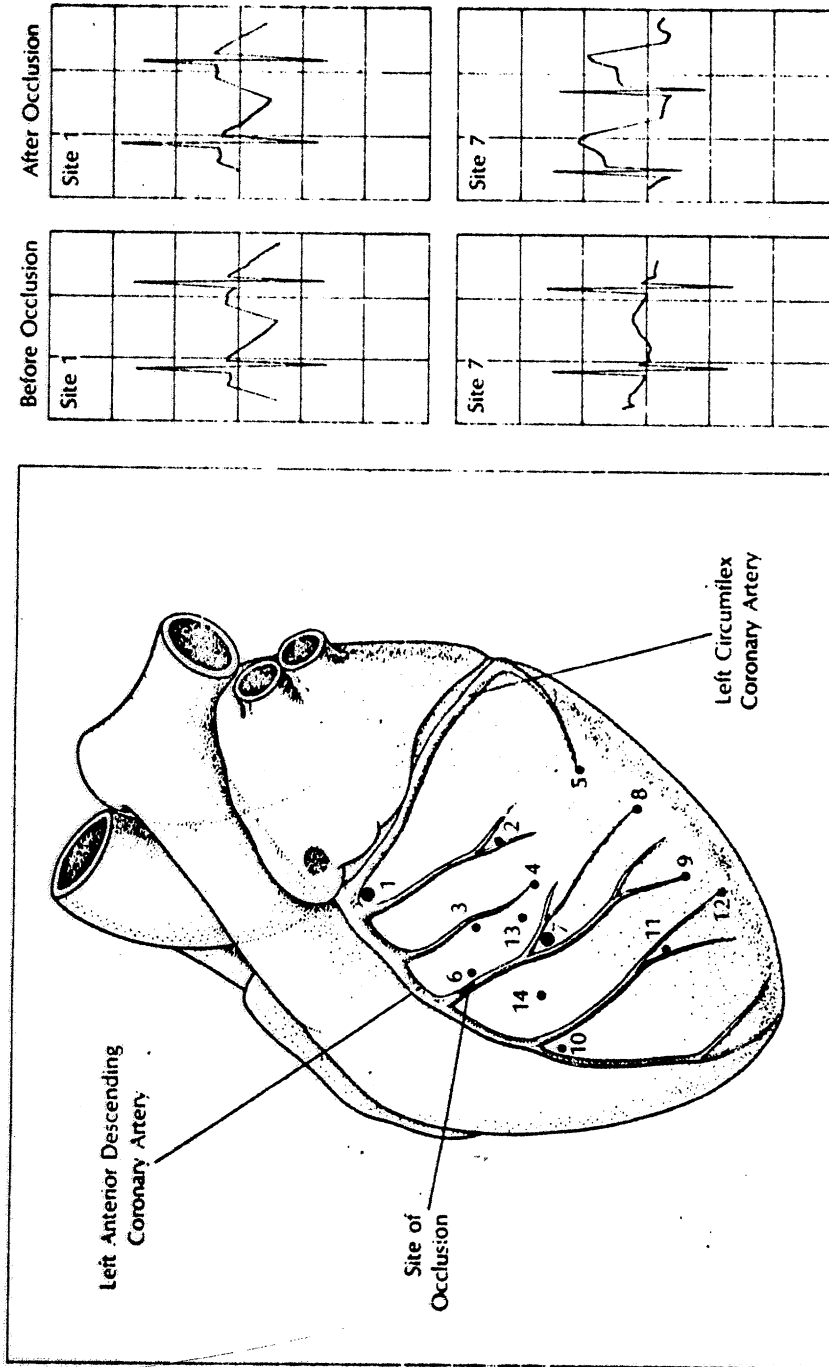


FIGURE 1.7 - "Mild" and "severe" ischemia: changes in the cardiac waveforms [Prinzmetal et al (1971)]. The "S-T segment" and the "MRP" referred to in the figure above are called the "ST-TQ segment" and the "TRP" in this work. Case A is from a "severely" ischemic area, in which the TRP is reduced in magnitude and the TQ segment is depressed (ST-TQ elevation). Case B is from a "mildly" ischemic area, in which the TRP is increased in magnitude and the TQ segment is elevated (ST-TQ depression).



Ischemic injury is revealed in epicardial ECG's obtained shortly after induced occlusion from sites on anterior surface of dog heart, as shown schematically at the left. Whereas ECG from a site that is remote from the injured zone (upper right), site in the area distal to the occluded vessel (lower right) shows marked S-T segment changes, none are seen in tracing from a site that is remote from the injured zone (upper right).

FIGURE 1.8 - Epicardial ST-TQ mapping [Braunwald and Maroko (1974)]. Sites in the region supplied by the occluded coronary artery have elevated ST-TQ segments.



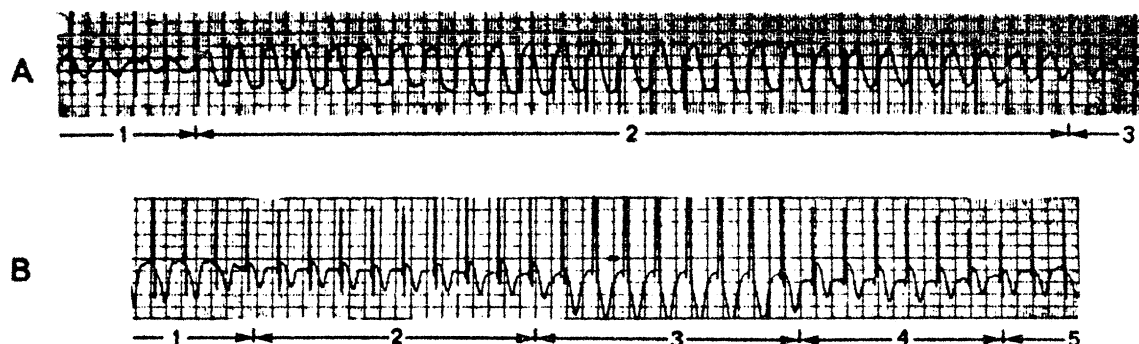


Figure 8

*The spatial characteristics of infarction block. Panel A) The epicardial electrogram as the electrode is swept continuously from a nonschemic area (1), to the center of an ischemic area (2), to a nonschemic area (3) in a dog without infarction block. Panel B: A sweep from a nonschemic area (1) to the margin of the ischemic area (2), to the center of the ischemic area (3), to the opposite margin of the ischemic area (4) to a nonschemic area (5) in a dog with a localized intraventricular conduction disturbance. Note the QRS prolongation and lack of ST segment elevation in the center of the area of ischemia.*

FIGURE 1.9 - Continuous a-c sweep recording of the epicardial electrogram during ischemia [Muller et al (1975)]. Panel A shows a maximum ST-TQ shift at the center of the ischemic zone, while panel B shows a maximum ST-TQ shift at the border of the ischemic zone.

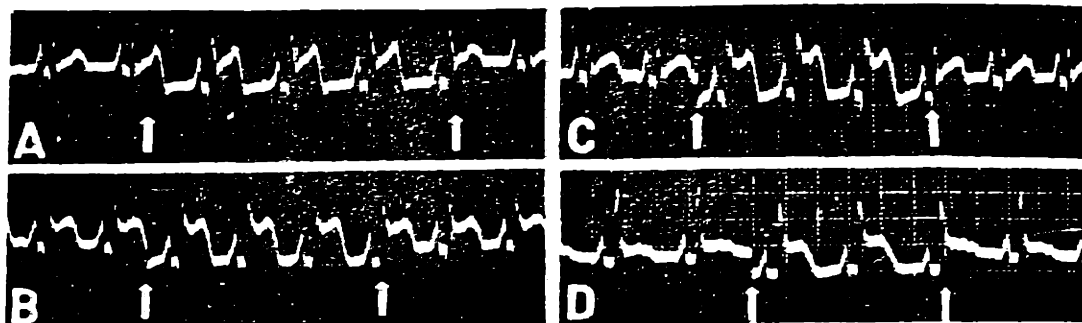


Fig. 2. A, B, C. November 3, 1942. Dog 9.0 kgm. Dial anesthesia. Infarct on posterior surface of left ventricle near apex. A. Small infarct totally insulated by small insulation size of plates (2.0 cm. in dia.). Between arrows the insulation was short-circuited. B. Larger infarct not totally covered by insulation the same size as short-circuiting plates. Between arrows the insulation was short-circuited. C. Large infarct totally covered by insulation much greater in area than the short-circuiting plates. Between arrows the insulation was short-circuited. D. September 9, 1942. Dog, 8.0 kgm. Dial anesthesia. Insulation of burned area on left apex 1.5 cm. in diameter. Between arrows the insulation was short-circuited. All records are lead III.

FIGURE 1.10 - Early evidence for d-c baseline currents during ischemia [Nahum et al (1943)]. Panels A and C are for ischemic zones which were totally insulated and then connected to the body. Panel B is for an ischemic zone only partially insulated, and panel D is for injury due to burning.

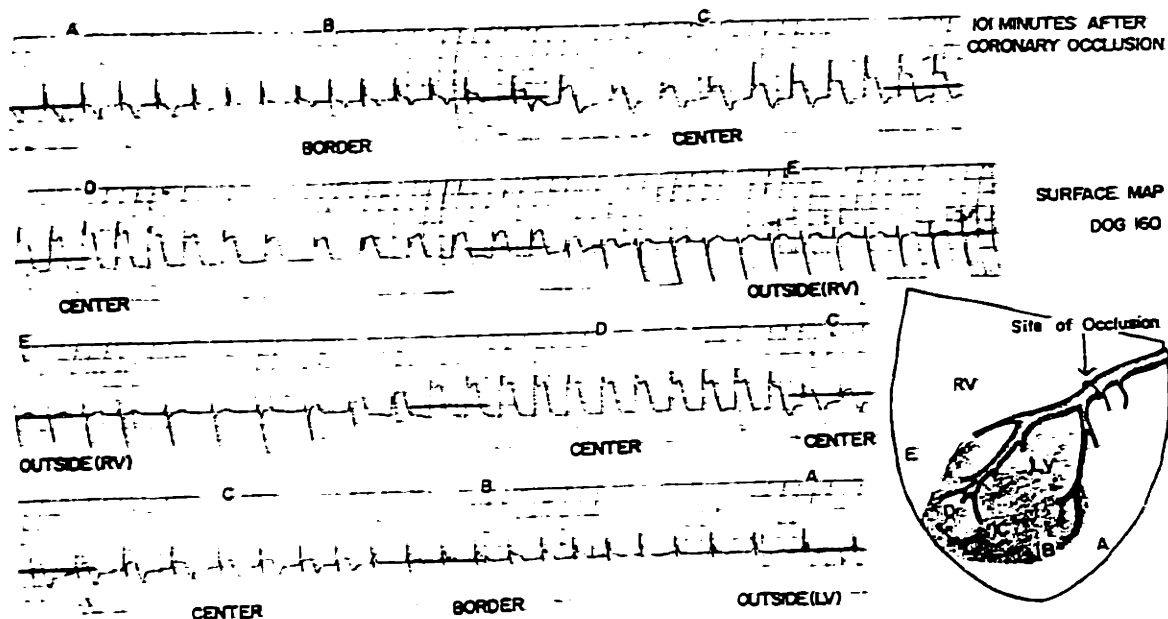


Figure 1

*Prolonged Coronary Occlusion: Single, Continuous Sweep Record from Central, Border and Outside Areas.*

The electrode was not removed from the heart while passing from position A (outside) through the ischemic area to position E (outside) and back again. There is no potential difference between baselines (level indicated by heaviest lines on record) and RS-T segments between areas A and E. The heaviest lines indicated the level of the baseline of the control areas. Slight differences of T-wave and QRS configuration are present due to differences of electrode placement.

The borders of the ischemic region (just within the area of cyanosis) show slight segment elevation without baseline depression. Along the line of this sweep there are no intervening islands of RS-T segment depression between outside and border areas. The centers show both elevation of the RS-T segment and depression of the baseline. Baseline depression in the center of the area reached a maximum 55 min. after the occlusion, when it was twice the amplitude seen in this record.

FIGURE 1.11 - Continuous d-c sweep recording of the epicardial electrogram during ischemia [Katcher et al (1960)]. Both TQ and ST shifts are seen in the ischemic zone, with maximum deviations at the center of the zone.

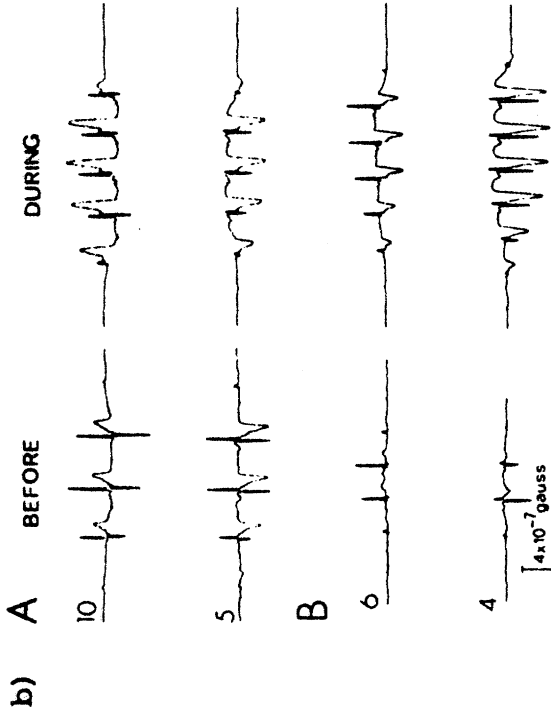


**FIGURE 4**  
 Selected d-c MCG records from two dogs showing the typical effect of occlusion; the resulting S-T and base-line shifts are approximately equal and opposite. In A (dog 3), DURING refers to a time 17 minutes after the final occlusion. In B, it refers to 2 minutes of a 5-minute trial (dog 4). The two positions for each dog were selected to illustrate that the opposing shifts are independent of polarity or position.

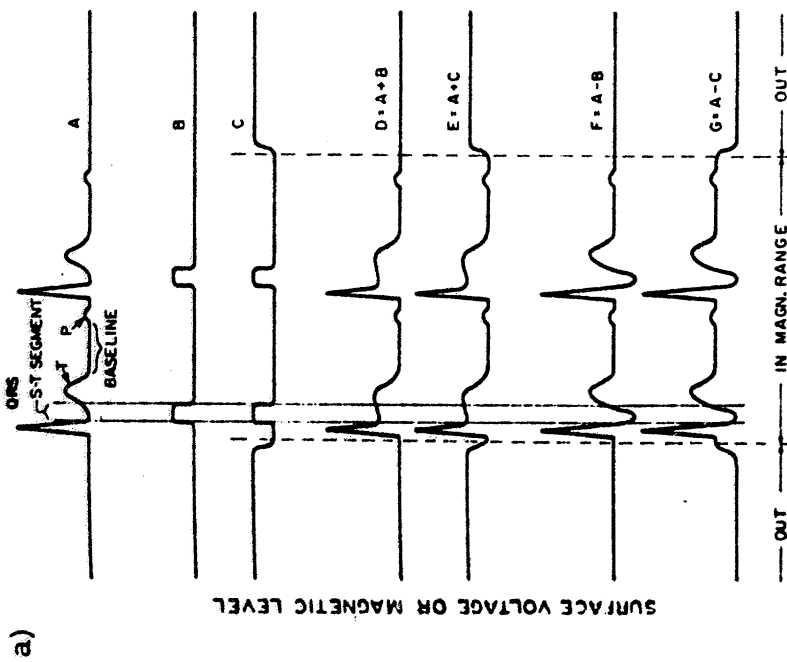


**FIGURE 1**  
 S-T segment shift formed either in a primary or a secondary way. The ordinate can be either the external magnetic field (d-c MCG) or the surface voltage (ECG). The d-c MCG is a three-step tracing: torso out of magnetometer range, in range, then out of range again. The base-line shift between the middle and the out-of-range position is a measurement of the steady field. The ECG, with arbitrary base line, can only show the middle portion. A: Normal tracing. B: Primary S-T event. C: Secondary event. D or F: A combined with B. E or G: A combined with C.

**FIGURE 1,12 - Ischemic magnetocardiogram [Cohen and Kaufman (1975)]**

- a) All possible combinations of TQ and ST shifts
- b) Observed waveforms - note that in the description, "S-T shift" refers to a ST-TQ shift

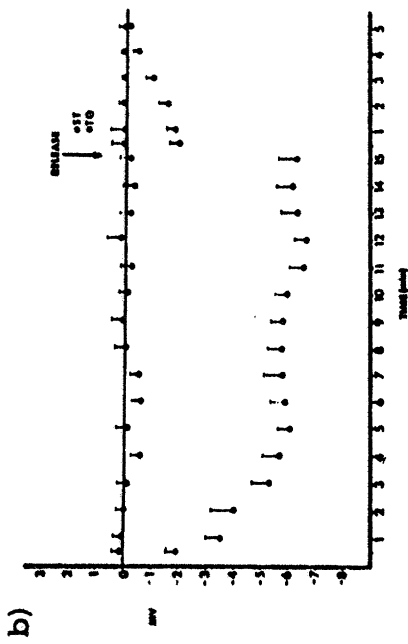


FIGURE 3. The time course and magnitude of potential changes occurring during 15 minute coronary artery occlusion. In these animals the pericardial sac and chest wall were closed after electrode application. The data are from four experiments in which 14 electrograms were recorded. Mean values and standard error for TQ and ST change are shown. Comparing TQ and ST,  $P < 0.001$  at each point in time of occlusion. The mean ST segment remains essentially at the control level. Significant TQ depression develops, with rapid decrease in TQ level for the first five minutes, and a slower rate of change through 15 minutes.

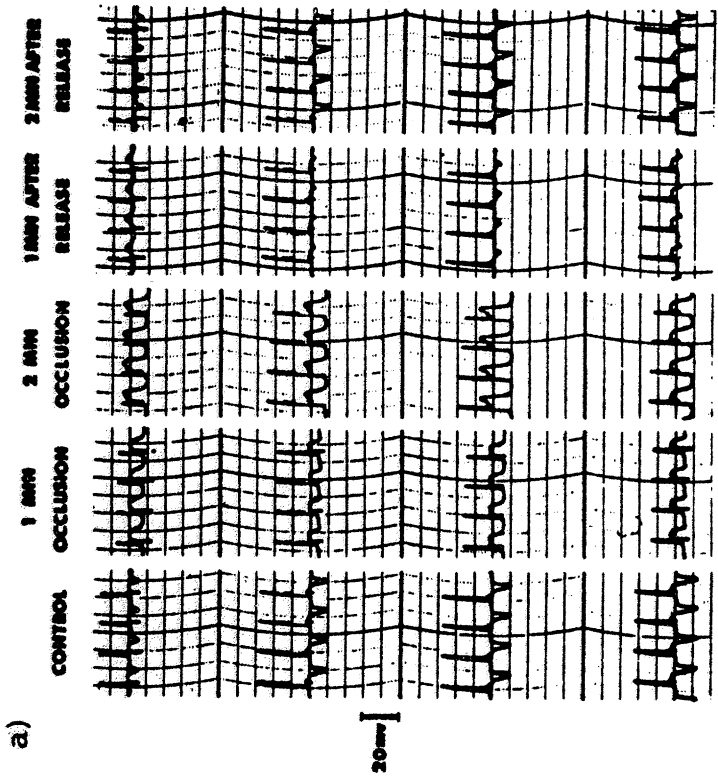


FIGURE 2. Simultaneous epicardial electrograms recorded from four electrodes. The electrodes were distributed randomly in the ischemic area, with some more toward the center of the ischemic area than others. At one minute of occlusion TQ depression is apparent in all recordings. After two minutes of occlusion the TQ depression has increased. The ST-segment take-off is slightly elevated or isoelectric in all recordings. The marked change in T waveform is apparent, and this figure emphasizes that major changes in action potential downstroke shape and timing can occur without significant alteration of phase 2 and the true ST segment.

FIGURE 1.13 - Temporal development of shift in the TQ and ST segments of the epicardial electrogram following an acute coronary occlusion [Vincent et al (1977)].

- a) Typical recordings
- b) Plot of data over a 15 minute period of occlusion

## CHAPTER 2: Previous Analytical Models

Previous models used to describe the potential distribution in cardiac muscle can be classified into the following four categories: 1) cable models; 2) branching networks; 3) biologically microscopic field models; and 4) biologically macroscopic field models. In this chapter we review, class by class, a number of the models reported in the literature. The models of greatest applicability to recordings made by the experimental cardiologist are the macroscopic field models, since these models describe the potentials which arise from a large population of cells, as measured by gross electrodes having dimensions on the order of  $10^2$  cell lengths.

### 2-A. Cable models

Many of the theoretical models which have been used to interpret experimental, electrical measurements obtained under the conditions of electrotonus (passive spread) or excitation in the ventricular myocardium are based on the one-dimensional, distributed cable model developed specifically for nerve axons [Hodgkin and Rushton (1946), Lorente de No (1947)]. Similar models have recently been used to describe the electrical behavior of isolated, cylindrical preparations of ventricular myocardium (either trabecular or papillary muscle). A one-dimensional cable

model was used by Weidmann to derive cable parameters for sheep trabeculae (1970). Lieberman et al (1975) used a more extravagant model, incorporating membrane folding and other morphological parameters to obtain cable parameters for cultured strands of chick myocardium. Clerc (1976) used one-dimensional analysis in two orthogonal directions to obtain directional cable parameters for anisotropic calf trabeculae.

A two-dimensional cable-like model was proposed by Woodbury and Crill (1961) to describe the passive spread of current in a thin-walled, atrial myocardial preparation. Their "flat plane" model described the intracellular space as a plane and the extracellular space as two adjacent, parallel planes, one on either side of the intracellular plane. Shiba and Kanno (1971) refined this model to account for anisotropy and for microelectrode point sources of current. Joyner et al (1975) developed a two-dimensional cable model in conjunction with the Hodgkin-Huxley (1952) equations to simulate the propagation of action potentials.

Three-dimensional models have only recently been proposed by Jack et al (1975) for electrically connected, but sourceless tissues; Barr and Jakobsson (1976) for sourceless, radially symmetric, smooth muscle, and Tung (1976) for cardiac muscle with a generalized (non-symmetric) geometry and source distribution.

### 2-B. Branching networks

A second type of model is the lattice array, or branching network. This is typified by the models of George (1961), Berkinblit et al (1965), Tanaka and Sasaki (1966), Smolyaninov (1971), and Eifler and Plonsey (1975). Each branch corresponds to a single myocardial cell (length on the order of .1 mm). These models consist of two- or three-dimensional nodal networks, with branches described either as lumped circuits or as distributed cables. These models were derived not only to describe electrotonic spread or activation from point sources, but also to estimate the dependence of the input resistance of intracellular microelectrodes upon the membrane resistance. The extracellular potentials can be computed on a point by point basis, using matrix algebra and numerical techniques. Unfortunately, in practice these models are incapable of describing potential distributions over volumes whose dimensions are on the order of 1-10 cm.

### 2-C. Biologically microscopic field models

A third type of model is the electrical field model intended to describe the current and potential distributions inside single cells resulting from the injection of current via microelectrodes. The mathematical techniques used have included eigenfunction expansions and singular perturbation analysis [Hellerstein (1968), Eisenberg and Johnson (1970),



Engel et al (1972), Peskoff and Eisenberg (1973,1975), Peskoff et al (1976)] for cases of cylindrical, spherical, and rectangular symmetry. These solutions are particularly important in interpreting microelectrode recordings of potentials arising from intracellular microelectrode current sources.

#### 2-D. Biologically macroscopic field models

These field models differ from the microscopic models of the previous section in that the particular volume distribution of the cellular membrane is not considered, because the local behavior around the membrane over dimensions on the order of a cell length is not of interest. Instead, the potentials of interest are those arising in a volume of tissue containing on the order of  $10^6 - 10^8$  cells, measured with electrodes which span on the order of  $10^4$  cells in cross section. One such macroscopic model is the solid angle model, a model most commonly used by experimental cardiologists to describe the distribution of ischemic ST-TQ segment shifts. These potentials are measured by gross surface electrodes either on the epicardium or on the chest. The cellular sources are taken to be on a surface which forms the border between ischemic and healthy tissue, and the magnitude of ST-TQ shift is taken to be proportional to the solid angle subtended by that surface as viewed from the recording site. We shall describe this model in greater

detail in the next chapter.

The subject of this thesis, the bi-domain model, is a hybrid between a biologically macroscopic field formulation and a three-dimensional cable formulation. As a macroscopic model, it describes the electric fields arising from a generalized source geometry, taking into account the effects of boundaries. As a three-dimensional cable, it differentiates current flow between that in intracellular space and that in extracellular space. The cellular membrane acts as an insulator between the two spaces, and a parameter analogous to the "space constant" parameter of cable theory can be defined. We shall discuss the basis and derivation of the bi-domain model in full detail in Chapter 4.

### CHAPTER 3: Use of the "Solid Angle" Model

We refer to the model most commonly used to describe the ischemic ST-TQ segment shift as the "solid angle" model, because in this model the ischemic shift is predicted to be directly proportional to the solid angle subtended by the border surface of an ischemic zone as seen from the recording electrode [illustrated in Fig. 3.1, taken from Holland and Brooks (1977a)]. This border surface is assumed to lie at the interface between healthy and ischemic myocardium. The polarity of the ischemic shift depends on the side of the border surface on which the recording electrode lies. The solid angle model is derived from classical electrostatic field theory for the situation of potentials arising in a volume conductor with a dipole layer source distributed over a surface. In this chapter we describe the significance and utility of the solid angle model to the cardiologist, and in Chapter 6 we shall examine in detail the basic physical and mathematical assumptions that underlie the model.

#### 3-A. Historical development

The theory for the electrical origin of the ST-TQ segment shift was slow to evolve (refer to the time line, Fig. 1.3). Perhaps the earliest formalization was the theory for "currents of injury", proposed by Wilson et al in 1933 for single myocardial fibers. Injury was defined as a state

of myocardium resulting in complete cellular depolarization during the entire cardiac cycle. Solid angle theory was used to obtain a quantitative relationship between the observed extracellular injury potential and an equivalent source, taken to be a current dipole layer distributed over a disk, lying across the intracellular space and separating the injured and healthy regions of the fiber. The source strength was taken to be proportional to the healthy membrane potential. However, three assumptions were made. First, the fiber was taken to be lying in an infinite conductive medium. Second, the intracellular and extracellular resistivities were assumed to be the same, and third, the width of the interface between healthy and injured myocardium was taken to be very small (much smaller than the fiber diameter).

In 1958, Bayley developed these concepts, first to extend Wilson's arguments for a single, injured fiber lying in an infinite medium to the complex fiber network found in myocardium, and second to identify the injury potential as the change in the height of the ST-TQ segment. The same three assumptions were implicitly made - the heart was taken to lie in an infinite medium; the heart and surrounding medium resistivities were taken to be the same; and the border between injured and healthy myocardium was taken to be abrupt (compared to the dimensions of the heart). As we noted in Chapter 1, the ST-TQ segment distribution can display both positive (primary) and negative (reciprocal)

polarities. Bayley's explanation for these polarities was complicated by the fact that the polarity of the source (positive or negative) could be defined at two instants of time (the TQ interval or the ST interval); hence, four possible combinations of source time-polarity were possible, although in practice only one combination - positive over the TQ interval and negative over the ST interval - was used. An equivalent source was assumed at the interface between healthy and injured tissue; this source was taken to be a dipole sheet during diastole (TQ interval) and another dipole sheet reversed in polarity during systole (ST interval). The reversal in the source polarity was to account for the fact that when the membranes of healthy cells depolarize, the gradient between the membrane potentials of healthy and injured cells reverses direction, provided that the injured cell membrane depolarizes incompletely. As we shall see in Chapter 6, this gradient in membrane potential acts as an equivalent current source. As a result, injury potentials with opposite polarities were predicted for the diastolic and systolic time intervals, with the difference in their values appearing as the ST-TQ segment. Depending on the shape of the injured zone and the relative location of the recording electrode (Fig. 3.2), different polarities could be predicted for the injury potential. Bayley depicted his equivalent sources as charge dipole sources, although it is more common to describe sources in conductive media as current sources.

He did not, however, describe the physical interpretation of his sources in detail, and this lack of a physical description for the sources is common among all of the models used to describe ischemic potentials.

A summary of the solid angle theory by Scher (Handbook of Physiology, 1962) presented a very confused picture for the electrical sources (Fig. 3.3). Charge dipoles were drawn at the epicardial (outside) and endocardial (inside) surfaces of the heart, although they were apparently intended to depict sources at the surface of the cell membrane, separating the inside and outside of a cell, rather than the inside and outside of the heart.

In 1965, Plonsey provided a theory more complex than that of Wilson et al by applying the Green's theorem to a microscopic description of individual cell membrane surfaces (see Appendix E). Although his formulation was intended to describe activation, we bring it into the discussion since it has been adapted by others to describe ischemia. Equivalent membrane sources were derived as a function of the intracellular and extracellular potentials at the membrane, although their relationship to physical processes at the membrane was not discussed. The extracellular potential was shown to be proportional to the solid angle subtended by the equivalent source, and the intracellular and extracellular resistivities were not constrained to be the same. Unfortunately, the resulting formulation was not very useful,

since the extracellular potential at the observation point was an implicit function of both the intracellular and the extracellular potentials at the membrane throughout space. In addition, Plonsey's sources were composed of terms which could not be interpreted physically. In a later paper (1974), Plonsey bypassed this restriction by ultimately resorting to a set of cable relationships between intracellular, extracellular, and transmembrane potentials, to obtain a source whose magnitude was proportional to the transmembrane potential.

### 3-B. Recent applications

Today, primarily through the efforts of Holland and Brooks (1975,1977a,1977b), the solid angle model is used to describe the ischemic ST-TQ segment shift in both precordial (chest) and epicardial surface leads. Holland and Brooks used solid angle analysis, but without the appropriate boundary conditions, to obtain quantitative spatial distributions of precordial and epicardial ischemic potentials in the pig. The theory for the analysis was adapted for ischemia from Plonsey's results (1974), which we recall described models of activation. Simple trigonometric models for various geometries of ischemic zones permitted calculations of the potential profiles. One significant result was the prediction that the ischemic ST-TQ segment shift, measured on the epicardium, decreases in magnitude

(note the concavity) as the center of the ischemic zone is approached (Fig. 3.4) [Holland and Brooks (1977b)]. This clearly has direct implications to those investigators who hope to use the magnitude of the ST-TQ segment as an index of local myocardial ischemia. The work of Muller et al (1975) (cf. Fig. 1.9) was cited as evidence supporting this prediction. Another consequence of the solid angle model is that ischemic zones entirely embedded in a healthy region of tissue (i.e. intramural ischemic zones) should be "electrically silent". That is, a zero potential will be observed at an electrode placed outside the ischemic zone, since the total solid angle subtended at the electrode is zero. We shall return to a discussion of these issues in Chapter 8.

Finally, we note that there seems to be a growing trend to use the solid angle model [Fozzard and DasGupta (1976), Richeson et al (1977)] without regard for the assumptions underlying the model. Holland and Arnsdorf (1977) published a paper describing "physiologic and quantitative interpretations" of both ischemic and activation potentials, using the solid angle model. In their rather brief discussion of the theory, they dismissed the limitations of the model. We shall summarize these limitations in the next section, and conclude that the assumptions underlying the solid angle model are inadequate for the experimental situations we have described in Chapter 1.



### 3-C. Difficulties with the solid angle model

Despite the present popularity of the solid angle model, its predictions have not yet been validated in experiments in which control of the geometry of the ischemic zone was attempted. Yet, this model has been commonly accepted to such a degree that it has been used by various investigators [Holland and Brooks (1975,1977a,1977b)] to lend "theoretical" credence to the interpretations of their data. Ironically, we note that from a theoretical point of view (Chapter 6), the solid angle model is inadequate in several respects. We summarize those results here.

The cardiac medium under consideration is not infinite, and this is particularly so for the open chest preparation. Even in the closed chest, where we allow for current flow through the surrounding body tissue and approximate the composite heart/body system as an "infinite" medium, changes in conductivity across the epicardial and endocardial surfaces will alter the flow of current. Consequently we have the objection that boundary conditions are ignored. Other investigators have shown significant effects of the body and the blood in the intraventricular cavity on the ECG [McFee and Rush (1967), Nagata (1970)].

We also conclude that it is not sufficient to describe the ischemic sources as a current dipole layer for several reasons. First, (as we shall discuss in Chapter 6-B) there are cases in which conservation of charge will be violated by

such a representation. Second, the representation of the ischemic sources at the border between ischemic and healthy tissue lacks a physical interpretation. Moreover, we seek a source description which is volume-distributed and which reflects the local ischemic condition, on a point by point basis. And third, we would like to be able to represent a diffuse border for the ischemic zone, which cannot now be described using the solid angle model. Such a representation is motivated by recent research into the width of the border zone. The volume of myocardium comprising the border zone represents the region of myocardium which is most likely to be potentially salvageable, if the proper hemodynamic or pharmacologic intervention could be found. There are investigators who regard the ischemic border as being abrupt, having a width of 1-2 mm [Hirzel et al (1977), Factor et al (1977)], and those who regard the border as being diffuse, having a width of 5-8 mm [Becker et al (1973), Hearse et al (1977)].

The bi-domain model which is proposed in the next chapter meets the various objections listed above. We shall return to the detailed mathematics of the solid angle model and its relationship to the bi-domain model in Chapter 6.

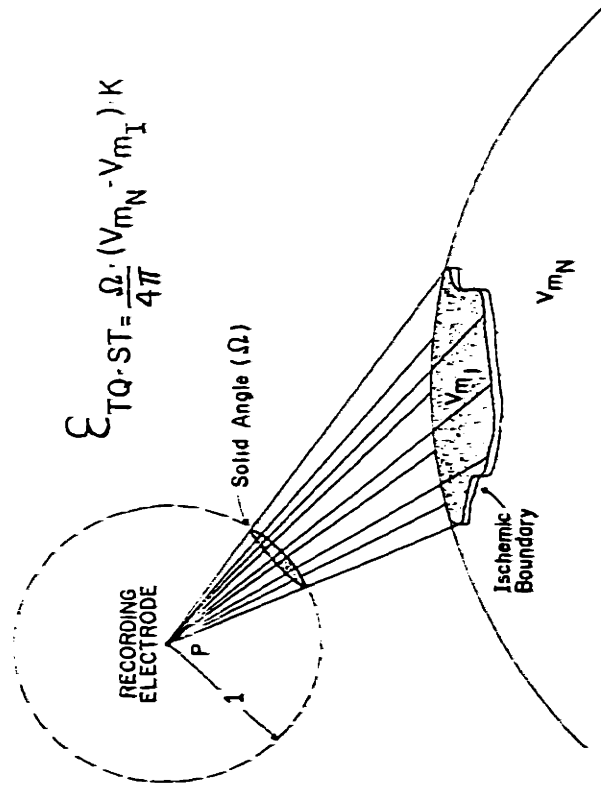


FIGURE 4. Mathematical and pictorial characterization of the solid angle theory. The TQ-ST segment voltage recorded at the electrode is given by the equation. The solid angle  $\Omega$  is defined as the area of spherical surface cut off a unit sphere (inscribed about the recording electrode) by a cone (formed by straight lines extending between the recording electrode and every point along the ischemic boundary. The ischemic boundary is a source of current flow established by differences in the transmembrane potentials of the normal ( $V_{mN}$ ) and ischemic ( $V_{mI}$ ) cells during diastole and systole.  $K$  is a term correcting for differences in intra- and extracellular conductivity and the occupancy of much of the heart muscle by interstitial tissue and space.

FIGURE 3.1 - The mathematical definition of the solid angle model  
[Holland and Brooks (1977a)]

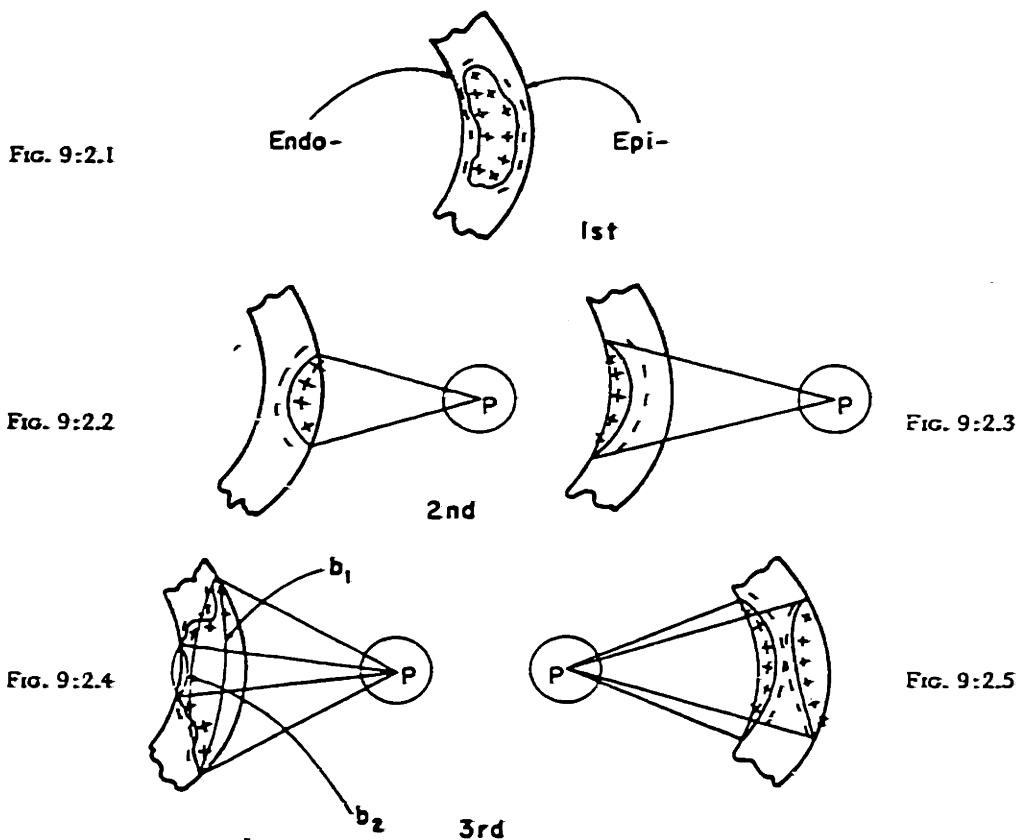


FIG. 9:2.1. Intramural injury where the double layer of injury is depicted during systole in the form of a closed surface.

FIG. 9:2.2. Epicardial surface injury. At P the solid angle  $\Omega_t$  subtended by the epicardial surface boundary of the double layer of injury is positive during systole.

FIG. 9:2.3. Endocardial surface injury. At P the solid angle  $\Omega_t$  subtended by the endocardial surface boundary of the double layer of injury is negative during systole.

FIG. 9:2.4. Transmural injury. The double layer of injury is of the third kind [2:10] with boundaries  $b_1$  and  $b_2$  at the epicardial and at the endocardial surfaces respectively. The solid angle at P is positive, a difference in the two indicated solid angles. The distribution is that ordinarily suggested for acute myocardial infarction.

FIG. 9:2.5. Transmural injury. Aside from the solid angle at P, the magnitude of the injury effect is proportional to the difference in the intensity of subnormal polarization at the two surfaces.

FIGURE 3.2 - The ischemic zones of interest: subepicardial, subendocardial, transmural, and intramural [Bayley (1958)].

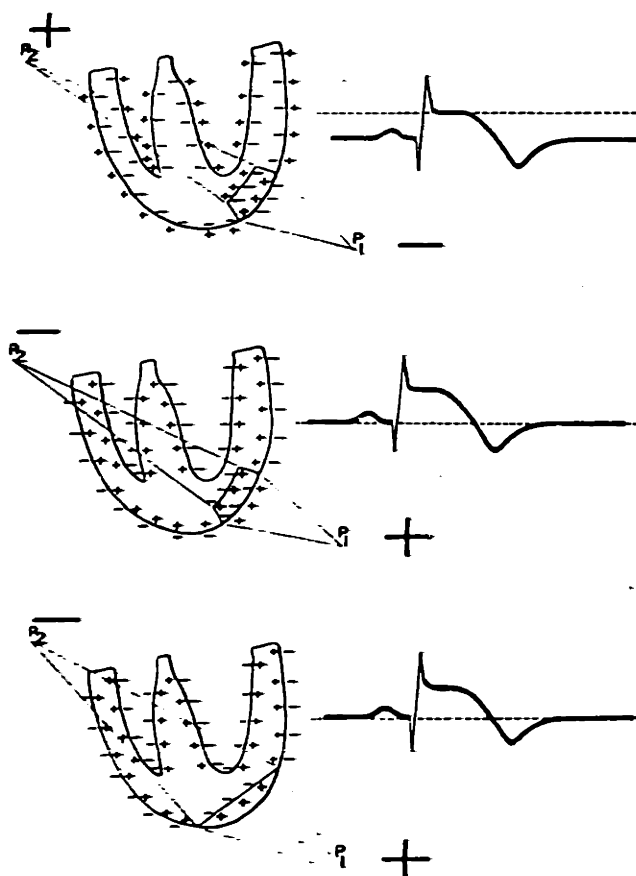


FIG. 41. Three possible mechanisms for S-T segment changes. In the top drawing, the base line is depressed at rest, i.e., during the T-Q interval. Since the injured cells are partially depolarized during this period, current flows into them. When all cells are uniformly depolarized during the S-T interval, the base line is at true zero. In the second case, the base line is normal at rest but elevated during the S-T interval due to a shortening of the action potential duration in the injured cells. In the third case, the injured cells cannot depolarize. A wave of activity reaches the border of the injured region but cannot invade it, so that the S-T segment is elevated. The second of these states occurs early in experimental infarction and is followed by the first.

FIGURE 3.3 - The theory for the ischemic ST-TQ segment in 1962 [Scher (1962)]

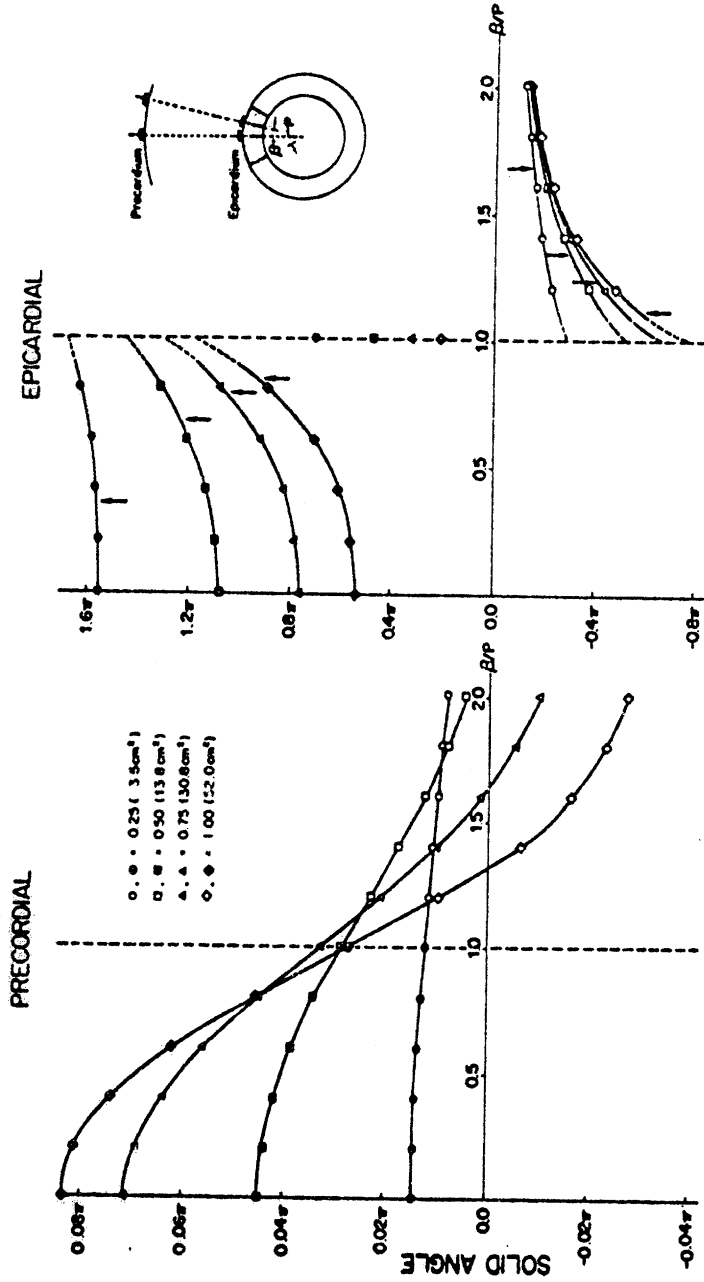


FIGURE 4 Influence of electrode position with respect to the ischemic boundary (dashed vertical line) on the polarity and magnitude of the solid angle computed at precordial and epicardial locations for different ischemic areas. Electrodes overlying ischemic regions (solid symbols) have positive solid angle values at either location. On the precordium, negative solid angle values occur at sites distant from the boundary while at the epicardium negative values are recorded from all nonischemic regions (clear symbols). Dashed lines indicate uncertainty of solid angle values at the epicardium and in the vicinity of the ischemic boundary. Arrows identify solid angle values at epicardial sites within 0.5 cm of ischemic boundary. Note that at the epicardium the negative solid angle values in the nonischemic region increase in magnitude with increases in ischemic area despite a reduction in the magnitude of the positive solid angle values of the ischemic region.

FIGURE 3.4 - Predicted precordial (chest) and epicardial surface distributions for the ischemic ST-TQ segment for various types of ischemic zones [Holland and Brooks (1977b)]. The solid angle subtended by the ischemic border surface is plotted, and the ischemic ST-TQ shift is assumed to be proportional to the solid angle. Note that there is a maximum predicted ST-TQ shift on the epicardium at sites over the border surface, with a relative minimum over the center of the ischemic zone.

## CHAPTER 4: The Bi-Domain Model

We begin this chapter by describing the physical basis for the bi-domain model and modifying the notions of Ohm's law and charge conservation (sections 4-A and 4-B). We are then able to describe the ischemic myocardium by a general set of bi-domain equations (section 4-C), whose general solutions are derived (section 4-D) subject to the appropriate boundary conditions (section 4-E). We examine two examples which illustrate the two modes of operation of the bi-domain model (section 4-F). Finally, we show that a mono-domain is a degenerate case of a bi-domain (section 4-G). The results are summarized in section 4-H.

### 4-A. Electrically coupled cells and interpenetrating domains

In Chapter 2-D we discussed the applicability of biologically macroscopic field models to a class of experimental situations. We will shortly discuss precisely what we mean by "macroscopic" as opposed to "microscopic" in the context of the bi-domain model, but first we would like to describe one approach which has been used to derive a biologically macroscopic field model from an essentially microscopic field description. It begins with a description of a single nerve or muscle cell lying in an infinite, homogeneous, isotropic, volume conductor. Assuming that the cell acts as an electrical source, the resulting

extracellular potential can be derived. If all the cellular elements in the tissue are independent of one another (i.e. there are no cellular interactions), superposition can be applied to the individual microscopic cellular descriptions to arrive at the composite macroscopic model. The model thus derived is generally mathematically complex, and since it is derived from a microscopic description, it requires a detailed knowledge of the underlying microscopic structure. An example of such a model is Plonsey's solid angle formulation, described in Appendix E.

However, for a number of tissue systems the cellular sources are not independent of each other but rather are interactive, since the intracellular spaces are electrically interconnected via low resistance membrane junctions. For example, in cardiac muscle the electrical connections appear to occur at the nexuses of the intercalated discs [Berger (1972)]. Several classical studies have demonstrated functional cell-to-cell coupling. Woodbury and Crill (1961) obtained a two-dimensional electrotonic spread of current from a microelectrode point source in a sheet of atrial myocardium. Barr and Berger (1964) used a sucrose gap preparation to test whether activity was propagated across an isolated myocardial fiber via chemical or electrical means. The sucrose gap prevented the flow of electrical current in the extracellular space, and action potentials were unable to propagate across the gap. However, when an external return



path for current was provided across the gap, action potentials were able to propagate, strongly suggesting that the intracellular spaces of the myocardial cells were electrically interconnected. Weidmann (1966) used radioactive potassium to measure the longitudinal intracellular diffusion time to obtain a low estimated value for the cell-to-cell resistance. Other examples of electrically coupled tissue systems are epithelial tissue and smooth muscle.

In general, electrically coupled tissue systems consist of an intertwining of electrically connected extracellular and intracellular spaces separated by a complicated, "crinkled" membrane boundary. Consequently, the structure is a complex, passive ohmic conductor whose various extracellular and intracellular spaces permit the flow of ionic currents in the neighborhood of individual cells. However, we are not concerned with the local behavior of potential or current density around single cells. Instead, electrical signals of clinical interest are generally potentials arising from large ( $10^6 - 10^7$ ) populations of cells, measured with electrodes which span perhaps  $10^2$  cells in cross-section. We refer to these potentials as "macroscopic" potentials, a spatial average of the local, "microscopic" potentials which would be measured on a cellular level with microelectrodes. We shall also be concerned with the "macroscopic" current density defined over cross-sectional areas hundreds of cells in diameter. This

"macroscopic" current density, oriented along the macroscopic electric field, is to be distinguished from the "microscopic" current density, defined over a distance scale on the order of a cell length and oriented along the individual myocardial cell axis. The bi-domain model to be discussed attempts to describe the spatial distribution of the "macroscopic" potential as it is measured on the heart surface.

If there is a sufficiently complex microstructure in which the extracellular and intracellular spaces are interconnected, highly packed (with respect to macroscopic dimensions), and randomly oriented, we consider each space separately as a distinct, homogeneous mono-domain structure, for the purposes of describing a macroscopic potential and current density in that domain. In this work we will use the word "space" to refer to the convoluted, microscopic description for the intracellular and extracellular volumes, and the word "domain" to refer to the homogeneous, macroscopic description. We then distinguish between the potential and current flow in the intracellular space, and the potential and current flow in the extracellular space, as illustrated in Fig. 4.1. Although the two spaces are physically separate, their description as macroscopic domains will require that they occupy the same 3-D space and overlap at every point. The coupling between domains is through the cell membrane, macroscopically viewed as a volume-distributed insulating boundary which separates the two domains. We

refer to the composite structure as a "bi-domain structure". The bi-domain structure developed here is a detailed, quantitative realization of the concept of interpenetrating domains, described qualitatively by Schmitt (1969). The development which follows is both an extension of cable theory into three dimensions and a field-theoretic description.

Inasmuch as we are pursuing a macroscopic bi-domain model, it will be necessary to convert the microscopic electrical variables into macroscopic variables. We shall take the macroscopic (dimensions on the order of several hundred cell lengths) potential  $\phi$  and current density  $J$  to be spatial averages of the microscopic (dimensions on the order of a cell length) quantities  $\hat{\phi}$  and  $\hat{J}$ . In order to be consistent with classical volume conductor descriptions, the potential and current density in each of the two domains must satisfy a constitutive law of conduction and charge conservation. We will return to the statement of charge conservation in the next section and turn now to the constitutive conduction relationship between potential and current density, which takes the form of Ohm's law,

$$-\nabla\phi = PJ \quad (4.1)$$

where  $P$  has the usual dimensions of resistivity, ohm-cm. The macroscopic resistivity ( $P$ ) can be related to the microscopic resistivity ( $\rho$ ) for each of the two domains by a geometric factor ( $a$ ) which depends on cell orientation. We proceed to

derive this geometric factor here for cells whose longitudinal axes are aligned in parallel. In doing so we will need to make some assumptions regarding the relationship between the macroscopic variables  $\phi$  and  $J$ , and the microscopic variables  $\hat{\phi}$  and  $\hat{J}$ . We will then argue how these results are modified for cells which are randomly oriented. In the discussion which follows, the subscript "o" will be used to denote the extracellular medium, the subscript "i" the intracellular medium, and the subscript "m" the cell membrane.

We begin by defining more precisely the scale of distance implicit in our use of the terms "macroscopic" and "microscopic". The following discussion is complicated, since there are three characteristic dimensions of importance - the cell membrane thickness (on the order of  $10^{-6}$  cm), the cell diameter or length (on the order of  $10^{-3}$ - $10^{-2}$  cm), and the recording electrode diameter (on the order of 1 cm). Potential variations over dimensions on the order of the membrane thickness have usually been ignored in the literature, even for microelectrode measurements. Therefore we will neglect potential variations over distances on this scale. In fact, we shall assume that the actual intracellular or extracellular potential is constant over distances on the order of a cell length and varies only over distances on the order of 1-10 cell lengths. Consequently, we formally identify the microscopic potential with the

potential which varies over dimensions on the order of several cell lengths, and the macroscopic potential as an average of the potential over several tens of cell lengths, varying over macroscopic dimensions on the order of  $10^2$ - $10^3$  cell lengths. We make our first identification, namely that the macroscopic potential is equal to the average value of the microscopic potential over a volume large compared to microscopic dimensions, but small compared to macroscopic dimensions.

The relationship between the current densities  $J$  and  $\hat{J}$  can be established as follows. We construct the following arguments with respect to the intracellular space, although analogous arguments can be made with respect to the extracellular space. Suppose we consider the intracellular space to be contained within a set of parallel tubes or pipes, with a single tube representing the membrane of a single myocardial cell. Each tube has a cross-sectional area  $A$  and only slightly "leaky" walls, so that current is constrained to flow primarily in a direction parallel to the walls (although over many cells the total leakage is appreciable on a macroscopic scale). We refer to the current per cross-sectional area of the cell as the "microscopic", intracellular current density. In the following discussion we shall assume no doubling back of the microscopic current. Consequently in a typical cross-section we have the situation shown in Fig. 4.2. The longitudinal axis of each incremental

cellular tube has an orientation directed along the z-axis. The "macroscopic" current density is the sum of the currents (charge transferred per unit time) taken over all the intracellular cross-sectional areas, divided by the total sum of intracellular and extracellular cross-sectional areas (the macroscopic cross-sectional area). Also taking the potential gradient to be aligned along the z-axis, so that the macroscopic potential is given by  $\phi_2$  at  $z = Z$ , and  $\phi_1$  at  $z = Z+dz$ , we write for the magnitude of the macroscopic current density (directed along the z-axis),

$$J_i = \sum_{k=1}^M (\hat{J}_i)_k A \quad (4.2)$$

where  $M$  = number of cell intersections in a unit macroscopic, cross-sectional area. Since the length of each tube is given by  $dz$ , we have,

$$(\hat{J}_i)_k = \frac{-\nabla \hat{\phi}_i}{\rho_i} = \frac{1}{\rho_i} \frac{\phi_2 - \phi_1}{dz} \quad (4.3)$$

Consequently we can express  $J_i$  in the form,

$$J_i = \frac{(\phi_2 - \phi_1)/dz}{P_i} \approx \frac{-\nabla \phi_i}{P_i} \quad (4.4)$$

where:

$$P_i = \frac{\rho_i}{MA} \equiv \frac{\rho_i}{a_o} \quad (4.5a)$$

The dimensionless geometric factor  $a_i$  is simply the proportion of intracellular space in a random cross section of tissue. In a similar manner, we relate the macroscopic

and microscopic resistivities for the extracellular space as,

$$P_o = \frac{\rho_o}{a_o} \quad (4.5b)$$

where  $a_o$  is the proportion of extracellular space in a random cross section of tissue.

For the more complicated case where the fiber axes are randomly oriented, we argue that the geometric factors  $a_o, a_i$  are 1/3 the proportion of the respective space in a random cross section of tissue. This is because on the average, only 1/3 of the fibers are oriented along the axis of the macroscopic electric field, while 2/3 of the fibers are oriented in a direction normal to the field axis. Thus, the effective cross-sectional area through which current can pass is reduced by a factor of 1/3 compared to the case for parallel fibers. Since the sum of the proportions of intracellular and extracellular cross-sectional areas must be 1, we then have the relations:

$$a_o + a_i = 1 \quad , \text{ parallel orientation} \quad (4.6a)$$

$$a_o + a_i = 1/3 \quad , \text{ random orientation} \quad (4.6b)$$

The total macroscopic resistance  $\Omega$  in either domain for a block of tissue is given by the usual relation:

$$\hat{a}_{i,o} = \frac{P_{i,o} l_M}{A_M} \quad (4.7)$$

where:  $l_M$  = macroscopic length  
 $A_M$  = macroscopic cross-sectional area

#### 4-B. Membrane current flow

We turn now to the treatment of the current flow between domains. To simplify the discussion, we shall assume d-c situations. Unlike the case for classical, mono-domain structures, the divergence of current density in either one of the domains alone is no longer zero for static conditions, since current can pass from one domain to the other. Hence conservation of charge takes the form:

$$\nabla \cdot \mathbf{J} = U_m \quad (4.8)$$

where the "volumetric current density"  $U_m$  represents the flow of current from one domain to the other and has the dimensions of amp/cm<sup>3</sup>. In addition to membrane current sources, electrical sources of current (divergence of current density) can arise from externally introduced current sources (i.e. from microelectrodes). Whatever the source of current, current within either space will either "appear" or "disappear". In our initial discussion, we shall take the externally introduced sources to be zero and focus on the inter-domain currents which couple the two domains together.

As before, we wish to relate the macroscopic variables to the microscopic variables. This time, we are concerned with an inter-domain "volumetric current density", to be compared to the microscopic membrane current density. The microscopic membrane current density is distinguished into active and passive components. The active membrane current results from some sort of active process at the cell membrane



which converts chemical energy to electrical energy, and behaves as an active current source,  $J_a$  with units of amp/cm<sup>2</sup>, to maintain the intracellular and extracellular ionic balance. The source may be explained in terms of a Hodgkin-Huxley (1952) battery created by the ionic gradients across the membrane, or as an active, electrogenic (sodium) pump [Thomas (1972)]. To complete the membrane description on a microscopic level, we take the passive component of the inter-domain current to be directly proportional to the membrane potential (according to an area-specific membrane resistance  $r_m$  with units of ohm-cm<sup>2</sup>). The total, large-signal current-voltage relationship for the membrane can be derived from either the empirical Hodgkin-Huxley equations or the theoretical constant-field Goldman equations. The equivalent Norton circuit representation for the cell membrane is illustrated in Fig. 4.3. The vector  $\underline{d}$  is directed normal to the membrane surface and has a magnitude  $d$  equal to the membrane thickness. We will shortly assume a random orientation for  $\underline{d}$ , so that only the magnitude of  $\underline{d}$  will enter the formulation. However, other authors generally retain the vector  $\underline{d}$  to justify models containing dipole sources.

In applying the model of Fig. 4.3 to ischemia, we shall consider the ischemic condition to be a perturbation around the normal (healthy) state. This notion is supported by the observation that the effects of ischemia are initially

reversible. We incorporate the effect of ischemia in the bi-domain model as a reduction of the intensity of the active membrane current [Kardesch et al (1958)]. Thus, we are concerned with a "small-signal" model in which the normal current sources are subtracted out, and we are left with the ischemic deviations. Since we shall assume that the ischemic condition results in a reduction of  $J_a$ , we are left with a source distribution  $J_{ms}$  which has a polarity opposite to that of  $J_a$ , as shown in Fig. 4.4. Consequently, the d-c ischemic potentials are deviations in the normal baseline potential (usually taken to be zero, or "isoelectric").

Suppose we now consider the distribution of currents arising from membrane current sources distributed in a three-dimensional (3-D) bi-domain structure. We argue that over dimensions small on the macroscopic scale, but large on the microscopic scale [i.e. on the order of 10 cell lengths], the orientations of the individual current sources in a given local region will cancel each other out due to the random structure. Hence, the macroscopic membrane current source which represents the sum of the local microscopic current sources has no net orientation with respect to the spatial coordinates of either domain (i.e. it is "normal" to both domains). This is equivalent, from the viewpoint of either domain, to modeling the source as a scalar, and not a vector, quantity. It is only the intensity of the macroscopic current source which will determine the resulting

extracellular or intracellular distribution, and any directionality in the distribution can only arise from boundary effects or from gradients in the source intensity.

Hence, we think of current flow across the "volumetric surface" of the membrane, "normal" to 3-D space. We depict this situation in Fig. 4.5 for a differential membrane current source,  $U_m$ . From the viewpoint of each domain, there is in effect a monopole current source at point Q, without a complementary source or sink of current anywhere else in the domain. However, charge conservation is preserved, since in the overall bi-domain system the complementary source or sink does exist and lies at the corresponding point in the other domain. We note that the current flow in either domain is radially symmetric around the source point. In a manner analogous to the microscopic situation depicted in Fig. 4.4, we take  $U_m$ , which we shall refer to as the macroscopic "volumetric current density", to be composed of two components (having the same dimensions of amp/cm<sup>3</sup>) -- a component ( $U_{ms}$ ) due to the active transport of ions across the membrane, and a component ( $U_{mp}$ ) resulting from the passive flow of ions down their electrochemical gradients across the membrane. In this work,  $U_{ms}$  is taken to be a current source whose magnitude is independent of the transmembrane potential difference  $\phi_m (= \phi_i - \phi_o)$ , while  $U_{mp}$  is a resistive current proportional to  $\phi_m$ . We illustrate the resulting macroscopic, Norton equivalent membrane circuit in Fig. 4.6.

The volumetric current density  $U_{ms}$  emerges as a monopole current source in one domain with a coupled, complementary monopole sink at the corresponding location in the other domain. The relationship between  $U_{mp}$  and  $\phi_m$  is assumed to take the following (resistive) form:

$$U_{mp} = \frac{\phi_m}{R_m} \quad (4.9)$$

where  $R_m$  has the dimensions of ohm-cm<sup>3</sup>. We will refer to  $R_m$  as the "volume-specific membrane resistance."

Finally, we relate the macroscopic volume-specific membrane resistance ( $R_m$ ) to the microscopic area-specific membrane resistance ( $r_m = \rho_m d$ ). Just as in the microscopic case, where the total membrane resistance between domains for an area  $A_T$  is equal to the area-specific resistance divided by the membrane surface area, we take for the macroscopic case a total, inter-domain resistance  $\Omega_m$  across all of the membrane area "crinkled up" in a volume  $V_T$ :

$$\Omega_m = \frac{r_m}{A_T} \equiv \frac{R_m}{V_T} \quad (4.10)$$

where  $V_T$  is the total volume. The macroscopic and microscopic membrane specific resistances are then related in the following manner:

$$R_m = \frac{r_m}{a_m} = \frac{\rho_m d}{a_m} \quad (4.11)$$

where:  $a_m$  = total "crinkled" membrane surface area per unit volume of tissue  
 $r_m$  = membrane area-specific resistance  
 $\rho_m$  = membrane resistivity  
 $d$  = membrane thickness

With this definition, we are able to think of the membrane as a geometrically simple, continuous, volume-distributed boundary, instead of a complicated, "crinkled", boundary surface.

The geometric factor  $a_m$  is independent of cell orientation and is proportional to  $N$  (the average cell density),  $l$  (the average cell length) and  $C$  (the average cell circumference):

$$a_m = NlC \quad (4.12)$$

#### 4-C. General equations

Having redefined Ohm's law and charge conservation for a bi-domain structure, together with the appropriate macroscopic variables, we can now derive the mathematical model which describes the electrical behavior. We shall show that a simple macroscopic model can be derived to describe the extracellular potential. Mathematically, we shall see that although potentials in a volume conductive, mono-domain system must satisfy Poisson's equation, those in a volume conductive, bi-domain system must satisfy a coupled set of scalar inhomogeneous Helmholtz equations. Consequently, the properties of a bi-domain system, as viewed from either domain, differ from, yet at the same time encompass those of a mono-domain.

We take the case where: each domain subsystem is homogeneous and isotropic, a resistive coupling describes the passive interaction between domains, and a volumetric current source distribution describes the active interaction between domains. Summarizing the results of the previous two sections, we have:

$$P_o J_{-o} = -\nabla \phi_o \qquad P_i J_{-i} = -\nabla \phi_i \qquad (4.13a), (4.13b)$$

Ohm's Law

$$\nabla \cdot J_{-o} = U_{mp} - U_{ms} \qquad \nabla \cdot J_{-i} = -U_{mp} + U_{ms} \qquad (4.14a), (4.14b)$$

Charge Conservation

$$U_{mp} = \frac{\phi_m}{R_m} \qquad (4.15a)$$

$$\phi_m = \phi_i - \phi_o \qquad (4.15b)$$

| <- EXTRA- -> | <- MEMBRANE -> | <- INTRA- CELLULAR -> |

Equations 4.13 describe Ohm's Law, and equations 4.14 describe charge conservation for the intracellular and extracellular domains. Equations 4.15 describe the membrane coupling between the two domains. Because the bi-domain system has been assumed to have completely random cellular orientations, we take the geometric parameters  $a_o$ ,  $a_i$ ,  $a_m$ , and  $d$  to be independent of orientation. We shall also assume that  $\rho_o$  and  $\rho_i$  are spatially constant, so that  $P_o$  and  $P_i$  describe domains which are isotropic volume conductors. Finally, for the purposes of simplifying the analysis, we have restricted our discussion to ischemic conditions which

are perturbations around the normal steady-state, so that we may take  $R_m$  to be spatially constant. In addition, since the model describes "small-signals", it cannot be used to describe action potentials, although such a model could be derived by incorporating a different set of coupling equations (such as the Hodgkin-Huxley model) to describe the membrane behavior (equations 4.15).

Eliminating the current densities from equations 4.13-4.15 yields:

$$\nabla^2 \phi_m = \frac{1}{\lambda^2} \phi_m - (P_o + P_i) U_{ms} \quad (4.16a)$$

$$\nabla^2 \phi_o = \frac{-P_o}{R_m} \phi_m + P_o U_{ms} = \frac{-P_o}{P_o + P_i} \nabla^2 \phi_m \quad (4.16b)$$

$$\nabla^2 \phi_i = \frac{P_i}{R_m} \phi_m - P_i U_{ms} = \frac{P_i}{P_o + P_i} \nabla^2 \phi_m \quad (4.16c)$$

where:

$$\lambda = \text{space constant} = \left[ \frac{R_m}{P_o + P_i} \right]^{1/2} \quad (4.17)$$

Equations 4.16 have been written in parametric form, with  $\phi_m$  as the parameter, and equation 4.16a can be recognized as the scalar form of the inhomogeneous Helmholtz equation.

If we examine the homogeneous solutions to equations 4.16, writing  $\phi_m = \phi_H$  (a solution to the scalar inhomogeneous Helmholtz equation), we see that:

$$\nabla^2 \left( \phi_o + \frac{P_o}{P_o + P_i} \phi_H \right) = 0 \quad (4.18a)$$

$$\nabla^2 \left( \phi_i - \frac{P_i}{P_o + P_i} \phi_H \right) = 0 \quad (4.18b)$$

so that:

$$\phi_m = \phi_H \quad (4.19a)$$

$$\phi_o = \frac{-P_o}{P_o + P_i} \phi_H + \phi_L \quad (4.19b)$$

$$\phi_i = \frac{P_i}{P_o + P_i} \phi_H + \phi_L \quad (4.19c)$$

where  $\phi_L$  is a solution to Laplace's equation. The two Laplace terms in equations 4.19b and 4.19c must be identical, since  $\phi_m = \phi_i - \phi_o$ . Therefore  $\phi_L$  reflects the mono-domain characteristics of the system, since  $\phi_L$  does not distinguish between the extracellular and intracellular domain, appearing in both  $\phi_o$  and  $\phi_i$ , and is independent of the behavior of  $\phi_m$ . The Helmholtz terms in equations 4.19b and 4.19c result from the coupling of  $\phi_o$  and  $\phi_i$  to  $\phi_m$  and reflect the bi-domain nature of the system. We shall return to a discussion of the Laplace and Helmholtz terms in section F.

External, non-membrane current sources can be introduced into a bi-domain tissue system either through surface plate or point electrodes. We can treat situations involving surface plate electrodes as boundary value problems (see section E); however it will be convenient to allow for externally applied, imbedded, current sources. Consequently we write:



$$\nabla \cdot \mathbf{J}_o = U_{mp} + U_{so} \quad \nabla \cdot \mathbf{J}_i = -U_{mp} + U_{si} \quad (4.20a), (4.20b)$$

$$U_{so} = U_{eo} - U_{ms} \quad U_{si} = U_{ei} + U_{ms} \quad (4.21a), (4.21b)$$

to replace equations 4.14.  $U_{eo}$  is an externally applied volumetric current source in the extracellular domain, and  $U_{ei}$  an externally applied source in the intracellular domain.  $U_{so}$  is the total extracellular volumetric current source, and  $U_{si}$  the total intracellular volumetric current source. The general equations 4.16 now become:

$$\nabla^2 \phi_m = \frac{1}{\lambda^2} \phi_m + P_o U_{so} - P_i U_{si} \quad (4.22a)$$

$$\nabla^2 \phi_o = \frac{-P_o}{P_o + P_i} \nabla^2 \phi_m - P_h (U_{so} + U_{si}) \quad (4.22b)$$

$$\nabla^2 \phi_i = \frac{P_i}{P_o + P_i} \nabla^2 \phi_m - P_h (U_{so} + U_{si}) \quad (4.22c)$$

The formulation above describes potentials in a bi-domain system which contains both active membrane and externally applied current sources. As we shall see in the next section, the extra source terms in equations 4.22b and 4.22c will give rise to solutions to Poisson's equation.

#### 4-D. General solutions

In this section we derive the general solutions to the bi-domain Helmholtz equations (4.16). We begin by finding the solutions to a membrane point source (the Green's function solutions) for the two domains, and then apply

superposition to obtain the general solutions.

The solutions for the potentials arising from a membrane point source (a monopole source in each domain) are radially symmetric, since the source is a scalar, with no preferred direction. Consequently, the homogeneous solutions to equations 4.16 for  $r \neq 0$  take the form of equations 4.19 with:

$$\phi_H(r) = \frac{A}{r} e^{-r/\lambda} + \frac{B}{r} e^{r/\lambda} \quad (4.23a)$$

$$\phi_L(r) = \frac{C}{r} + D \quad (4.23b)$$

where A, B, C, and D are constants. Since equations 4.14 can be written together as:

$$\nabla \cdot (\underline{J}_o + \underline{J}_i) = 0 \quad (4.24)$$

this permits,

$$4\pi r^2 [J_o(r) + J_i(r)] = \text{constant} = I \quad (4.25)$$

where I is a constant, net, radial current. Substituting equations 4.13, 4.19, and 4.23 into 4.25 yields for the value of C:

$$C = \frac{P_h I}{4\pi} \quad (4.26)$$

where:

$$P_h = \text{equivalent myocardial bulk resistivity} = \frac{P_o P_i}{P_o + P_i} \quad (4.27)$$

$P_h$  is the parallel combination of the macroscopic bulk

resistivities for the two domains,  $P_o$  and  $P_i$ , and can be interpreted as the equivalent bulk resistivity for the myocardium as measured by surface electrodes. We will discuss this physical interpretation in greater detail in section F.

We now proceed to find the particular solution to equations 4.16 for a coupled pair of membrane point sources. We can then use superposition to find the solution to a general distribution of current sources. We set  $U_{ms} = I_s \delta(r)$  [the 3-D spatial impulse function]. Applying the boundary conditions,

$$\lim_{r \rightarrow 0} 4\pi r^2 J_o(r) = -I_s \quad (4.28a)$$

$$\lim_{r \rightarrow 0} 4\pi r^2 J_i(r) = I_s \quad (4.28b)$$

$$\lim_{r \rightarrow \infty} \phi_o(r) = \lim_{r \rightarrow \infty} \phi_i(r) = 0 \quad (4.28c)$$

to the radially symmetric, homogeneous solutions, we obtain:

$$\phi_m(r) = \frac{(P_o + P_i)I_s}{4\pi r} e^{-r/\lambda} \quad (4.29a)$$

$$\phi_o(r) = \frac{-P_o I_s}{4\pi r} e^{-r/\lambda} \quad (4.29b)$$

$$\phi_i(r) = \frac{P_i I_s}{4\pi r} e^{-r/\lambda} \quad (4.29c)$$

The Laplace term of equation 4.23b does not appear in equations 4.29b and 4.29c, since the net radial current  $I$  is zero, and the potential at infinity is zero.

Using equations 4.29, we can apply superposition to find the particular solutions to equations 4.16 for the general source distribution  $U_{ms}$ . Consequently, the membrane potential is given by,

$$\phi_m(\underline{r}_p) = \frac{(P_o + P_i)}{4\pi} \int_{V_Q} U_{ms}(\underline{r}_Q) \frac{e^{-r_{QP}/\lambda}}{r_{QP}} dv \quad (4.30a)$$

the extracellular potential is given by,

$$\phi_o(\underline{r}_p) = \frac{-P_o}{4\pi} \int_{V_Q} U_{ms}(\underline{r}_Q) \frac{e^{-r_{QP}/\lambda}}{r_{QP}} dv \quad (4.30b)$$

and the intracellular potential is given by,

$$\phi_i(\underline{r}_p) = \frac{P_i}{4\pi} \int_{V_Q} U_{ms}(\underline{r}_Q) \frac{e^{-r_{QP}/\lambda}}{r_{QP}} dv \quad (4.30c)$$

where  $P$  is the observation point,  $Q$  is a source point, and  $V_Q$  is the volume containing the source distribution.

We reiterate the fact that equations 4.16, and their corresponding solutions, form a macroscopic description of the electrical behavior of a bi-domain system containing active membrane current sources. This differs from conventional descriptions of mono-domain systems in that the divergence of extracellular or intracellular current density is non-zero even in the absence of externally introduced sources.

In a manner similar to that used to arrive at equations 4.30, we can find the general solutions to equations 4.22 for the case where both active membrane and externally introduced current sources are present. For a point source in

extracellular space, we employ equations 4.23, 4.26, and 4.27 and set  $U_{s_o} = I_o \delta(r)$ ,  $U_{s_i} = 0$ , and  $I = I_o$ . Applying the boundary conditions,

$$\lim_{r \rightarrow 0} 4\pi r^2 J_o(r) = I_o \quad (4.31a)$$

$$\lim_{r \rightarrow 0} 4\pi r^2 J_o(r) = 0 \quad (4.31b)$$

$$\lim_{r \rightarrow \infty} \phi_o(r) = \lim_{r \rightarrow \infty} \phi_i(r) = 0 \quad (4.31c)$$

to the radially symmetric, homogeneous solutions, we obtain:

$$\phi_m(r) = \frac{-P_o I_o}{4\pi r} e^{-r/\lambda} \quad (4.32a)$$

$$\phi_o(r) = \frac{P_o P_i I_o}{4\pi r P_i} e^{-r/\lambda} + \frac{P_i I_o}{4\pi r} \quad (4.32b)$$

$$\phi_i(r) = \frac{-P_i I_o}{4\pi r} e^{-r/\lambda} + \frac{P_i I_o}{4\pi r} \quad (4.32c)$$

Similarly, for an intracellular point source, we set  $U_{s_o} = 0$ ,  $U_{s_i} = I_i \delta(r)$ , and  $I = I_i$ . We obtain,

$$\phi_m(r) = \frac{P_i I_i}{4\pi r} e^{-r/\lambda} \quad (4.33a)$$

$$\phi_o(r) = \frac{-P_i I_i}{4\pi r} e^{-r/\lambda} + \frac{P_i I_i}{4\pi r} \quad (4.33b)$$

$$\phi_i(r) = \frac{P_i P_o I_i}{4\pi r P_o} e^{-r/\lambda} + \frac{P_o I_i}{4\pi r} \quad (4.33c)$$

From equations 4.32-4.33 we can write the particular solution to equations 4.22 for potentials in a bi-domain system containing both active membrane and external sources:

$$\phi_m(r_Q) = \int_{V_Q} \frac{[-P_o U_{so}(r_Q) + P_i U_{si}(r_Q)]}{4\pi r_{QP}} e^{-r_{QP}/\lambda} dv_Q \quad (4.34a)$$

$$\begin{aligned} \phi_o(r_Q) &= \int_{V_Q} \frac{P_h [(P_o/P_i)U_{so}(r_Q) - U_{si}(r_Q)]}{4\pi r_{QP}} e^{-r_{QP}/\lambda} dv_Q \\ &+ \int_{V_Q} \frac{P_h [U_{so}(r_Q) + U_{si}(r_Q)]}{4\pi r_{QP}} dv_Q \end{aligned} \quad (4.34b)$$

$$\begin{aligned} \phi_i(r_Q) &= \int_{V_Q} \frac{P_h [-U_{so}(r_Q) + (P_i/P_o)U_{si}(r_Q)]}{4\pi r_{QP}} e^{-r_{QP}/\lambda} dv_Q \\ &+ \int_{V_Q} \frac{P_h [U_{so}(r_Q) + U_{si}(r_Q)]}{4\pi r_{QP}} dv_Q \end{aligned} \quad (4.34c)$$

We see that equations 4.34 take the form of equations 4.19, and when  $U_{eo} = U_{ei} = 0$ , equations 4.34 reduce to equations 4.30, as expected. The latter, mono-domain term of equations 4.34b and 4.34c is the general solution to Poisson's equation. It arises when external electrodes are applied and cannot arise from membrane sources alone. Note also that this mono-domain term does not appear in the description of  $\phi_m$ , a purely bi-domain quantity.

#### 4-E. Boundary conditions

The effect of boundary conditions must be taken into account to describe the discontinuity from a bi-domain to a mono-domain structure, or any discontinuity in conductance at the tissue boundaries. For example, in the case of heart muscle (h), in which the myocardium is bounded on one side by the sourceless intramyocardial cavity (c) and on the other

side by the sourceless body tissue (b), we write the general system equations as follows:

$$\nabla^2 \phi_b = 0 \quad (4.35a)$$

$$\nabla^2 \phi_c = 0 \quad (4.35b)$$

$$\nabla^2 \phi_m = \frac{1}{\lambda^2} \phi_m + (P_o U_{so} - P_i U_{si}) \quad (4.22a)$$

$$\nabla^2 \phi_o = \frac{-P_o}{P_o + P_i} \nabla^2 \phi_m - P_h (U_{so} + U_{si}) \quad (4.22b)$$

$$\nabla^2 \phi_i = \frac{P_i}{P_o + P_i} \nabla^2 \phi_m - P_h (U_{so} + U_{si}) \quad (4.22c)$$

subject to the following boundary conditions at the heart/body (H/B) interface, where  $\underline{n}_b$  is the unit surface normal directed from heart to body, and  $P_b$  is the bulk resistivity of the body tissue:

$$\text{H/B:} \quad \frac{1}{P_o} \frac{\partial \phi_o}{\partial n_b} = \frac{1}{P_b} \frac{\partial \phi_b}{\partial n_b} \quad (4.36a)$$

$$\frac{1}{P_i} \frac{\partial \phi_i}{\partial n_b} = 0 \quad (4.36b)$$

$$\phi_o = \phi_b \quad (4.36c)$$

and the boundary conditions at the heart/cavity (H/C) interface, where  $\underline{n}_c$  is the unit surface normal directed from heart to cavity, and  $P_c$  is the bulk resistivity of the cavity:

$$\text{H/C:} \quad \frac{1}{P_o} \frac{\partial \phi_o}{\partial n_c} = \frac{1}{P_c} \frac{\partial \phi_c}{\partial n_c} \quad (4.36d)$$

$$\frac{I}{P_i} \frac{\partial \phi_i}{\partial n_c} = 0 \quad (4.36e)$$

$$\phi_o = \phi_c \quad (4.36f)$$

Physically, the boundary conditions specify that the normal component of the current flow in the extracellular space must be continuous with the normal component of the adjacent mono-domain current across both the H/B and H/C interfaces. The normal component of current flow in the intracellular space must be zero at the H/B and H/C interfaces (i.e. current terminates there). Also, the extracellular potential of the bi-domain must be continuous with the adjacent mono-domain potential across the H/B and H/C interfaces. With these boundary conditions, a unique solution for  $\phi_o$ ,  $\phi_i$ , and  $\phi_m$  will be obtained (see Appendix A on uniqueness).

In general, the boundary conditions of equations 4.28 will lead to solutions with discontinuities in the electric field at the boundaries. Consequently a surface charge layer,  $\sigma_s$ , is set up at the boundaries and is given by:

$$\text{H/B:} \quad j_{sb} = \epsilon_h \frac{\partial \phi_o}{\partial n_b} - \epsilon_b \frac{\partial \phi_b}{\partial n_b} \quad (4.37a)$$

$$\text{H/C:} \quad j_{sc} = \epsilon_h \frac{\partial \phi_o}{\partial n_c} - \epsilon_c \frac{\partial \phi_c}{\partial n_c} \quad (4.37b)$$

where  $\epsilon$  is the permittivity constant.



#### 4-F. "Differential" and "common" modes

If either the Helmholtz or the Laplace components of the bi-domain model dominate, we obtain a simplifying case which has a useful physical interpretation. In the former case, we show that the two domain currents will flow in opposite directions at any given point in space. The bi-domain Helmholtz equations (4.16) reduce to a set of bi-domain Poisson equations. In the latter case, the domain currents will flow in the same direction, and the bi-domain can be approximated as a mono-domain, provided that the appropriate boundary conditions are chosen. For each case we shall consider a specific, one-dimensional example. In general, a combination of the modes illustrated by the two cases will arise for the various ischemic zones of interest, illustrated in Fig. 3.2.

Case 1) Helmholtz components dominate: "differential" mode

We recall that the Laplace components arise from the boundary conditions. If their effects can be neglected (as in the case where the boundaries are at infinity only) so that  $\phi_L = 0$ , then equations 4.16 reduce to the set of uncoupled equations:

$$\nabla^2 \phi_m = \frac{1}{\lambda^2} \phi_m - (P_o + P_i) U_{ms} \quad (4.38a)$$

$$\nabla^2 \phi_o = \frac{1}{\lambda^2} \phi_o + P_o U_{ms} \quad (4.38b)$$

$$\nabla^2 \phi_i = \frac{1}{\lambda^2} \phi_i - P_i U_{ms} \quad (4.38c)$$

The solutions to equations 4.38 take the form:

$$\phi_m = \phi_H \quad (4.39a)$$

$$\phi_o = \frac{-P_o}{P_o + P_i} \phi_H \quad (4.39b)$$

$$\phi_i = \frac{P_i}{P_o + P_i} \phi_H \quad (4.39c)$$

We see from equations 4.39 that the two domains have potentials which are opposite in sign and are proportional to each other. Furthermore, the two domain current densities are equal in magnitude but oppositely directed at each point in space. We refer to this situation as the "differential-mode" of the bi-domain model.

To illustrate the concepts presented above, we analyze the one-dimensional example shown in Fig. 4.7. A rectangular membrane current source distribution is assumed in an infinite medium, and the intracellular and extracellular potential and current density distributions are derived. The one-dimensional equations corresponding to equations 4.38 are given by:

$$\frac{d^2 \phi_m}{dx^2} = \frac{1}{\lambda^2} \phi_m - (P_o + P_i) U_{ms} \quad (4.40a)$$

$$\frac{d^2 \phi_o}{dx^2} = \frac{1}{\lambda^2} \phi_o + P_o U_{ms} \quad (4.40b)$$

$$\frac{d^2\phi_i}{dx^2} = \frac{1}{\lambda^2} \phi_i - P_i U_{ms} \quad (4.40c)$$

The solutions to equations 4.40 for the source distribution illustrated in Fig. 4.7b are shown in Fig. 4.7c and are given by equations 4.39 with:

$$\phi_H = \begin{cases} [1 - e^{-L/\lambda} \cosh x/\lambda] R_m U_o & , |x| \leq L \\ \sinh L/\lambda e^{-|x|/\lambda} R_m U_o & , |x| > L \end{cases} \quad (4.41)$$

Because there are no local boundary constraints,  $\phi_L = 0$ .

We observe that the exact solution, equations 4.39 and 4.41, can be approximated by the solutions shown as dotted lines in Fig. 4.7c, where  $\phi_m$  is approximated by:

$$\phi_m = \begin{cases} R_m U_o & , |x| \leq L \\ 0 & , |x| > L \end{cases} \quad (4.42)$$

These solutions are identical to those which satisfy Poisson's equation with a dipole current source at  $x = \pm L$ . We will generalize this approximation to the bi-domain Helmholtz equations, by solutions to a set of bi-domain Poisson equations, in Chapter 6.

Case 2) Laplace components dominate: "common" mode

If there is no current flow due to membrane current sources, but rather flow arising from the boundaries, then over most of the volume of the bi-domain system (except at the boundaries), the Laplace components will dominate,

i.e.  $\phi_H \ll \phi_L$ , and the potentials take the form:

$$\rho_m = 0 \quad (4.43a)$$

$$\rho_o = \phi_L \quad (4.43b)$$

$$\phi_i = \phi_L \quad (4.43c)$$

For most of the volume (bulk) of the bi-domain system, the two domains have potentials which are identical to one another. In addition, the two domain current densities are proportional in magnitude and directed in parallel. Consequently, we refer to this situation as the "common-mode" of the bi-domain model. Only in a region within a distance of  $\lambda$ , the space constant, from the boundary will the Helmholtz currents be significant. Therefore, in this region equations 4.43 will no longer be valid approximations.

In particular, we examine the case where  $U_{ms} = 0$ ; i.e. there are no cellular sources within the system. We have,

$$\nabla^2 \phi_o = \nabla^2 \phi_L = \nabla^2 \phi_i = 0 \quad (4.44)$$

in the bulk. The appropriate boundary conditions for normal current can be derived from the general boundary conditions, equations 4.36a-b, which become ( $S_h$  is the heart surface):

$$\frac{1}{P_o} \frac{\partial \phi_o}{\partial n} \Big|_{S_h} = \frac{1}{P_b} \frac{\partial \phi_b}{\partial n} \Big|_{S_h} \quad (4.45a)$$

$$\frac{1}{P_i} \frac{\partial \phi_i}{\partial n} \Big|_{S_h} = 0 \quad (4.45b)$$

Combining equations 4.45b and 4.19c,

$$\frac{P_i}{P_o + P_i} \frac{\partial \phi_H}{\partial n} \Big|_{S_h} + \frac{\partial \phi_L}{\partial n} \Big|_{S_h} = 0 \quad (4.46)$$

and therefore, from equations 4.19b and 4.46,

$$\frac{\partial \phi_o}{\partial n} \Big|_{S_h} = \left(1 + \frac{P_o}{P_i}\right) \frac{\partial \phi_L}{\partial n} \Big|_{S_h} \quad (4.47)$$

Finally, from equations 4.45a and 4.47,

$$\frac{1}{P_h} \frac{\partial \phi_L}{\partial n} \Big|_{S_h} = \frac{1}{P_b} \frac{\partial \phi_b}{\partial n} \Big|_{S_h} \quad (4.48)$$

where the equivalent bulk resistivity  $P_h$  is given by equation 4.27. Consequently we expect to be able to describe the bulk of the bi-domain as a mono-domain with a bulk resistivity given by  $P_h$  and with a potential given by  $\phi_L$ .

However, the behavior of the bulk at the boundaries is complicated, due to the fact that the Helmholtz component of  $\phi_o$  plays a large role. We point out that in observing the bi-domain system from the boundaries, we cannot select the mono-domain bulk resistivity as  $P_o$  rather than  $P_h$ , while selecting the mono-domain potential as  $\phi_L$ . The reason for this is that although  $\phi_L$  may be a good approximation to  $\phi_o$  in the bulk and even on the boundary (we shall soon discuss this shortly in equation 4.49), the normal gradient of  $\phi_L$  is not a good approximation to the normal gradient of  $\phi_o$  at the boundary. We see from equation 4.46 that the normal gradient of the Helmholtz component is comparable in magnitude to the normal gradient of the Laplace component and therefore cannot

be neglected.

We have shown that the continuity equation for the normal gradient of current density is given by equation 4.48. We now derive the continuity equation for the potential. The general, bi-domain boundary condition is:

$$\phi_o \Big|_{S_h} = \frac{-P_o}{P_o + P_i} \phi_H \Big|_{S_h} + \phi_L \Big|_{S_h} \quad (4.49)$$

Unfortunately,  $\phi_o$  may not be well approximated by  $\phi_L$  on the boundary, since this is precisely where  $\phi_H$  is large.

However, if equation 4.43b is a good approximation in the bulk, then we can approximate  $\phi_o$  on the boundary by using equation 4.47 and a Taylor series expansion:

$$\begin{aligned} \phi_o \Big|_{S_h} &= \phi_o \Big|_{\text{bulk}} + \lambda \frac{\partial \phi_o}{\partial n} \Big|_{S_h} = \phi_L \Big|_{\text{bulk}} + \lambda \left( \frac{P_o + P_i}{P_i} \right) \frac{\partial \phi_L}{\partial n} \Big|_{S_h} \\ &= \phi_L \Big|_{\text{bulk}} + \lambda \frac{\partial \phi_L}{\partial n} \Big|_{S_h} + \lambda \left( \frac{P_o}{P_i} \right) \frac{\partial \phi_L}{\partial n} \Big|_{S_h} \\ &= \phi_L \Big|_{S_h} + \lambda \left( \frac{P_o}{P_i} \right) \frac{\partial \phi_L}{\partial n} \Big|_{S_h} \end{aligned} \quad (4.50)$$

Thus, the boundary condition for continuity of potential, equation 4.36c, becomes:

$$\left[ \phi_L + \lambda \left( \frac{P_o}{P_i} \right) \frac{\partial \phi_L}{\partial n} \right]_{S_h} = \phi_b \Big|_{S_h} \quad (4.51)$$

In conclusion, we note that for the case we have been discussing, the behavior of the bi-domain is well described as a mono-domain with bulk resistivity  $P_h$  with regard to the normal current boundary conditions. Unfortunately, we can

only approximate the potential boundary conditions using  $\phi_L$ , since at the boundary the actual extracellular potential deviates from  $\phi_L$  in the manner of equation 4.50. If this deviation is small, however, then we can fully describe the behavior of the bi-domain as a mono-domain whose potential distribution satisfies Laplace's equation and whose normal current and potential constraints at the boundaries take the classical form.

We take a simple, one-dimensional example to illustrate the concepts presented above. For the case shown in Fig. 4.8, there are no membrane sources in the bi-domain system. However, a flow of current is introduced across the boundaries at  $x = \pm L$ . The boundary conditions, equations 4.45, become:

$$x = -L: -\frac{1}{P_o} \frac{d\phi_o}{dx} = I \quad ; \quad \frac{d\phi_i}{dx} = 0 \quad (4.52a), (4.52b)$$

$$x = L: -\frac{1}{P_o} \frac{d\phi_o}{dx} = I \quad ; \quad \frac{d\phi_i}{dx} = 0 \quad (4.53a), (4.53b)$$

Consequently, the potentials must satisfy the general equations (4.40) and the boundary conditions (4.52 and 4.53) and take the form of equations 4.19 with:

$$\phi_H = 2\lambda P_o I \frac{\sinh L/\lambda}{\sinh 2L/\lambda} \sinh x/\lambda \quad (4.54a)$$

$$\phi_L = -P_h I x \quad (4.54b)$$

For most of the bulk, except near  $x = \pm L$ ,  $\phi_H \ll \phi_L$ ; that is,

we can approximate  $\phi_o$  and  $\phi_i$  by  $\phi_L$  (see Fig. 4.8b) as in equations 4.43. We note that equation 4.48 is satisfied:

$$-\frac{I}{P_h} \left. \frac{\partial \phi_L}{\partial x} \right|_{x=\pm L} = I \quad (4.55)$$

In this example the potential at the boundary is not constrained, so that continuity of potential, expressed by equation 4.49, is not required. However, we note that  $\phi_o$  satisfies the approximation of equation 4.50, since,

$$\begin{aligned} \phi_o(L) &= \frac{-P_o}{P_o + P_i} \phi_H(L) + \phi_L(L) = -\lambda \left( \frac{P_o}{P_i} \right) P_h I - P_h I L \\ &= \frac{\lambda P_o}{P_i} \left. \frac{d\phi_L}{dx} \right|_{x=L} + \phi_L(L) \end{aligned} \quad (4.56)$$

for  $L \gg \lambda$ . Therefore we find that at the boundary electrodes, the input resistivity is given by:

$$\frac{-\phi_o(L)}{IL} = P_h \left( 1 + \frac{\lambda P_o}{LP_i} \right) \quad (4.57)$$

If  $L \gg \lambda$ , we see that the bi-domain, measured by boundary electrodes, can be approximated by a mono-domain with bulk resistivity given by  $P_h$ .

Thus, we conclude that since the intracellular and extracellular potentials in the bulk are approximately the same, and since the bi-domain appears to act as a mono-domain to the boundaries, we can effectively replace the bi-domain by a mono-domain description. This "common-mode", mono-domain description is valid, however, only in the absence of active membrane sources and only where the



dimensions of the bi-domain system are much greater than the space constant.

4-G. The mono-domain and the bi-domain

We show that the classical volume conductor (a mono-domain) can be considered to be a degenerate case of a bi-domain system. Taking a myocardial bi-domain system, if we let the membrane resistance  $R_m$  go to zero, this will effectively "short out" the membrane current sources. Furthermore, the transmembrane potential ( $\phi_m$ ) will go to zero. Consequently, the general equations (4.22) for a bi-domain system containing both active membrane and externally applied current sources become,

$$\nabla^2 \phi_o = \nabla^2 \phi_i = -P_h (U_{eo} + U_{ei}) \quad (4.58)$$

where we have used equations 4.21 to express the sources of equation 4.58 as externally applied current sources only. Equation 4.58 is in the form of Poisson's equation, and its solution can be written accordingly. Alternatively, we can reduce the general solutions (4.34) of equations 4.22, for the case where  $R_m$  goes to zero. Since  $\lambda$  (cf. equation 4.17) and therefore  $e^{-r/\lambda}$  will go to zero, we obtain from equations 4.34 the general solution for equation 4.58:

$$\phi_o(\underline{r}_p) = \phi_i(\underline{r}_p) = \int_{V_Q} \frac{P_h [U_{eo}(\underline{r}_Q) + U_{ei}(\underline{r}_Q)]}{4\pi r_{QP}} dv_Q \quad (4.59)$$

Equations 4.58 and its solution 4.59 describe a mono-domain having a bulk resistivity equal to  $P_h$  (the parallel

combination of the intracellular and extracellular bulk resistivities). Thus, we can refer to  $P_h$  as the "myocardial bulk resistivity."

As we have already stated,  $\phi_m$  will go to zero as  $R_m$  goes to zero. From the definition of  $\phi_m$ , this implies that  $\phi_o$  and  $\phi_i$  become equal to each other. Thus, the boundary conditions (equations 4.36a-c) can be combined and rewritten for the heart/body interface as,

$$\frac{1}{P_h} \frac{\partial \phi_o}{\partial n_b} = \frac{1}{P_b} \frac{\partial \phi_b}{\partial n_b} \quad (4.60a)$$

$$\phi_o = \phi_b \quad (4.60b)$$

which we recognize as the classical boundary conditions for a volume conductor having a bulk resistivity  $P_h$ .

Thus, we conclude that the classical volume conductor (a mono-domain), described by the usual Poisson's equation and boundary conditions, is a degenerate case of a bi-domain system (where  $R_m$  is zero).

#### 4-H. Summary

In this chapter, we discussed the concepts of macroscopic potential and current density, and related these quantities to the microscopic potential and current density. This viewpoint, together with evidence for intercellular electrical connections which result in an electrically continuous intracellular space, led to the notion of two

interpenetrating mono-domains separated by a volume-distributed boundary. Ohm's law and charge conservation were modified to account for the new physical structure, and the electrical membrane behavior was described by a Norton equivalent circuit. Consequently, a set of general equations was derived for the case of active membrane current sources, and for the case of both active membrane and externally introduced current sources. The general solutions were obtained from the Green's function solutions, subject to a set of boundary conditions reflecting the physical nature of the bi-domain structure. The electrical behavior of a bi-domain system could be separated into a "common-mode" or a "differential-mode." Finally, the classical volume conductor (a mono-domain) can be considered to be a degenerate case of a bi-domain system.

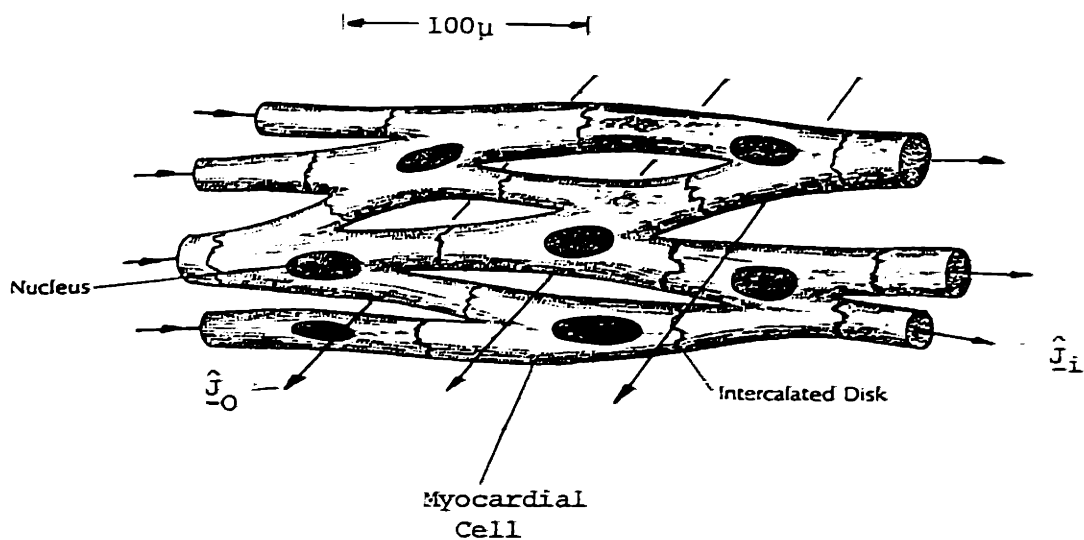


FIGURE 4.1 - Current flow in the intracellular and extracellular spaces [original drawing from Sonnenblick (1974)]. Note that current in the two spaces can flow in grossly different directions.

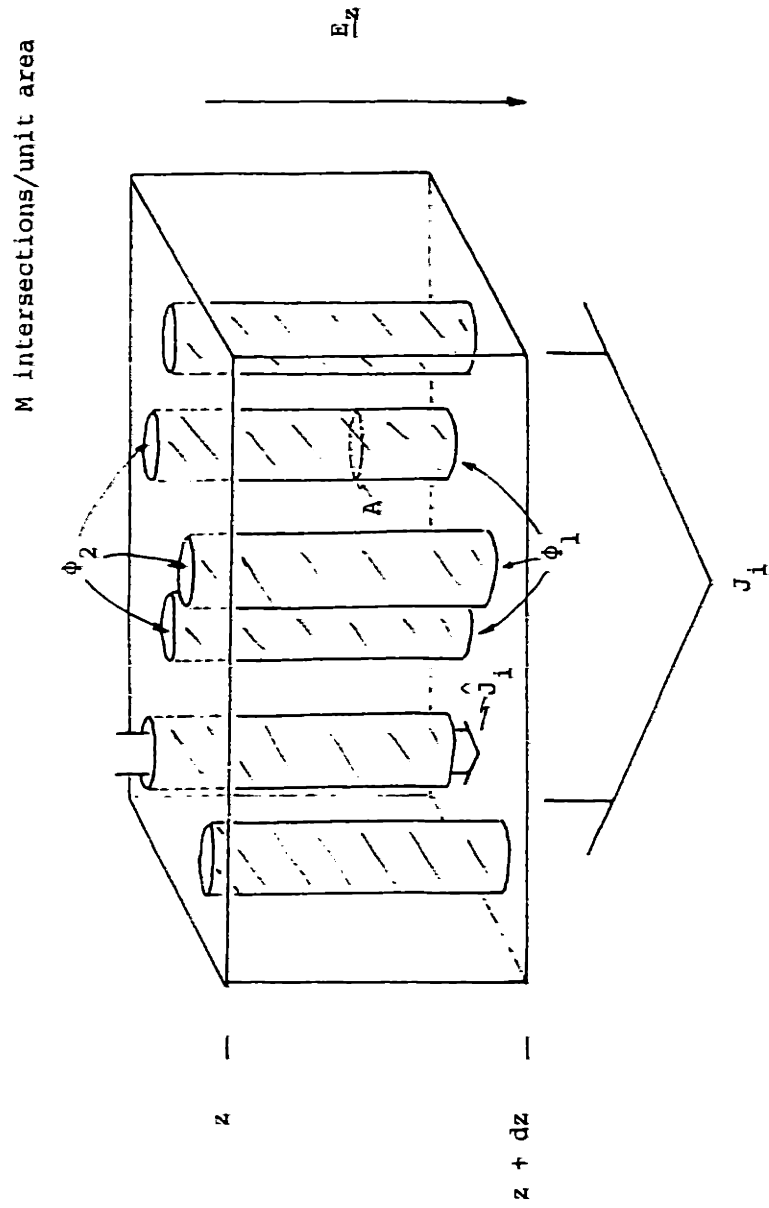


FIGURE 4.2 - Relationship between the macroscopic and microscopic intracellular current densities for parallel cells

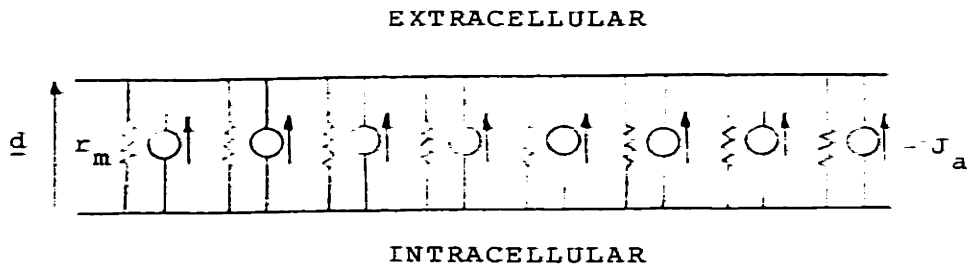


FIGURE 4.3 - Equivalent "large signal" model for the cell membrane separating the intracellular and extracellular spaces

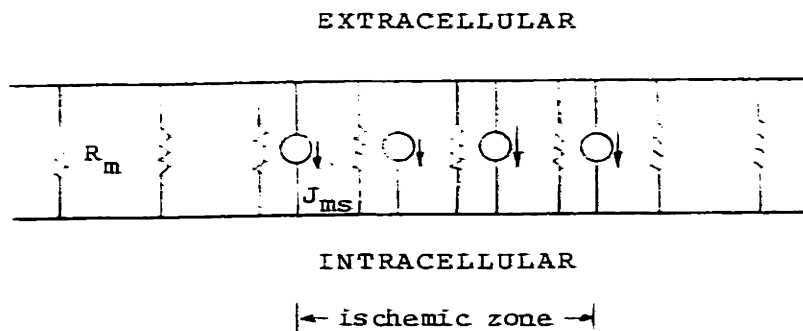
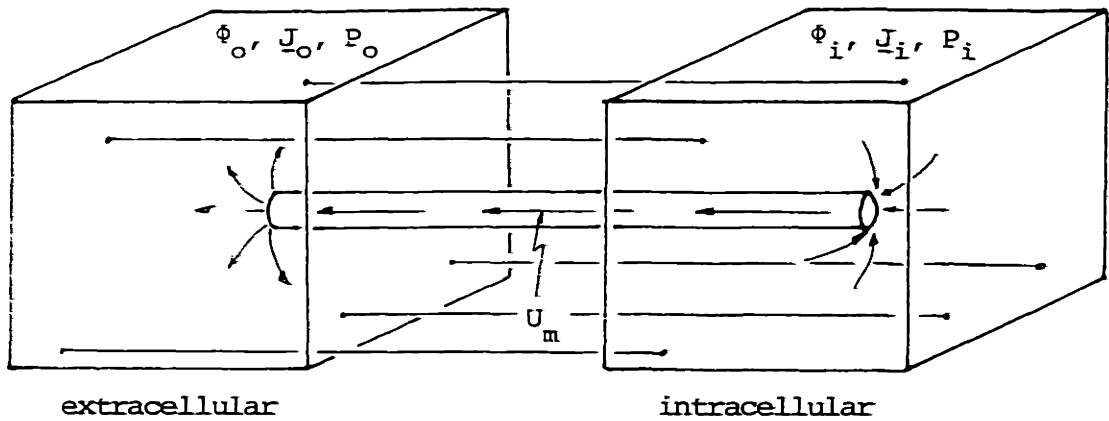


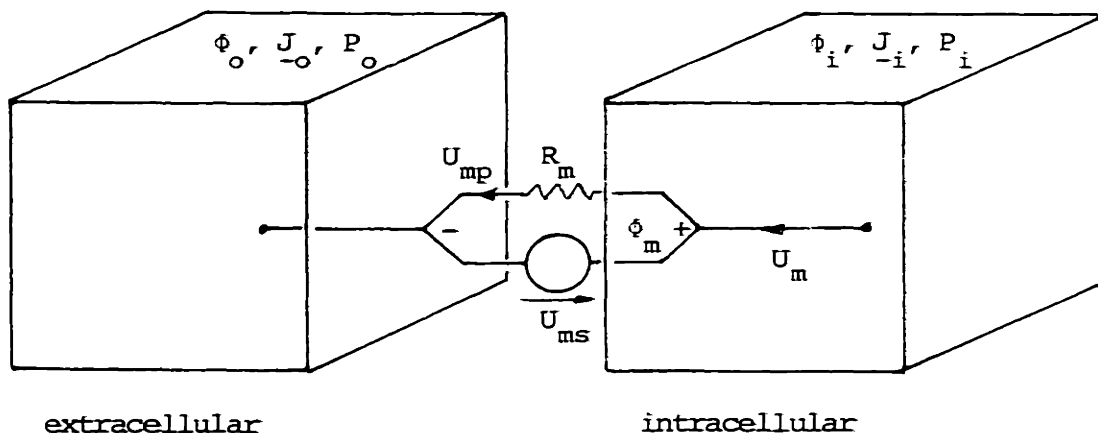
FIGURE 4.4 - Equivalent "small-signal" model for the cell membrane separating the intracellular and extracellular spaces



Features:

- 1) Source in one domain coupled to sink in the other
- 2) Current flow in each domain is radially symmetric
- 3) Sources are scalar, monopole current sources

FIGURE 4.5 - Complementary monopole source pair, representing the flow of membrane current between domains



$$\nabla \cdot \underline{J}_o = -\nabla \cdot \underline{J}_i = U_m \quad (\text{Charge Conservation})$$

$$U_m = U_{mp} - U_{ms} = \text{"volumetric current density" (amp/cm}^3\text{)}$$

$$U_{ms} = \text{active membrane current source, independent of } \phi_m$$

$$U_{mp} = \frac{\phi_m}{R_m} = \text{passive membrane current}$$

$$R_m = \text{"volume-specific membrane resistance" (ohm-cm}^3\text{)}$$

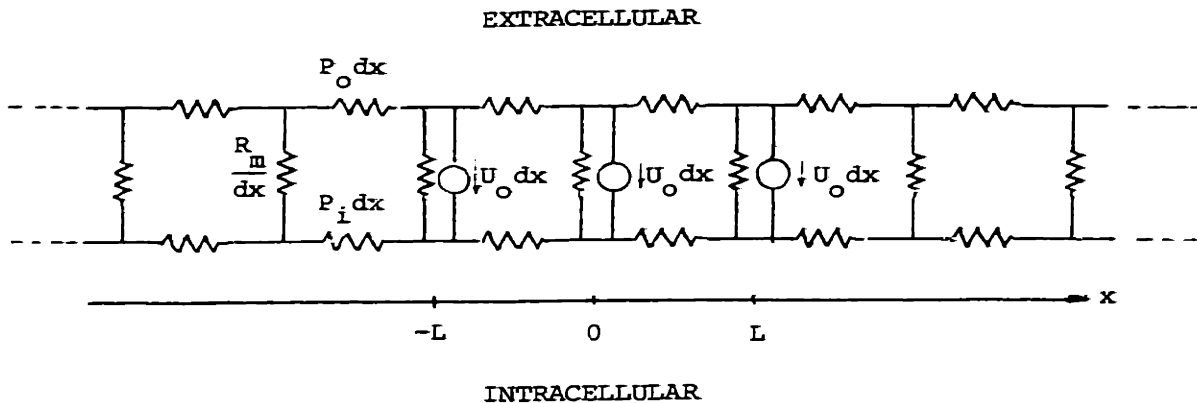
$$= \frac{\rho_m d}{a_m} \quad (\rho_m = \text{membrane resistivity; } d = \text{membrane thickness)}$$

$$a_m = \text{total membrane surface area/unit volume of tissue}$$

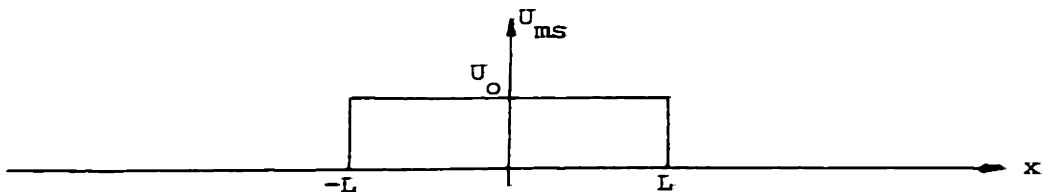
FIGURE 4.6 - Equivalent "small-signal" model for the cell membrane separating the intracellular and extracellular domains



a) Circuit model



b) Source distribution



c) Potential distribution

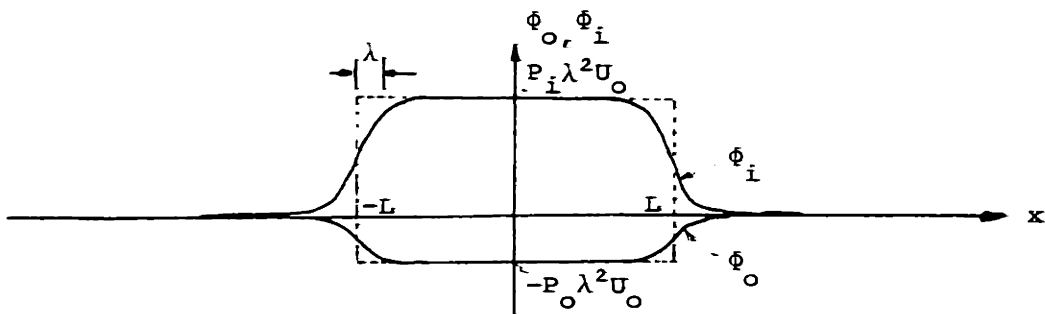
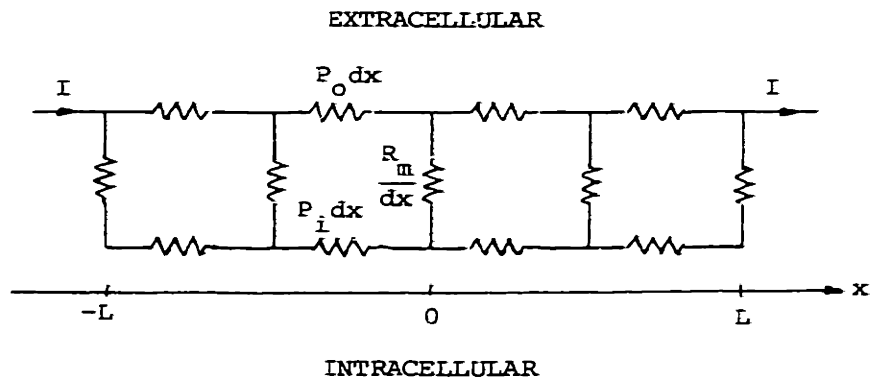


FIGURE 4.7 - Example illustrating the "differential-mode" of the bi-domain structure

a) Circuit model



b) Potential distribution

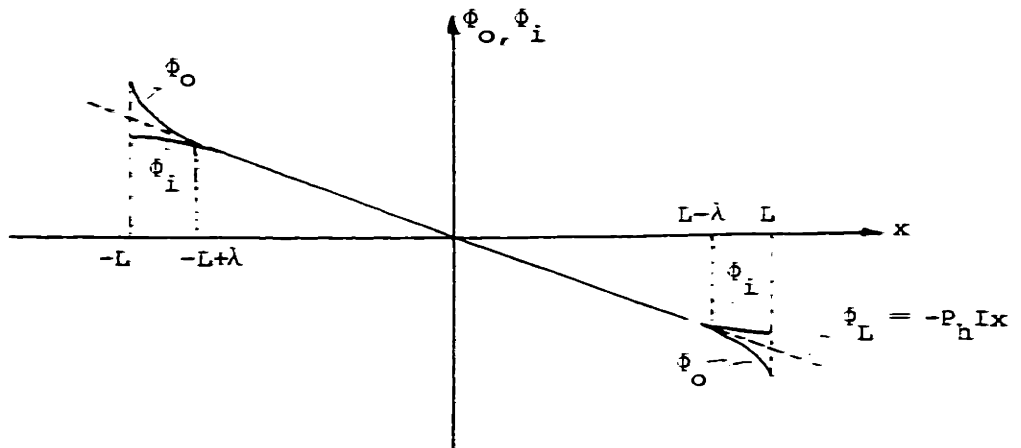


FIGURE 4.8 - Example illustrating the "common-mode" of the bi-domain structure

CHAPTER 5: Case Studies Using the Bi-Domain Model

In this chapter we study the effect of various source geometries, boundary conditions, and ischemic border widths on the shape of the ischemic potential distribution. We will focus on the features of polarity and concavity, often described for epicardial ST-TQ maps (cf. Chapter 1-A). We shall use the term "monophasic" to refer to a potential distribution which has a single polarity relative to the reference potential (usually taken to be the value of the distribution at infinity), and the term "biphasic" to refer to a distribution which is both positive and negative with respect to the reference potential. The general bi-domain model can be used with any distribution of cellular sources, having either diffuse (thick) or abrupt (thin) borders. We assume that the cells are uniformly ischemic in the region enclosed by the border, with a transition to the normal state occurring across the border zone. In section 5-A we analyze the case of a rectangular source distribution with an abrupt border, using the bi-domain Helmholtz equations of Chapter 4. In sections 5-B and 5-C, we consider diffuse border cases, again using the bi-domain equations. The results of these three sections are summarized in section 5-D, where we show that depending on the width and location of the border zone, the concavity and polarity of the surface ischemic potential distribution can be altered.

### 5-A. Rectangular, transmural, ischemic zone with abrupt borders

In this section we consider a rectangular source distribution with an abrupt border. Using the bi-domain equations developed in Chapter 4, we propose to find the spatial distribution of the ischemic potential for the case of a myocardial strip (taken to be infinite in the z-direction) in contact with a conductive fluid on one side, and air (non-conductive) on the other (illustrated in Fig. 5.1). This case corresponds to the free wall of myocardium in the exposed heart preparation, with blood on one side and air on the other. We are particularly interested in the potential distribution over the upper (exposed) surface, as this corresponds to epicardial potential maps. Cases for spherical geometries, which correspond more closely to the geometry of the heart, are considered in Chapter 7.

To solve this problem, we use the method of imaging and analyze instead the problem illustrated in Fig. 5.2. A myocardial strip twice as thick as the original strip is totally immersed in a conductive fluid having the same conductivity as before. The boundary conditions at the lower surface are the same as before. In addition, by symmetry the gradients of  $\phi_o$  and of  $\phi_i$  are both zero in the y-direction at the x-axis ( $y=0$ ). These are precisely the boundary constraints at the upper surface of the myocardial strip in

our original problem (Fig. 5.1). Thus, the potentials of Fig. 5.2 for the region  $y \leq 0$  (the symmetrical, image case) can be identified with the potentials of Fig. 5.1 for the region  $y \leq b$  (the desired, asymmetrical case). Formally stated,

$$\phi_o(x,y) \Big|_{\text{sym}} = \phi_o(x,y-b) \Big|_{\text{asym}} \quad (5.1)$$

Thus, we proceed to solve for the potentials for the symmetrical case of Fig. 5.2, and from equation 5.1 we can solve for the potentials for the asymmetrical case of Fig. 5.1.

To begin, we take the source  $U_{ms}$  to have the distribution shown in Fig. 5.3a. Because of symmetry the potentials are independent of  $z$ , and we can solve the two-dimensional, instead of the three-dimensional, Helmholtz equations (cf. equations 4.16):

$$\frac{d^2\phi_m}{dx^2} + \frac{d^2\phi_m}{dy^2} = \frac{1}{\lambda^2} \phi_m - (P_o + P_i) U_{ms} \quad (5.2a)$$

$$\frac{d^2\phi_o}{dx^2} + \frac{d^2\phi_o}{dy^2} = \frac{-P_o}{P_o + P_i} \left( \frac{d^2\phi_m}{dx^2} + \frac{d^2\phi_m}{dy^2} \right) \quad (5.2b)$$

$$\frac{d^2\phi_i}{dx^2} + \frac{d^2\phi_i}{dy^2} = \frac{P_i}{P_o + P_i} \left( \frac{d^2\phi_m}{dx^2} + \frac{d^2\phi_m}{dy^2} \right) \quad (5.2c)$$

The solutions to equations 5.2 take the form of equations 4.19, and we choose to rewrite  $\phi_H$  of equation 4.19a as a homogeneous ( $\phi_{hH}$ ) and particular ( $\phi_{pH}$ ) solution to the Helmholtz equation. The reason for separating  $\phi_H$  into these

two components is that in the next chapter on the solid angle model approximation to the bi-domain model, we show that  $\phi_{pH}$  is approximated by a solution to Poisson's equation, while  $\phi_{hH}$  is neglected. Equations 4.19 become:

$$\phi_m = \phi_H = \phi_{pH} + \phi_{hH} \quad (5.3a)$$

$$\phi_o = \frac{-P_o}{P_o + P_i} \phi_{pH} - \frac{P_o}{P_o + P_i} \phi_{hH} + \phi_L = \phi_{po} - \frac{P_o}{P_o + P_i} \phi_{hH} + \phi_L \quad (5.3b)$$

$$\phi_i = \frac{P_i}{P_o + P_i} \phi_{pH} + \frac{P_i}{P_o + P_i} \phi_{hH} + \phi_L = \phi_{pi} + \frac{P_i}{P_o + P_i} \phi_{hH} + \phi_L \quad (5.3c)$$

where  $\phi_{po}$  is the particular solution for the extracellular domain and  $\phi_{pi}$  is the particular solution for the intracellular domain:

$$\phi_{po} = \frac{-P_o}{P_o + P_i} \phi_{pH} \quad (5.4a)$$

$$\phi_{pi} = - \left( \frac{P_i}{P_o} \right) \phi_{po} \quad (5.4b)$$

Thus we have:

$$\frac{d^2 \phi_{pH}}{dx^2} = \frac{1}{\lambda^2} \phi_{pH} - (P_o + P_i) U_{ms} \quad (5.5a)$$

$$\frac{d^2 \phi_{po}}{dx^2} = \frac{1}{\lambda^2} \phi_{po} + P_o U_{ms} \quad (5.5b)$$

From equations 5.5, we obtain for  $\phi_{pH}$ ,

$$\phi_{pH}(x) = \begin{cases} R_m U_o [1 - e^{-a/\lambda} \cosh x/\lambda] & , |x| \leq a \\ R_m U_o \sinh a/\lambda e^{-|x|/\lambda} & , |x| > a \end{cases} \quad (5.6a)$$

and for  $\phi_{po}$  :

$$\phi_{po}(x) = \begin{cases} -P_o \lambda^2 U_o [1 - e^{-a/\lambda} \cosh x/\lambda] & , |x| \leq a \\ -P_o \lambda^2 U_o \sinh a/\lambda e^{-|x|/\lambda} & , |x| > a \end{cases} \quad (5.6b)$$

Our approach to solving equations 5.2 is through the eigenfunction expansions (cosine integrals) for  $\phi_m$ ,  $\phi_o$ , and  $\phi_i$ , or equivalently,  $\phi_H$  and  $\phi_L$ . Anticipating the need, we can expand  $\phi_{po}$  as a Fourier cosine integral:

$$\phi_{po}(x) = \frac{2}{\pi} \int_0^{\infty} A(k) \cos kx \, dk \quad (5.7a)$$

$$A(k) = \int_0^{\infty} \phi_{po}(x) \cos kx \, dx \quad (5.7b)$$

If we write  $U_{ms}$  as a Fourier cosine integral,

$$U_{ms}(x) = \frac{2}{\pi} \int_0^{\infty} E(k) \cos kx \, dk \quad (5.8a)$$

with  $E(k)$  given by,

$$E(k) = \frac{U_o \sin ka}{k} \quad (5.8b)$$

we can substitute equations 5.7a and 5.8a into 5.5b to obtain,

$$A(k) = \frac{-P_o \lambda^2}{1 + (k\lambda)^2} E(k) \quad (5.9)$$

We can also obtain equation 5.9 by direct integration, using equation 5.7b.

We use a separation of variables on  $\phi_L$  and express the eigenfunctions of Laplace's equation as:  $\cos kx \cosh ky$ .

Consequently, we can write  $\phi_L$  as a Fourier cosine integral expansion along the x-direction:

$$\phi_L(x, y) = \frac{2}{\pi} \int_0^{\infty} B(k) \cosh ky \cos kx \, dk \quad (5.10)$$

Similarly, we can express  $\phi_b$  as:

$$\phi_b(x, y) = \frac{2}{\pi} \int_0^{\infty} C(k) e^{-k(|y|-b)} \cos kx \, dk \quad (5.11)$$

where  $e^{-k(|y|-b)}$  replaces  $\cosh ky$ , since we require  $\phi_b \rightarrow 0$  as  $|y| \rightarrow \infty$ .

We also use a separation of variables on  $\phi_{hH}$  to express the eigenfunctions of the homogeneous Helmholtz equation as:  $\cosh \sqrt{k + (1/\lambda^2)} y \cos ky$ . Thus we can express  $\phi_{hH}$  as:

$$\phi_{hH}(x, y) = \frac{2}{\pi} \int_0^{\infty} D(k) \cosh y \sqrt{k + (1/\lambda^2)} \cos kx \, dk \quad (5.12)$$

Substituting equations 5.3b, 5.7a, and 5.10-5.12 into the boundary conditions (cf. equations 4.36),

$$\phi_o(x, b) = \phi_b(x, b) \quad (5.13a)$$

$$\frac{1}{P_o} \left. \frac{\partial \phi_o}{\partial y} \right|_{y=b} = \frac{1}{P_b} \left. \frac{\partial \phi_b}{\partial y} \right|_{y=b} \quad (5.13b)$$

$$\frac{1}{P_i} \left. \frac{\partial \phi_i}{\partial y} \right|_{y=b} = 0 \quad (5.13c)$$

we obtain,

$$A(k) - \frac{P_o}{P_o + P_i} \cosh \beta D(k) + \cosh \alpha B(k) = C(k) \quad (5.14a)$$



$$\frac{1}{P_o} \left[ \frac{-P_o}{P_o + P_i} \frac{\beta}{b} \sinh \beta D(k) + k \sinh \alpha B(k) \right] = -\frac{k}{P_b} C(k) \quad (5.14b)$$

$$\frac{1}{P_i} \left[ \frac{P_i}{P_o + P_i} \frac{\beta}{b} \sinh \beta D(k) + k \sinh \alpha B(k) \right] = 0 \quad (5.14c)$$

where,

$$\alpha = kb \quad (5.15a)$$

$$\beta = \sqrt{k^2 + (1/\lambda^2)} b \quad (5.15b)$$

Solving equations 5.14 together with 5.8b and 5.9 for A(k), B(k), C(k), and D(k), we obtain,

$$\phi_{pH} : \quad A(k) = \frac{-P_o \lambda^2 U_o}{\gamma} \frac{\sin ka}{k} \quad (5.16a)$$

$$\phi_L : \quad B(k) = \frac{-A(k)}{\cosh \alpha + \left(\frac{P}{P_h} b\right) \sinh \alpha + \left(\frac{P_o}{P_i}\right) \left(\frac{\alpha}{\beta}\right) \left(\frac{\sinh \alpha}{\tanh \beta}\right)} \quad (5.16b)$$

$$\phi_b : \quad C(k) = -\frac{P_b}{P_h} \sinh \alpha B(k) \quad (5.16c)$$

$$\phi_{nH} : \quad D(k) = -\frac{P_o}{P_h} \frac{\alpha}{\beta} \frac{\sinh \alpha}{\tanh \beta} B(k) \quad (5.16d)$$

where  $P_h$  is given by equation 4.16, and  $\gamma$  is given by:

$$\gamma = 1 + (k\lambda)^2 \quad (5.17)$$

From the Fourier cosine coefficients A(k), B(k), C(k), and D(k), we can use the transformations of equations 5.7a and 5.10-5.12 to obtain the potential distributions for  $\phi_{po}$ ,  $\phi_L$ ,  $\phi_b$ , and  $\phi_{nH}$ . In making the transformation, we can use the

FFT to reduce computation time (see Appendix F). Finally, we use equation 5.3b to obtain the spatial distribution for  $\phi_o$  (which we recall is for the symmetrical case) and then use equation 5.1 to obtain  $\phi_o$  for the original asymmetrical problem of Fig. 5.1.

We take a specific case in which  $a = 2$  cm,  $b = .5$  cm,  $P_i = 3P_o$ ,  $P_o = 4P_b$ , and  $P_o \lambda^2 U_o$  has been normalized to 1. The results for  $\phi_o(x,y)$  in the original problem of Fig. 5.1 are shown in Fig. 5.4a in the form of an equipotential plot, and in Fig. 5.4b as spatial distributions over the two surfaces of the strip. Since the distributions are symmetric about the  $y$ -axis, we have plotted them only for  $x \geq 0$ . We see that the magnitude of the potential distribution over the exposed surface displays a local minimum at the center of the ischemic zone, a local maximum at the border of the ischemic zone, and an overall biphasic behavior. This behavior is due to the large Laplace current flowing across the boundaries. The Laplace potential is opposite in polarity to the particular solution  $\phi_{po}$  and has the greatest amplitude at  $x = 0$ . If the lower surface had also been in contact with a non-conducting medium, there would be no Laplace current flow, and  $\phi_o$  would then be identical to  $\phi_{po} - P_o \phi_{hH} / (P_o + P_i)$  (cf. equation 5.3b), which when evaluated, is a monophasic distribution. The potential distribution for the intracellular potential, if it could be measured, is shown in Fig. 5.4c. In this plot we have normalized  $P_i \lambda^2 U_o = 1$ . We

see that the Laplace potential augments rather than subtracts from  $\phi_{pi}$ , and thus a monophasic potential results. In addition, because of the boundary conditions (5.13c) at  $y = \pm b$ , the gradient of  $\phi_{pi}$  is primarily in the x-direction.

5-B. Rectangular, transmural, ischemic zone with lateral diffuse borders

We take the geometry of Fig. 5.1 of a myocardial strip in contact with a conductive medium on one side and air on the other, but where the source  $U_{ms}$  now has a diffuse, rather than an abrupt, border. We expect that this will be a more realistic model of the ischemic zone. Taking the distribution of Fig. 5.3b, we have,

$$U_{ms}(x) = \begin{cases} \frac{1 - e^{-a/\lambda_s} \cosh x/\lambda_s}{1 - e^{-a/\lambda_s}} \\ \frac{\sinh a/\lambda_s e^{-|x|/\lambda_s}}{1 - e^{-a/\lambda_s}} \end{cases} \quad (5.18)$$

As before, we solve the image problem of Fig. 5.2.

Expressing  $U_{ms}$  as a Fourier cosine integral (eq. 5.8a), we have,

$$E(k) = \frac{U_o}{1 - e^{-a/\lambda_s}} \frac{\sin ka}{k} \frac{1}{1 + (k\lambda_s)^2} \quad (5.19)$$

Hence, from equation 5.9,

$$A(k) = \frac{-P_o \lambda^2 U_o}{1 - e^{-a/\lambda_s}} \frac{\sin ka}{k} \frac{1}{1 + (k\lambda)^2} \frac{1}{1 + (k\lambda_s)^2} \quad (5.20)$$

The relationship of  $B(k)$ ,  $C(k)$ , and  $D(k)$  to  $A(k)$  remain

unchanged (equations 5.16b-d), since the boundary conditions, and therefore equations 5.14, are unaltered. Hence, we can use equations 5.16b-d and 5.20 to obtain  $A(k)$ ,  $B(k)$ ,  $C(k)$ , and  $D(k)$ , from which we can determine  $\phi_{po}$ ,  $\phi_L$ ,  $\phi_b$ , and  $\phi_{hH}$  as before. Taking the same values for the parameters as in the abrupt case, we obtain results which are shown in Fig. 5.5a as an equipotential plot and Fig. 5.5b as the surface potential distributions. The potentials of the image problem have been translated, as before, to the potentials of the original problem via equation 5.1. Comparing Fig.'s 5.5 to 5.4, we see that the concavity of the exposed surface distribution of  $\phi_o$  has changed. There is now a local maximum of the magnitude of the ischemic potential at the center of the ischemic zone, although the maximum magnitude has decreased. Nevertheless, the distribution retains its biphasic nature. As expected, in the case where  $\lambda_s \rightarrow 0$ , the distributions of Fig.'s 5.5 reduce to those of Fig.'s 5.4. We shall explore more fully in section 5-D the effects of a varying, lateral border width on the exposed surface potential distribution. In the next section we shall see that it is possible for the distribution to become monophasic.

### 5-C. Rectangular ischemic zone with both lateral and transverse diffuse borders

We now consider the more general case where the ischemic zone has both lateral and transverse diffuse borders --

i.e. where there is a  $y$ - as well as an  $x$ -dependence. Again, we take the case of Fig. 5.1, where  $U_{ms}$  is given by the distribution of Fig. 5.3c:

$$U_{ms}(x,y) = \begin{cases} \frac{1 - e^{-a/\lambda_s} \cosh x/\lambda_s}{1 - e^{-a/\lambda_s}} \cos \frac{\pi(y-b)}{2b_s} & , |x| \leq a \\ \frac{\sinh a/\lambda_s e^{-|x|/\lambda_s}}{1 - e^{-a/\lambda_s}} \cos \frac{\pi(y-b)}{2b_s} & , |x| > a \end{cases} \quad \begin{matrix} (5.21a) \\ \text{(asymmetrical)} \end{matrix}$$

As before, we solve the image problem for a new  $U_{ms}$ , given by,

$$U_{ms}(x,y) = \begin{cases} \frac{1 - e^{-a/\lambda_s} \cosh x/\lambda_s}{1 - e^{-a/\lambda_s}} \cos \frac{\pi y}{2b_s} & , |x| \leq a \\ \frac{\sinh a/\lambda_s e^{-|x|/\lambda_s}}{1 - e^{-a/\lambda_s}} \cos \frac{\pi y}{2b_s} & , |x| > a \end{cases} \quad \begin{matrix} (5.21b) \\ \text{(symmetrical)} \end{matrix}$$

and express the new  $U_{ms}$  as a Fourier cosine integral along the  $x$ -direction,

$$U_{ms}(x,y) = \frac{2}{\pi} \int_0^{\infty} E(k) \cos \frac{\pi y}{2b_s} \cos kx \, dk \quad (5.22)$$

where  $E(k)$  is given in equation 5.19.

We now express  $\phi_{po}$  as:

$$\phi_{po}(x,y) = \frac{2}{\pi} \int_0^{\infty} A(k) \cos \frac{\pi y}{2b_s} \cos kx \, dk \quad (5.23)$$

Substituting equations 5.22 and 5.23 into 5.5b, we obtain (compare to equation 5.9):

$$A(k) = \frac{-P_o \lambda^2}{1 + (k\lambda)^2 + \left(\frac{\pi\lambda}{2b_s}\right)^2} E(k) \quad (5.24)$$

Substitution of equations 5.3, 5.7a, and 5.10-5.12 into the boundary conditions 5.13 yield:

$$\cos \frac{\pi b}{2b_s} A(k) - \frac{P_o}{P_o + P_i} \cosh \beta D(k) + \cosh \alpha B(k) = C(k) \quad (5.25a)$$

$$\begin{aligned} \frac{1}{P_o} \left[ \frac{-\pi}{2b_s} \sin \frac{\pi b}{2b_s} A(k) - \frac{P_o}{P_o + P_i} \frac{\beta}{b} \sinh \beta D(k) \right. \\ \left. + k \sinh \alpha B(k) \right] = -\frac{k}{P_b} C(k) \quad (5.25b) \end{aligned}$$

$$\begin{aligned} \frac{1}{P_i} \left[ \frac{-\pi}{2b_s} \sin \frac{\pi b}{2b_s} \left(-\frac{P_i}{P_o}\right) A(k) + \frac{P_o}{P_o + P_i} \frac{\beta}{b} \sinh \beta D(k) \right. \\ \left. + k \sinh \alpha B(k) \right] = 0 \quad (5.25c) \end{aligned}$$

where  $\alpha$  and  $\beta$  are as before. Solving equations 5.25 together with equations 5.19 and 5.24, we obtain for  $A(k)$ ,  $B(k)$ ,  $C(k)$ , and  $D(k)$ :

$$\psi_{pH}: \quad A(k) = \frac{-P_o \lambda^2 U_o}{1 - e^{-a/\lambda_s}} \frac{\sin ka}{k} \frac{1}{\gamma} \frac{1}{1 + (k\lambda_s)^2} \quad (5.26a)$$

$$\psi_L: \quad B(k) = \frac{-(\cos \frac{\pi b}{2b_s} + \frac{\pi b}{2b_s} \frac{\sin \pi b / 2b_s}{\tanh \beta})}{\cosh \alpha + \left(\frac{P_b}{P_h}\right) \sinh \alpha + \left(\frac{P_o}{P_i}\right) \left(\frac{\beta}{b}\right) \frac{\sinh \alpha}{\tanh \beta}} A(k) \quad (5.26b)$$

$$\psi_b: \quad C(k) = -\frac{P_b}{P_h} \sinh \alpha B(k) \quad (5.26c)$$

$$\psi_{hH}: \quad D(k) = -\frac{P_o}{P_h} \frac{\alpha}{\beta} \frac{\sinh \alpha}{\sinh \beta} B(k) - \frac{P_i}{P_h} \frac{\pi b \sin \frac{\pi b}{2b_s}}{2b_s \sinh \beta} A(k) \quad (5.26d)$$

where,

$$\gamma = 1 + (k\lambda)^2 + \left(\frac{\pi\lambda}{2b_s}\right)^2 \quad (5.27)$$

As in the previous two cases, we can apply the Fourier cosine transformations of equations 5.23 and 5.10-5.12 to obtain  $\phi_{po}$ ,  $\phi_L$ ,  $\phi_b$ , and  $\phi_{hH}$ . Taking the same values for the parameters as before, we obtain the results shown in Fig.'s 5.6a,b. We see that Fig.'s 5.6 are similar to Fig.'s 5.5, but now the exposed surface distributions can become monophasic (and monotonic) for suitable values of  $b_s$ . This has significance in explaining the results of Rakita et al (1954), discussed in Chapter 8-A. In the case where  $b_s$  becomes very large, the distributions of Fig.'s 5.6 reduce to those of Fig.'s 5.5.

#### 5-D. Sensitivity analysis

In this section we will summarize and compare the results of the previous three sections by exploring the sensitivity of the ischemic potential distribution, taken on the exposed surface, to the parameter values. We propose to vary one parameter at a time, holding the others fixed, and see what changes result in the exposed surface distribution. When varying  $P_o$ ,  $P_i$ , and  $\lambda$ , we choose to examine the abrupt border case of section 5-A, since this will indicate any changes in the high frequency behavior. When varying  $\lambda_s$  and  $b_s$ , we must of course consider the diffuse border cases of sections 5-B and 5-C.

We begin the analysis by examining the magnitude of the ischemic potential. We recall that the distributions for the ischemic potential were all normalized, with  $P_o \lambda^2 U_o = 1$ . However, the amplitude for the ischemic potential is directly proportional to  $P_o \lambda^2 U_o$ , or from the definition of  $\lambda$ , to:

$$|\phi_o| \sim \frac{P_o R_m U_o}{P_o + P_i} \quad (5.28)$$

Changes in the values of  $P_o$ ,  $P_i$ ,  $R_m$ , or  $U_o$  will influence the magnitude of the ischemic potential according to the relationship of equation 5.28.

We turn now to changes in the shape of the potential distribution on the exposed surface; in particular we focus on changes in concavity and changes in polarity. These features are particularly important, because they have been used to make qualitative statements regarding the shape and extent of the ischemic zone (see Chapter 8-A). We start by examining the changes which result by varying  $P_o$ , the extracellular bulk resistivity. In Fig. 5.7,  $P_o$  has been varied over a 9:1 range, yet the shape of the distribution is not greatly affected, and the concavity is only slightly altered. We note that the curves have been normalized to remove the dependence of the magnitude on  $P_o / (P_o + P_i)$ , as given by equation 5.28. In Fig. 5.8,  $P_i$  has been varied over a 9:1 range; again the shape of the distribution is not greatly affected, although the changes are greater than in the previous case.



In Fig. 5.9,  $P_h (= P_o P_i / (P_o + P_i))$  has been varied, with  $P_o = P_i$ . We see that there is a fairly large sensitivity of the concavity of the potential to the value of  $P_h$  (relative to  $P_b$ ). To test whether it is  $P_h$  or the particular value of  $P_o$  or  $P_i$  which is important, we varied the ratio  $(P_o/P_i)$ , as in Fig. 5.10, holding  $P_h$  fixed. The distribution is almost unchanged. Thus, we conclude that  $P_h$  is the sensitive parameter.

In Fig. 5.11, we see the effects of varying the space constant,  $\lambda$ . As expected, with increasing  $\lambda$  there is a decrease in the high frequency content of the distribution, and the transition in polarity at the border becomes more rounded. This "rounding off" effect is most pronounced for ischemic zones with abrupt borders. When the source distribution varies slowly instead of abruptly across the border zone, we expect that there will be a minimal effect of  $\lambda$  on the distribution. We verify this hypothesis in Fig. 5.12 for an ischemic zone with a lateral diffuse border.

In Fig. 5.13 we examine the effect of varying the lateral border width. As the width increases, the concavity of the potential distribution for  $x < a$  reverses polarity and then decreases in magnitude. For  $x > a$ , the concavity decreases in magnitude without a change in polarity. We see that when  $\lambda_s$  equals the thickness of the myocardial strip (2b), the potential distribution becomes monotonic for the region  $x < a$ . The overall potential distribution remains

biphasic, however, for all values of  $\lambda_s$ .

Finally, in Fig. 5.14 we examine the effect of varying the transverse border width at the lower boundary. When  $b_s$  becomes sufficiently small, the potential distribution becomes monophasic. This is because the Laplace current flow at the lower boundary has been reduced to the point where it no longer can produce a reversal in the polarity of  $\phi_o$ .

We conclude that the amplitude of the ischemic potential distribution at the surface of a myocardial strip is directly influenced by  $P_o$ ,  $P_i$ ,  $R_m$ , and  $U_o$ . The concavity of the distribution is affected primarily by the ratio  $(P_h/P_b)$ , the lateral border width, and the space constant. The polarity of the distribution is affected primarily by the transverse border width.

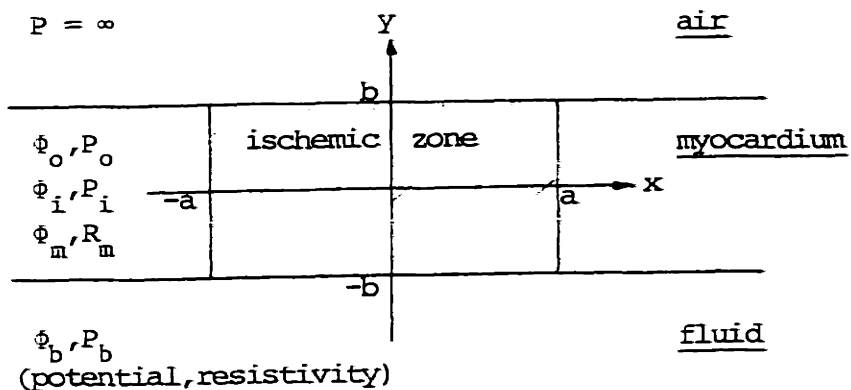


FIGURE 5.1 - The rectangular myocardial strip (asymmetrical case)

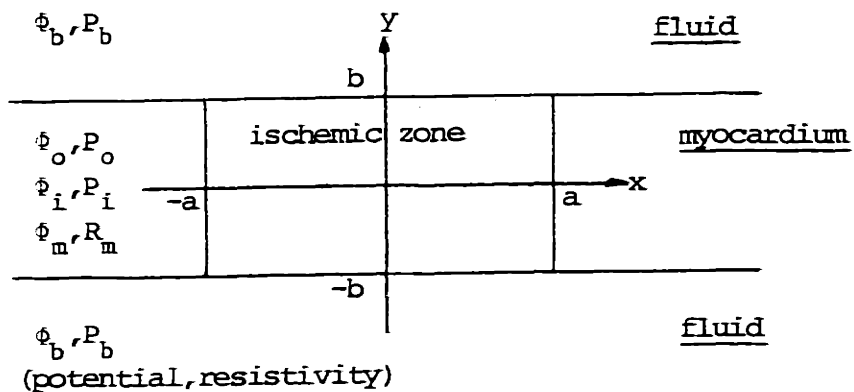
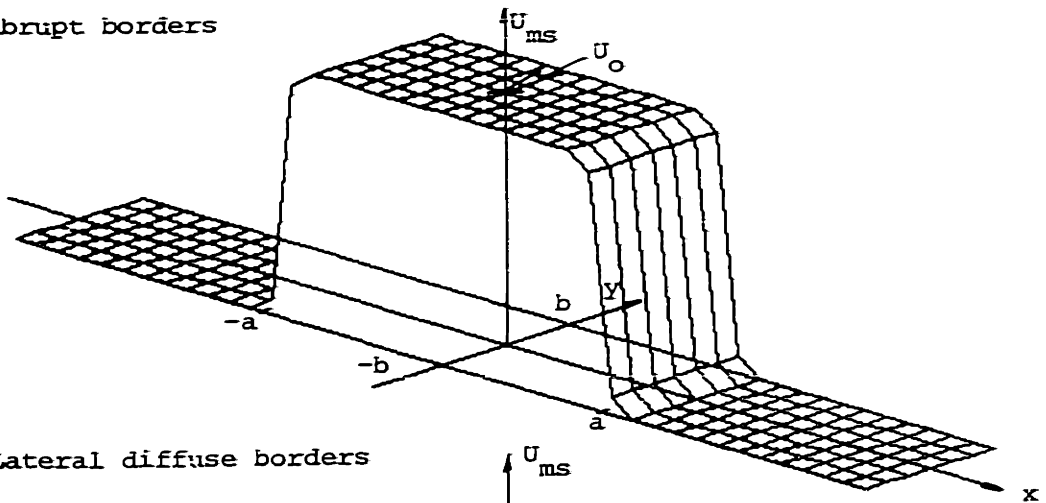
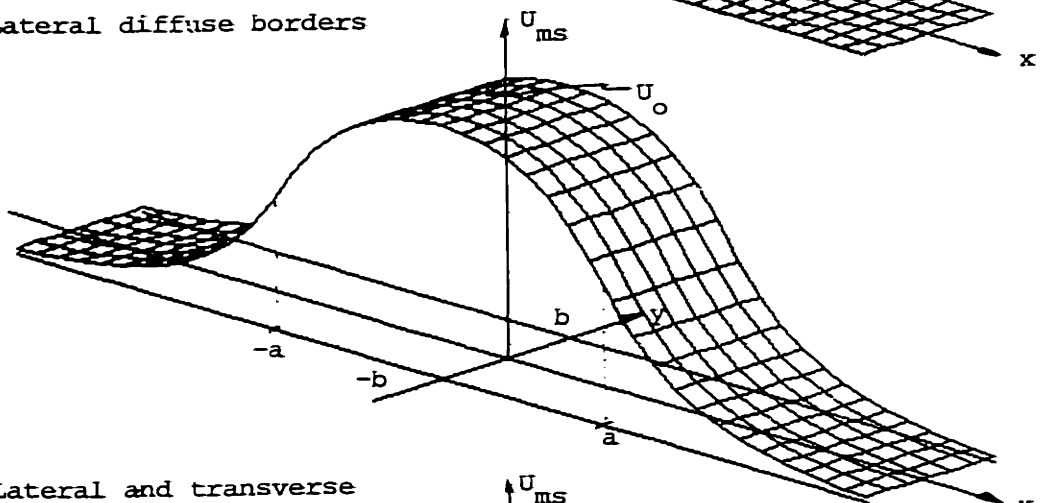


FIGURE 5.2 - The rectangular myocardial strip (symmetrical case)

a) Abrupt borders



b) Lateral diffuse borders



c) Lateral and transverse diffuse borders

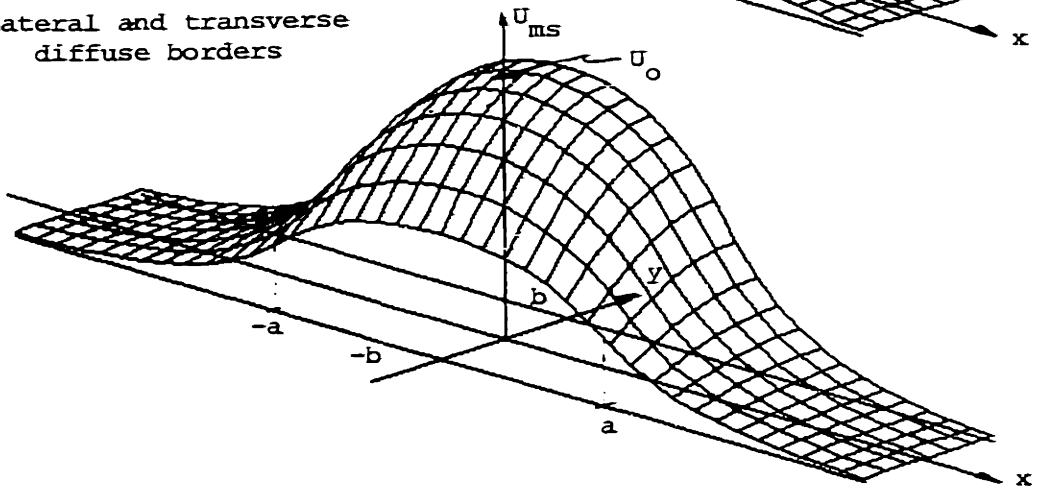


FIGURE 5.3 - The rectangular source distribution,  $U_{ms}$

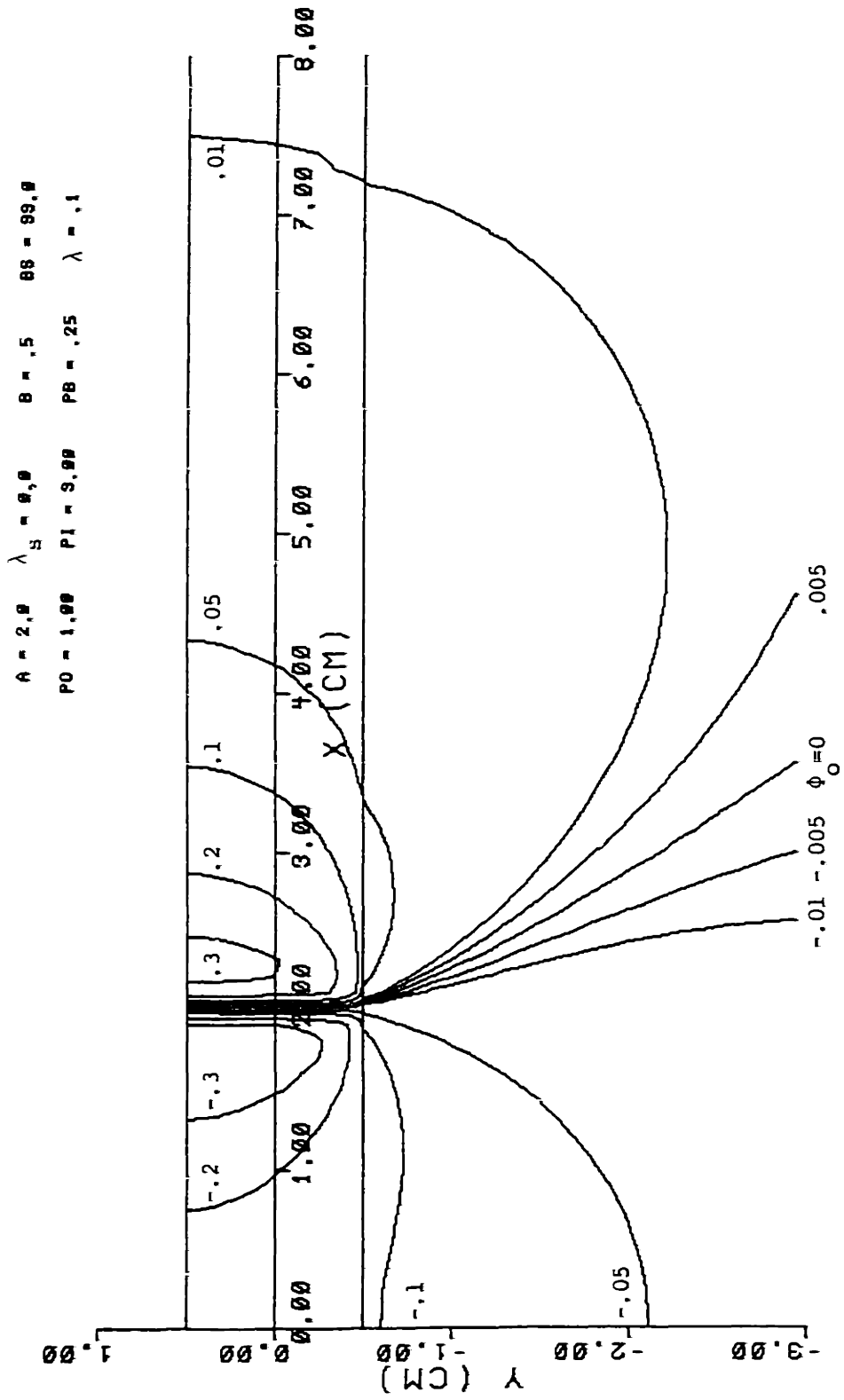


FIGURE 5.4a - Equipotential lines for the extracellular potential for the case of an abrupt ischemic border

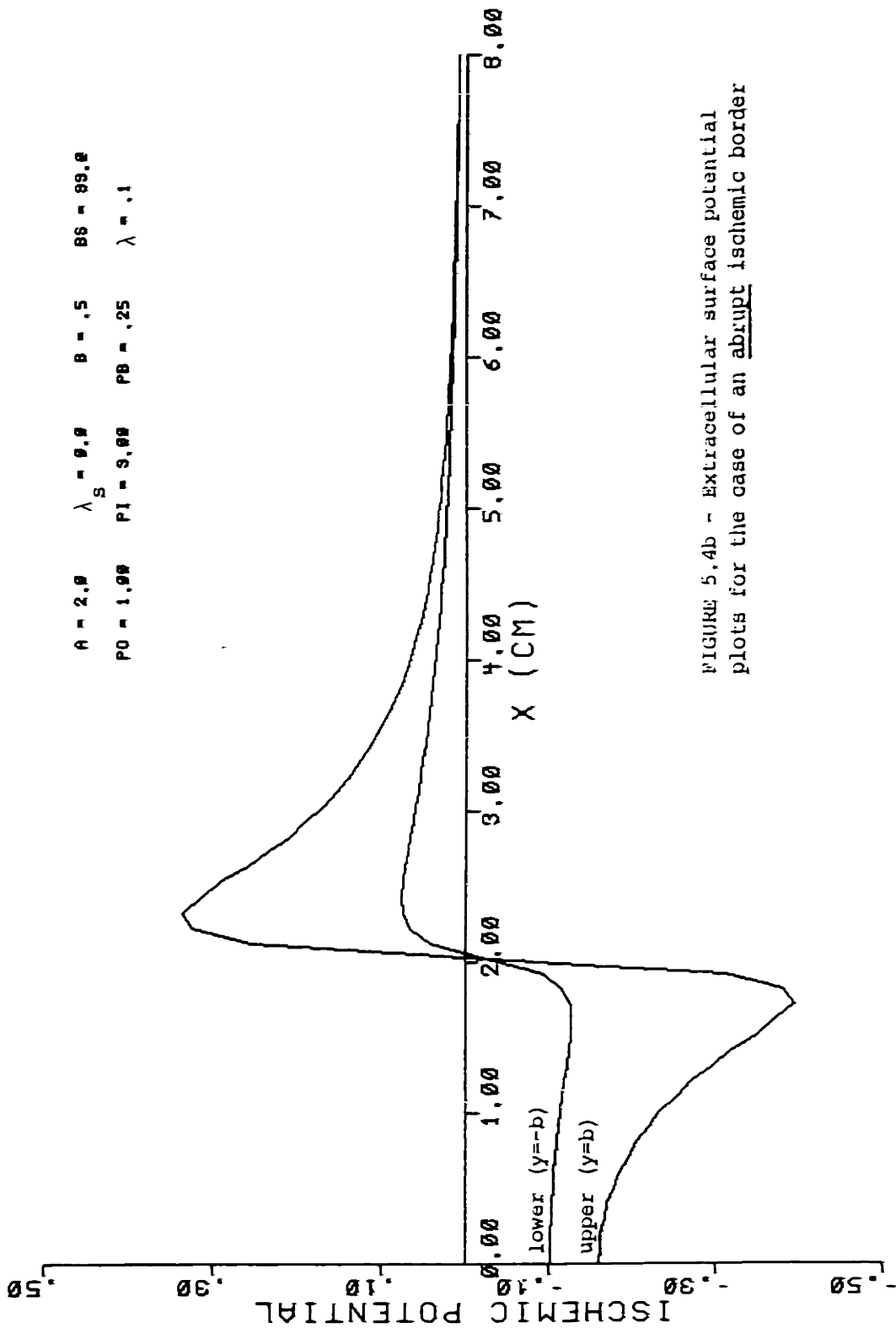


FIGURE 5.4b - Extracellular surface potential plots for the case of an abrupt ischemic border

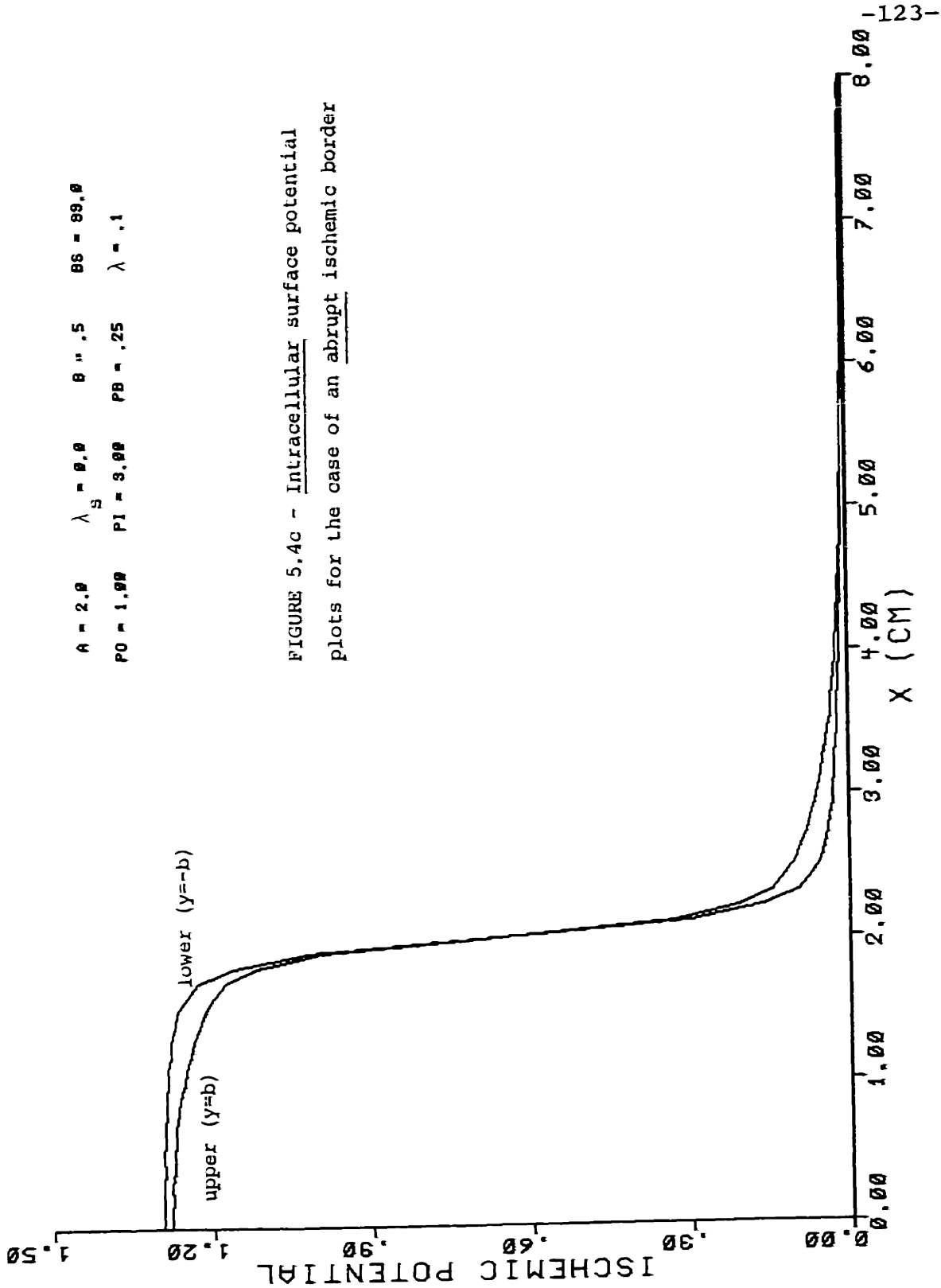


FIGURE 5.4c - Intracellular surface potential plots for the case of an abrupt ischemic border

$A = 2.0$     $\lambda_s = 2.0$     $B = .5$   
 $P_0 = 1.00$     $P_1 = 3.00$     $P_2 = .25$     $\lambda = .1$

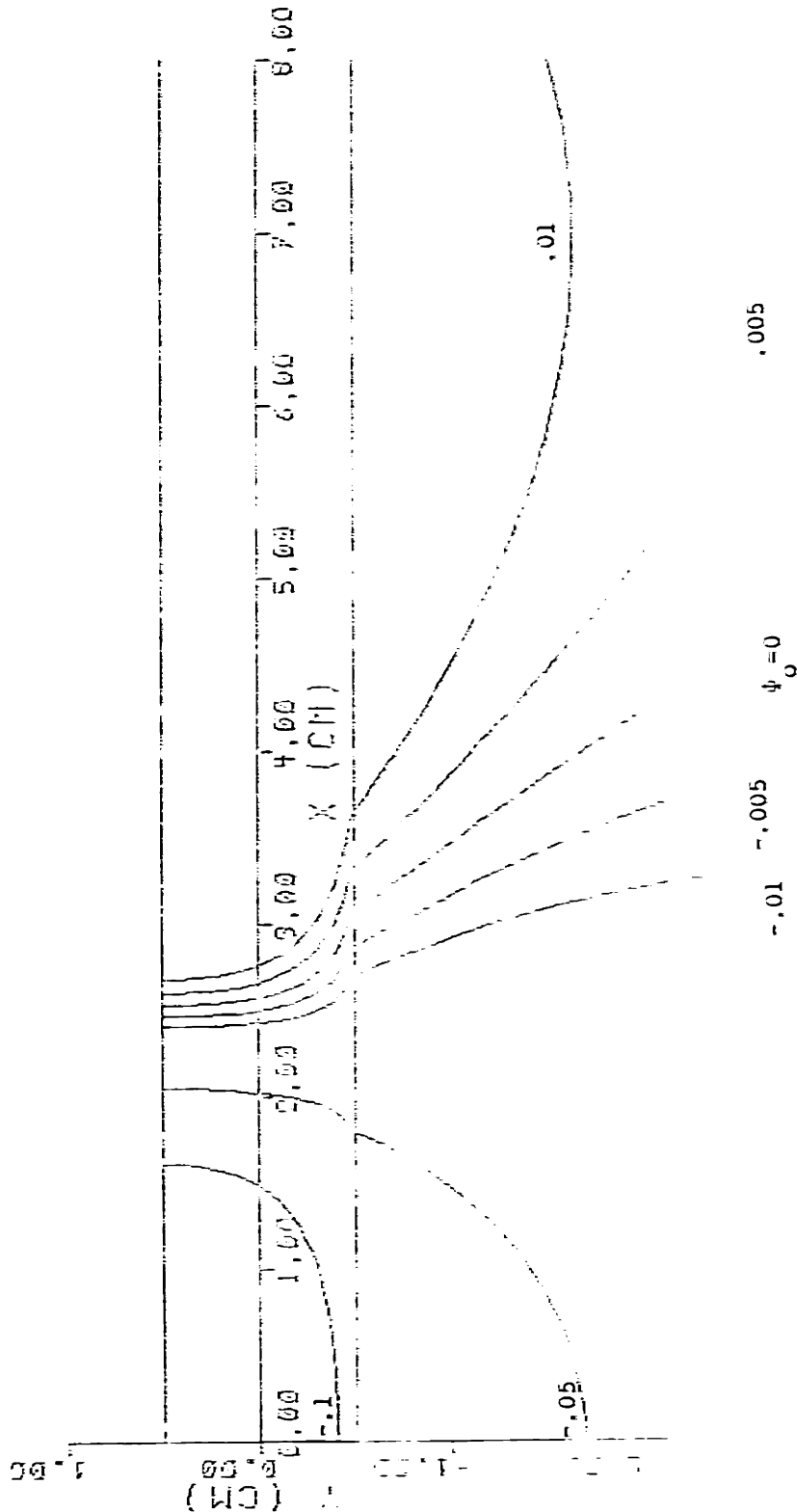


FIGURE 5.5a - Equipotential lines for the extracellular potential for the case  
 of a lateral diffuse ischemic border



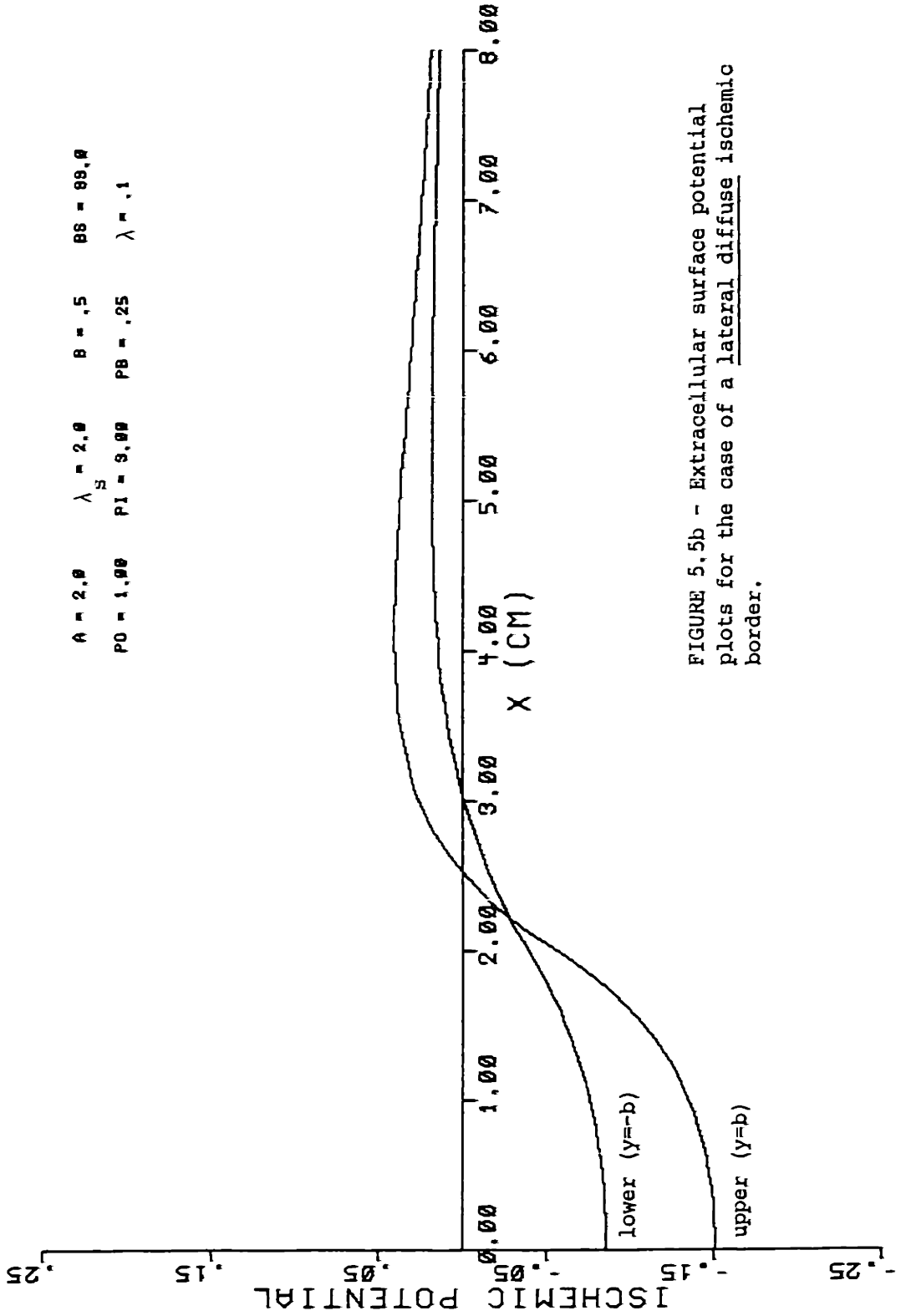


FIGURE 5.5b - Extracellular surface potential plots for the case of a lateral diffuse ischemic border.

A = 2.0    $\lambda_s = 2.0$    B = .5   BS = 2.0  
PO = 1.00   PI = 3.00   PB = .25    $\lambda = .1$

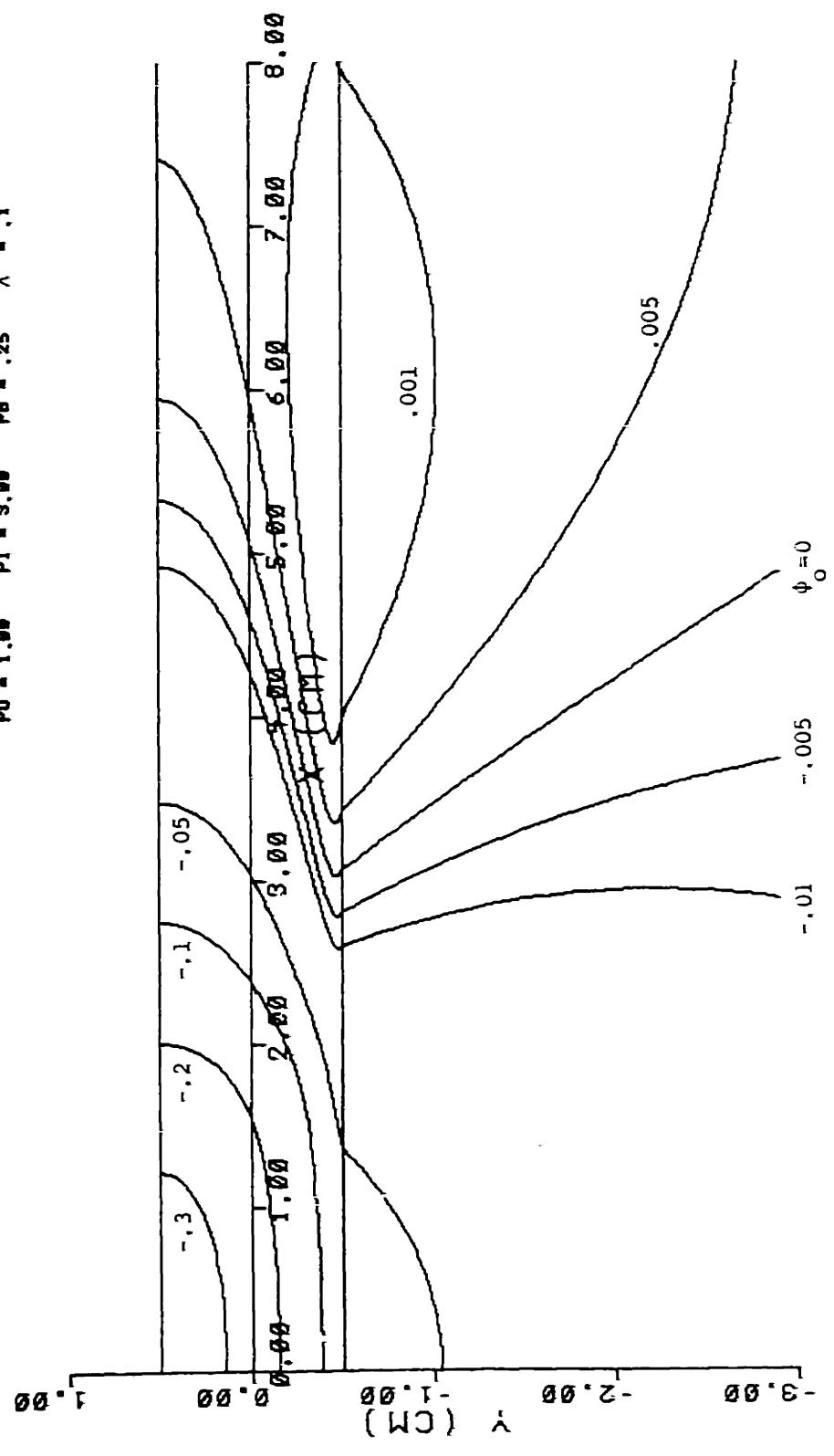


FIGURE 5.6a - Equipotential lines for the extracellular potential for the case of lateral and transverse diffuse ischemic borders

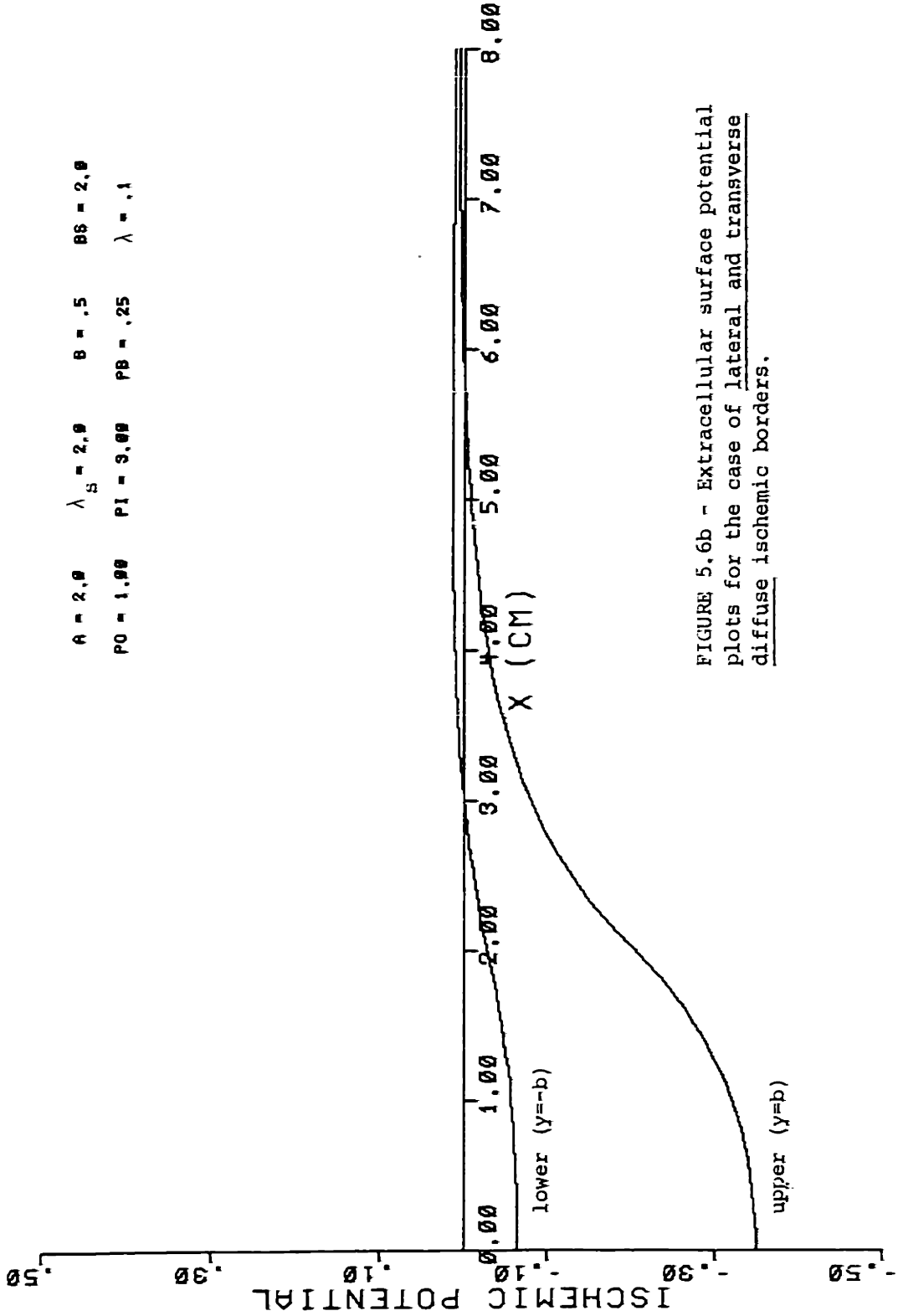


FIGURE 5.6b - Extracellular surface potential plots for the case of lateral and transverse diffuse ischemic borders.

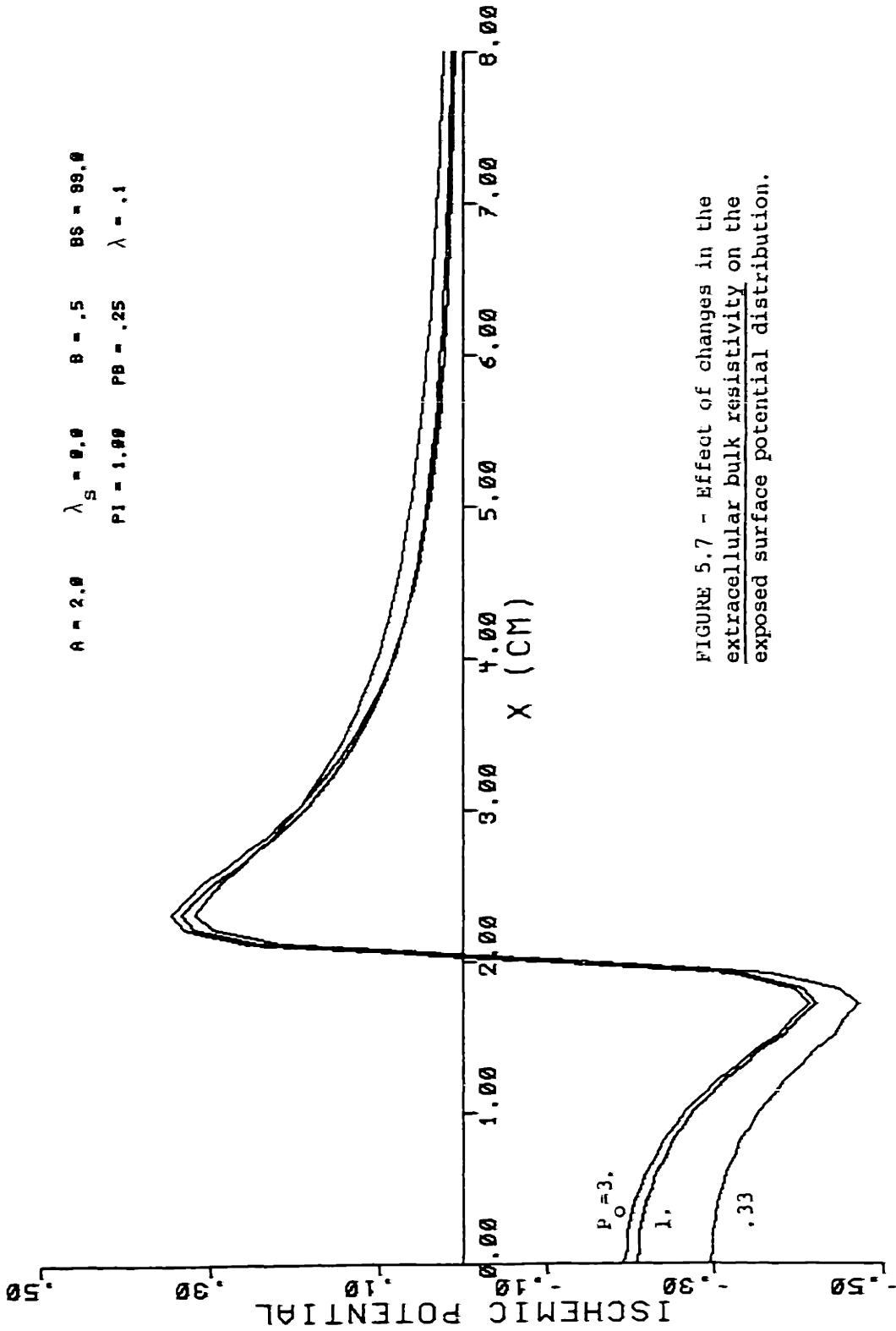


FIGURE 5.7 - Effect of changes in the extracellular bulk resistivity on the exposed surface potential distribution.

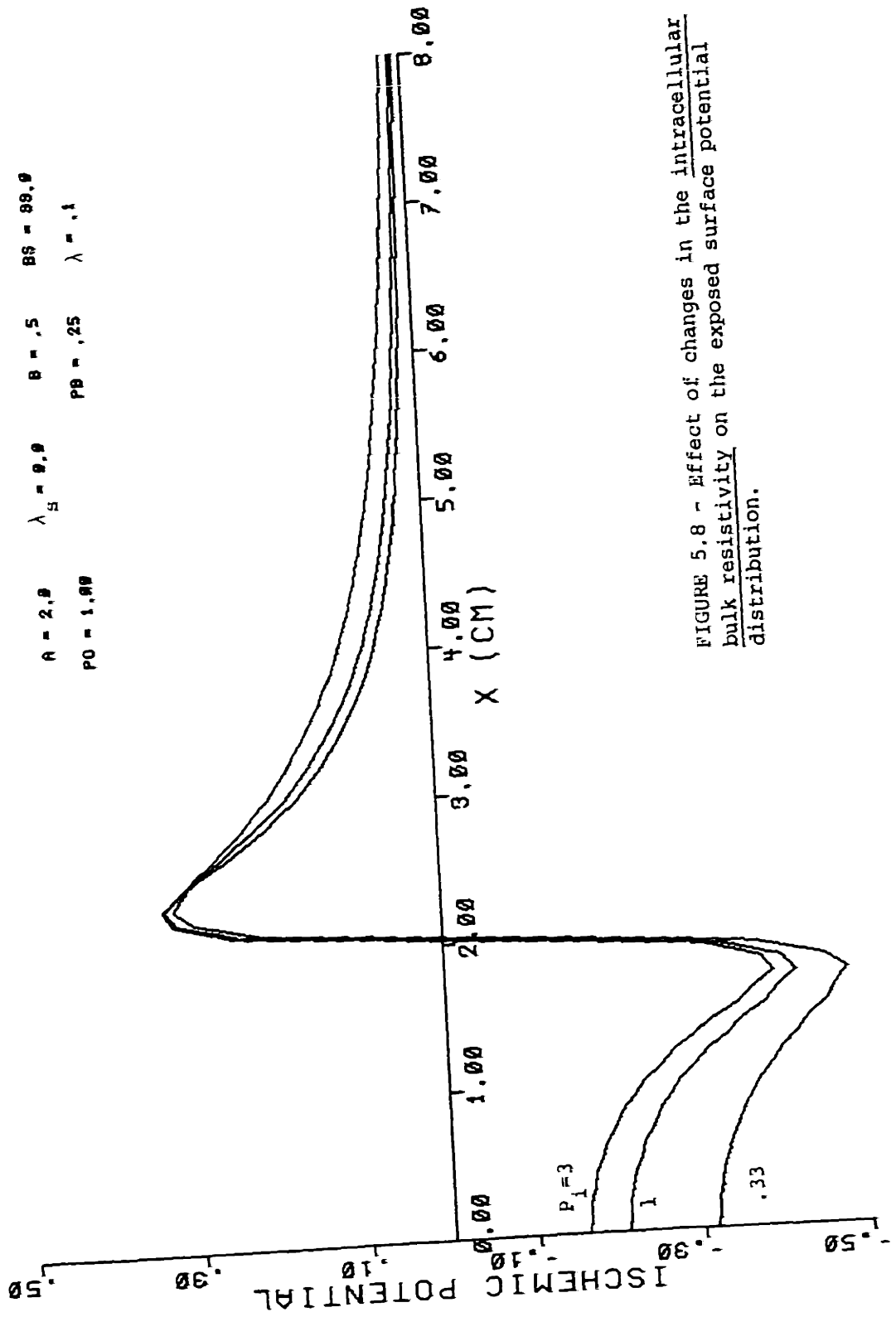


FIGURE 5.8 - Effect of changes in the intracellular bulk resistivity on the exposed surface potential distribution.

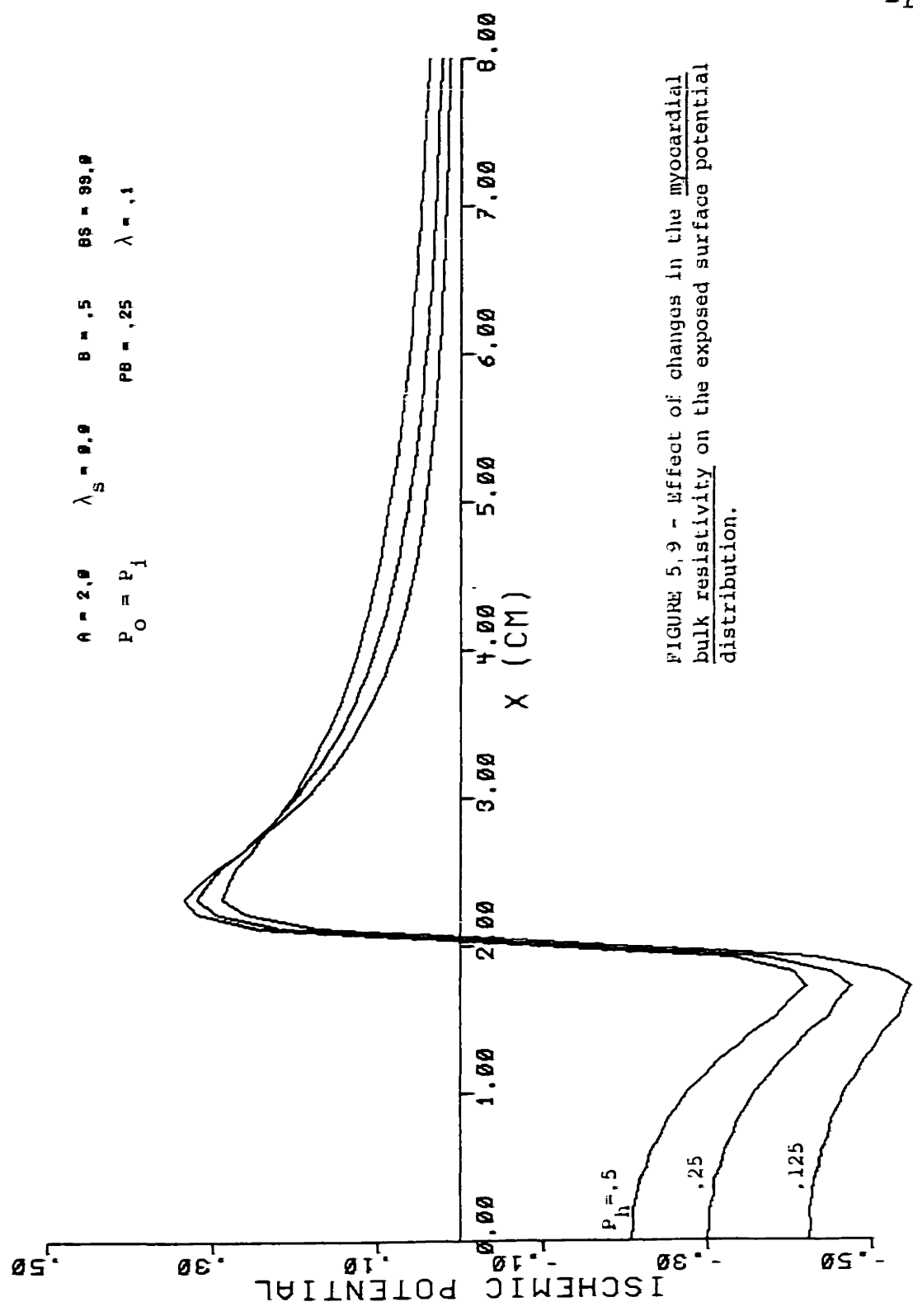


FIGURE 5.9 - Effect of changes in the myocardial bulk resistivity on the exposed surface potential distribution.

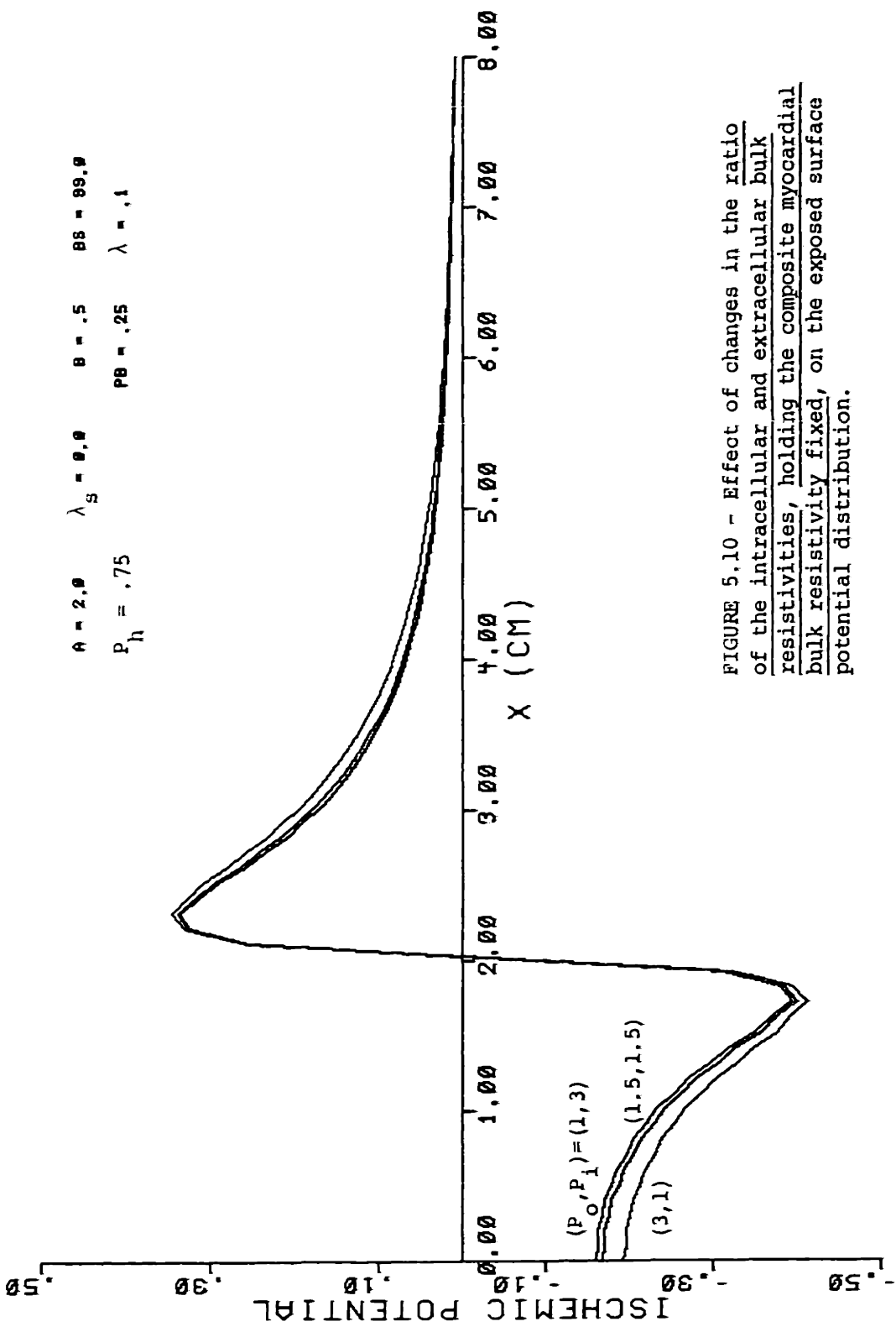


FIGURE 5.10 - Effect of changes in the ratio of the intracellular and extracellular bulk resistivities, holding the composite myocardial bulk resistivity fixed, on the exposed surface potential distribution.

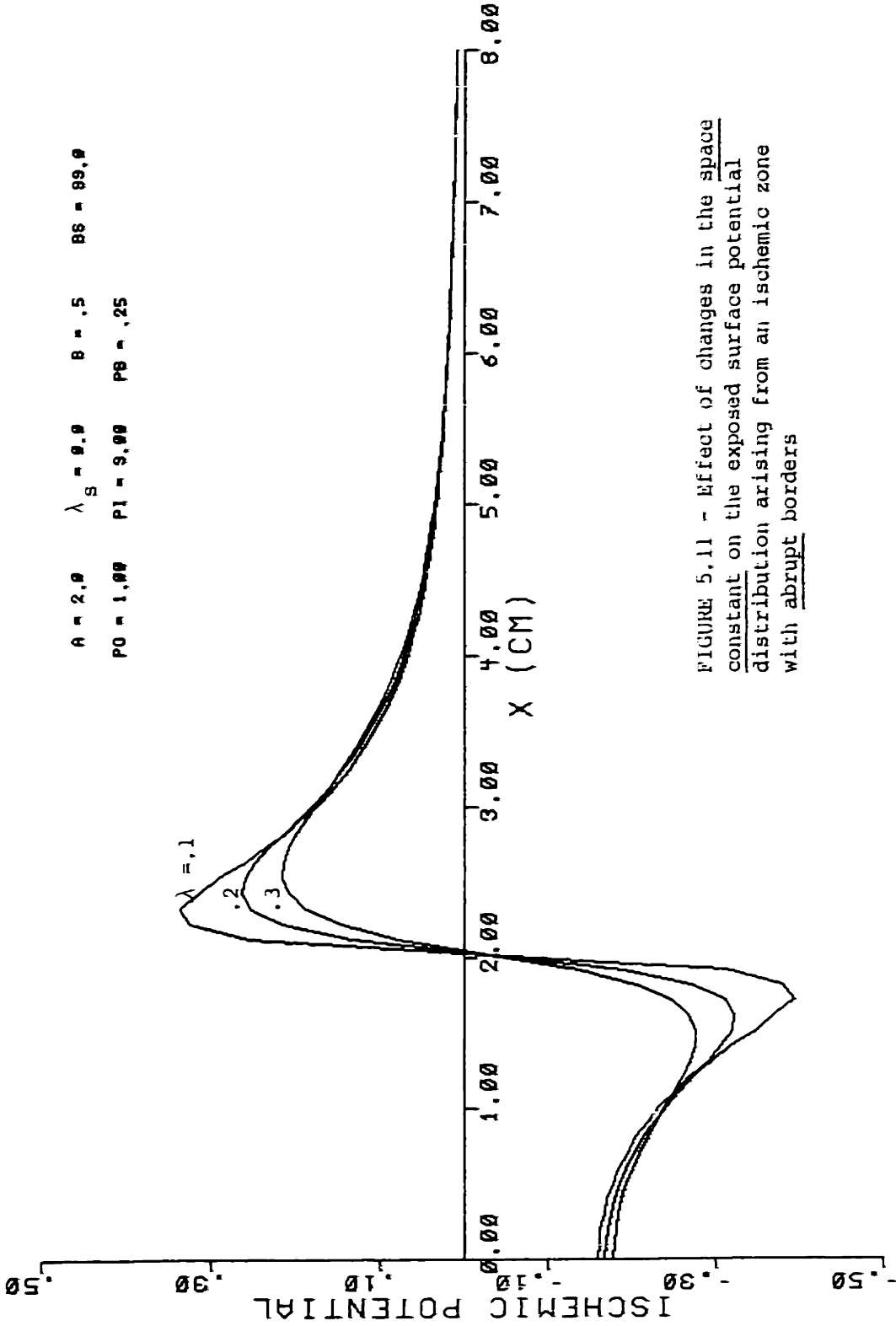


FIGURE 5.11 - Effect of changes in the space constant on the exposed surface potential distribution arising from an ischemic zone with abrupt borders



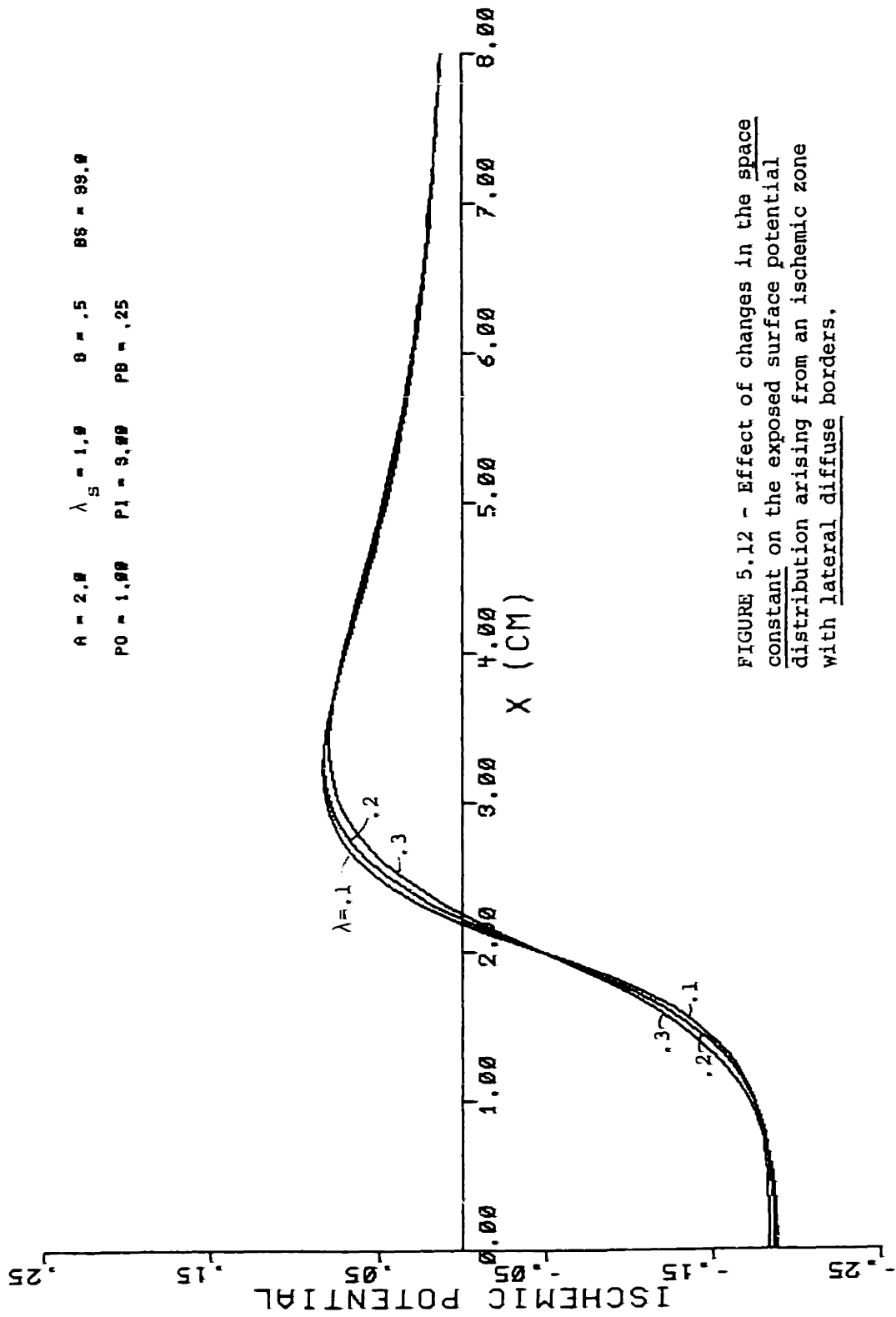


FIGURE 5.12 - Effect of changes in the space constant on the exposed surface potential distribution arising from an ischemic zone with lateral diffuse borders,

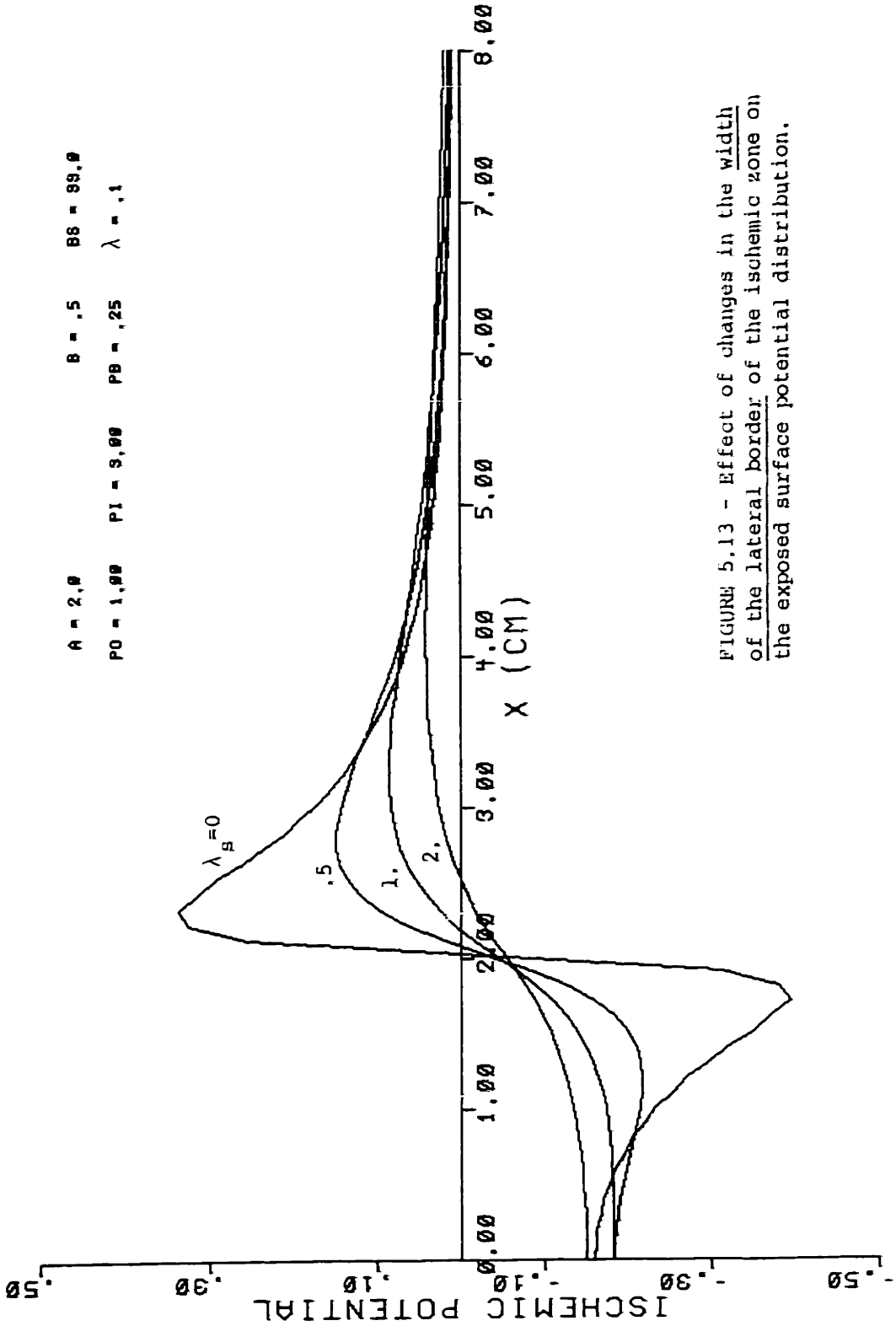


FIGURE 5.13 - Effect of changes in the width of the lateral border of the ischemic zone on the exposed surface potential distribution.

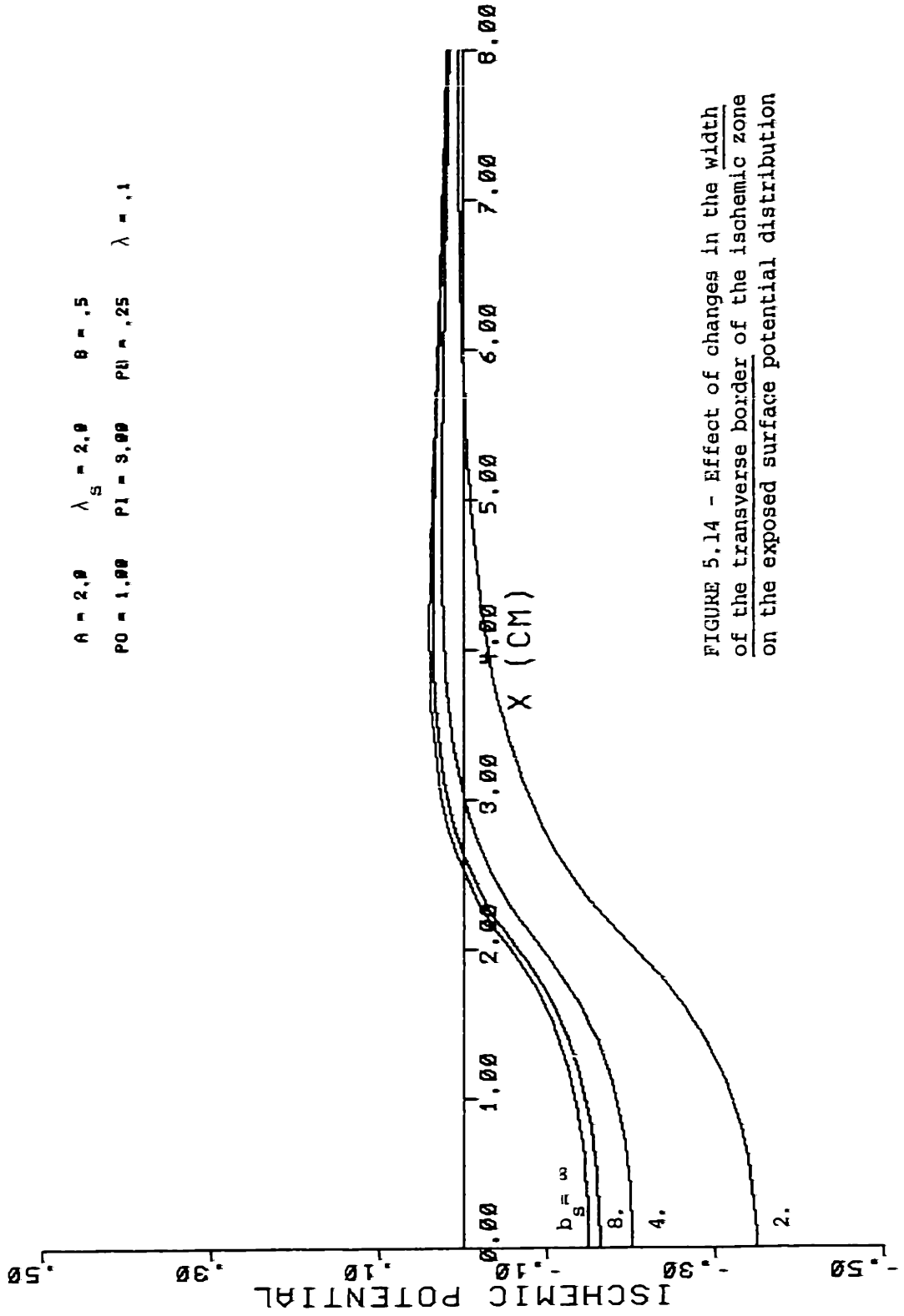


FIGURE 5.14 - Effect of changes in the width of the transverse border of the ischemic zone on the exposed surface potential distribution

CHAPTER 6: The Solid Angle Model, Derived from the  
Bi-Domain Model

There are a number of cases in which the bi-domain model can be simplified. In this chapter, the "solid angle" model described in Chapter 3 is shown to be an approximation to the bi-domain model and to be valid only under limited conditions.

6-A. Assumptions of the solid angle model

The so-called "solid angle" model which is commonly used in the literature to describe myocardial ischemic potentials describes a potential in a mono-domain and takes the form (cf. Appendix E),

$$\phi_e(\underline{r}_P) = \frac{P_e}{4\pi} \int_{S_b} \underline{M}_s(\underline{r}_Q) d\Omega_Q = - \frac{P_e}{4\pi} \int_{S_b} \underline{M}_s(\underline{r}_Q) \cdot \nabla \left( \frac{1}{r_{QP}} \right) da_Q \quad (6.1)$$

where  $\phi_e$  is the equivalent mono-domain potential,  $P$  is the observation point,  $\nabla$  is the usual differential operator (taken with respect to the  $P$  coordinate),  $P_e$  is the equivalent mono-domain bulk resistivity,  $S_b$  is the surface bordering the ischemic zone, and  $\underline{M}_s$  is a current dipole moment/unit volume distributed over the incremental volume surrounding  $S_b$ , and directed normal to the surface, with a magnitude proportional to the degree of ischemia. In this section we show that under three limiting assumptions, the solid angle model can be derived from the bi-domain model in

the manner illustrated in Fig. 6.1. In the derivation the first assumption is that of a low spatial frequency behavior for the distribution of the active membrane current source ( $U_{ms}$ ). This results in a simplification of the bi-domain Helmholtz equations to a set of bi-domain Poisson equations. The second assumption is that of a distribution for  $U_{ms}$  such that the intensity of  $U_{ms}$  is everywhere constant, except in the neighborhood of the surface  $S_b$ . The Poisson equations reduce still further to a set of bi-domain Laplace equations for regions excluding the border. Finally, with a third assumption of a spatially infinite medium, we arrive at the solid angle model in the form of equation 6.1.

We begin with the form of the bi-domain model for which there are no externally introduced sources of current (as from microelectrodes) in the bulk material. The only sources of current are those at the cellular membrane ( $U_{ms}$ ).

$$\nabla^2 \phi_m = \frac{1}{\epsilon^2} \phi_m - (P_o + P_i) U_{ms} \quad (4.16a)$$

$$\nabla^2 \phi_o = \frac{-P_o}{P_o + P_i} \nabla^2 \phi_m \quad (4.16b)$$

$$\nabla^2 \phi_i = \frac{P_i}{P_o + P_i} \nabla^2 \phi_m \quad (4.16c)$$

Observing that since the parameters  $P_o$ ,  $P_i$ , and  $R_m$  are assumed to be spatially constant, we can write the general solutions to equations 4.16 in the form of equations 4.19,

$$\hat{\phi}_m = \hat{\phi}_H \quad (4.19a)$$

$$\hat{\phi}_o = \frac{-P_o}{P_o + P_i} \hat{\phi}_m + \hat{\phi}_L \quad (4.19b)$$

$$\hat{\phi}_i = \frac{P_i}{P_o + P_i} \hat{\phi}_m + \hat{\phi}_L \quad (4.19c)$$

where  $\phi_H$  is a solution to the inhomogeneous Helmholtz equation, and  $\phi_L$  is a solution to Laplace's equation. We proceed with our first assumption:

ASSUMPTION 1: HIGH SPATIAL FREQUENCIES IN  $U_{ms}$  ARE NEGLIGIBLE.

The preceding statement is equivalent to:

$$\gamma^2 \phi_m \ll \frac{1}{\lambda^2} \phi_m \quad (6.2)$$

That is, if we think of  $\phi_m$  in terms of its spatial Fourier components, we are assuming that  $\phi_m$  is primarily composed of frequency terms with periods much greater than the space constant. Alternatively, since  $\phi_m$  is the forced response from the driving function  $U_{ms}$ , we are assuming that  $U_{ms}$  is primarily composed of frequency terms with periods much greater than the space constant. Thus, from equation 4.16a,

$$\frac{1}{\lambda^2} \phi_m = (P_o + P_i) U_{ms} \quad (6.3)$$

independent of boundary conditions.

An equivalent way to obtain equation 6.3 is to assume that  $U_m$ , the total membrane current, is much less than the active component  $U_{ms}$  (cf. Fig. 4.4). We have:

$$\phi_m = R_{mmp} U_{mmp} = R_m (U_m + U_{ms}) = R_m U_{ms} \quad (6.4)$$

Since  $\lambda^2 = R_m / (P_o + P_i)$ , equations 6.3 and 6.4 are identical.

Applying equation 6.4 to equations 4.19, we have:

$$\phi_m = R_m U_{ms} \quad (6.5a)$$

$$\phi_o = -P_o \lambda^2 U_{ms} + \phi_L \quad (6.5b)$$

$$\phi_i = P_i \lambda^2 U_{ms} + \phi_L \quad (6.5c)$$

Equations 6.5 can be expressed in the form of Poisson's equation,

$$\nabla^2 \phi_m = \frac{(P_o + P_i) P_e}{P_o} (\nabla \cdot \underline{M}_s) \quad (6.6a)$$

$$\nabla^2 \phi_o = -P_e (\nabla \cdot \underline{M}_s) \quad (6.6b)$$

$$\nabla^2 \phi_i = \frac{P_i P_e}{P_o} (\nabla \cdot \underline{M}_s) \quad (6.6c)$$

if we take:

$$P_e \underline{M}_s = P_o \lambda^2 \nabla U_{ms} \quad (6.7)$$

$\underline{M}_s$  has the units of amp/cm<sup>2</sup> and can be interpreted as a volume density of dipole current sources (dipole moment/unit volume). Thus, we could define:

$$P_e = P_o \quad (6.8a)$$

$$\underline{M}_s = \lambda^2 \nabla U_{ms} \quad (6.8b)$$

Equation 6.7 forms the equivalence relationship between the sources of the bi-domain Helmholtz model and the bi-domain Poisson model. We note that the magnitude of the

equivalent source cannot be chosen uniquely, as it is the product  $P_e M_s$  which is constrained. We could, for example, choose:

$$P_e = P_h \quad (6.9a)$$

$$\underline{M}_s = \frac{R_m}{P_i} \nabla U_{ms} \quad (6.9b)$$

We shall see in section 6-C that the definition of equations 6.9 will be the more useful.

Thus, from the viewpoint of either domain, we can equivalently represent the active membrane current sources  $U_{ms}$  as a dipole moment/unit volume  $\underline{M}_s$  whose magnitude is given by equation 6.7. A bi-domain representation is still essential for the overall picture, since opposite polarity dipole sources will exist at the corresponding locations in the two domains, and consequently the intracellular and extracellular current densities will have oppositely directed components.

We can write the general solution to equation 6.6b in the following form:

$$\phi_o(\underline{r}_p) = \frac{P_e}{4\pi} \int_V \frac{\nabla \cdot \underline{M}_s(\underline{r}_Q)}{r_{QP}} dv_Q + \phi_L(\underline{r}_Q) \quad (6.10)$$

Using the vector identity for the divergence of a product, and the fact that  $\underline{M}_s$  vanishes at infinity, we then have:

$$\phi_o(\underline{r}_p) = - \frac{P_e}{4\pi} \int_V \underline{M}_s(\underline{r}_Q) \cdot \nabla \left( \frac{1}{r_{QP}} \right) dv_Q + \phi_L(\underline{r}_p) \quad (6.11)$$



Comparing equation 6.11 to 6.1, we see that the only sources are at the incremental volume formed by the surface  $S_b$ , having an incremental thickness. Therefore, since the equivalent sources are defined from the spatial gradient of  $U_{ms}$ , we have our second assumption.

ASSUMPTION 2: MAGNITUDE OF MEMBRANE CURRENT SOURCE  $U_{ms}$  CHANGES ONLY ACROSS A BORDER SURFACE.

Consequently,  $U_{ms}$  experiences a change in value across the surface  $S_b$ , and otherwise has a constant value. Since  $U_{ms}$  is identified as the ischemic membrane current source leading to changes in the resting potential (cf. Chapter 4-B), we take the value for  $U_{ms}$  to be zero for regions bounded by  $S_b$  and infinity (i.e. for the healthy myocardium).

In addition, we see that the term  $\phi_L$  in equation 6.11 is neglected. Therefore we have our third assumption.

ASSUMPTION 3: NO LOCAL BOUNDARY CONSTRAINTS.

This means that the myocardium is considered to be an infinite medium.

In a manner similar to the derivation of equation 6.11, we can show that under the same three assumptions listed above, a solid angle model can describe the intracellular potential distribution. The equivalence relation (equation 6.7) becomes,

$$P \frac{M}{e-s} = -P_i \lambda^2 \nabla U_{ms} \quad (6.12)$$

for the intracellular domain.

To conclude, we see that three assumptions are made to

reduce the general bi-domain model of equations 4.16 to the so-called "solid angle" model of equation 6.1. These are: 1) low spatial frequency behavior in the active membrane source distribution, 2) a change in the active membrane source intensity only at a border surface, and 3) no local boundary constraints. This implies that in the absence of local boundary constraints, the mathematical solutions for the bi-domain model and the solid angle model differ only in the high spatial frequency terms (i.e. for frequencies with wavelength less than the space constant), provided that the sources follow a suitable equivalence relationship (equation 6.7). Consequently, for source distributions which change slowly in magnitude over distances much greater than a space constant, the solid angle model yields reasonably accurate solutions, but only if local boundary constraints can be neglected. In general, the ischemic zones of interest which are illustrated in Fig. 3.2 have boundary constraints which cannot be neglected, but nevertheless the solid angle model has been applied incorrectly to these situations.

We will have occasion in Chapter 7 to use the bi-domain model under Assumptions 1 and 2 only (equation 6.11, taken with sources at the incremental volume around  $S_p$ , subject to the appropriate boundary conditions), and we will refer to this simplified model as the "bi-domain Poisson model."

6-B. Equivalence relationships between solid angle and bi-domain sources

We would like now to discuss the physical differences between the source representations for the bi-domain model and for the solid angle model, as it is currently used. Let us begin by examining the source representations for an intramural ischemic zone, one which is entirely embedded in the myocardium, as shown in Fig. 6.2a. According to the solid angle model, there is a uniformly dense, current dipole layer situated on the boundary  $S_b$ , directing current into the enclosed volume. Immediately, there is a problem with charge conservation; in steady state a constant flow of current into the enclosed volume cannot be sustained without an infinite buildup of charge. Hence the source representation used by the solid angle model violates physical constraints.

However, the bi-domain model can support a constant flow of current into an enclosed volume of the extracellular domain, since a return path for the current is provided through the intracellular domain. Although the potentials determined by the two models are the same (except at high spatial frequencies), charge conservation is preserved by the bi-domain model and violated by the solid angle model.

Let us consider another case - that of a subepicardial ischemic zone, illustrated in Fig. 6.2b, where the epicardium is in contact with air (a zero conductive medium). Again, with the solid angle model there is a uniformly dense,

current dipole layer situated on the boundary  $S_b$  and directed toward the epicardium. Although there is physically a boundary at the epicardium which prevents a flow of normal current, the solid angle model assumes that the medium is infinite, as in Fig. 6.2c. Consequently, the surface  $S_b$  is not taken to be closed, and charge conservation is preserved. But now, the physical boundary constraint at the epicardium is violated. However, the bi-domain model again provides a self-consistent physical description for the current distribution. The epicardial boundary constraint is taken into account, and as in the case of the intramural ischemic zone, the return path for the current (now taken to be in the extracellular domain) is provided through the intracellular domain. Hence charge conservation and the boundary constraints are satisfied by the bi-domain model, whereas charge conservation but not the boundary constraints are satisfied by the solid angle model.

Let us now consider in more detail the equivalence relationship of equation 6.7. The sources  $\underline{M}_s$  of the bi-domain Poisson model have been equated to the spatial gradient of the active membrane current source distribution, times a proportionality factor. Since  $\underline{M}_s$  is defined as a gradient of a scalar function, the curl of  $\underline{M}_s$  must be zero. This implies that the line integral of  $\underline{M}_s$  around a closed contour in space must also be zero. Alternatively, the line integral of  $\underline{M}_s$  from point A to point B must be independent of

the path. If we take point A to be on one side of the border surface  $S_b$  and point B to be on the other side of  $S_b$ , then the above constraint implies that the surface  $S_b$  must be closed in an infinite medium (as shown in Fig. 6.2a). We reason this as follows. The only contribution to the line integral of  $\underline{M}_s$  is at  $S_b$ . If the surface  $S_b$  were not closed (as in Fig. 6.2c), then two paths from A to B could be chosen such that one path traversed the surface  $S_b$  and the other did not. In that case, the two line integrals would not be the same. If the medium is not infinite, then the surface  $S_b$  need not be closed, but the surface  $S_b$  must then terminate at the boundary of the medium, as illustrated in Fig. 6.2b. The curl equal zero constraint would then still be satisfied, since the line integral between points A and B, chosen anywhere in the myocardium on either side of  $S_b$ , must traverse  $S_b$  and is therefore constant. Consequently, the bi-domain Poisson model has in part a solid angle-like appearance but nevertheless satisfies the physical conditions of charge conservation and boundary constraints.

We conclude from this discussion that there are cases of ischemic zones for which the solid angle model violates either charge conservation or boundary constraints. The bi-domain model, however, is a self-consistent model which satisfies both physical conditions. An equivalent density of current dipole sources,  $\underline{M}_s$ , can be derived to simplify the bi-domain Helmholtz equations to a set of bi-domain Poisson

equations. Because of the nature of the equivalence relationship between  $\underline{M}_s$  and  $\bar{U}_{ms}$ ,  $\underline{M}_s$  is defined only over closed surfaces or over open surfaces which are terminated on the boundary surface of the myocardium.

### 6-C. Boundary conditions

In the case where Assumptions 1 and 2 are valid but where boundary conditions can significantly alter the distribution of current, the bi-domain Poisson model, rather than the solid angle model, must be used. As before, provided that the appropriate equivalence relationship is used for the source, and the appropriate boundary conditions are carefully selected, the mathematical solutions for the bi-domain Poisson model will approximate those for the complete bi-domain Helmholtz model. We consider the situation shown in Fig. 6.3 in which the border surface meets a boundary between bi-domain and mono-domain media.

As we discussed in the previous section, in the presence of local boundary conditions, it may now be the case that the equivalent current dipole sheet of the bi-domain Poisson model does not form a closed surface. Consequently extracellular current loops can now close through the adjacent mono-domain, in addition to the intracellular domain. Since there will then be a net current flowing out of the bi-domain into the adjacent mono-domain, this current will take the form of a Laplace ("common-mode") current

(refer to the discussion of Chapter 4-F). Using the notation of equations 5.3, the boundary conditions of equation 4.36a,b (accounting for the flow of normal current) can be written as:

$$\frac{1}{P_o} \frac{\partial (\phi_{po} - \frac{P_o}{P_o + P_i} \phi_{hH} + \phi_L)}{\partial n} = \frac{1}{P_b} \frac{\partial \phi_b}{\partial n} \quad (6.13a)$$

$$\frac{1}{P_i} \frac{\partial (\phi_{pi} + \frac{P_i}{P_o + P_i} \phi_{hH} + \phi_L)}{\partial n} = 0 \quad (6.13b)$$

Combining equations 6.13 and using the relationship of equation 5.4b, we obtain,

$$\frac{1}{P_h} \frac{\partial \phi_L}{\partial n} = \frac{1}{P_b} \frac{\partial \phi_b}{\partial n} \quad (6.14)$$

The above boundary condition differs significantly from the classical boundary condition for the normal gradient of potential in a mono-domain with bulk resistivity  $P_o$ ,

$$\frac{1}{P_o} \frac{\partial (\phi_{pe} + \phi_L)}{\partial n} \Big|_{S_h} = \frac{1}{P_b} \frac{\partial \phi_b}{\partial n} \Big|_{S_h} \quad (6.15)$$

( $\phi_{pe}$  is the particular solution) and from the same boundary condition for a mono-domain with bulk resistivity  $P_h$ :

$$\frac{1}{P_h} \frac{\partial (\phi_{pe} + \phi_L)}{\partial n} \Big|_{S_h} = \frac{1}{P_b} \frac{\partial \phi_b}{\partial n} \Big|_{S_h} \quad (6.16)$$

The term  $\phi_{pe}$  of equations 6.15 and 6.16 can be identified as the low frequency approximation to  $\phi_{po}$ , since the sources for  $\phi_{pe}$  and  $\phi_{po}$  are related by the equivalence relation (equation

6.7). Because the normal gradient of  $\phi_H$  is large at the boundary (even though  $\phi_{hH}$  itself may be small), we cannot ignore  $\partial\phi_{hH}/\partial n$  to obtain equation 6.15 directly from equation 6.13a. However, in the case where the normal gradient of the particular solution is zero at the boundary we can use equation 6.16 to approximate the bi-domain behavior (equation 6.14) by a classical mono-domain with bulk resistivity  $P_n$ . For ischemic zones with abrupt borders, we can in general obtain a particular solution which satisfies this condition.

For the intracellular domain, there is no simple representation of the intracellular potential by a mono-domain. The reason for this is that the Laplace potential  $\phi_L$  is determined by the combination of the intracellular and extracellular boundary conditions which lead to equation 6.14. There is no way to convert the intracellular boundary condition of equation 6.13b to the form of equation 6.14, as we did for the extracellular domain. Hence, the Laplace potential can be found only by solving for the extracellular potential. The resulting  $\phi_L$  can then be added to the intracellular particular solution  $\phi_{pi}$  to arrive at the total solution (where we take the term  $\phi_{hH}$  to be negligible).

We conclude that under Assumptions 1 and 2 only, a bi-domain Poisson model of the form of equation 6.11, incorporating the boundary condition of equation 6.14, approximates the behavior of the complete bi-domain Helmholtz



model. Under Assumption 1 only, we have the more general condition of a source distribution which is not limited to the neighborhood of a surface and can be volume-distributed. We can summarize the results of this section for this general condition by expressing  $\phi_e$ , the potential of the equivalent mono-domain which approximates the extracellular potential of the bi-domain, as a particular and homogeneous solution to Poisson's equation:

$$\phi_e = \phi_{pe} + \phi_{he} \tag{6.17a}$$

$$\nabla^2 \phi_{pe} = -P_h (\nabla \cdot \underline{M}_s) \tag{6.17b}$$

$$\nabla^2 \phi_{he} = 0 \tag{6.17c}$$

$\phi_{pe}$  can be identified as the low frequency approximation to  $\phi_{po}$  of the bi-domain model (equation 5.3b), and  $\phi_{he}$  as  $\phi_L$ . The term  $\phi_{hh}$  of equation 5.3b is totally neglected. The boundary conditions are then given by:

$$[\phi_{pe} + \phi_{he}]_{S_h} = \phi_b]_{S_h} \tag{6.18a}$$

$$\frac{1}{P_h} \left. \frac{\partial \phi_{he}}{\partial n} \right|_{S_h} = \frac{1}{P_b} \left. \frac{\partial \phi_b}{\partial n} \right|_{S_h} \tag{6.18b}$$

#### 6-D. Applicability of the solid angle model

The solid angle model, commonly used to interpret ischemic ST-TQ shifts in the electrocardiogram (see Chapter 3), is a model in which local boundary conditions are

ignored. Consequently, for the majority of source distributions of interest (subepicardial, subendocardial, transmural), we expect that with the use of Assumption 3, that of negligible boundary effects, large errors will result. A study of these errors is the subject of Chapter 7.

Furthermore, there is little justification for Assumption 2, that of an abrupt ischemic border, which leads to the representation of the source as a current dipole layer distributed over a surface. The original motivation for such a dipole representation [Wilson et al (1933)] was not to explain the "injury" current but rather to explain the "activation" current at the border between polarized and depolarized myocardial cells. A dipole layer at the (moving) activation border may be a valid equivalent source representation, because there is a relatively abrupt spatial gradient in transmembrane potential, due to the rapid depolarization of the cell membrane compared to the transit time of the activation border across the myocardium. However, unlike the case for activation there is no physical basis for assuming an abrupt spatial transition in transmembrane potential due to ischemia.

To conclude, we expect only Assumption 1 to be valid for most situations. Thus we take the bi-domain Poisson equation approximation (equations 6.17), rather than the solid angle model, to be the more appropriate model for most cases of experimental interest.

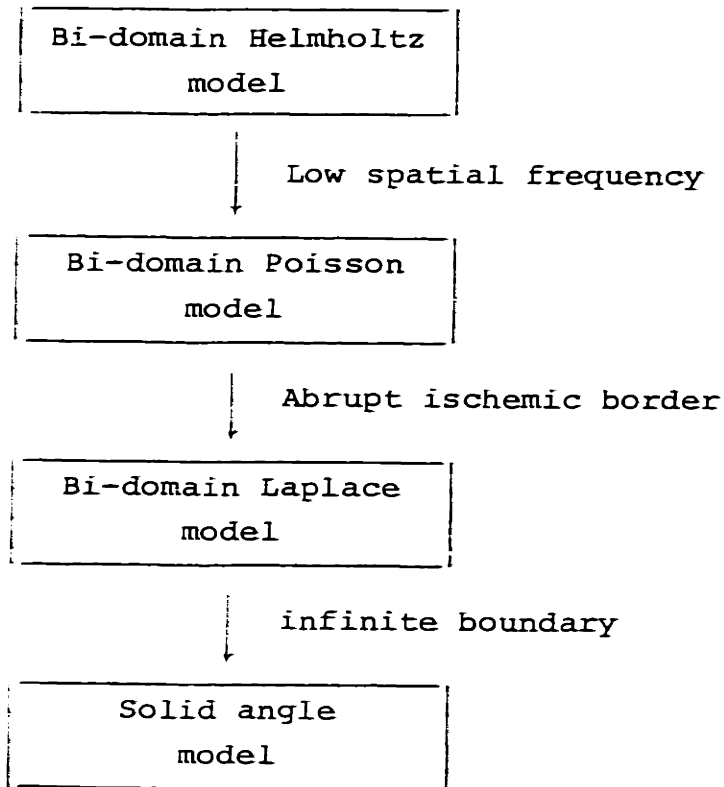
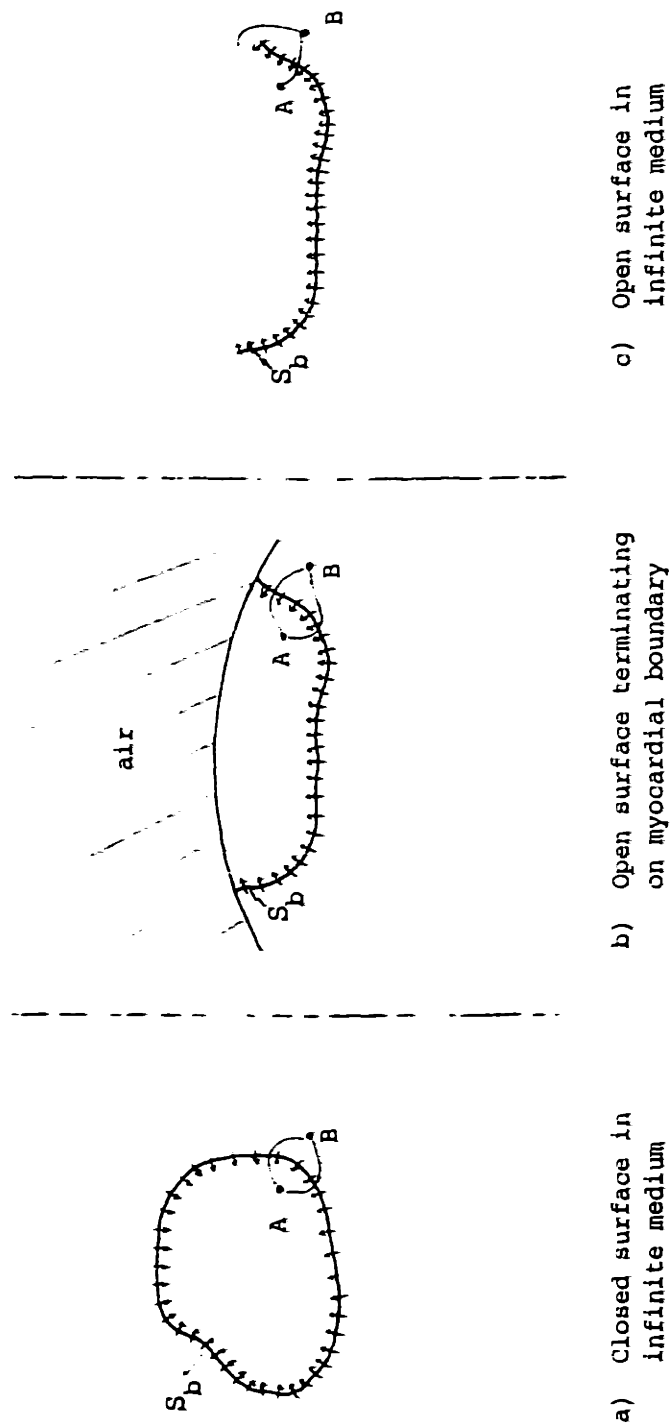
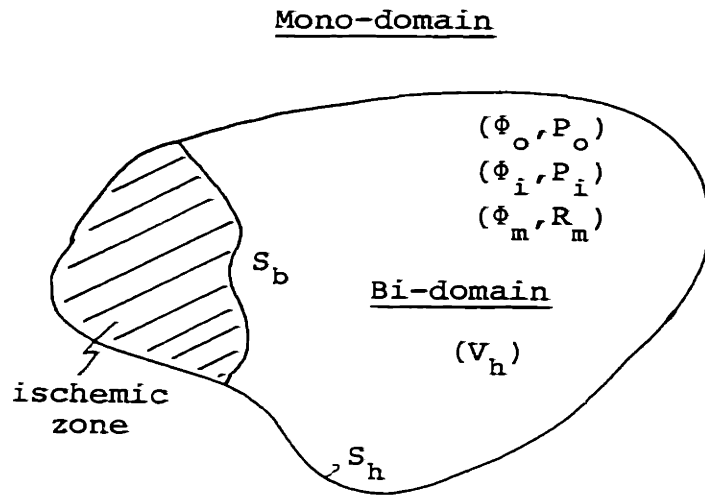


FIGURE 6.1 - The derivation of the solid angle model from the bi-domain Helmholtz model



a) Closed surface in infinite medium  
 b) Open surface terminating on myocardial boundary in air  
 c) Open surface in infinite medium

FIGURE 6.2 - Open and closed ischemic border surfaces



$(\phi_b, P_b) = (\text{potential, resistivity})$

FIGURE 6.3 - Boundary conditions for the bi-domain Poisson model

CHAPTER 7: Case Studies Comparing the Bi-Domain and Solid  
Angle Models

Four primary source distributions (cf. Fig. 3.2) are commonly described in the literature in open-chest animal experiments: subepicardial, subendocardial, transmural, and intramural. It is of experimental, and ultimately clinical, interest to determine to what extent the "inverse" problem can be solved, i.e. what kind of information can be obtained from epicardial or precordial recordings of the ischemic potential regarding the shape and extent, or more specifically the area and depth, of the ischemic zone. This information could potentially be used to assess the effectiveness of various interventions following an acute coronary occlusion.

We shall be considering various cases of ischemic zones with abrupt borders. Since the ischemic zone contains a constant intensity source ( $\bar{U}_{ms}$ ) which changes value only at the border, there is no gradient in  $\bar{U}_{ms}$  at the epicardial or endocardial boundaries (which are not considered to be border surfaces) for subepicardial, subendocardial, or transmural ischemic zones. This implies that the gradient of  $\Phi_{po}$  normal to the boundaries can be taken to be zero, so that we can apply the bi-domain, Poisson approximation, equations 6.17-6.18.

Before we begin, we would like to make a point regarding

the reference potential. The potential distributions derived in this chapter assume that the reference potential is taken at infinity. However, this is not the potential implicitly used by the cardiologist. In the open-chest preparation in which the heart is exposed and is in contact with the body only over part of its surface, the reference potential is usually taken to be Wilson's central terminal, a potential which is an average of the limb potentials. If the ischemic zone is entirely contained within the exposed myocardium, then most of the ischemic current will be confined to the heart and very little will leak through the body. Therefore, the limb potentials will be nearly equal to the potential of the portion of the heart surface which is in contact with the body. Therefore, to interpret the distributions for the ischemic potential which are derived in this chapter, it will be necessary to treat some potential on the heart surface as the "real-world" reference potential. If the ischemic zone is centered around  $\theta = 0$  (as in Fig. 7.4a), and only the epicardium around  $\theta = \pi$  is in contact with the body, then the epicardial potential at  $\theta = \pi$  becomes the "real-world" reference potential. When we refer to a potential distribution as being "monophasic" or "biphasic", so that we can relate our theoretical results here to the experimental results in the literature, we are then taking the epicardial potential at  $\theta = \pi$ , rather than the potential at infinity, to be the reference potential. Difficulties in the

interpretation of the epicardial potential distribution can arise however, particularly when a portion of the ischemic zone comes into contact with the body, so that an appreciable amount of current can be shunted through the body. Not only will this affect the current distribution within the heart, but it will also alter what is taken to be the "real-world" reference potential. For simplicity, we shall assume that the ischemic zone is confined to the exposed portion of the heart, and that the "real-world" reference potential is taken to be the potential on the epicardial surface of the wall of the heart opposite to the ischemic zone.

#### A. Subepicardial ischemic zone

In this section, we derive the epicardial surface potential distribution arising from a subepicardial ischemic zone, taking the reference potential to be at infinity. We shall show that the surface distribution directly reflects the area (but not the depth) of the underlying source distribution. We take the geometry of Fig. 7.1a, where we assume an axial symmetry in spherical co-ordinates, so that the potentials will not have a  $\phi$ -dependence. We define the cavity potential ( $\phi_c$ ) for the region  $r < R_c$ , the homogeneous ( $\phi_{he}$ ) and particular ( $\phi_{pe}$ ) solution potentials for the region  $R_c \leq r \leq R_b$ , and the body potential ( $\phi_b$ ) for  $r > R_b$ .

Consequently we have (cf. equations 6.17),

$$\phi_e = \phi_{pe} + \phi_{he} \quad (7.1a)$$



$$\nabla^2 \phi_{pe} = -P_h (\nabla \cdot \underline{M}_s) \quad (7.1b)$$

$$\nabla^2 \phi_{he} = \nabla^2 \phi_b = \nabla^2 \phi_c = 0 \quad (7.1c)$$

where the homogeneous ( $\phi_{he}$ ) and particular ( $\phi_{pe}$ ) solutions, when added together, form the complete solution ( $\phi_e$ ), and where  $\nabla \cdot \underline{M}_s$  is a dipole layer distributed over the surface located at  $\theta = \theta_a$  ( $R_a \leq r \leq R_b$ ) and at  $r = R_a$  ( $0 \leq \theta \leq \theta_a$ ). The solutions to equations 7.1 are subject to the boundary conditions (cf. equations 6.18),

$$r = R_c: \quad \phi_{pe} + \phi_{he} = \phi_c \quad (7.2a)$$

$$\frac{1}{P_h} \frac{\partial \phi_{he}}{\partial r} = \frac{1}{P_c} \frac{\partial \phi_c}{\partial r} \quad (7.2b)$$

$$r = R_b: \quad \phi_{pe} + \phi_{he} = \phi_b \quad (7.2c)$$

$$\frac{1}{P_h} \frac{\partial \phi_{he}}{\partial r} = \frac{1}{P_b} \frac{\partial \phi_b}{\partial r} \quad (7.2d)$$

We choose the particular solution ( $\phi_{pe}$ ) as follows, using a separation of variables:

$$\phi_{pe}(r, \theta) = \phi_1(r) \phi_2(\theta) \quad (7.3a)$$

where,

$$\phi_1(r) = \begin{cases} 1 & , R_a \leq r \leq R_b \\ 0 & , \text{otherwise} \end{cases} \quad (7.3b)$$

$$\phi_2(\theta) = \begin{cases} -M & , -\theta_a \leq \theta \leq \theta_a \\ 0 & , \text{otherwise} \end{cases} \quad (7.3c)$$

The solution 7.3a corresponds to the complete solution for the region  $R_c \leq r \leq R_b$ , when the boundary at  $R_b$  is extended to infinity. From physical arguments, we expect that in fact, this solution is equal to the complete solution! The reason for this is that  $\phi_{pe}$  satisfies all the required boundary conditions (equations 7.2). Specifically, the normal derivative of  $\phi_{pe}$  is zero at both the endocardium and epicardium, as is the normal derivative of  $\phi_{pi}$ . In addition, the value of  $\phi_{pe}$  is zero at the endocardium, permitting a solution to Laplace's equation of a constant (zero) value in the intraventricular cavity ( $r < R_c$ ). Hence, by uniqueness,  $\phi_{pe}$  must be the complete solution ( $\phi_e$ ). However, a more complex technique will be needed in the later sections for the cases of subendocardial and transmural ischemic zones, so we develop the method here in this section. We can then check our computed answer against our physically motivated answer.

We proceed to solve the given problem in a manner analogous to the method of Chapter 5, by finding the solution in terms of its eigenfunction expansion. We anticipate the need to expand  $\phi_2(\theta)$  in terms of an infinite series of Legendre polynomials (the spherical eigenfunctions along  $\theta$ , in the case of axial symmetry). Hence,

$$\phi_2(0) = \sum_{k=0}^{\infty} E_k P_k(\cos \theta) \quad (7.4a)$$

We can invert the above expansion to obtain,

$$\begin{aligned}
 E_k &= \frac{\int_0^\pi \phi_2(\theta) P_k(\cos \theta) \sin \theta \, d\theta}{\int_0^\pi P_k^2(\cos \theta) \sin \theta \, d\theta} \\
 &= \frac{2k+1}{2} \int_0^\pi \phi_2(\theta) P_k(\cos \theta) \sin \theta \, d\theta
 \end{aligned}
 \tag{7.4b}$$

by using the orthogonal properties of  $P_n(\cos \theta)$ :

$$\int_0^\pi P_n(\cos \theta) P_m(\cos \theta) \sin \theta \, d\theta = \begin{cases} 0 & , n \neq m \\ \frac{2}{2n+1} & , n \geq m \end{cases}
 \tag{7.5}$$

Substituting for  $\phi_2(\theta)$ , equation 7.4b becomes:

$$E_k = \begin{cases} \frac{\cos \theta_a - 1}{2} M & , k = 0 \\ \frac{P_{k+1}(\cos \theta_a) - P_{k-1}(\cos \theta_a)}{2} M & , k \geq 1 \end{cases}
 \tag{7.6}$$

We use a separation of variables on  $\phi_{he}(r, \theta)$  and express the eigenfunctions of Laplace's equation as:  $r^k P_k(\cos \theta)$  and  $r^{-(k+1)} P_k(\cos \theta)$ . Thus, we can express  $\phi_{he}(r, \theta)$  as:

$$\phi_{he}(r, \theta) = \sum_{k=0}^{\infty} \left[ A_k \left(\frac{r}{R_b}\right)^k + B_k \left(\frac{R_b}{r}\right)^{k+1} \right] P_k(\cos \theta)
 \tag{7.7}$$

In a similar manner, we can expand  $\phi_b(r, \theta)$  and  $\phi_c(r, \theta)$  as Legendre polynomial expansions along  $\theta$ :

$$\phi_b(r, \theta) = \sum_{k=0}^{\infty} C_k \left(\frac{R_b}{r}\right)^{k+1} P_k(\cos \theta)
 \tag{7.8}$$

$$\phi_c(r, \theta) = \sum_{k=0}^{\infty} D_k \left(\frac{r}{R_c}\right)^k P_k(\cos \theta)
 \tag{7.9}$$

Substituting equations 7.3, 7.4a, and 7.7-7.9 into the

boundary conditions 7.2, and solving for  $A_k$ ,  $B_k$ ,  $C_k$ , and  $D_k$ , we obtain:

$$k = 0 : \quad A_0 = D_0 = E_0 \quad (7.10a)$$

$$B_0 = C_0 = 0 \quad (7.10b)$$

$$k \geq 1 : \quad A_k = \frac{-\left(\frac{k+1}{P_b}\right) f_4}{f_1 f_4 - f_2 f_3 (R_c/R_b)^{2k+1}} E_k \quad (7.10c)$$

$$B_k = \frac{\left(\frac{k+1}{P_b}\right) f_2 (R_c/R_b)^k}{f_1 f_4 - f_2 f_3 (R_c/R_b)^{2k+1}} E_k \quad (7.10d)$$

$$C_k = E_k + A_k + B_k \left(\frac{R_c}{R_b}\right)^{k+1} \quad (7.10e)$$

$$D_k = A_k \left(\frac{R_c}{R_b}\right)^k + B_k \quad (7.10f)$$

where,

$$f_1 = \frac{k+1}{P_b} + \frac{k}{P_h} \quad (7.11a)$$

$$f_2 = \frac{k}{P_c} - \frac{k}{P_h} \quad (7.11b)$$

$$f_3 = \frac{k+1}{P_b} - \frac{k+1}{P_h} \quad (7.11c)$$

$$f_4 = \frac{k}{P_c} + \frac{k+1}{P_h} \quad (7.11d)$$

Using equations 7.6 and 7.10, we can find  $A_k$ ,  $B_k$ ,  $C_k$ , and  $D_k$ . From equations 7.4a, and 7.7-7.9, we can then obtain  $\phi_2(r, \theta)$ ,  $\phi_{he}(r, \theta)$ ,  $\phi_b(r, \theta)$ , and  $\phi_c(r, \theta)$ . In evaluating the Legendre polynomial expansions, we first convert the Legendre

polynomial of each term of the expansion into its Fourier cosine series expansion (see Appendix G). Thus, the Legendre polynomial expansion of the form,

$$F(r, \theta) = \sum_{k=0}^{\infty} f_p(r, k) P_k(\cos \theta) \quad (7.12)$$

is expressed as a Fourier cosine series by expanding each  $P_k(\cos \theta)$  into a Fourier cosine series:

$$P_k(\cos \theta) = \sum_{j=0}^{\infty} p(j, k) \cos j\theta \quad (7.13)$$

Substituting equation 7.13 into 7.12, we obtain,

$$F(r, \theta) = \sum_{j=0}^{\infty} f_c(r, j) \cos j\theta \quad (7.14)$$

where:

$$f_c(r, j) = \sum_{k=0}^{\infty} f_p(r, k) p(j, k) \quad (7.15)$$

We then use the FFT to invert each cosine series expansion (cf. Appendix F). In this manner we can improve accuracy and reduce computation time. Finally, from equations 7.1a and 7.3, we can find the ischemic potential,  $\phi_e(r, \theta)$ .

We take a specific case where  $R_c = 2$  cm,  $R_a = 2.5$  cm,  $R_b = 3$  cm,  $P_h = 3 P_c$ , and  $P_b = 1000 P_h$  (simulating an air interface). Despite the complex method, a very simple distribution is obtained for the epicardial potential, as expected. From the results of the computation, we see that a uniform, non-zero ischemic potential will be observed within the ischemic zone, and a zero potential observed outside the

ischemic zone (Fig. 7.2). As in Chapter 5, the magnitude  $M$  of the source has been normalized to 1. Because of the air-interface at the epicardial boundary, no current can traverse the boundary. Consequently there is no flow of Laplace ("common-mode") current, and the ischemic potential is identically equal to  $\phi_{pe}$ . This result dramatically illustrates the difference between the bi-domain and solid angle models. The results predicted by the solid angle model can be obtained by setting  $P_b = P_h = P_c$  and are shown in Fig. 7.3a as an equipotential plot and in Fig. 7.3b as potential distributions on the epicardial and endocardial surfaces. Because the boundary is ignored by the solid angle model, the results of Fig. 7.3b differ significantly from those of Fig. 7.2. We see that the Poisson approximation to the bi-domain model predicts a monophasic, epicardial ischemic potential distribution, while the solid angle model predicts a biphasic distribution.

A second result of interest is the fact that the epicardial surface potential distribution is independent of the location of the transverse border for the ischemic zone (given by the radius  $R_a$ ). There is no provision in the boundary conditions (equations 7.2) for the parameter  $R_a$ , and therefore the coefficients for the Legendre polynomial expansions of the various potentials (equations 7.10) have no dependence on  $R_a$ . Consequently for subepicardial ischemic zones, the ischemic potential distribution is a poor

indicator of the depth of the ischemic zone. In section 7-C we will discuss what happens in the limit where the parameter  $R_a$  goes to  $R_c$ , the radius of the endocardial surface.

B. Subendocardial ischemic zone

In open-chest preparations we show that the influence of subendocardial ischemic zones on the epicardial electrocardiogram is larger than what the solid angle model would predict, since significant boundary effects arise at the epicardium.

We proceed in a manner exactly analogous to the method of the previous section. We assume the geometry shown in Fig. 7.1b. We redefine  $\phi_1(r)$  of equation 7.3b to be:

$$\phi_1(r) = \begin{cases} 1 & , R_c < r < R_a \\ 0 & , \text{otherwise} \end{cases} \quad (7.16)$$

Substituting equations 7.3a, 7.3c, 7.4a, 7.7-7.9, and 7.16 into the boundary conditions 7.2, we can solve for  $A_k$ ,  $B_k$ ,  $C_k$ , and  $D_k$  to obtain:

$$k = 0 : \quad D_0 = E_0 \quad (7.17a)$$

$$A_0 = B_0 = C_0 = 0 \quad (7.17b)$$

$$k \geq 1 : \quad A_k = \frac{\left(\frac{k}{P_c}\right) \epsilon_3 (R_c/R_b)^{k+1}}{\epsilon_1 \epsilon_4 - \epsilon_2 \epsilon_3 (R_c/R_b)^{2k+1}} E_k \quad (7.17c)$$

$$B_k = \frac{-\left(\frac{k}{P_c}\right) f_1}{f_1 f_4 - f_2 f_3 (R_c/R_b)^{2k+1}} E_k \quad (7.17d)$$

$$C_k = A_k + B_k \left(\frac{R_c}{R_b}\right)^{k+1} \quad (7.17e)$$

$$D_k = E_k + A_k \left(\frac{R_c}{R_b}\right)^k + B_k \quad (7.17f)$$

where  $f_1$ ,  $f_2$ ,  $f_3$ , and  $f_4$  are defined as before, in equations 7.11. From equations 7.17 we can obtain the various potentials,  $\phi_2$ ,  $\phi_{he}$ ,  $\phi_b$ , and  $\phi_c$ , from which we can obtain the complete solution  $\phi_e$ . Again, we solve a specific example for the same parameter values used in the example of Fig. 7.2, and the results of the computation are shown in Fig.'s 7.4a,b. The precise area of the ischemic zone appears as a "blurred" image in the potential distribution at the epicardial surface. As before, by setting  $P_b = P_h = P_c$ , we can obtain the results predicted by the solid angle model (shown in Fig.'s 7.5a,b). In both cases, a monophasic potential distribution can be observed on the epicardium; however its polarity will be opposite to that for the subepicardial case (recall that a positive ischemic potential indicates a positive baseline shift, or a negative ST-TQ shift). Due to the boundary effects, however, we see that a larger potential is obtained on the epicardium than that predicted by the solid angle model.

In addition, we see that as in the subepicardial case,



the epicardial surface potential distribution is independent of the location of the transverse border (given by the radius  $R_a$ ) of the ischemic zone. Referring to Fig. 7.4a, a shift in the location of the border at  $R_a$  will not affect the distribution of the equipotential lines, which we note are continuous in slope through the border surface; it will merely shift the location at which the jump in potential from one equipotential line to its continuous counterpart (having a potential difference of 1) will occur. Consequently, the epicardial ischemic potential is a poor indicator of the depth of a subendocardial ischemic zone. However, we have been assuming an abrupt border for the ischemic zone. If the border is diffuse, we would then expect a better sensitivity to the depth (cf. Chapter 5-D).

### C. Transmural ischemic zone

We take the same procedure used in the previous two sections to find the potential distribution arising from a transmural source distribution (Fig. 7.1c). We shall see that the amplitude of the potential distribution is larger than what the solid angle model would predict, although the two distributions are qualitatively similar.

We redefine  $\phi_1(r)$  of equation 7.3b to be:

$$\phi_1(r) = 1 \quad (7.18)$$

and substitute equations 7.3a, 7.3c, 7.4a, 7.7-7.9, and 7.18 into the boundary conditions 7.2 to obtain:

$$k = 0 : \quad A_0 = -E_0 \quad (7.19a)$$

$$B_0 = C_0 = D_0 = 0 \quad (7.19b)$$

$$k \geq 1 : \quad A_k = \frac{\left(\frac{k}{P_c}\right) f_3 (R_c/R_b)^{k+1} - \left(\frac{k+1}{P_b}\right) f_2}{f_1 f_4 - f_2 f_3 (R_c/R_b)^{2k+1}} E_k \quad (7.19c)$$

$$B_k = \frac{\left(\frac{k+1}{P_b}\right) f_2 (R_b/R_c)^k - \left(\frac{k}{P_c}\right) f_1}{f_1 f_4 - f_2 f_3 (R_c/R_b)^{2k+1}} E_k \quad (7.19d)$$

$$C_k = E_k + A_k + B_k \left(\frac{R_c}{R_b}\right)^{k+1} \quad (7.19e)$$

$$D_k = E_k + A_k \left(\frac{R_c}{R_b}\right)^k + B_k \quad (7.19f)$$

where  $f_1$ ,  $f_2$ ,  $f_3$ , and  $f_4$  are defined as before, in equations 7.11.

We again solve for  $\phi_e(r, \theta)$  for the same parameters as for the case of Fig. 7.2, and the results are shown in Fig.'s 7.6a,b. As before, we can compare these results to the predictions of solid angle model by setting  $P_b = P_h = P_c$  (Fig.'s 7.7a,b). We show that transmural ischemic zones with abrupt borders will yield a decreasing (in magnitude) ischemic potential toward the center of the zone. The epicardial, ischemic potential distribution will be biphasic, with a reversal in polarity at the border. Due to the boundary effects, the distribution is larger than that predicted by the solid angle model.

From the discussion of Chapter 5-B, we expect that

lateral diffuse borders for transmural ischemic zones can yield an increasing (in magnitude) ischemic potential toward the center of the zone, despite the presence of Laplace current flow across the endocardial boundary. However, the ischemic potential distribution on the epicardium will still be biphasic, with one polarity at the center of the zone, and an opposite (reciprocal) polarity at some distance away from the center, although the magnitude of the reciprocal potential can be much smaller than that of the primary potential (as in Fig. 5.5b). The reciprocal potential will not decay to zero but will instead decay to some constant, non-zero value at  $\theta = \pi$ , where the "real-world" reference potential is taken. This will serve to reduce the effective magnitude of the reciprocal potential even further. If, as in Chapter 5-C, there is also a transverse diffuse border at the endocardium, it is then possible for the ischemic potential distribution to be monophasic (as in Fig. 5.6b). Thus, we expect that the width of the transverse border at the endocardium will play a major role in the shape of the epicardial potential distribution.

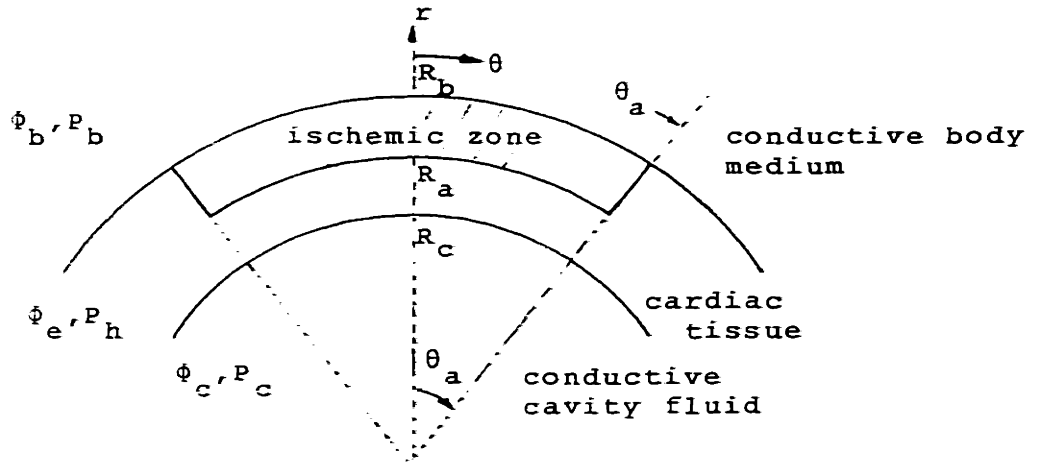
Finally, we make one more observation. In 1942 Bayley proposed that a thin layer of the subendocardium adjacent to the cavity escapes the ischemic condition. From our analysis, we see that this could have a rather large effect of determining whether the epicardial potential distribution is monophasic or biphasic. If we have a subepicardial

ischemic zone whose transverse ischemic border (located at radius  $R_a$ ) approaches the endocardial surface, we expect to go abruptly from the distribution of Fig. 7.2 to the distribution of Fig. 7.6b. Apparently, there is a discontinuity involved. But this arises because we have approximated the complete bi-domain Helmholtz model by the bi-domain Poisson equations. Had we included the high spatial frequency terms neglected in the Poisson formulation, we would see a smooth transition from one distribution to the other as the transverse border approaches the endocardium.

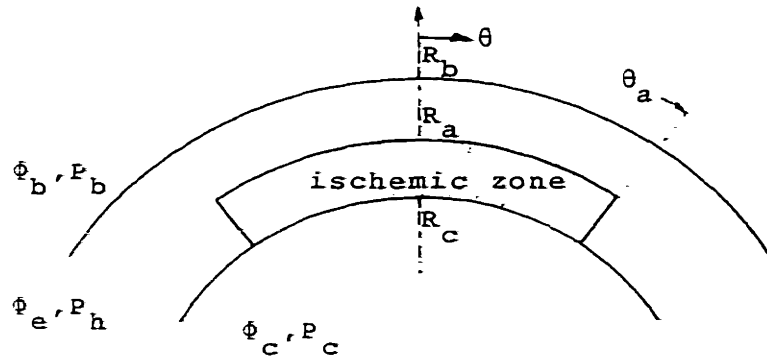
#### D. Intramural ischemic zone

In chapter 6-B we discussed the case of an ischemic zone whose border surface is completely closed. This, in fact, is the definition of an intramural ischemic zone. A non-zero, uniform ischemic potential will be obtained inside the zone, and a zero potential outside the zone. Consequently, the Poisson approximation predicts that intramural ischemic zones will be "invisible" to the epicardial electrode. However, from the complete, Helmholtz bi-domain model we expect a "diffusion" of potential from the ischemic border over distances on the order of the space constant,  $\lambda$  (cf. Fig. 4.7). Therefore, if an intramural zone were to approach either the epicardial or endocardial boundary to within a space constant, we would then expect to be able to detect its presence from epicardial measurements.

a) Subepicardial zone



b) Subendocardial zone



c) Transmural zone

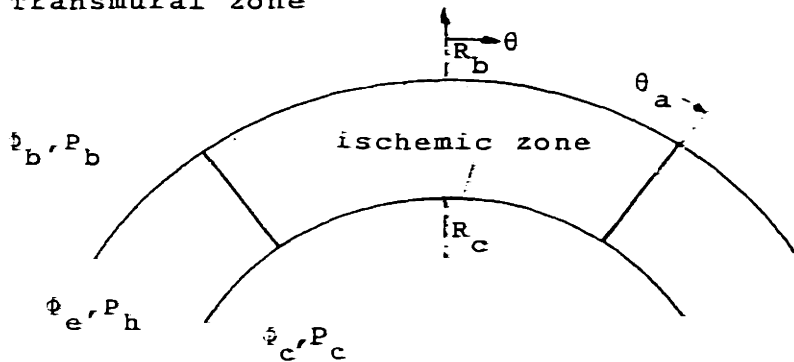


FIGURE 7.1 - Ischemic zones lying in the spherical myocardial wall

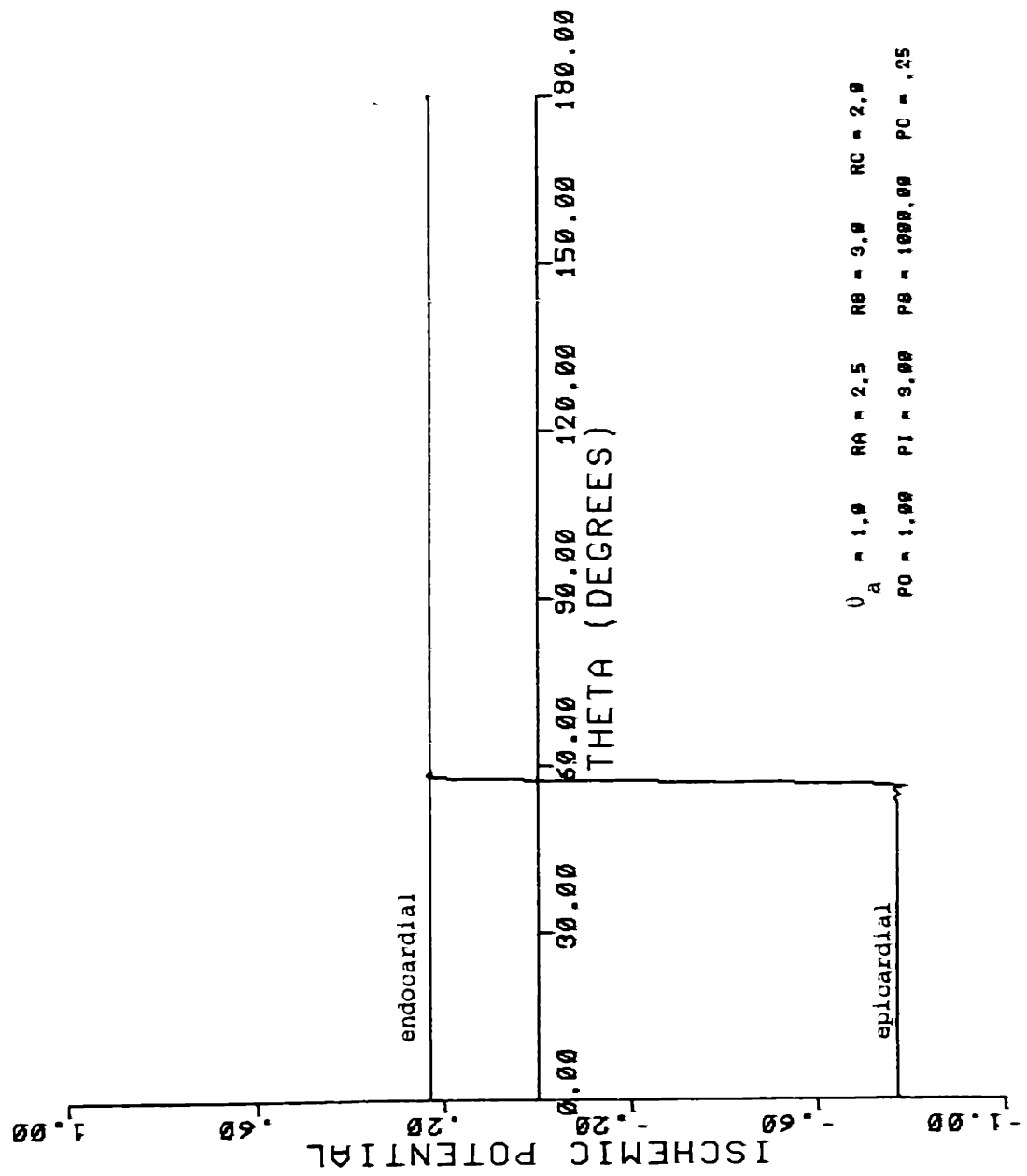


FIGURE 7.2 - Extracellular surface potential plots for the case of a subepicardial ischemic zone, using the bi-domain Poisson model

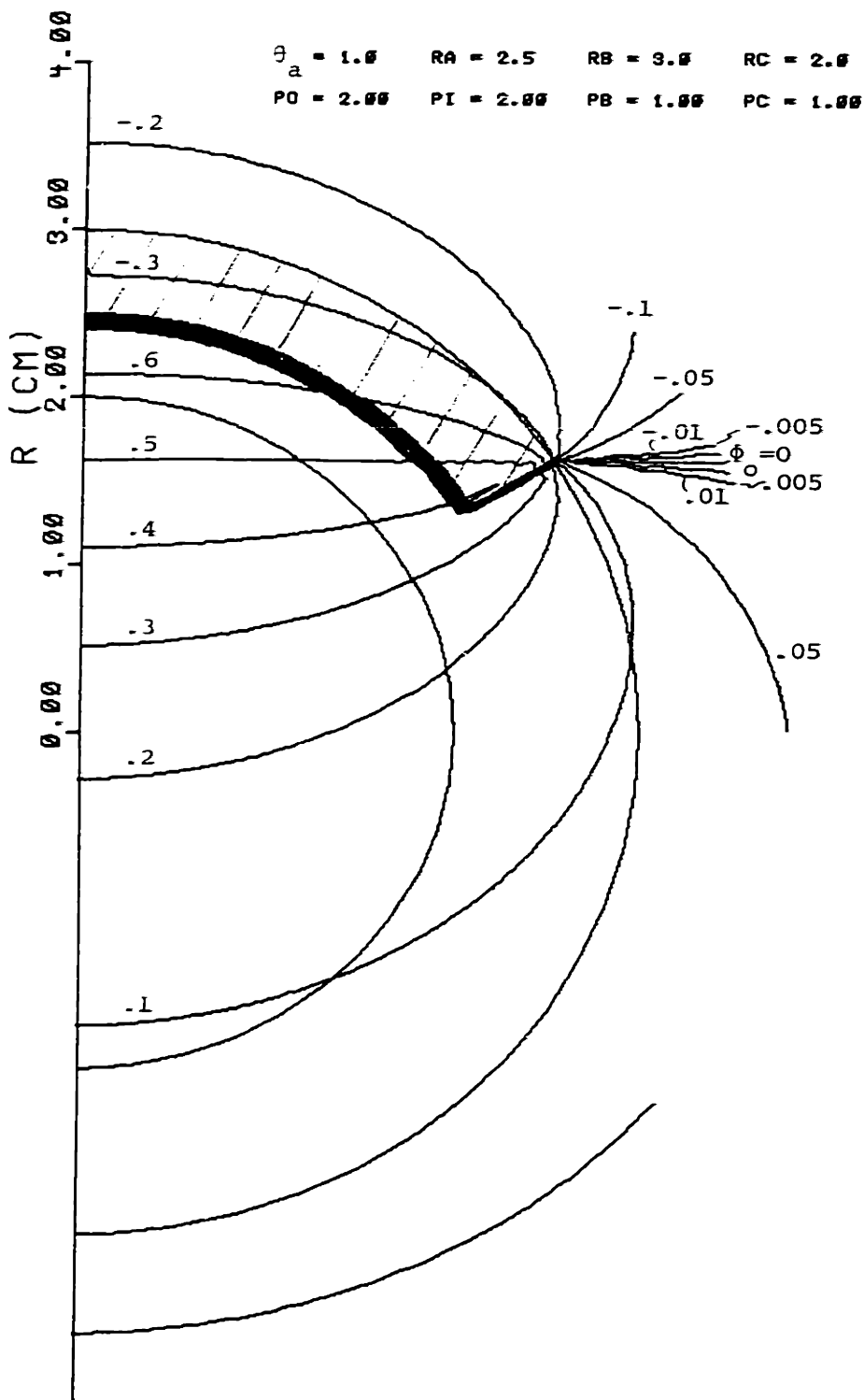


FIGURE 7.3a - Equipotential lines for the extracellular potential for the case of a subepicardial ischemic zone, using the solid angle model.

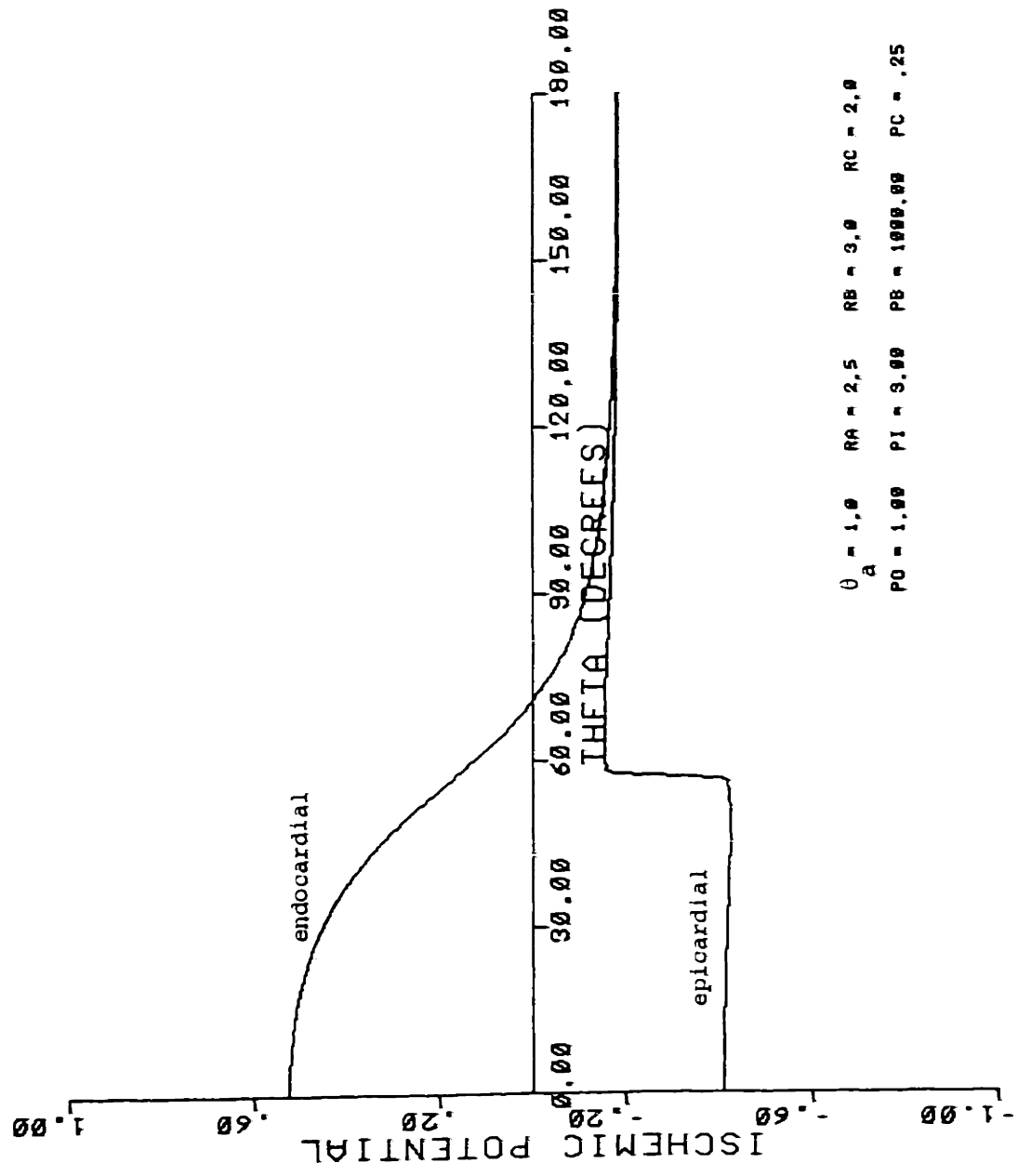


FIGURE 7.3b - Extracellular surface potential plots for the case of a subepicardial ischemic zone, using the solid angle model.



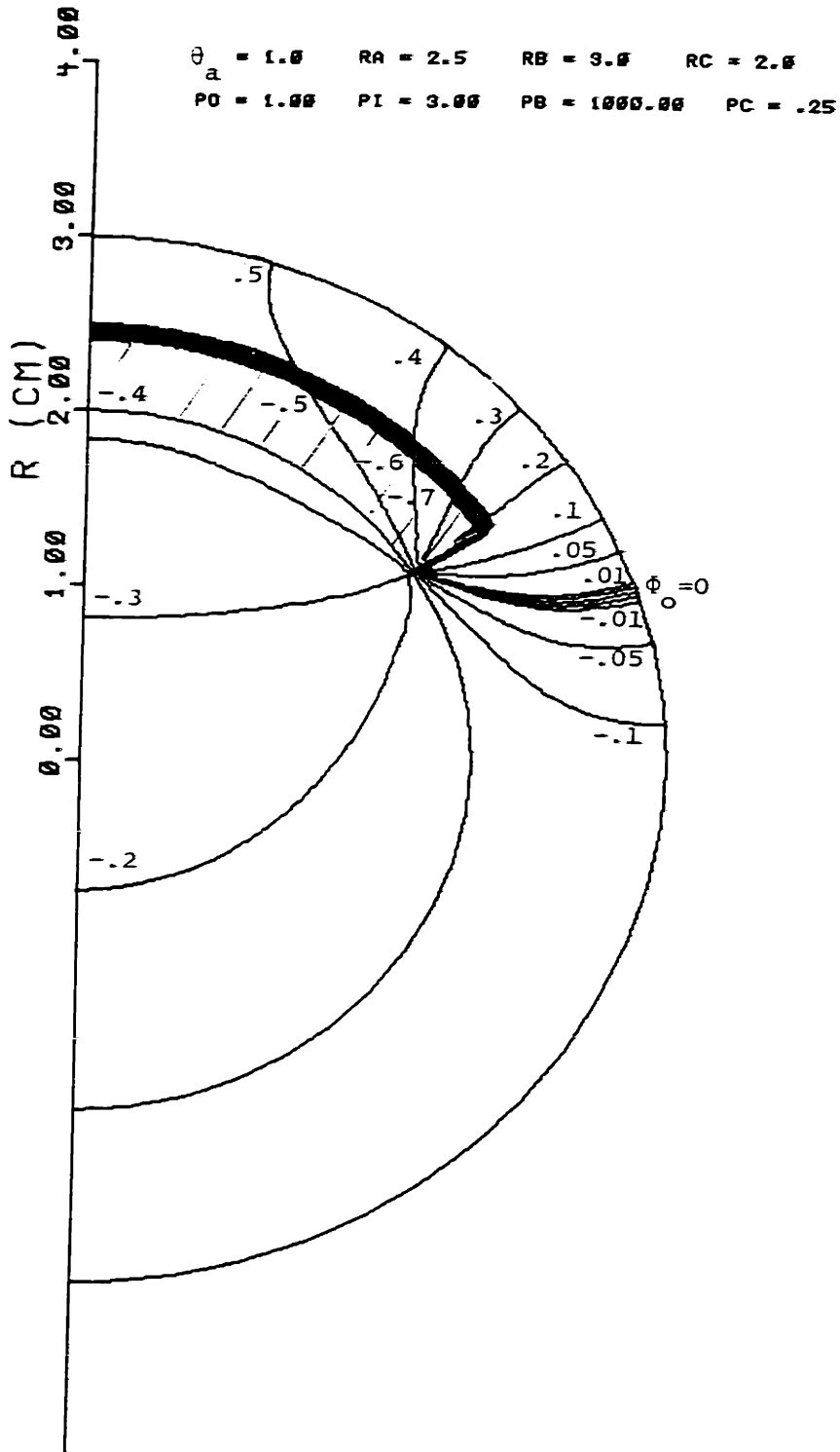
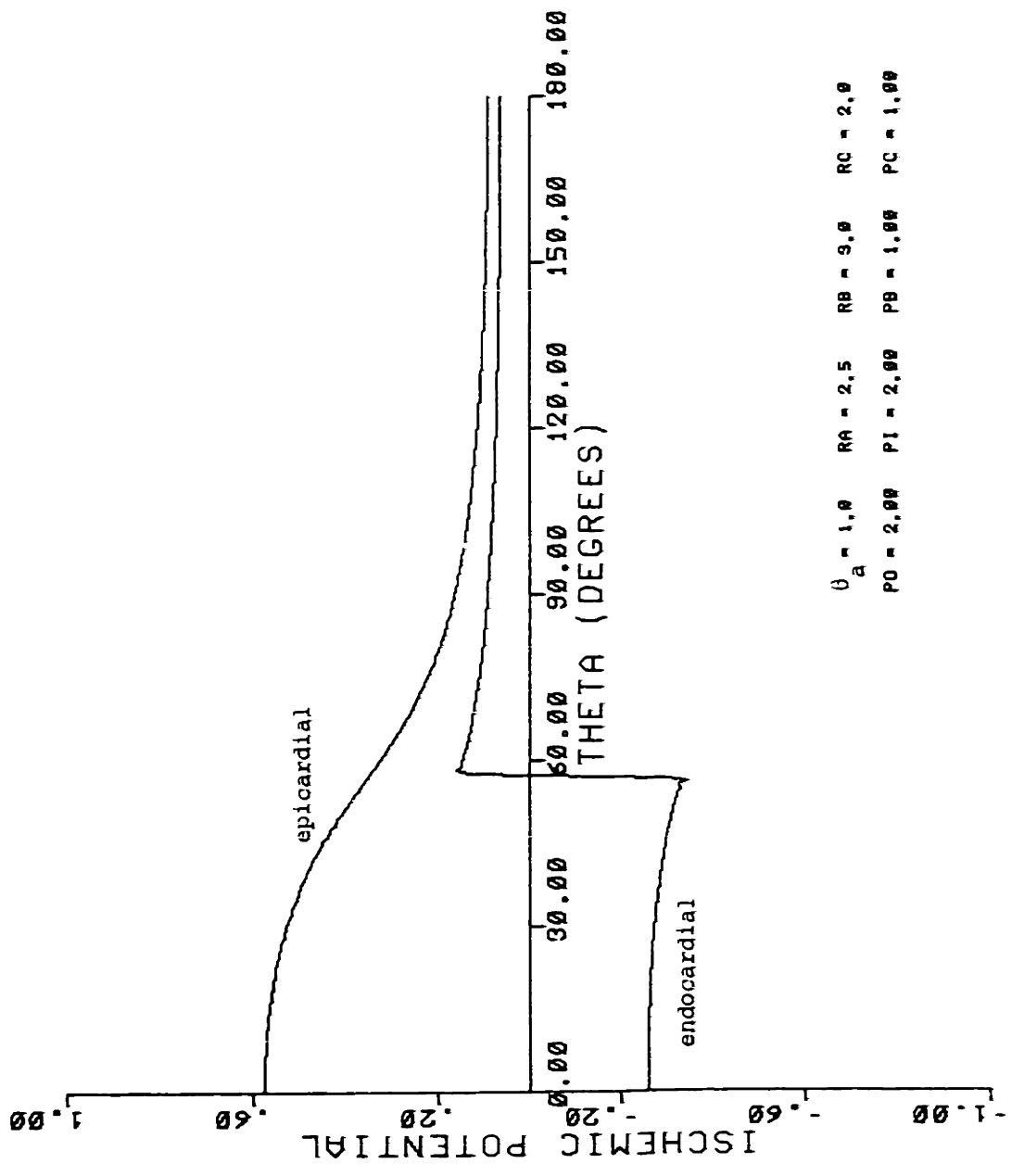


FIGURE 7.4a - Equipotential lines for the extracellular potential for the case of a subendocardial ischemic zone, using the bi-domain Poisson model



$\hat{U}_a = 1.0$  RA = 2.5 RB = 9.0 RC = 2.0  
PO = 2.00 PI = 2.00 PB = 1.00 PC = 1.00

FIGURE 7.4b - Extracellular surface potential plots for the case of a subendocardial ischemic zone, using the bi-domain Poisson model

$\theta_a = 1.0$     RA = 2.5    RB = 3.0    RC = 2.0  
PO = 2.00    PI = 2.00    PB = 1.00    PC = 1.00

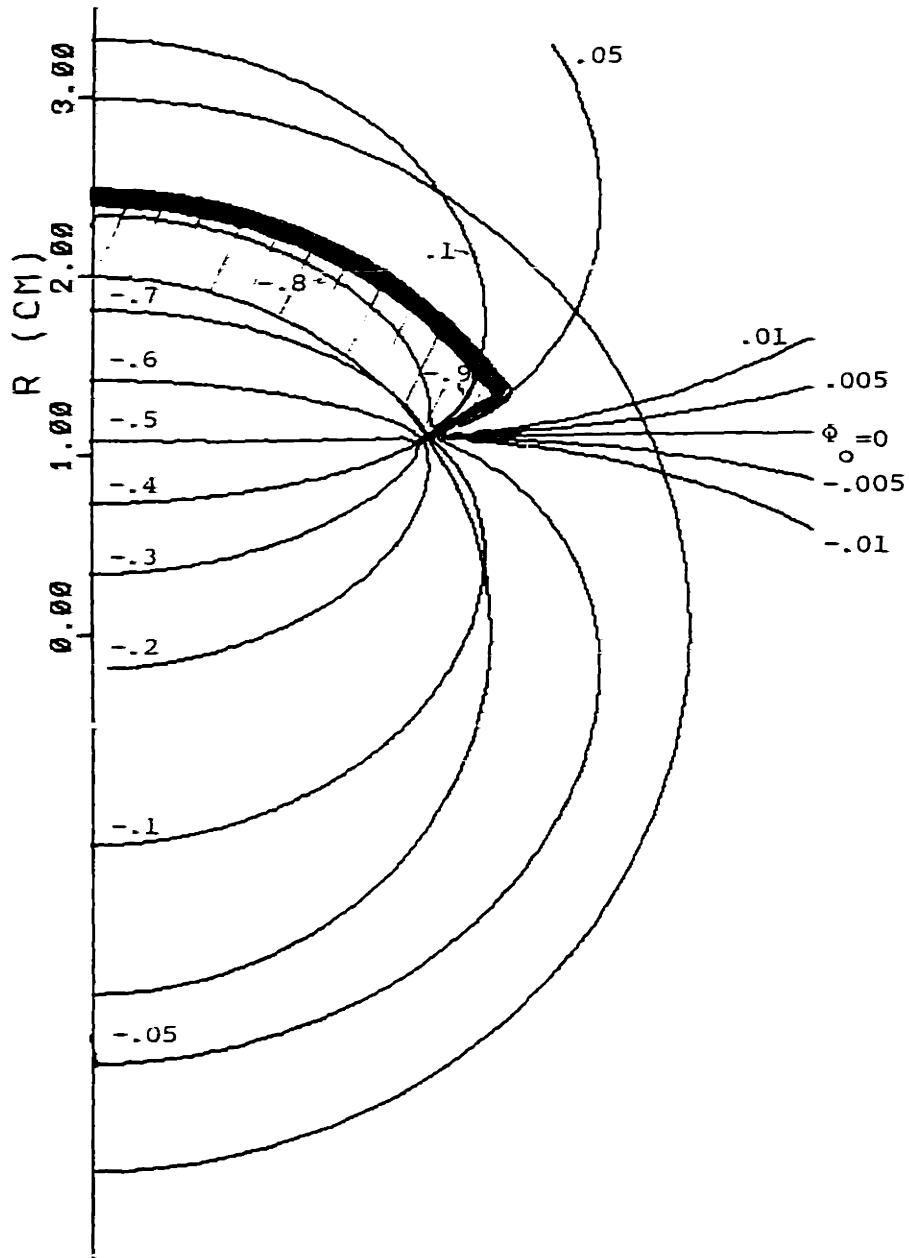


FIGURE 7.5a - Equipotential lines for the extracellular potential for the case of a subendocardial ischemic zone, using the solid angle model.

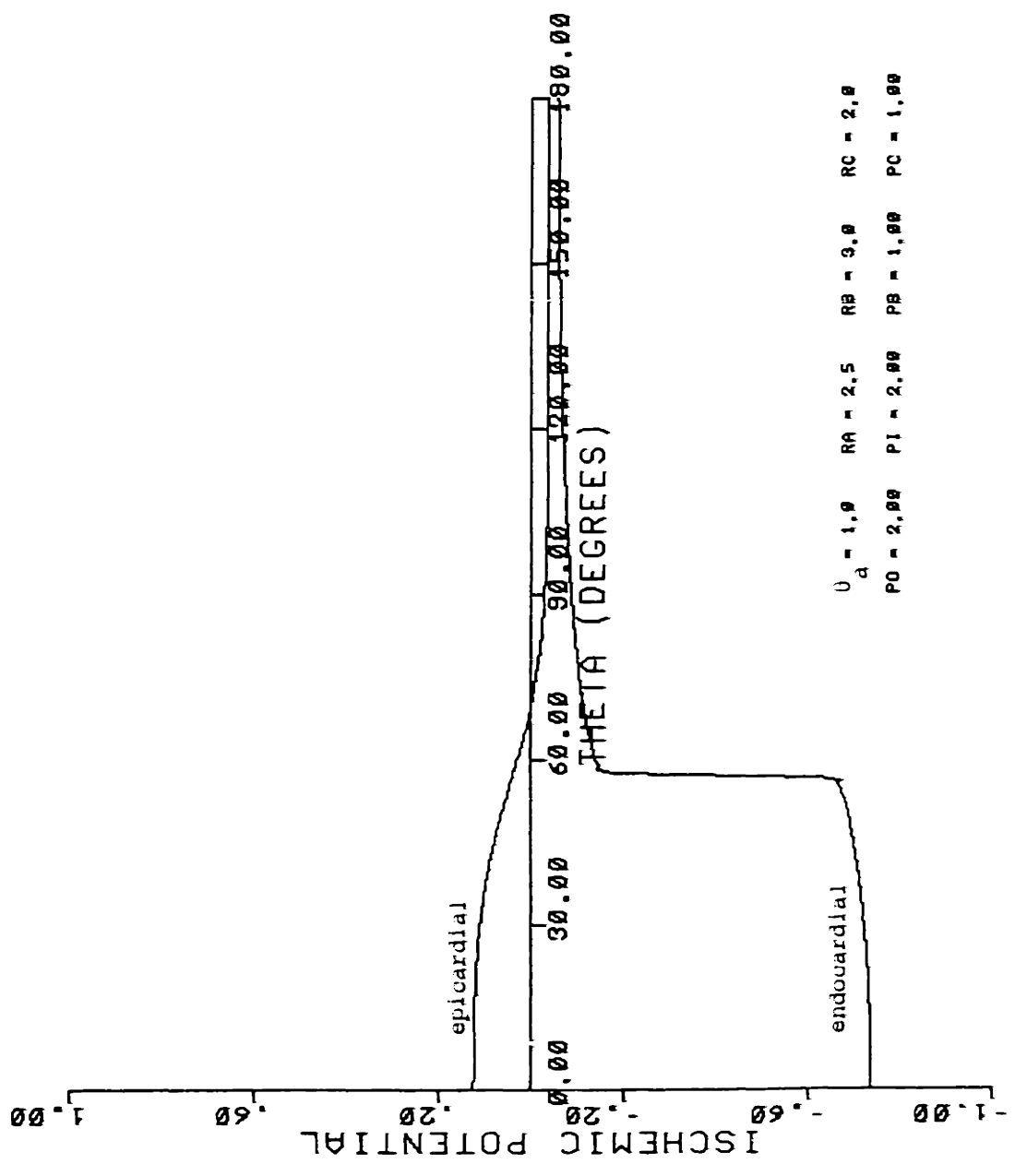


FIGURE 7.5b - Extracellular surface potential plots for the case of a subendocardial ischemic zone, using the solid angle model

$\theta_a = 1.0$      $RB = 9.0$      $RC = 2.0$   
 $PO = 1.00$      $PI = 9.00$      $PB = 100.00$      $PC = .25$

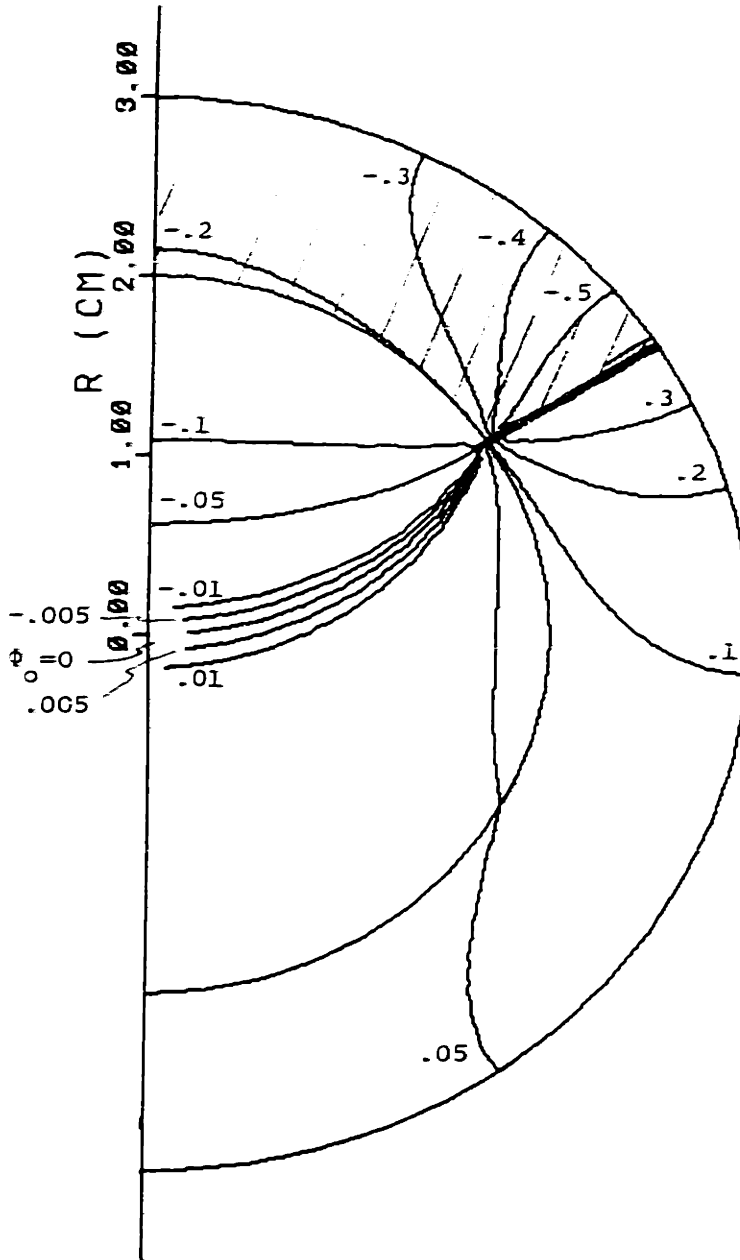


FIGURE 7.6a - Equipotential lines for the extracellular potential for the case of a transmural ischemic zone, using the bi-domain model.

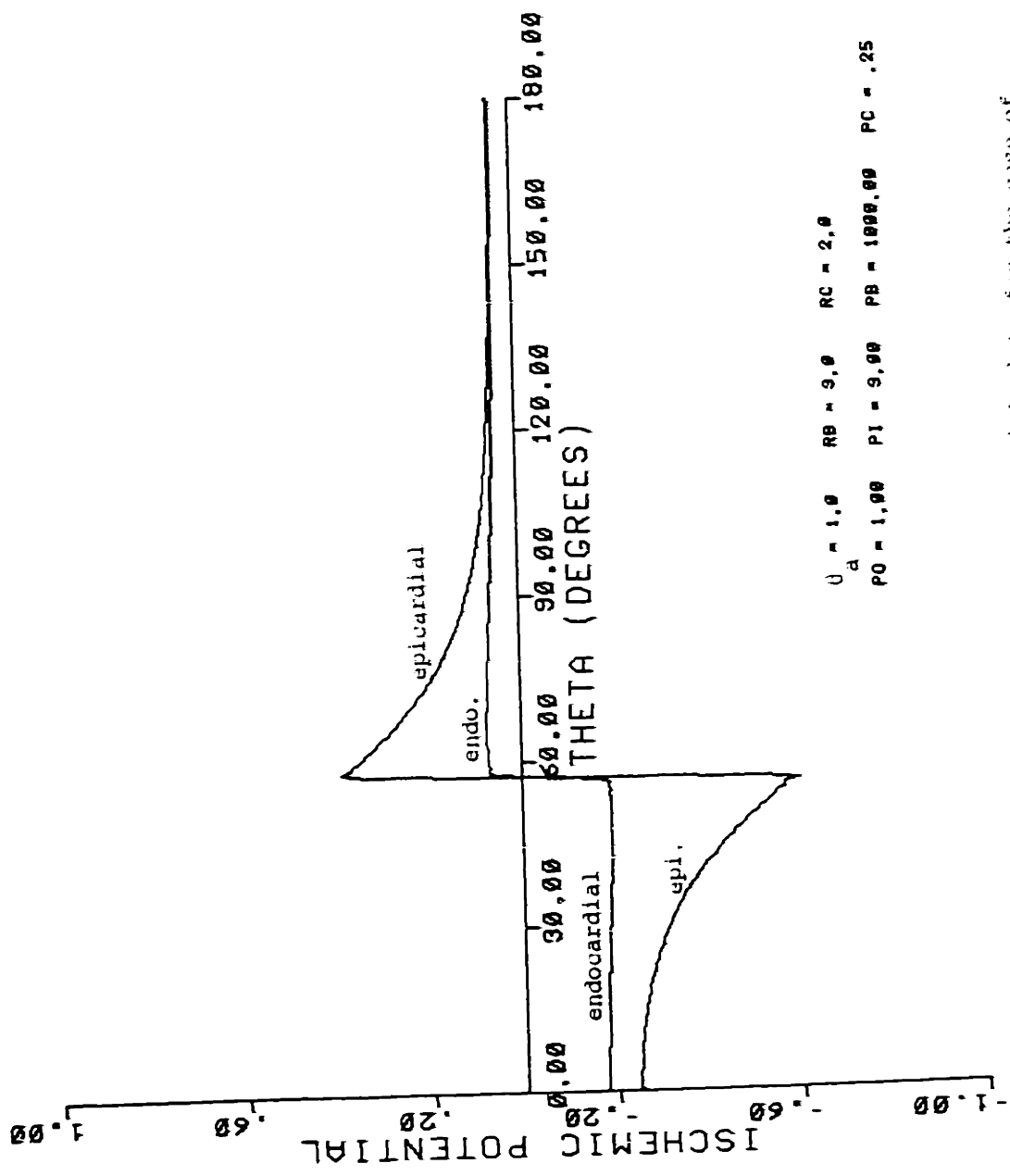


FIGURE 7.6b - Extracellular surface potential plots for the case of a transmural ischemic zone, using the bi-domain Poisson model

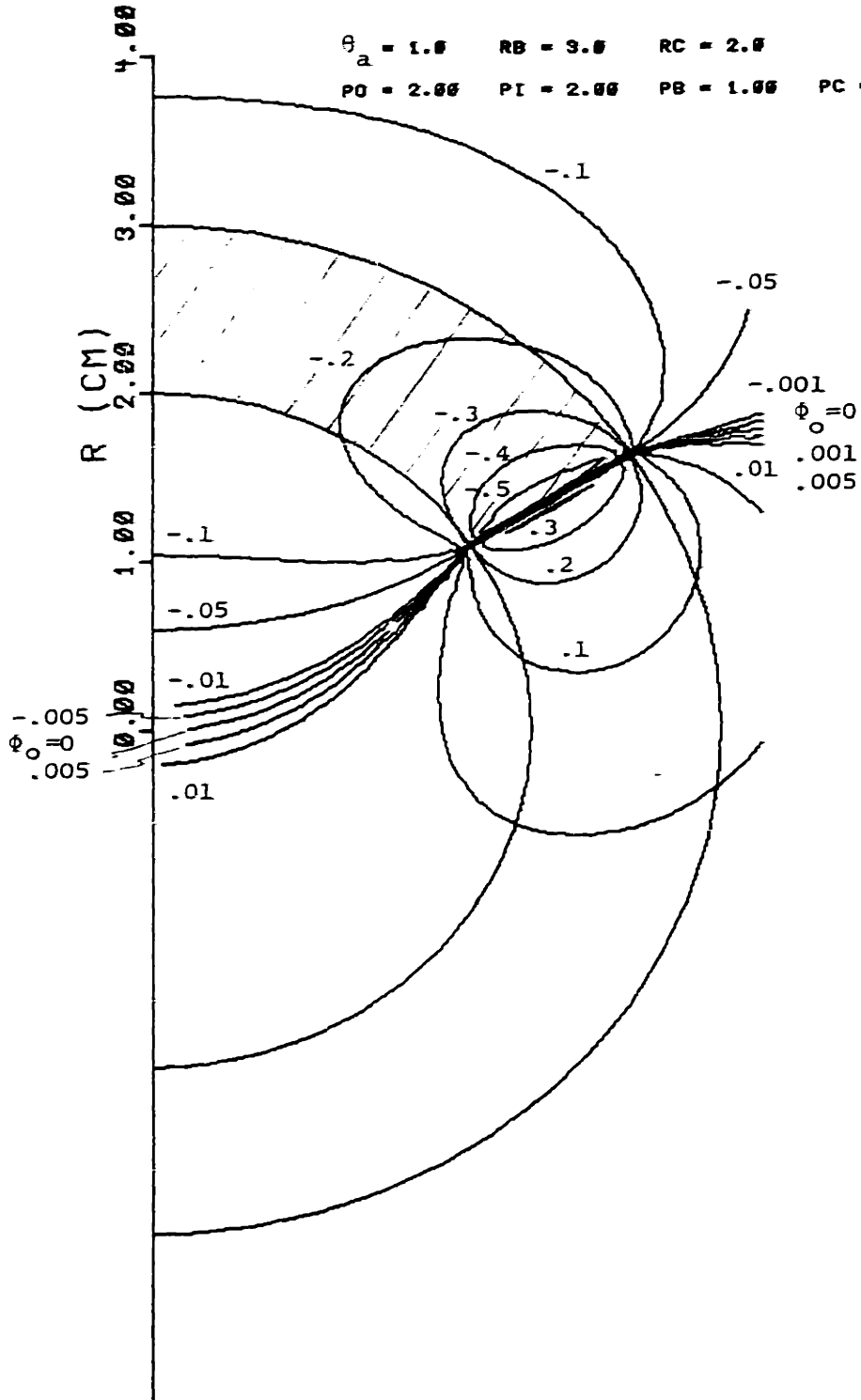


FIGURE 7.7a - Equipotential lines for the extracellular potential for the case of a transmural ischemic zone, using the solid angle model

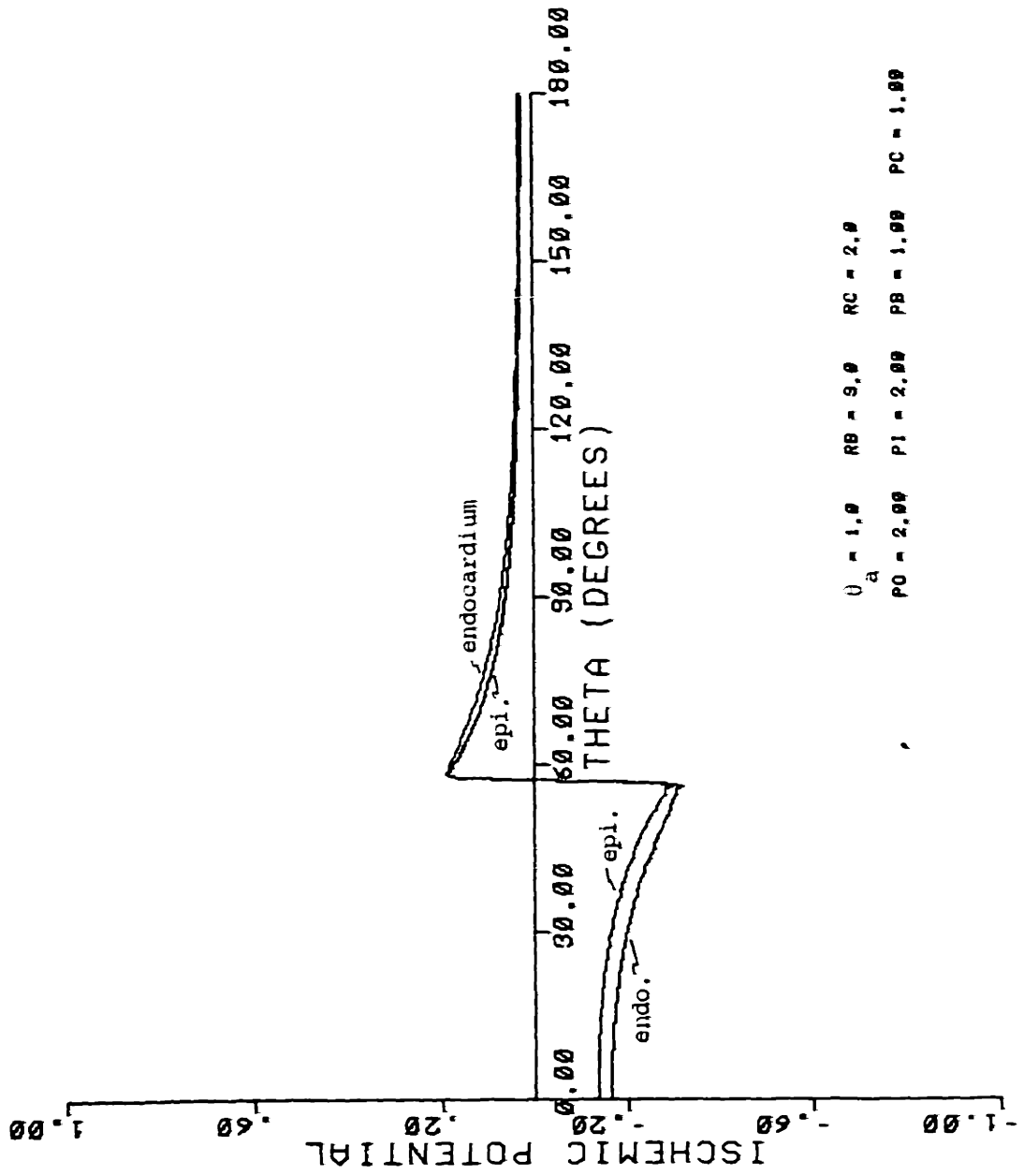


FIGURE 7.7b - Extracellular surface potential plots for the case of a transmural ischemic zone, using the solid angle model.



CHAPTER 8: Issues of Experimental Interest

In reviewing the electrocardiological and electrophysiological literature for both theoretical and experimental results regarding electrical models for myocardial ischemia, a number of issues become evident. First, there clearly is an experimental and clinical interest in developing a reliable electrical measurement which reflects the extent and severity of an ischemic myocardial region. Such a measurement would be convenient, since it would then be relatively easy to perform and would provide instantaneous information. It could be used, for example, to measure the effectiveness of a drug intervention. Second, experimental measurements of myocardial electrical signals are obtained through a variety of techniques. These techniques can be divided into two categories: those consisting of biologically microscopic (e.g. microelectrode) and those consisting of biologically macroscopic (e.g. cotton wick electrode) recordings. The precise nature of the microscopic potential distribution is a question only recently being asked (cf. Chapter 2-C), whereas the macroscopic potential distribution has long been measured clinically. Third, much weight has been given to evidence using the magnetocardiogram [Cohen and Kaufman (1975)] which identifies shifts in the baseline of the ECG as the primary electrical event associated with myocardial ischemia. In

this chapter we propose to explore each of these three issues in detail in the light of the bi-domain model.

#### 8-A. ST-TQ spatial maps and the "inverse" problem

As we have briefly discussed above, an electrical technique to measure the extent and/or the severity of an ischemic zone would be both valuable and convenient. In electrical field theory, this is known as the "inverse" problem; i.e. what information can be obtained regarding the sources by measuring the potentials arising from those same sources? A spatial map of an electrical index which reflects the local ischemic myocardial condition might prove to be such a technique, at least for solving the spatial aspect (extent) of the inverse problem.

Recently, the ST-TQ segment of the ECG has been used as an ischemic index in conjunction with mapping techniques, as described in Chapter 1-A, although the technique of ST-TQ mapping is now a controversial one. We point out here that the use of ST-TQ maps as they have been applied to myocardial ischemia, and the use of these same maps to solve the inverse problem, are not the same. The difference is that ST-TQ segment maps have been experimentally used as qualitative indices as to the improvement or worsening of the "ischemic condition", a condition which is not defined except as the amount of necrotic (dead) myocardium at some future time. This is at variance with the usual "input-output" concepts in

engineering, in which the electrical output variable (ST-TQ segment) is related to some other input variable at the same instant of time (assuming no delay in the system).

Consequently, we are led to a usage and interpretation of spatial ST-TQ maps which differs from that of the experimental cardiologist. Ideally, we would like to measure two-dimensional spatial maps which are continuous over the epicardium and have coordinates which are quantified. On the other hand, the cardiologist would, for simplicity, like to have a minimal sampling of epicardial potentials which yields a single number (whether it be the sum of sites having ST-TQ elevation, or the total ST-TQ elevation summed over all the sites) sufficient to tell him whether or not the overall ischemic condition has worsened or improved.

Justification of mapping procedures to attack the inverse problem involves a two-step process. First, an electrical index must be found which can be correlated to an independent, alternative, localized index of ischemia (e.g. a metabolic, histologic, enzymatic, or pathologic index) [for a review of myocardial indices, see Hillis and Braunwald (1977a,b)]. Second, a theoretical electrical model must be developed in order to make statements regarding the inverse problem. We would like to be able to discuss issues such as the sensitivity of an epicardial electrode to cellular sources located far away from the electrode. We note that in practice, the inverse problem of translating a spatial map to

a source distribution is made even more difficult since spatial maps cannot be performed in three dimensions throughout the myocardium; they can be made only on the epicardial or possibly on the endocardial surface.

Unfortunately, the parameter of the ST-TQ segment, used as an ischemic index, is not one which lends itself to theoretical support, since it involves the difference in potential at two different times. All the theoretical multicellular models described in Chapter 2, including the solid angle model, are essentially quasi-static models, and predict the potential distribution arising from a given distribution of sources at one instant of time. The height of the ST-TQ segment, however, is the difference in potentials at two instants of time - the interval of the TQ segment (electrical diastole) and the interval of the ST segment (electrical systole). Consequently the ST-TQ map results from a combination of the source distributions at two instants of time, and these distributions may act independently. In addition the plateau of the cellular transmembrane action potential has a time-varying amplitude, suggesting that one of the two source distributions is not stable in time (the one during electrical systole). This is reflected in the difficulty in defining the level of the ST segment. By focussing as we did on just the TQ segment, we avoided the problem of measuring a potential which arises from two possibly independent source distributions.

There is, however, one obvious condition in which we would expect the source distributions to be the same during electrical diastole and electrical systole. That is the condition where the ischemic membrane is completely inert; i.e.  $U_{ms}$  is zero. Hence the spatial distribution of the ischemic zone will remain fixed during the cardiac cycle and will not change as metabolic conditions change. However, from the results of Prinzmetal et al (1961,1962), an inert condition does not accompany acute ischemia, as the ischemic cell is still electrically quite active.

There is another condition in which the ST-TQ map may indeed reflect the source distribution, and that is when one of the components of the ST-TQ segment dominates over the other. As we discussed earlier in Chapter 1-C, there is evidence that the baseline shift is consistently the predominant component of the ischemic ST-TQ shift. Unfortunately, there have not been many investigators who have used d-c electrodes to measure changes in the TQ segment with ischemia. Thus we underline the need for obtaining d-c data.

Then, regarding electrical models, investigators such as Holland and Brooks (1975,1977a,1977b) and Holland and Arnsdorf (1977) have attempted to apply the solid angle model to provide, in their words, a "theoretical basis" for the ischemic ST-TQ shift. As we have already discussed in Chapter 6-D, there are difficulties in using the model even

for the appropriate potential, much less when it is used in relation to the ST-TQ shift (as in Chapter 3-B). Thus, we have the situation of a poor model being used to describe a somewhat erratic potential, hardly the basis for a "theoretical" discussion. On the other hand, the bi-domain model described in this work avoids the limitations inherent in the solid angle model, having been constructed with the physical structure of the myocardium in mind.

Despite the problems with defining the electrical ischemic index, we are left with several interesting theoretical questions. Let us presume for the moment that the ischemic ST-TQ distribution is similar to the TQ distribution which would be measured by d-c electrodes, a valid assumption if the TQ shift is the major component of the ST-TQ shift (as it appears to be). Using the results of the bi-domain model obtained in Chapters 5 and 7, we can interpret various data in the literature for the following areas: 1) reciprocal ST-TQ shifts; 2) monophasic epicardial potential distributions; and 3) sensitivity of the ST-TQ segment to local tissue changes. We recall that the figures of Chapters 5 and 7 plot the distribution of the predicted ischemic potential (TQ shift). Negative values for the TQ shift in these figures correspond to positive values for the ST-TQ shift.

1) Monophasic epicardial potential distributions

Studies by Rakita et al (1954) - Fig. 1.5, and Katcher et al (1960) - Fig. 1.11, on exposed canine hearts reported spatial distributions of ST-TQ shifts on the epicardium which were monophasic, slowly monotonic, and positive, with a maximum over the center of the ischemic zone. From the cases studied in Chapters 5 and 7, we saw that positive, monophasic ST-TQ distributions (or negative TQ distributions) could arise either from hypopolarized (positive  $U_{ms}$ ) subepicardial ischemic zones, or from hyperpolarized (negative  $U_{ms}$ ) subendocardial ischemic zones. In the former case, the potential distribution directly reflected the nature of the underlying source distribution (Fig. 7.2). Thus, to explain the results of Rakita et al and Katcher et al, we would conclude that the ischemic zone must have a diffuse border, since no abrupt transition in the ischemic potential was observed. In the latter case, it would not be necessary for the ischemic border to be diffuse in order to obtain a slow transition in the ischemic potential, since the epicardial image of the ischemic zone is one which is spatially filtered (Fig. 7.4b).

In order to differentiate between the two cases, another measurement must be performed. We suggest that if an endocardial map of the spatial distribution could be obtained, the shape of the ischemic zone could be identified. If the zone were subepicardial, the endocardial potential

distribution would be nearly isoelectric (Fig. 7.2). On the other hand, if the zone were subendocardial, the distribution would reflect the nature of the underlying source distribution (Fig. 7.4b).

We include here some other observations which may be relevant. In their studies which recorded simultaneous transmembrane resting potentials and d-c TQ-segment levels, Prinzmetal et al (1961) observed that in cases which they classified as "mild" ischemia, cellular hyperpolarization occurred, while in cases of "severe" ischemia, hypopolarization occurred (Fig. 1.7). This result, if not supportive of the two possible cases described above, at least does not contradict either possibility. On the other hand, all the intracellular recordings taken from the in vivo heart are necessarily from the epicardium, so that the behavior described by Prinzmetal et al for "mild" and "severe" ischemia is not necessarily indicative of endocardial cells.

## 2) Reciprocal ST-TQ shifts

The early results of Wolferth et al (1945) reported the existence of "reciprocal" ST-TQ shifts on the side of the heart opposite to the ischemic zone. The ST-TQ shift over the ischemic zone was generally elevated, while the "reciprocal" shift was depressed. Rakita et al (1954), Katcher et al (1960), and Prinzmetal et al (1961) all reported the occasional appearance of "reciprocal" ST-TQ



depression at the epicardial borders of the ischemic zone. Other studies have been performed into the nature of ST-TQ depression [Ekmekeci et al (1961), Sayen et al (1961), Toyoshima et al (1964), Kato et al (1968), Guyton et al (1977)].

The experiments of Sayen et al (1961) are particularly interesting. They observed that epicardial ischemic potential recordings contained reciprocal ST-TQ shifts only if the ischemic zone came into contact with the body, where the reference potential was taken. We can interpret these findings from the results of Chapter 7. In the following discussion, we assume as we did in Chapter 7 that the polarity of  $U_{ms}$  is positive, corresponding to the case where the ischemic membrane is hypopolarized.

Apparently, there are two effects involved. First, reciprocal shifts will be observed across the border of transmural ischemic zones, since the distributions are biphasic (Fig. 7.6b). As we described in Chapter 7-C, the biphasic nature arises because of the Laplace current flow across the endocardial boundary into the intraventricular cavity. Second, we concluded in Chapter 7-A,B that the distributions for subepicardial and subendocardial zones will be monophasic, although with opposite polarity (Fig.'s 7.2,7.4b). This implies, however, that reciprocal shifts will be observed if an epicardial potential other than the one at  $\theta = \pi$  is taken as the reference potential. For

example, in the case of a subepicardial ischemic zone, if a portion of the zone comes into contact with the body, a potential somewhere between the maximum and minimum of the monophasic epicardial distribution will effectively become the reference potential (refer to the discussion at the beginning of Chapter 7). Consequently, a biphasic distribution will be measured, although for the reasons just stated it will in part be an artifact of the recording system. Furthermore, current loops can close from the extracellular domain across the epicardial boundary into the body. This will contribute further to a biphasic distribution (refer to Fig. 5.14) in which varying degrees of current, resulting from a varying transverse border width, can flow across the myocardial boundary.

We can differentiate between these two interpretations by performing the following measurement. We propose to insulate the heart from the body by interposing a suitable sheet of non-conductive material, thereby altering the location of the reference potential. We then remeasure the epicardial potential distribution. If the zone is transmural, reciprocal ST-TQ depression will still be observed. However, if the zone is either subepicardial or subendocardial, the reciprocal depression will disappear, as the only heart/body connection is through the great vessels, which we presume are connected to non-ischemic myocardium.

### 3) Sensitivity of the ST-TQ segment to local tissue changes

As we discussed in Chapter 6-B, the active membrane sources are given by  $U_{ms}$ . In an infinite medium the extracellular ischemic potential will directly reflect the source distribution, provided that there is no Laplace current flow and that the source distribution changes slowly over distances much greater than a space constant. In the presence of an air interface at the epicardium, this relationship will still hold for subepicardial ischemic zones but not for transmural zones or for subendocardial zones. From Fig. 7.2, we saw that the ischemic shift will directly reflect the lateral distribution (area), but not depth, of the underlying subepicardial zone, since the air interface at the epicardium will prevent any Laplace current flow. However, this relationship will be corrupted for transmural zones (Fig. 7.6b), due to the Laplace current flow across the endocardial boundary. Finally, an image of a subendocardial ischemic zone will be observed on the epicardium (Fig. 7.4b), but it will be spatially filtered and have a polarity opposite to that of the source. In addition, the magnitude of the epicardial potential will be considerable, indicating that the subendocardial layers are not, as previously thought, "electrically silent". Thus, we conclude that the epicardial potential distribution may or may not represent the lateral distribution of the underlying ischemic zone, depending on the relative location of the ischemic zone to

the epicardium, and is a poor indicator of the depth of the ischemic zone, at least in the case of abrupt ischemic borders.

Finally, we mention the experiments of Muller et al (1975), in which a monophasic, positive distribution was obtained for the ST-TQ segment, but where a local minimum was observed over the center of the ischemic zone (Fig. 1.9). This distribution does not match any of the distributions obtained in Chapter 7, and we come back to a point discussed earlier. This is the fact that the ST-TQ segment reflects the source distribution at two different instants of time. The decrease of the ST-TQ segment at the center of the ischemic zone is not necessarily a response to the source distribution or the result of boundary effects, but possibly the result of potentials at two different times becoming similar for independent reasons. This is especially suggested by the evident widening of the QRS complex of the SEG, indicating local conduction block, which alters the sequence of repolarization (ST-T wave) but does not affect the potentials during the TQ segment.

#### 8-B. Biologically microscopic vs. macroscopic measurements

In summarizing the literature regarding experimental measurements of the space constant from in vitro preparations of myocardium, Sperelakis (1969) noted a discrepancy between microscopic and macroscopic measurements. There was up to an

order of magnitude difference in the values obtained, depending on whether the technique used involved current introduced and potential measured through a microelectrode, or current introduced and potential measured through electrodes in the surrounding bath. Thus, we are introduced to the two different classes of electrode measurements — those taken with microelectrodes having dimensions on the order of a cell length, and those taken with gross (macro) electrodes having dimensions on the order of 10-100 cell lengths.

The various models described in Chapter 2 also fall into two similar categories. We could classify the branching network and biologically microscopic field models as models which describe the local potential on the cellular level, while the cable and biologically macroscopic field models describe the global, multicellular (tissue) potential. There has been little attempt to bridge the gap between these two extremes. However, George (1961) used a hybrid model consisting of a lumped parameter model to describe the potential distribution "near" the microelectrode source, and a continuum to describe the potential distribution "far" from the source. We recognize that the bi-domain model discussed in this work falls into the category of biologically macroscopic field models. Therefore, in order to apply the bi-domain model to cases in which microelectrodes are used as stimulating electrodes, a hybrid model similar to that of

George may be necessary to describe the fields around the source. The bi-domain model is limited in that it cannot be used to describe the various parameters measured with a microelectrode source, such as the input impedance (used to determine the membrane impedance). However, we feel that the model appropriately describes preparations with dimensions down to lengths on the order of a space constant, such as those used in an in vitro sucrose gap.

#### 8-C. Magnetocardiograms

Cohen and Kaufman (1975) used magnetocardiographic techniques to determine whether the ischemic ST-TQ potential arises from diastolic (TQ) or systolic (ST) current flow (Fig. 1.12). Using an "out-in-out" technique, consisting of a continuous, magnetic scan of ischemic, closed-chest dogs from one end of the body to the other, they were able to detect the flow of d-c current arising from the heart. They concluded that significant ischemic current occurred only during electrical diastole and resulted in a baseline shift.

We can interpret these findings in the light of the bi-domain model. As we discussed in Chapter 4-F, currents arising from primary cellular sources will give rise to Helmholtz ("differential-mode") currents. Because of their differential nature, these currents might not be expected to generate an externally observable magnetic field. However, in the presence of current flow across the epicardial

boundary in the closed chest, Laplace ("common-mode") currents will arise and can account for the observed magnetic shift. We could test this hypothesis with an experiment modeled after that of Nahum et al (1943) (see Chapter 1-C). We predict that if an insulating sheet were interposed between the heart and the body, the observed magnetic shift would disappear, provided that the Laplace current flow across the endocardial boundary were small enough (e.g. with a primarily subepicardial ischemic zone), so that the generated magnetic field is undetectable.

In addition, we take the position that Ampere's law, relating the curl of the magnetic field to the current density, must be written with the current density being equal to the sum of the current densities for the two domains -- i.e.  $(\underline{J}_o + \underline{J}_i)$ . This definition for the magnetic field is consistent with equation 4.24 (which requires that the divergence of  $(\underline{J}_o + \underline{J}_i)$  be zero), since the divergence of a curl must always be zero. On this basis, we also conclude that two separate magnetic fields,  $\underline{H}_o$  and  $\underline{H}_i$ , cannot be independently defined from the current densities  $\underline{J}_o$  and  $\underline{J}_i$ , since the divergence of either  $\underline{J}_o$  or  $\underline{J}_i$  is not equal to zero but is equal to the inter-domain volumetric current density  $U_m$  (cf. equation 4.8).

## CHAPTER 9: Future Experiments

During the course of the research described in this thesis, it became evident that there is a lack of experimental data from which theoretical models can be evaluated. In this chapter we outline several directions along which future research would be useful.

### 9-A. D-C spatial maps

As we discussed in Chapter 8-A, the ST-TQ segment of the electrocardiogram cannot be expected to be an electrical index which can be consistently correlated with simultaneous measurements of a single, alternative ischemic index. We suggested that the TQ segment may prove to be a more reliable index. However, this necessitates the use of a d-c recording system. As we mentioned in Chapter 1-C, there is currently an effort to make this type of measurement, and these measurements will yield valuable information regarding 1) the relative weight of the TQ segment to the ST-TQ segment, and 2) the correlation between TQ shifts and the ischemic condition.

### 9-B. Changes in potential distribution with altered boundary conditions

As we discussed in Chapter 8-A, the inverse problem can be solved more completely if additional measurements were available. We restrict ourselves to measurements which do



not physically traumatize the myocardium; i.e. intramural, "plunge electrodes" are not permissible. Two approaches are suggested here.

First, we can alter the epicardial boundary condition and observe the changes in the epicardial potential distribution. For example, we could place a saline soaked pad on the epicardium, permitting the flow of Laplace current across the epicardial boundary. The greatest change in the potential distribution would be seen for subepicardial ischemic zones, followed by subendocardial and then transmural ischemic zones. Alternatively, we could interpose a non-conductive sheet between the heart and body. The greatest change in the potential distribution would occur for the case where the ischemic zone is in contact with the body, in which case "reciprocal" effects would be eliminated.

Second, we could attempt to obtain an endocardial map of the ischemic potential. Despite the presence of the conductive cavity, these potentials should be large enough to be measured by conventional ECG amplifiers. This measurement would provide the greatest resolution between subepicardial and subendocardial ischemic zones.

#### 9-C. Measurements of electrical parameters during ischemia

The discussion of Chapters 4 and 6 on the bi-domain and solid angle models assume that the bulk parameters  $P_o$ ,  $P_i$ , and  $R_m$  are temporally and spatially constant throughout the

healthy and ischemic myocardium. Under prolonged or severely ischemic conditions, we expect that these parameters may change (for a discussion, see Appendix B-4). From the sensitivity analysis of Chapter 5-D, we have seen that the the most important factors in determining the concavity and polarity of the epicardial ischemic potential distribution are 1) the ratio of  $P_h$  to  $P_b$  (i.e. ratio of the resistivities of bulk myocardium to blood); 2) the width of the border zone ( $\lambda_s$  and  $b_s$ ); and 3) the space constant  $\lambda$  (but only for large values, on the order of several millimeters). Consequently interpretations of the epicardial spatial map must be moderated by a knowledge of the effects resulting from changes in these parameters.

The myocardial bulk resistivity can be measured with a four-electrode, impedance technique [for a review, see Rush (1963)]. However, it will be difficult to estimate the changes in space constant and in border width with in vivo microelectrode recordings, since the heart moves over relatively enormous distances. It may be necessary to measure these parameters in isolated preparations freshly obtained from ischemic myocardium.

#### 9-D. In vitro experiments

A study of the fine detail of the ischemic zone (i.e. values for space constant, width of the border zone, electrical connections between cells, intracellular and

extracellular electrolyte concentrations, membrane properties, homogeneity of ischemic cells) may necessitate the use of in vitro, isolated preparations. In these preparations, a variety of techniques can be applied. The sucrose gap is a biologically macroscopic technique used to examine membrane properties by forcing extracellular current to enter the intracellular space in order to complete an electrical circuit. Ion selective microelectrodes can provide estimates for ionic flux across the cell membrane. Fluorescent dyes have been used to indicate quantities such as calcium levels or the transmembrane potential. Iontophoresis can be used to inject specific ions into the intracellular space.

With this array of techniques and with the greater control of experimental variables inherent with in vitro preparations, the fine detail of the ischemic zone can be studied to an extent much greater than for the in vivo, open heart preparation. We conclude that studies of the basic mechanisms for ischemia at the cellular level must ultimately resort to these types of in vitro experiments.

## SUMMARY

We discussed open-chest animal preparations in which the relative ST-TQ segment of the epicardial electrogram has been used as an electrical index of myocardial ischemia. If this index can be justified, it could prove to be an extremely valuable technique for the experimental cardiologist and possibly for the physician as well, as it would not only provide an instantaneous measurement of ischemia, but could be easily measured. Unfortunately, there are practical as well as theoretical reasons which discourage the use of the ST-TQ segment as the ischemic index. We cited evidence which suggests that the d-c baseline, rather than the ST-TQ segment, is a more appropriate index. There are practical advantages as well for using the d-c baseline.

We then summarized a number of models which have been used to describe electrical potentials in myocardium. Among these models, the solid angle model stands out, since it is currently the only model which has been applied to myocardial ischemia. It is attractive, since it is relatively simple to use and provides the framework for a theoretical discussion. Unfortunately, a hard look at the assumptions underlying the solid angle model results in the inescapable conclusion that the model is inadequate for describing the open-heart, experimental situation.

As an alternative, we formulated the bi-domain model, a

general model for describing electrical potentials in electrically coupled cellular systems, of which myocardium is a member. This model is a hybrid between three-dimensional cable models and field-theoretic models. As a cable model, it differentiates between current flow in the intracellular space and current flow in the extracellular space. As a field-theoretic model, it describes the electric fields which arise from a generalized source distribution, taking into account the effects of the myocardial boundaries.

Conceptually, the bi-domain system is constructed from two mono-domain systems (classical volume conductors) which:

- 1) represent the intracellular and extracellular domains,
- 2) overlap each other at every point, and 3) thus occupy the same three-dimensional volume.

Consequently, the bi-domain model differs from classical (mono-domain) volume conductor models in its description of the volume conductive medium and in its treatment of the sources. In fact, the mono-domain can be considered to be a degenerate case of a bi-domain. A theory analogous to classical electrostatic field theory was developed to describe the extracellular and intracellular potential distributions, as well as boundary conditions, uniqueness, and anisotropy. Because of the bi-domain structure, current flow in the system could be described as "common-mode" in which the currents in the two domains are parallel, or as "differential-mode" in which the currents in the two domains are opposed.

We then applied the bi-domain model to analyze a number of cases involving various ischemic zones of interest. Since the parameters of the model were identified with physically measurable quantities, they were assigned reasonable values based on experimental data. We were primarily interested in the effect of these parameters on the shape of the surface distribution of the ischemic potential. This later enabled us to interpret experimental, ischemic ST-TQ segment maps. We concluded that the concavity of the ischemic potential distribution is determined primarily by the ratio of the resistivity of bulk myocardium to blood, the width of the lateral ischemic border, and the space constant. The polarity (positive or negative) is determined by the shape of the ischemic zone (subepicardial, subendocardial, or transmural), the relative position of the recording electrode to the zone, and the polarity of the ischemic source ( $U_{ms}$ ). The monophasic or biphasic nature of the potential distribution is determined primarily by the width of the transverse ischemic border at the endocardium.

We then related the solid angle model to the bi-domain model, showing that it is an approximation to the bi-domain model under certain assumptions. Not all these assumptions are satisfied, however, for the open-heart preparation to which the solid angle model has been applied. We concluded that a Poisson approximation to the general bi-domain equations is justified and can be used instead.

We showed that the difference between the bi-domain Poisson and the solid angle models was greatest for subepicardial zones, less for subendocardial zones, even less for transmural zones, until finally not at all for intramural zones. The greatest difference in the potential distributions occurred between the distribution arising for the subepicardial and the distribution for the subendocardial ischemic zone. In addition, the epicardial surface potential distribution for these two zones was a good indicator of the area of the zone, but a poor indicator of the depth.

We discussed the general issues related to using the ST-TQ epicardial spatial map as a data base to solve the inverse problem of determining the ischemic membrane source distribution. In particular, we focused on the questions of "reciprocal" ST-TQ shifts, monophasic epicardial potential distributions, and the sensitivity of ST-TQ shifts to local as opposed to distant ischemic sources. We also briefly discussed the suitability of the bi-domain model to biologically microscopic measurements, and the "common-mode" feature of the bi-domain model which enables an externally observable magnetic field to arise.

Finally, we outlined a number of topics for future experimental research. We feel that the ischemic source distribution can be estimated more consistently from d-c measurements. More information can be obtained about the source distribution with the use of endocardial as well as

epicardial maps. Regarding the parameters of the bi-domain model, it is likely that they will change during prolonged or severe ischemia, and it would be useful in the application of the bi-domain model to know in what way these parameters change. Ultimately, a study of the basic cellular mechanisms underlying ischemia must consist of studies involving isolated, in vitro preparations, in which the experimental variables are well controlled, and a variety of techniques are available.



## APPENDIX A: Uniqueness

In Chapter 4-E we proposed a set of extracellular and intracellular boundary conditions which must be specified in order to completely determine the potential distributions for a given problem. From the physical situation we postulated that the extracellular potential or its normal derivative is constrained by the adjacent medium. Furthermore, we assumed an implicit boundary condition at the edge of the bi-domain structure -- namely that the normal component of the intracellular current is zero, or equivalently, that the normal gradient of the intracellular potential is zero. In this section we show that a specification of the extracellular potential or its normal derivative, together with the implicit constraint on the normal derivative of the intracellular potential, uniquely specifies the homogeneous extracellular and intracellular potential distributions.

From equations 4.19 we can write,

$$\nabla\phi_m = \nabla\phi_H \quad (\text{Ala})$$

$$\nabla\phi_o = \frac{-P_o}{P_o + P_i} \nabla\phi_H + \nabla\phi_L \quad (\text{Alb})$$

$$\nabla\phi_i = \frac{P_i}{P_o + P_i} \nabla\phi_H + \nabla\phi_L \quad (\text{Alc})$$

and,

$$\nabla^2 \phi_m = \nabla^2 \phi_H = \frac{1}{\lambda^2} \phi_H \quad (\text{A2a})$$

$$\nabla^2 \phi_o = \frac{-P_o}{P_o + P_i} \nabla^2 \phi_H = \frac{-P_o}{R_m} \phi_H \quad (\text{A2b})$$

$$\nabla^2 \phi_i = \frac{P_i}{P_o + P_i} \nabla^2 \phi_H = \frac{P_i}{R_m} \phi_H \quad (\text{A2c})$$

We demonstrate uniqueness in a manner similar to that for Laplace's equation. We consider three cases: 1) a simply connected surface enclosing a bi-domain structure; 2) a simply connected surface enclosing a bi-domain structure in contact with a mono-domain structure; and 3) multiply connected surfaces enclosing a bi-domain structure.

A-1. Simply connected surface enclosing a bi-domain structure (Fig. A1)

We assume two solutions  $\phi_{o1}$  and  $\phi_{o2}$  which satisfy the general constraint on  $\phi_o$  and  $\partial\phi_o/\partial n$  at the boundary:

$$a\phi_o + b \frac{\partial\phi_o}{\partial n} = c \quad (\text{A3})$$

Consequently the difference solution  $\phi_{od} = \phi_{o1} - \phi_{o2}$  and its normal derivative are constrained to satisfy,

$$a\phi_{od} + b \frac{\partial\phi_{od}}{\partial n} = 0 \quad (\text{A4})$$

at the boundary. We write  $\phi_{od}$  in terms of its Helmholtz ( $\phi_{dH}$ ) and Laplace ( $\phi_{dL}$ ) components,

$$\phi_{od} = \frac{-P_o}{P_o + P_i} \phi_{dH} + \phi_{dL} \quad (\text{A5a})$$

so we can then write:

$$\phi_{id} = \frac{P_i}{P_o + P_i} \phi_{dH} + \phi_{dL} \quad (A5b)$$

$$\phi_{md} = \phi_{dH} \quad (A5c)$$

The divergence theorem can be used to describe  $\phi_o$ ,  $\phi_i$ , and  $\phi_m$ , provided that these potential distributions and their partial derivatives are continuous over the 3-D volume  $V$  and on the surface  $S$  enclosing  $V$ , and that  $S$  is piecewise smooth. Consequently we can apply the first form of Green's theorem to  $\phi_{od}$  and  $\phi_{id}$  to obtain:

$$\int_V (\phi_{od} \nabla^2 \phi_{od} + \nabla \phi_{od} \cdot \nabla \phi_{od}) dv = \oint_S \phi_{od} \nabla \phi_{od} \cdot d\mathbf{a} \quad (A6a)$$

$$\int_V (\phi_{id} \nabla^2 \phi_{id} + \nabla \phi_{id} \cdot \nabla \phi_{id}) dv = \oint_S \phi_{id} \nabla \phi_{id} \cdot d\mathbf{a} \quad (A6b)$$

Note that for equation A6b, the implicit boundary condition  $\partial \phi_i / \partial n = 0$  will imply that  $\partial \phi_{id} / \partial n = 0$  over  $S$ . In addition, applying equations A1, A2, A4, and A5 to equations A6 yields:

$$\int_V \left[ \frac{P_o P_h}{P_i R_m} \phi_{dH}^2 - \frac{P_o}{R_m} \phi_{dH} \phi_{dL} + \left( \frac{P_h}{P_i} \right)^2 \nabla \phi_{dH} \cdot \nabla \phi_{dH} - \frac{2P_h}{P_i} \nabla \phi_{dH} \cdot \nabla \phi_{dL} + \nabla \phi_{dL} \cdot \nabla \phi_{dL} \right] dv + \oint_S ab \phi_{od}^2 da = 0 \quad (A7a)$$

$$\int_V \left[ \frac{P_i P_h}{P_o R_m} \phi_{dH}^2 + \frac{P_i}{R_m} \phi_{dH} \phi_{dL} + \left( \frac{P_h}{P_o} \right)^2 \nabla \phi_{dH} \cdot \nabla \phi_{dH} + \frac{2P_h}{P_o} \nabla \phi_{dH} \cdot \nabla \phi_{dL} + \nabla \phi_{dL} \cdot \nabla \phi_{dL} \right] dv = 0 \quad (A7b)$$

Multiplying equation A7a by  $P_i$  and equation A7b by  $P_o$  and

then adding the two equations yields:

$$\int_V \left[ \frac{P_o P_i}{R_m} \phi_{dH}^2 + P_i \nabla \phi_{dH} \cdot \nabla \phi_{dH} + (P_o + P_i) \nabla \phi_{dL} \cdot \nabla \phi_{dL} \right] dv + \oint_S ab P_o \phi_{od}^2 da = 0 \quad (A8)$$

Uniqueness is demonstrated in the case where a and b possess the same sign, since then all the integrands of equation A8 are positive definite. This implies that  $\phi_{dH} = 0$ ,  $\nabla \phi_{dH} = 0$ , and  $\nabla \phi_{dL} = 0$ . For those cases in which only the normal derivative of  $\phi_o$  is specified on the boundary (Neumann condition), we expect  $\phi_H$  to be uniquely specified, and  $\phi_L$  to be specified to within an additive constant.

A-2. Simply connected surface enclosing a bi-domain in contact with a mono-domain structure (Fig. A2)

We take the general boundary condition A9 over  $S_1$  and A10 over  $S_2$ :

$$S_1: \quad a_1 \phi_M + b_1 \frac{\partial \phi_M}{\partial n_1} = c_1 \quad (A9)$$

$$S_2: \quad a_2 \phi_o + b_2 \frac{\partial \phi_o}{\partial n_2} = c_2 \quad (A10)$$

together with the implicit boundary condition on  $\phi_i$  over  $S_2$  and  $S_3$ . We also specify continuity of potential and its normal derivative across  $S_3$  in the following manner:

$$S_3: \quad \phi_M = \phi_o \quad (A11a)$$

$$S_3: \quad \frac{\partial \phi_M}{\partial n_1} = - \frac{\partial \phi_o}{\partial n_2} \quad (A11b)$$

As before, we assume two solutions which satisfy the given boundary conditions and construct the difference solution:  $\phi_{dM}$ ,  $\phi_{od}$ , and  $\phi_{id}$ . The difference solutions  $\phi_{dM}$  and  $\phi_{od}$  must now satisfy boundary conditions of the form of equation A4. Consequently, applying Green's theorem to  $\phi_{dM}$  and using the fact that the Laplacian of  $\phi_M$  and therefore of  $\phi_{dM}$  is zero, we obtain,

$$\int_{V_1} (\nabla \phi_{dM} \cdot \nabla \phi_{dM}) \, dv = \int_{S_1} \phi_{dM} \nabla \phi_{dM} \cdot d\mathbf{a} + \int_{S_3} \phi_{dM} \nabla \phi_{dM} \cdot d\mathbf{a} \quad (A12)$$

Applying Green's theorem to  $\phi_{od}$  and  $\phi_{id}$ , we obtain,

$$\int_{V_2} (\phi_{od} \nabla^2 \phi_{od} + \nabla \phi_{od} \cdot \nabla \phi_{od}) \, dv = \int_{S_2} \phi_{od} \nabla \phi_{od} \cdot d\mathbf{a} + \int_{S_3} \phi_{od} \nabla \phi_{od} \cdot d\mathbf{a} \quad (A13a)$$

$$\int_{V_2} (\phi_{id} \nabla^2 \phi_{id} + \nabla \phi_{id} \cdot \nabla \phi_{id}) \, dv = 0 \quad (A13b)$$

Combining equations A11-A13 in a manner analogous to used for obtaining equation A8, we arrive at:

$$P_o \int_{V_1} (\nabla \phi_{dM} \cdot \nabla \phi_{dM}) \, dv + P_o \int_{S_1} a_1 b_1 \phi_{dM}^2 \, da + \int_{V_2} \left[ \frac{P_o P_i}{R_m} \phi_{dH}^2 + P_h \nabla \phi_{dH} \cdot \nabla \phi_{dH} + (P_o + P_i) \nabla \phi_{dL} \cdot \nabla \phi_{dL} \right] \, dv + P_o \int_{S_2} a_2 b_2 \phi_{od}^2 \, da = 0 \quad (A14)$$

where  $P_h$  is defined in equation 4.27. We note that the contributions on  $S_3$  by  $\phi_{od} \nabla \phi_{od}$  and  $\phi_{dM} \nabla \phi_{dM}$  cancel each other out in obtaining equation A14. As in case A-1, provided that  $a_1$  and  $b_1$  (and  $a_2$  and  $b_2$ ) both possess the same sign, all the

integrands in equation A14 are positive definite, implying that each term in each integrand must be zero and again proving uniqueness.

A-3. Multiply connected surfaces enclosing a bi-domain structure (Fig. A3)

Finally, the case of multiply connected surfaces can be treated as in mono-domain systems by constructing an imaginary cut between the two surfaces  $S_1$  and  $S_2$  to form a simply connected surface. The result, however, is not quite equivalent to case A-1, since we do not assume the implicit boundary condition on  $S_3$  and  $S_4$ , but rather a continuity of intracellular potential and its normal derivative. The analogous equation to equation A6b would be:

$$\int_V (\phi_{id}^2 + \nabla\phi_{id} \cdot \nabla\phi_{id}) dv = \int_{S_3} \phi_{id} \nabla\phi_{id} \cdot d\mathbf{a} + \int_{S_4} \phi_{id} \nabla\phi_{id} \cdot d\mathbf{a} \quad (A15)$$

However, the contributions from surfaces  $S_3$  and  $S_4$  on either side of the cut will cancel each other out, so that equation A15 will reduce to equation A6b. For the extracellular potential, the analogous equation to equation A6a is identical to A6a, except that  $S$  is replaced by  $S_1+S_2+S_3+S_4$ . Since the extracellular potential and its normal derivative are continuous across  $S_3$  and  $S_4$ , the contributions from  $S_3$  and  $S_4$  will again cancel out. Thus we are left with equation A6a, with  $S$  replaced by  $S_1+S_2$ . The proof for uniqueness then proceeds exactly as in case A-1.

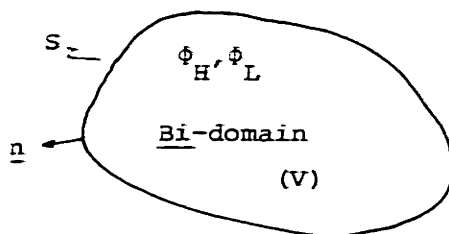


FIGURE A1 - Simply connected surface enclosing a bi-domain structure

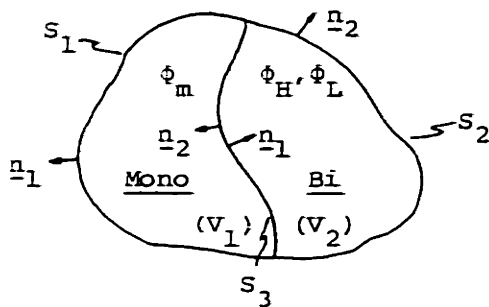


FIGURE A2 - Simply connected surface enclosing a bi-domain in contact with a mono-domain structure

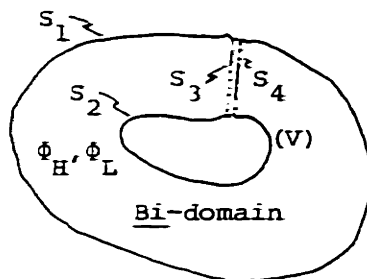


FIGURE A3 - Multiply connected surfaces enclosing a bi-domain structure

APPENDIX B: Experimental Values for the Parameters of the  
Bi-Domain Model

The passive components of the bi-domain model consist of three resistive bulk parameters -  $P_o$ ,  $P_i$ , and  $R_m$ . These parameters are derived from three morphological parameters ( $a_o$ ,  $a_i$ ,  $a_m$ ) and three resistivity parameters ( $\rho_o$ ,  $\rho_i$ , and  $\rho_m$ ), which have been estimated by a variety of techniques. In this appendix we summarize a number of experiments which estimate the morphological and electrical parameters and which suggest how these parameters might change under conditions of prolonged ischemia.

B-1. Morphological parameters

Estimates for the proportion of extracellular space [equal to  $3(a_o)$  for randomly oriented fibers, or  $a_o$  for parallel fibers] are not numerous and appear to be species dependent. These estimates vary from 19% [Polimeni (1974), on rat trabeculae], to 26% [Lieberman et al (1975), on cultured strands of embryonic chick cells] to 30% [Page (1962), on cat ventricle]. The proportion of intracellular space can be approximated as  $1-3(a_o)$  for randomly oriented fibers, and  $1-a_o$  for parallel fibers (cf. Chapter 4-A).

Estimates for the ratio of membrane surface to total volume ( $a_m$ ) are also few in number and again appear to be dependent on the preparation. They range from  $2.0 \times 10^3 \text{ cm}^{-1}$



[derived from Weidmann (1970) on sheep trabeculae], to  $3.0 \times 10^3 \text{ cm}^{-1}$  [Page and Niedergerke (1972) on frog ventricle] to  $8.76 \times 10^3 \text{ cm}^{-1}$  [Lieberman et al (1975) on cultured strands of embryonic chick cells].

## B-2. Electrical parameters

In the following experiments, the bulk (macroscopic) cable parameters corresponding to  $P_o$ ,  $P_i$ , and  $R_m$  of the bi-domain model were generally measured. The microscopic resistivities  $\rho_o$ ,  $\rho_i$ , and  $r_m$  were then obtained by estimating values for the morphological parameters (recall that  $\rho_i = P_i a_i$ ,  $\rho_o = P_o a_o$ ,  $r_m = R_m a_m$ ). Unfortunately the microscopic, rather than the macroscopic, parameters are usually reported. The rather wide scatter of the values of the microscopic electrical parameters reported in the literature is probably primarily due to the wide variation in the estimates for the morphological parameters.

In a study on sheep trabeculae, Weidmann (1970) obtained estimates for the intracellular and extracellular resistivities (also referred to in the literature as "specific resistivities"). The value for  $\rho_o$  was estimated to be  $47 \Omega\text{-cm}$ , while that for  $\rho_i$  to be  $470 \Omega\text{-cm}$ . The estimate for the membrane resistivity, normalized for membrane thickness, was  $9.1 \times 10^3 \Omega\text{-cm}^2$ . The space constant obtained was  $.088 \text{ cm}$ .

In a separate study, Clerc (1976) used plate electrodes

to measure directional intracellular and extracellular resistivities, which depended on the orientation of the electrodes with respect to the fibers in the tissue sample. For the purposes of analysis, he assumed the same geometry in both the longitudinal and transverse directions -- i.e. parallel cylindrical rods in a conductive medium. The intracellular resistivity had a mean value of  $402 \Omega\text{-cm}$  in the longitudinal direction and  $3620 \Omega\text{-cm}$  in the transverse direction. The extracellular resistivity varied from  $48 \Omega\text{-cm}$  in the longitudinal direction to  $127 \Omega\text{-cm}$  in the transverse direction. We note here that the bi-domain model can be written as in Appendix D to describe tissue anisotropy in both domains.

### B-3. Impedance measurements

In a paper by Geddes and Baker (1967) a summary of various measurements of the resistivity of myocardial tissue was given. Most of the techniques listed used two electrodes both to pass the source current and to record the resulting voltage. In general, these techniques are sensitive to small variations in the precise spatial distribution of current at the electrodes. However, Rush (1963) used a four-electrode technique on dog hearts to obtain a more uniform current distribution. He obtained estimates for the tissue resistivity in directions both parallel and perpendicular to the axis of the underlying fibers. The longitudinal

resistivity was given as  $252 \Omega\text{-cm}$ , while the transverse resistivity was  $563 \Omega\text{-cm}$ . These values are approximately equal to, but a factor of 2.0 in the longitudinal direction and 1.4 in the transverse direction higher than, those calculated from the results of Clerc (1976) using the bi-domain model ( $125 \Omega\text{-cm}$  and  $391 \Omega\text{-cm}$ , respectively).

#### B-4. Expected changes under severely ischemic conditions

As the cell membrane loses its permselective properties, we expect that potassium will flow out of the cell and sodium into the cell. Consequently there will be some alteration of the intracellular and extracellular conductivities, which are proportional to the ionic concentrations. However, since the total conductivity is the sum of the individual ionic conductivities, the changes in the potassium and sodium conductivities in each domain will be offsetting. Thus, we expect that changes in conductivity will be a second order effect. A change in the membrane conductance will most likely be the predominant effect; however from the sensitivity analysis of Chapter 5-D we show that changes in  $R_m$  will affect the spatial distribution of the ischemic potential only through the space constant parameter, and that this effect will be small for typical values of  $\lambda$ .

Recently Whalen et al (1974) has shown that cells undergoing acute ischemia for a period of forty minutes or more apparently lose their ability to regulate their volume,

and swell. Studies by Leaf (1973) and DiBona and Powell (1977) have arrived at similar conclusions, although there appears to be some evidence to the contrary [Pine et al (1977)]. If cellular swelling does occur, this should have the effect of increasing the morphological parameter  $a_i$ , and consequently reducing the value of  $P_i$ .

However, this increase in  $P_i$  will most likely be masked by increases in the resistivity of the intercalated disks. Evidence which supports this hypothesis consists of the observation that myocardial cells uncouple following intracellular injection of sodium [De Mello (1976)], in hypoxia and hypothermia [Sperelakis (1969)], and in conditions which cause cellular swelling, such as infusion with hypertonic sucrose [Barr et al (1965)]. In addition, local conduction disturbances often arise in severely ischemic myocardium [Muller et al (1975)], suggesting a disruption of the normal cell-to-cell, electrical connections. Since in severe ischemia the myocardial free wall undergoes systolic bulging [Katcher et al (1960)], the myocardial cells may undergo excessive stretch, causing changes in the propagation velocity and shape of the cellular action potential [Penefsky and Moore (1963), Spear and Moore (1972)]. This may also contribute to cell-to-cell uncoupling. Therefore it seems likely that at some time before or during cell necrosis (death), complete uncoupling occurs. This will have the effect of substantially

increasing  $P_i$ . Stated another way, the bi-domain will reduce to a mono-domain with imbedded, independent, cellular structures having high impedance boundaries (similar to the situation for blood).

A rather surprising result, reported by Polimeni and Al-Sadir (1975) in studies with rat myocardium, is that the extracellular space in normal tissue surrounding an infarcted (necrotic) area apparently expands by about 15%. This means that at the periphery of an infarct, the parameter  $a_o$  will increase, resulting in a decrease in  $P_o$ . This may or may not be related to studies which claim that there is a region of hyperperfused myocardium surrounding an infarct [Rees and Redding (1969), Becker et al (1973)].

Finally, studies by Iseri et al (1952), Jennings (1965), and Bodenheimer (1976) indicate that the total potassium content of ischemic tissue slowly decreases, with a time constant on the order of 1 hr. This suggests that it is not changes in the total ionic content of the tissue which generates the early ischemic potential but rather the distribution of ions between intracellular and extracellular spaces. However, in the late stages of ischemia in which there is a breakdown of the cell membrane, the extracellular and intracellular ionic concentrations can be expected to equilibrate, as the cells uncouple and the transmembrane potential goes to zero. The ischemic potential may still arise, however, in the form of liquid junction potentials due

to ionic concentration gradients in the extracellular space. These potentials will eventually disappear either from the diffusion of ions into the healthy, myocardial region or from the development of collateral circulation, which would "flush out" the extracellular space and which might explain long term ST-TQ segment elevations which decay over a period of hours to days. Although estimates have been made for the ionic, compartmental distribution in healthy tissue [Iseri et al (1952), Hecht (1961), Sodi-Pallares et al (1966), Polimeni (1974)], there appears to be little data for the distribution in ischemic cells.

APPENDIX C: The Integral Form of the Bi-Domain Model

In this appendix we obtain the integral form of equations 4.16 for bi-domain structures. We consider the biologically microscopic structure shown in Fig. C1. We take  $S_o+S_i$  to be the macroscopic boundary surface  $S$ , and  $S_m$  to be the volume distributed membrane surface. We shall show that just as Gauss' law leads to the integral form of Laplace's equation for sourceless mono-domains, Gauss' law leads to the integral form of the Helmholtz equation for sourceless bi-domains.

We begin with the divergence theorem (Gauss' law), written for the structure of Fig. C1,

$$\oint_{S_o+S_m} \hat{E}_o \cdot d\mathbf{a} = \int_{V_o} \nabla \cdot \hat{E}_o \, dv = 0 \quad (C1a)$$

$$\oint_{S_i+S_m} \hat{E}_i \cdot d\mathbf{a} = \int_{V_i} \nabla \cdot \hat{E}_i \, dv = 0 \quad (C1b)$$

where we have taken  $\nabla \cdot \hat{E}_o = \nabla \cdot \hat{E}_i = 0$  in the absence of a free charge distribution. The corresponding macroscopic equations take the form,

$$\oint_S \mathbf{E}_o \cdot d\mathbf{a} = \int_V \nabla \cdot \mathbf{E}_o \, dv \quad (C2a)$$

$$\oint_S \mathbf{E}_i \cdot d\mathbf{a} = \int_V \nabla \cdot \mathbf{E}_i \, dv \quad (C2b)$$

where the expressions above are non-zero even for media without a free charge distribution, since charge can appear

and disappear from one domain to the other across  $S_m$ .

Equations C1 can be rewritten as:

$$\int_{S_o} \hat{E}_{-o} \cdot d\vec{a} = - \int_{S_m} \hat{E}_{-o} \cdot d\vec{a} = -\rho_o \int_{S_m} \hat{J}_{-o} \cdot d\vec{a} \quad (C3a)$$

$$\int_{S_i} \hat{E}_{-i} \cdot d\vec{a} = - \int_{S_m} \hat{E}_{-i} \cdot d\vec{a} = -\rho_i \int_{S_m} \hat{J}_{-i} \cdot d\vec{a} \quad (C3b)$$

We can apply the membrane equivalent circuit of Fig. 4.4 relating the membrane current density to the transmembrane potential  $\phi_m$ , the membrane resistivity  $\rho_m$ , the membrane thickness  $d$ , and the membrane sources  $J_{ms}$  to obtain,

$$\hat{J}_i \Big|_{S_m} = -\hat{J}_o \Big|_{S_m} = \hat{J}_m = \frac{\hat{\phi}_m}{\rho_m d} - \hat{J}_{ms} \quad (C4)$$

Thus, equations C3 together with C4 become:

$$\int_{S_o} \hat{E}_{-o} \cdot d\vec{a} = \frac{\rho_o}{\rho_m d} \int_{S_m} \hat{\phi}_m da - \rho_o \int_{S_m} \hat{J}_{ms} da \quad (C5a)$$

$$\int_{S_i} \hat{E}_{-i} \cdot d\vec{a} = \frac{-\rho_i}{\rho_m d} \int_{S_m} \hat{\phi}_m da + \rho_i \int_{S_m} \hat{J}_{ms} da \quad (C5b)$$

At this point we convert the microscopic description to a macroscopic description, using the morphological parameters  $a_o$ ,  $a_i$ ,  $a_m$  (defined in equations 4.5 and 4.11), and assuming that the microscopic variables for the potential and current density are relatively constant over macroscopic, incremental dimensions (a valid approximation, since the characteristic space constant is many times a cell length). Thus, from the definition of  $a_o$  and  $a_i$  as the ratios  $S_o/S$  and  $S_i/S$  respectively, we convert the left hand side of equations C5 to:



$$\int_{S_o} \hat{E}_o \cdot d\mathbf{a} \equiv a_o \int_S E_o \cdot d\mathbf{a} \quad (C6a)$$

$$\int_{S_i} \hat{E}_i \cdot d\mathbf{a} \equiv a_i \int_S E_i \cdot d\mathbf{a} \quad (C6b)$$

From the definition of  $a_m$ , we convert the right hand side of equations C5 to:

$$\int_{S_m} \hat{\phi}_m \, da \equiv a_m \int_V \phi_m \, dv \quad (C7a)$$

$$\int_{S_m} \hat{J}_{ms} \, da \equiv \int_V U_{ms} \, dv \quad (C7b)$$

Combining equations C5-C7 we obtain:

$$- \int_S \nabla \phi_o \cdot d\mathbf{a} = \frac{P_o}{R_m} \int_V \phi_m \, dv - P_o \int_V U_{ms} \, dv \quad (C8a)$$

$$- \int_S \nabla \phi_i \cdot d\mathbf{a} = \frac{-P_i}{R_m} \int_V \phi_m \, dv + P_i \int_V U_{ms} \, dv \quad (C8b)$$

Finally, applying the definition that  $\phi_m = \phi_i - \phi_o$ , we obtain,

$$\int_S \nabla \phi_m \cdot d\mathbf{a} = \frac{P_o + P_i}{R_m} \int_V \phi_m \, dv - (P_o + P_i) \int_V U_{ms} \, dv \quad (C9a)$$

$$\int_S \nabla \phi_o \cdot d\mathbf{a} = \frac{-P_o}{P_o + P_i} \int_S \nabla \phi_m \cdot d\mathbf{a} \quad (C9b)$$

$$\int_S \nabla \phi_i \cdot d\mathbf{a} = \frac{P_i}{P_o + P_i} \int_S \nabla \phi_m \cdot d\mathbf{a} \quad (C9c)$$

which we recognize as the integral form of equations 4.16.

We conclude this appendix with a brief discussion of the macroscopic form of Green's theorem for bi-domains. For

microscopic mono-domain systems, we have,

$$\int_V (\phi \nabla^2 \psi - \psi \nabla^2 \phi) \, dv = \int_S (\phi \frac{\partial \psi}{\partial n} - \psi \frac{\partial \phi}{\partial n}) \, da \quad (C10)$$

Taking  $\phi = \phi_o$ ,  $\psi = 1/r_{QP}$ ,  $V = V_o$ ,  $S = S_o + S_m$ , we have  $\nabla^2(1/r_{QP}) = -4\pi\delta(\underline{r}_P)$  and  $\nabla^2\phi_o = 0$ . Thus:

$$\phi_o(\underline{r}_P) = \frac{-1}{4\pi} \int_{S_o + S_m} [\phi_o(\underline{r}_Q) \frac{\partial}{\partial n}(\frac{1}{r_{QP}}) - \frac{1}{r_{QP}} \frac{\partial \phi_o(\underline{r}_Q)}{\partial n}] \, da_Q \quad (C11)$$

The equivalent sources are all on the boundary and represent sources external to  $V_o$ . The macroscopic Green's theorem for bi-domains takes the same form as equation C10. Again, we take  $\phi = \phi_o$ ,  $\psi = 1/r_{QP}$ , with  $\nabla^2(1/r_{QP}) = -4\pi\delta(\underline{r}_P)$ , but now  $\nabla^2\phi_o = -(P_o/(P_o + P_i)) \nabla^2\phi_m$ . Thus, we have:

$$\begin{aligned} \phi_o(\underline{r}_P) = & \frac{-1}{4\pi} \int_S [\phi_o(\underline{r}_Q) \frac{\partial}{\partial n}(\frac{1}{r_{QP}}) - \frac{1}{r_{QP}} \frac{\partial \phi_o(\underline{r}_Q)}{\partial n}] \, da_Q \\ & - \frac{1}{4\pi} \frac{P_o}{P_o + P_i} \int \frac{\nabla^2\phi_m(\underline{r}_Q)}{r_{QP}} \, dv_Q \end{aligned} \quad (C12)$$

The extra term on the right hand side of equation C12 represents a source distribution throughout  $V$  which arises from the appearance or disappearance of current in the extracellular domain due to flow across the membrane.

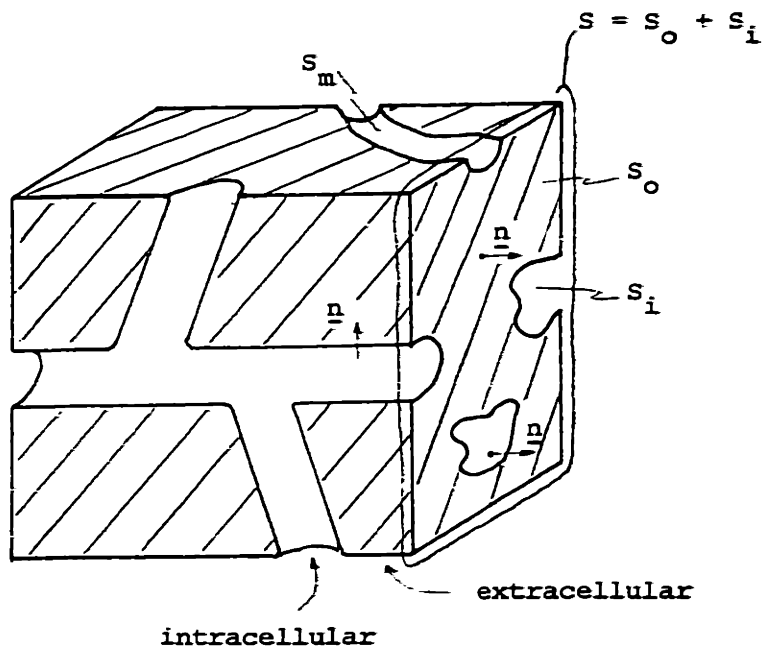


FIGURE C1 - The microscopic structure of a bi-domain system

APPENDIX D: Anisotropy

In this appendix we rewrite the general equations 4.16 to account for anisotropy (in one dimension, along the z-axis) in the intracellular and extracellular media. We begin by rewriting equations 4.13 to account for directional differences in the medium resistivity:

$$J_{-o} = -\frac{1}{P_{ox}} \frac{\partial \phi_o}{\partial x} \hat{i}_x - \frac{1}{P_{oy}} \frac{\partial \phi_o}{\partial y} \hat{i}_y - \frac{1}{P_{oz}} \frac{\partial \phi_o}{\partial z} \hat{i}_z \quad (D1a)$$

$$J_{-i} = -\frac{1}{P_{ix}} \frac{\partial \phi_i}{\partial x} \hat{i}_x - \frac{1}{P_{iy}} \frac{\partial \phi_i}{\partial y} \hat{i}_y - \frac{1}{P_{iz}} \frac{\partial \phi_i}{\partial z} \hat{i}_z \quad (D1b)$$

The macroscopic, bulk resistivities  $P_o$  and  $P_i$  are now written with x, y, and z components. Equations 4.14 and 4.15 remain unchanged. Therefore, we obtain:

$$-\frac{1}{P_{ox}} \frac{\partial^2 \phi_o}{\partial x^2} - \frac{1}{P_{oy}} \frac{\partial^2 \phi_o}{\partial y^2} - \frac{1}{P_{oz}} \frac{\partial^2 \phi_o}{\partial z^2} = \frac{\phi_m}{R_m} - U_{ms} \quad (D2a)$$

$$-\frac{1}{P_{ix}} \frac{\partial^2 \phi_i}{\partial x^2} - \frac{1}{P_{iy}} \frac{\partial^2 \phi_i}{\partial y^2} - \frac{1}{P_{iz}} \frac{\partial^2 \phi_i}{\partial z^2} = -\frac{\phi_m}{R_m} + U_{ms} \quad (D2b)$$

Because we are assuming isotropy in the x-y plane, we have:

$$P_{ox} = P_{oy} \quad (D3a)$$

$$P_{ix} = P_{iy} \quad (D3b)$$

Thus, we obtain from equations D2 the coupled equations,

$$\frac{\partial^2 \phi_o}{\partial x^2} + \frac{\partial^2 \phi_o}{\partial y^2} + \frac{1}{\alpha_o} \frac{\partial^2 \phi_o}{\partial z^2} = -\frac{P_{ox}}{R_m} (\phi_i - \phi_o) + P_{ox} U_{ms} \quad (D4a)$$

$$\frac{\partial^2 \phi_i}{\partial x^2} + \frac{\partial^2 \phi_i}{\partial y^2} + \frac{1}{\alpha_i} \frac{\partial^2 \phi_i}{\partial z^2} = \frac{P_{ix}}{R_m} (\phi_i - \phi_o) - P_{ox} U_{ms} \quad (D4b)$$

where:

$$\alpha_o = \frac{P_{oz}}{P_{ox}} \quad (D5a)$$

$$\alpha_i = \frac{P_{iz}}{P_{ix}} \quad (D5b)$$

In the case where the degree of anisotropy is the same in both domains,  $\alpha_o = \alpha_i = \alpha$ , and equations D4 can be written in a form analogous to equations 4.16:

$$\nabla_{\alpha}^2 \phi_m = \frac{1}{\lambda_x^2} \phi_m - (P_{ox} + P_{ix}) U_{ms} \quad (D6a)$$

$$\nabla_{\alpha}^2 \phi_o = \frac{-P_o}{P_o + P_i} \nabla_{\alpha}^2 \phi_m \quad (D6b)$$

$$\nabla_{\alpha}^2 \phi_i = \frac{P_i}{P_o + P_i} \nabla_{\alpha}^2 \phi_m \quad (D6c)$$

where the operator  $\nabla_{\alpha}^2$  is given by:

$$\nabla_{\alpha}^2 = \frac{\partial}{\partial x^2} + \frac{\partial}{\partial y^2} + \frac{1}{\alpha} \frac{\partial}{\partial z^2} \quad (D7)$$

and:

$$\lambda_x = \left( \frac{R_m}{P_{ox} + P_{ix}} \right)^{1/2} \quad (D8)$$

The resulting potential distribution appears as a "stretched-out" version of the distribution in an isotropic

medium.

The (Green's function) solutions to equations D6 for a membrane point source,  $U_{ms} = I_s \delta(r)$ , take the form (compare to equations 4.29):

$$\phi_m = \frac{(P_o + P_i) I_s}{4\pi r_\alpha} e^{-r_\alpha/\lambda_x} \quad (D9a)$$

$$\phi_o = \frac{-P_o I_s}{4\pi r_\alpha} e^{-r_\alpha/\lambda_x} \quad (D9b)$$

$$\phi_i = \frac{P_i I_s}{4\pi r_\alpha} e^{-r_\alpha/\lambda_x} \quad (D9c)$$

where:

$$r_\alpha = (x^2 + y^2 + \alpha z^2)^{1/2} \quad (D10)$$

APPENDIX E: Microscopic to Macroscopic Description

Plonsey (1965) derived a biologically microscopic, partial space description for the extracellular potential using Green's theorem. This formulation was in the form of a "solid angle" model, with an equivalent dipole current source distributed over the volume of the myocardium. Unfortunately, the source intensity was expressed as a function not only of the intracellular potential, but the extracellular potential as well. In a later paper, Plonsey (1974) used cable relations, which expressed the intracellular and extracellular potentials as a function of the transmembrane potential, to extricate himself from this complication. In this appendix, we rewrite Plonsey's original formulation according to the notation used in this work. We then show that starting from this formulation, it is possible to arrive at not the complete, but rather a portion of the bi-domain model. The membrane sources are not included in the following derivation, except indirectly through the transmembrane potential. This is not necessarily a restrictive condition, since we have shown that in the case where high spatial frequencies can be neglected (cf. Chapter 6-A), the transmembrane potential can be taken to be proportional to  $U_{ms}$ , the cellular transmembrane current source. In addition, the following derivation is made for an infinite medium.

We begin by finding the extracellular potential arising from a single, myocardial cell [adapted from Plonsey (1965)]. The point P is the observation point which remains in the extracellular space, and Q is an arbitrary point which for the first case at hand will remain in the intracellular space (see Fig. E1). The variable  $r_{QP}$  is equal to the distance between points P and Q. Writing the second form of Green's theorem, we have:

$$\int_V (\phi \nabla^2 \psi - \psi \nabla^2 \phi) \, dv = \int_S (\phi \frac{\partial \psi}{\partial n} - \psi \frac{\partial \phi}{\partial n}) \, da \quad (E1)$$

Taking the volume V to be  $V_i$ , bounded by  $S_i$ , and letting  $\phi = \phi_i$  and  $\psi = 1/r_{QP}$ , we have  $\nabla^2(1/r_{QP}) = 0$  inside  $V_i$ , since  $r_{QP}$  cannot be zero there. Furthermore,  $\nabla^2 \phi_i = 0$ , assuming no microelectrode sources. Thus:

$$0 = \int_{S_i} \phi_i(\underline{r}_Q) \frac{\partial}{\partial n} \left( \frac{1}{r_{QP}} \right) \, da_Q - \int_{S_i} \frac{1}{r_{QP}} \frac{\partial \phi_i(\underline{r}_Q)}{\partial n} \, da_Q \quad (E2)$$

Writing,

$$-\left. \frac{\partial \phi_i}{\partial n} \right|_{S_i} = \rho_i J_m \quad (E3)$$

where  $\rho_i$  is the intracellular resistivity, and  $J_m$  is the net outward membrane current density, we can combine equations E2 and E3 to obtain:

$$0 = \int_{S_i} \phi_i(\underline{r}_Q) \frac{\partial}{\partial n} \left( \frac{1}{r_{QP}} \right) \, da_Q + \rho_i \int_{S_i} \frac{J_m(\underline{r}_Q)}{r_{QP}} \, da_Q \quad (E4)$$

We now apply equation E1 to the extracellular space. Taking the volume V to be  $V_o$ , bounded by  $S_o$  and infinity, and



letting  $\phi = \phi_o$  and  $\psi = 1/r_{QP}$ ,  $Q$  is now in  $V_o$  and  $r_{QP}$  can be zero. Furthermore, we have  $\nabla^2(1/r_{QP}) = -4\pi\delta(\underline{r}_P - \underline{r}_Q)$ , and  $\nabla^2\phi_o = 0$ . Therefore:

$$\phi_o(\underline{r}_P) = \frac{1}{4\pi} \int_{S_o} \phi_o(\underline{r}_Q) \frac{\partial}{\partial n} \left( \frac{1}{r_{QP}} \right) da_Q - \frac{1}{4\pi} \int_{S_o} \frac{1}{r_{QP}} \frac{\partial \phi_o(\underline{r}_Q)}{\partial n} da \quad (E5)$$

The normal  $\underline{n}$  has been taken to be inward into  $V_o$  (see Fig. E1), and the surface integral taken to vanish at infinity. Writing,

$$-\frac{\partial \phi_o}{\partial n} \Big|_{S_o} = \rho_o J_m \quad (E6)$$

we have:

$$\phi_o(\underline{r}_P) = \frac{1}{4\pi} \int_{S_o} \phi_o(\underline{r}_Q) \frac{\partial}{\partial n} \left( \frac{1}{r_{QP}} \right) da_Q + \frac{1}{4\pi} \int_{S_o} \frac{J_m(\underline{r}_Q)}{r_{QP}} da_Q \quad (E7)$$

We can combine equations E4 and E7 to arrive at:

$$\begin{aligned} \phi_o(\underline{r}_P) = & \frac{-1}{4\pi} \left[ \frac{\rho_o}{\rho_i} \int_{S_i} \phi_i(\underline{r}_Q) \frac{\partial}{\partial n} \left( \frac{1}{r_{QP}} \right) da_Q - \int_{S_o} \phi_o(\underline{r}_Q) \frac{\partial}{\partial n} \left( \frac{1}{r_{QP}} \right) da_Q \right] \\ & + \frac{\rho_o}{4\pi} \left[ \int_{S_o} \frac{J_m(\underline{r}_Q)}{r_{QP}} da_Q - \int_{S_i} \frac{J_m(\underline{r}_Q)}{r_{QP}} da_Q \right] \end{aligned} \quad (E8)$$

Since the surface  $S_o$  is located an incremental distance  $d$  away from the surface  $S_i$ , we can rewrite equation E8 as an integral over the mean membrane surface  $S_m$ :

$$\begin{aligned} \phi_o(\underline{r}_P) = & \frac{-1}{4\pi} \int_{S_m} \left[ \frac{\rho_o}{\rho_i} \phi_i(\underline{r}_Q) - \phi_o(\underline{r}_Q) \right] \nabla \left( \frac{1}{r_{QP}} \right) \cdot d\mathbf{a}_Q \\ & + \frac{\rho_o}{4\pi} \int_{S_m} J_m(\underline{r}_Q) dV \left( \frac{1}{r_{QP}} \right) \cdot d\mathbf{a}_Q \end{aligned} \quad (E9)$$

Recognizing that,

$$-\nabla\left(\frac{1}{r_{QP}}\right) \cdot da_Q = -\nabla\left(\frac{1}{r_{QP}}\right) \cdot \underline{n} da_Q = d\Omega_Q \quad (E10)$$

where  $d\Omega$  is the solid angle subtended by the surface element  $da$  as seen from point  $P$ , we obtain:

$$\phi_o(r_P) = \frac{1}{4\pi} \int_{S_m} \left[ \frac{\rho_o}{\rho_i} \phi_i(r_Q) - \phi_o(r_Q) - \sigma_o J_m(r_Q) d \right] d\Omega_Q \quad (E11)$$

For typical values for the various parameters in equation E11, the last term can be neglected compared to the first two terms, since  $d$  (the thickness of the cell membrane) is very small, on the order of  $10^{-6}$  cm. This is equivalent to the statement that the equivalent ohmic potential drop due to the membrane current density over a distance of the cell membrane thickness is small compared to the magnitude of the potential function which forms the first two terms under the integral of equation E11. Therefore we take:

$$\phi_o(r_P) = \frac{1}{4\pi} \int_{S_m} \left[ \frac{\rho_o}{\rho_i} \phi_i(r_Q) - \phi_o(r_Q) \right] d\Omega_Q \quad (E12)$$

We extend the above formulation for a single cell to a formulation for the potential in the extracellular, partial space for a collection of cells by using superposition, taking  $S_m$  now to be the total cellular membrane surface.

Starting with equation E12, an essentially microscopic description, we now proceed to obtain a macroscopic description [adapted from Plonsey (1974)]. We rewrite equation E12 into the following form,

$$\phi_o(\underline{r}_p) = \frac{\rho_o}{4\pi} \int_{S_m} \underline{m}_s(\underline{r}_Q) \cdot \nabla \left( \frac{1}{r_{QP}} \right) da_Q \quad (E13)$$

where  $\underline{m}_s$  is the microscopic surface dipole moment/unit area density:

$$\underline{m}_s(\underline{r}_Q) = \left[ \frac{\phi_o(\underline{r}_Q)}{\rho_o} - \frac{\phi_i(\underline{r}_Q)}{\rho_i} \right] \underline{n} \quad (E14)$$

We invoke one of the basic assumptions of the bi-domain model, namely that the cells are highly packed and randomly oriented. We can then replace  $\underline{m}_s$  with a macroscopic, dipole moment/unit volume density,  $\underline{m}_v$ ,

$$\underline{m}_v(\underline{r}_Q) = 3 a_i \nabla |\underline{m}_s(\underline{r}_Q)| \quad (E15)$$

where the factor  $a_i$  enters because of the existence of "holes" in the volume density due to the extracellular space. The above relationship can be made somewhat clearer by considering the one-dimensional case with cells aligned in parallel, as illustrated in Fig. E2.

Over each differential region  $dx$ , the integral over  $dS$  can be replaced by the negative of an equivalent integral over the two end surfaces  $da(x)$  and  $da(x+dx)$ , since the solid angle subtended by the three surfaces is zero. The equivalent dipole moment/volume source distribution can be found from the relation:

$$\underline{m}_v(x) A dx = [ \underline{m}_s(x+dx) - \underline{m}_s(x) ] a_i A \quad (E16)$$

A generalization of equation E16 for three dimensions results in equation E15. The extra factor of 3 enters because  $a_i$  is only 1/3 the intracellular cross-sectional area for randomly

oriented fibers (cf. Chapter 4-A). Changing equation E13 to a volume integral, and using equation E15, we obtain:

$$\begin{aligned} \phi_o(\underline{r}_P) &= \frac{\rho_o}{4\pi} \int_V \underline{m}_v(\underline{r}) \cdot \nabla \left( \frac{1}{r_{QP}} \right) dv_Q \\ &= \frac{3a_i \rho_o}{4\pi} \int_V \nabla \left[ \frac{\phi_o(\underline{r}_Q)}{\rho_o} - \frac{\phi_i(\underline{r}_Q)}{\rho_i} \right] \cdot \nabla \left( \frac{1}{r_{QP}} \right) dv_Q \end{aligned} \quad (E17)$$

Exploiting the relationships between the microscopic and macroscopic parameters  $\rho$  and  $P$ ,

$$\rho_o = a_o P_o \quad (E18a)$$

$$\rho_i = a_i P_i \quad (E18b)$$

we obtain:

$$\begin{aligned} \phi_o(\underline{r}_P) &= \frac{3a_i a_o P_o}{4\pi} \int_V \nabla \left[ \frac{\phi_o(\underline{r}_Q)}{a_o P_o} - \frac{\phi_i(\underline{r}_Q)}{a_i P_i} \right] \cdot \nabla \left( \frac{1}{r_{QP}} \right) dv_Q \\ &= \frac{3}{4\pi} \int_V \nabla \left[ a_i \phi_o(\underline{r}_Q) - \frac{a_o P_o \phi_i(\underline{r}_Q)}{P_i} \right] \cdot \nabla \left( \frac{1}{r_{QP}} \right) dv_Q \end{aligned} \quad (E19)$$

We can transform the integral of E19 from one involving a vector quantity to one involving a scalar quantity. Thus:

$$\phi_o(\underline{r}_P) = \frac{-3}{4\pi} \int_V \frac{1}{r_{QP}} \nabla^2 \left[ a_i \phi_o(\underline{r}_Q) - \frac{a_o P_o \phi_i(\underline{r}_Q)}{P_i} \right] dv_Q \quad (E20)$$

From the second form of Green's theorem applied over an infinite medium, we have:

$$\phi_o(\underline{r}_P) = \frac{-1}{4\pi} \int_V \frac{1}{r_{QP}} \nabla^2 \phi_o(\underline{r}_Q) dv_Q \quad (E21)$$

Equating the integrands of equations E20 and E21, we obtain:

$$\nabla^2 \phi_o = 3 \nabla^2 (a_i \phi_o - a_o \frac{P_o}{P_i} \phi_i) \quad (\text{E22})$$

Using the identity,

$$a_o + a_i = 1/3 \quad (\text{E23})$$

for randomly oriented fibers (cf. equation 4.6b), equation E22 becomes:

$$\nabla^2 \phi_o = \frac{-P_o}{P_i} \nabla^2 \phi_i \quad (\text{E24})$$

Since we have defined,

$$\phi_m = \phi_i - \phi_o \quad (\text{E25})$$

we have,

$$\nabla^2 \phi_m = \nabla^2 \phi_i - \nabla^2 \phi_o \quad (\text{E26})$$

Finally, combining equations E24 and E26, we obtain:

$$\nabla^2 \phi_o = \frac{-P_o}{P_o + P_i} \nabla^2 \phi_m \quad (\text{E27a})$$

$$\nabla^2 \phi_i = \frac{P_i}{P_o + P_i} \nabla^2 \phi_m \quad (\text{E27b})$$

The formulation obtained above places no constraint on the variable  $\phi_m$ . If we take the transmembrane potential to be proportional to the membrane current source  $U_{ms}$  (see Chapter 6-A),

$$\phi_m = R_m U_{ms} \quad (\text{E28})$$

and substitute this relationship into equations E27, we obtain the macroscopic, bi-domain Poisson equations which describe the spatial, low frequency behavior.

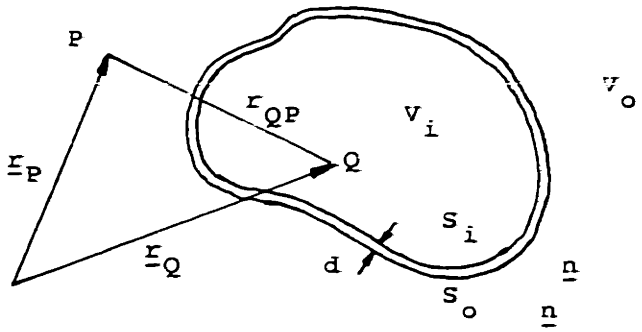


FIGURE E1 - Extracellular potential arising from a single cell

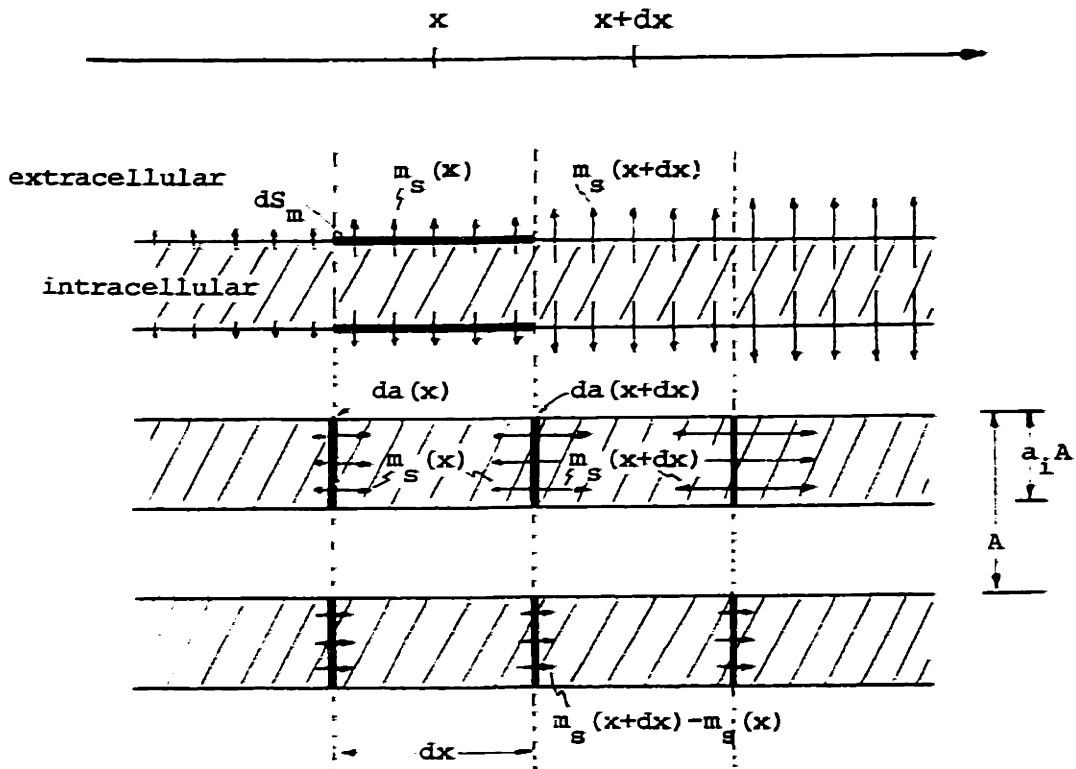


FIGURE E2 - Replacing the surface density by a volume density. Over each differential region  $dx$ , the solid angle subtended by  $dS_m$  having a source with intensity  $m_s(x)$  can be replaced by the negative of the solid angle subtended by the two end surfaces  $da(x)$  and  $da(x+dx)$ , since the total solid angle subtended by the three surfaces is zero. The now opposing differential sources for the regions  $x$  and  $x+dx$  can be combined into a net source  $m_s(x+dx) - m_s(x)$ .

APPENDIX F: The FFT, Fourier Cosine Integral, and Fourier Cosine Series

The Fourier cosine transformations of Chapters 5 and 7 are of the integral form and the series form. We wish to use the FFT (Fast, discrete, Fourier Transform) to reduce computation time. In this appendix, we derive the normalization coefficients which relate the series terms of the FFT to the discrete Fourier transform representing either the Fourier cosine integral or the Fourier cosine series.

F-1. The Fourier cosine integral

For real, even functions, the Fourier cosine integral transformation takes the form:

$$f_a(x) = \frac{2}{\pi} \int_0^{\infty} F_a(x) \cos kx \, dk \quad (\text{Fla})$$

$$F_a(k) = \int_0^{\infty} f_a(x) \cos kx \, dx \quad (\text{Flb})$$

We take the case where  $F_a(k)$  can be derived analytically, but the inverse transformation is performed using the DFT (Discrete Fourier Transform). Consequently, we take  $2N$  samples of  $F_a(k)$  such that (refer to Fig. F1):

$$\hat{F}[m] \equiv F_a\left(m \frac{\pi}{N\Delta x}\right), \quad -N+1 \leq m \leq N \quad (\text{F2})$$

$\hat{F}[m]$  is a periodic function, with period  $2N$ . We define  $\hat{f}[n]$ , the spatial complement to  $\hat{F}[m]$ , as:



$$\hat{f}[n] = \sum_{-N+1}^N \hat{F}[m] e^{-j\pi mn/N} = \sum_0^{2N-1} \hat{F}[m] e^{-j\pi mn/N} \quad (F3a)$$

$$\hat{F}[m] = \frac{1}{2N} \sum_0^{2N-1} \hat{f}[n] e^{j\pi mn/N} \quad (F3b)$$

We can find the approximate relationship (ignoring aliasing effects) between  $\hat{f}[n]$  and  $f_a(x)$  by assuming that  $F_a(k)$  is bandlimited between  $(1-N)\pi/(N\Delta x)$  and  $\pi/\Delta x$ , and that  $N$  is large. In that case, we have:

$$\begin{aligned} f_a(x) &= \frac{2}{\pi} \int_0^{\infty} F_a(k) \cos kx \, dk = \frac{1}{\pi} \int_{-\infty}^{\infty} F_a(k) e^{-jkx} \, dk \\ &= \frac{1}{\pi} \int_{(1-N)\pi/(N\Delta x)}^{\pi/\Delta x} F_a(k) e^{-jkx} \, dk \\ &= \frac{1}{\pi} \sum_{-N+1}^N F_a\left(\frac{m\pi}{N\Delta x}\right) e^{-j\pi mx/(N\Delta x)} \left(\frac{\pi}{N\Delta x}\right) \\ &= \frac{1}{N\Delta x} \sum_0^{2N-1} F_a\left(\frac{m\pi}{N\Delta x}\right) e^{-j\pi mx/(N\Delta x)} \end{aligned} \quad (F4)$$

Consequently, we can identify  $\hat{f}[n]$  as:

$$\hat{f}[n] = N\Delta x f_a(n\Delta x) \quad (F5)$$

Alternatively, if we premultiply  $\hat{F}[m]$  by  $1/(N\Delta x)$ , the resulting  $\hat{f}[n]$  will approximate  $f_a(N\Delta x)$ .

## F-2. The Fourier cosine series

For real, even functions, the Fourier cosine series transformation takes the form:

$$f_a(\theta) = \sum_{k=0}^{\infty} A_k \cos k\theta \quad (F6a)$$

$$A_k = \begin{cases} \frac{1}{\pi} \int_0^{\pi} f(\theta) d\theta & , k = 0 \\ \frac{2}{\pi} \int_0^{\pi} f(\theta) \cos \theta d\theta & , k \geq 1 \end{cases} \quad (F6b)$$

We can find  $A_k$  analytically, and we again wish to use the DFT to invert the transformation. We wish to find a periodic set  $\tilde{f}[m]$  from the  $A_k$  such that when the DFT (or FFT) is applied to  $\tilde{f}[m]$ , the resulting  $\tilde{f}[n]$  is a period sampling of  $f_a(\theta)$ . In other words, we wish to find a  $\tilde{f}[m]$  such that by using the transformation of equation F3a, the resulting  $\tilde{f}[n]$  is:

$$\tilde{f}[n] = f_a\left(\frac{n\pi}{N}\right) \quad (F7)$$

From equations F6b and F7, we have,

$$A_k = \begin{cases} \frac{1}{\pi} \sum_{n=0}^{N-1} f_a(n\Delta\theta) \Delta\theta & , k = 0 \\ \frac{2}{\pi} \sum_{n=0}^{N-1} f_a(n\Delta\theta) \left[ \frac{e^{jkn\Delta\theta} + e^{-jkn\Delta\theta}}{2} \right] \Delta\theta & , k \geq 1 \end{cases} \quad (F8)$$

We rewrite equation F8 using the fact that  $f(\theta)$  is even,

$$A_k = \begin{cases} \frac{1}{2} \frac{\Delta\theta}{\pi} \sum_{-(N-1)}^{(N-1)} f_a(n\Delta\theta) \Delta\theta & , k = 0 \\ \frac{\Delta\theta}{\pi} \sum_{-(N-1)}^{(N-1)} f_a(n\Delta\theta) e^{-jkn\Delta\theta} & , k \geq 1 \end{cases} \quad (F9)$$

where  $\Delta\theta = \pi/N$ . Since  $f(\theta)$  is a periodic function, equation F9 becomes:

$$A_k = \begin{cases} \frac{1}{2N} \sum_0^{2N-1} f_a\left(\frac{n\pi}{N}\right) & , k = 0 \\ \frac{1}{N} \sum_0^{2N-1} f_a\left(\frac{n\pi}{N}\right) e^{-j\pi kn/N} & , k \geq 1 \end{cases} \quad (\text{F10})$$

Comparing equation F10 to F3b, we obtain the desired relationship:

$$\hat{F}[m] = \begin{cases} A_0 & , k = 0 \\ (1/2) A_k & , k \geq 1 \end{cases} \quad (\text{F11})$$

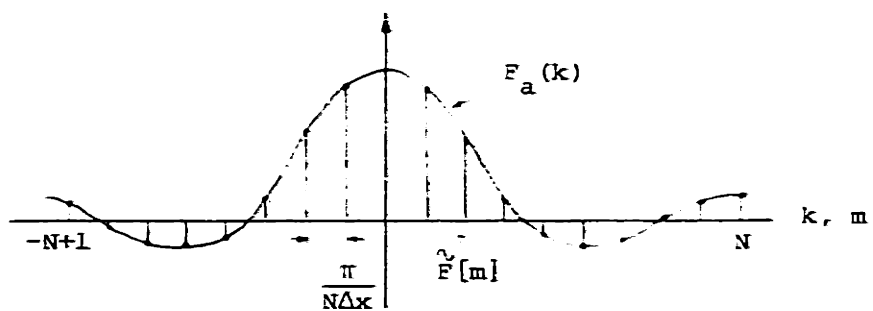


FIGURE F1 - Sampling of the analog waveform

APPENDIX G: Legendre Polynomials and Fourier Cosine Series

If we express a function  $F(r, \theta)$  as a Legendre polynomial expansion of the form,

$$F(r, \theta) = \sum_{k=0}^{\infty} \bar{f}_p(r, k) P_k(\cos \theta) \quad (G1)$$

we discover that the coefficients  $\bar{f}_p(r, k)$  decrease very slowly in magnitude as  $k$  increases. Computationally, this is important, since the truncation error obtained by approximating the infinite series by a finite series can be large. Furthermore, the computational time for each term in the series increases roughly as  $k^2$ , since each  $P_k(\cos \theta)$  must be computed from a series expression (equations G4).

The reason for the slow decay in  $\bar{f}_p(r, k)$  is evident if we use the orthogonal properties of Legendre polynomials to solve for  $\bar{f}_p(r, k)$ :

$$\bar{f}_p(r, k) = \frac{2k+1}{2} \int_0^{\pi} F(r, \theta) P_k(\cos \theta) \sin \theta \, d\theta \quad (G2)$$

In general,  $P_k(\cos \theta)$  has an oscillatory nature which decays slowly with increasing  $k$ , and contains Fourier cosine components (either all odd or all even frequencies) from zero to  $k$  (see Fig. G1).  $F(r, \theta)$  contains Fourier cosine components which in general, decay at a rate depending on the frequency spectrum of the signal. However, the decay in the integrand is offset to some degree by the factor  $((2k+1)/2)$ , which increases with  $k$ .

Therefore we are motivated to rewrite equation G1 in terms of a Fourier cosine series, which as far as we know has not been done before, in the hope of reducing both truncation error and computation time. We proceed by expressing  $F(r, \theta)$  as a Fourier cosine expansion, assuming that  $F(r, \theta)$  is an even function over  $\theta$ :

$$F(r, \theta) = \sum_{k=0}^{\infty} f_p(r, k) P_k(\cos \theta) = \sum_{j=0}^{\infty} f_c(r, j) \cos j\theta \quad (G3)$$

We can express the  $k$ th order Legendre polynomial in terms of its Fourier cosine expansion [Wylie (1966)]:

$$P_k(\cos \theta) = \sum_{j=0}^{\infty} p(j, k) \cos j\theta \quad (G4a)$$

where,

$$p(j, k) = \begin{cases} 0 & , j > k \text{ or } (j-k) \text{ odd} \\ 2 \frac{1 \cdot 3 \cdots (2j-1)}{2 \cdot 4 \cdots (2j)} & , j=k \\ 2 \frac{1 \cdot 3 \cdots (k-j-1)}{2 \cdot 4 \cdots (k-j)} \frac{1 \cdot 3 \cdots (k+j-1)}{2 \cdot 4 \cdots (k+j)} & , j < k \text{ and } (j-k) \text{ even} \\ \left[ \frac{1 \cdot 3 \cdots (k-1)}{2 \cdot 4 \cdots (k)} \right]^2 & , j=0 \text{ and } k \text{ even} \end{cases} \quad (G4b)$$

The coefficients  $p(j, k)$  are such that if  $k$  is odd (even),  $p(j, k)$  is non-zero only for  $j$  odd (even)  $\leq k$ . For  $k$  even, the Legendre polynomial will contain a d-c term equal to  $[1 \cdot 3 \cdots (k-1) / (2 \cdot 4 \cdots k)]^2$ . We have tabulated the values for  $p(j, k)$  for  $0 \leq k \leq 10$  in Fig. G1.

Substituting equation G4a into G3, we obtain:

$$\begin{aligned}
 F(r, \theta) &= \sum_{k=0}^{\infty} f_p(r, k) \sum_{j=0}^{\infty} p(j, k) \cos j\theta \\
 &= \sum_{j=0}^{\infty} \left[ \sum_{k=0}^{\infty} f_p(r, k) p(j, k) \right] \cos j\theta
 \end{aligned} \tag{G5}$$

Hence we identify:

$$\epsilon_c(r, j) = \sum_{k=0}^{\infty} f_p(r, k) p(j, k) \tag{G6}$$

Consequently, from equations G4b and G6, we can write:

$$\epsilon_c(r, j) = \begin{cases} f_p(r, 0) + \sum_{\substack{k=2 \\ k \text{ even}}}^{\infty} \left[ \frac{1 \cdot 3 \cdots (k-1)}{2 \cdot 4 \cdots (k)} \right]^2 f_p(r, k) & , j = 0 \\ \\ 2 \left[ \frac{1 \cdot 3 \cdots (2j-1)}{2 \cdot 4 \cdots (2j)} \right] f_p(r, j) \\ + 2 \sum_{\substack{k=j+2 \\ k \text{ odd}}}^{\infty} \left[ \frac{1 \cdot 3 \cdots (k-j-1)}{2 \cdot 4 \cdots (k-j)} \right] \left[ \frac{1 \cdot 3 \cdots (k+j-1)}{2 \cdot 4 \cdots (k+j)} \right] f_p(r, k) & , j \text{ odd} \\ \\ 2 \left[ \frac{1 \cdot 3 \cdots (2j-1)}{2 \cdot 4 \cdots (2j)} \right] f_p(r, j) \\ + 2 \sum_{\substack{k=j+2 \\ k \text{ even}}}^{\infty} \left[ \frac{1 \cdot 3 \cdots (k-j-1)}{2 \cdot 4 \cdots (k-j)} \right] \left[ \frac{1 \cdot 3 \cdots (k+j-1)}{2 \cdot 4 \cdots (k+j)} \right] f_p(r, k) & , j \text{ even} \end{cases} \tag{G7}$$

We can rewrite and combine the latter two expressions of equation G7 by substituting,

$$k - j = 2i \quad , \quad k + j = 2i + 2j \quad , \quad i \geq 1 \tag{G8}$$

in which case,

$$f_c(r, j) = \begin{cases} f_p(r, 0) + \sum_{i=1}^{\infty} \left[ \frac{1 \cdot 3 \cdots (2i-1)}{2 \cdot 4 \cdots (2i)} \right]^2 f_p(r, 2i) & , j=0 \\ 2 \left[ \frac{1 \cdot 3 \cdots (2j-1)}{2 \cdot 4 \cdots (2j)} \right] f_p(r, j) & \\ + 2 \sum_{i=1}^{\infty} \left[ \frac{1 \cdot 3 \cdots (2i-1)}{2 \cdot 4 \cdots (2i)} \right] \left[ \frac{1 \cdot 3 \cdots (2i+2j-1)}{2 \cdot 4 \cdots (2i+2j)} \right] f_p(r, 2i+j) & , j \geq 1 \end{cases} \quad (G9)$$

Finally, if we define the function,

$$g(i) = \frac{1 \cdot 3 \cdots (2i-1)}{2 \cdot 4 \cdots (2i)} - \frac{(2i)!}{[2^i (i)!]^2} \quad (G10)$$

then,

$$f_c(r, j) = \begin{cases} f_p(r, 0) + \sum_{i=1}^{\infty} g^2(i) f_p(r, 2i) & , j=0 \\ 2 \left[ g(j) f_p(r, j) + \sum_{i=1}^{\infty} g(i) g(i+j) f_p(r, 2i+j) \right] & , j \geq 1 \end{cases} \quad (G11)$$

The factors  $g^2(i)$  and  $g(i)g(i+j)$  reduce the magnitude of the truncation error (obtained by limiting  $1 \leq i \leq I$ ), since they decay as  $((2i-1)/i)^2$  and  $((2i-1)/2i)((2i+2j-1)/(2i+2j))$  respectively. Furthermore, by computing a finite number of  $f_c(r, j)$ , with  $0 \leq j \leq N-1$ , we can use the techniques of the FFT to quickly compute  $N$  equally spaced samples of  $F(r, \theta)$ , with  $0 \leq \theta \leq \pi$ .



cos j 0	cos 20	cos 30	cos 40	cos 50	cos 60	cos 70	cos 80	cos 90	cos 100
1	1.0	-	-	-	-	-	-	-	-
2	.2500	.7500	-	-	-	-	-	-	-
3	.3750	.6250	-	-	-	-	-	-	-
4	.1406	.3125	.5469	-	-	-	-	-	-
5	.2344	.2734	.4922	-	-	-	-	-	-
6	.0977	.2051	.2461	.4512	-	-	-	-	-
7	.1706	.1842	.2251	.4181	-	-	-	-	-
8	.0748	.1538	.1692	.2095	.3928	-	-	-	-
9	.1346	.1410	.1571	.1964	.3709	-	-	-	-
10	.0686	.1234	.1309	.1473	.1855	.3524	-	-	-

j = k

j = 0 (d-c)

FIGURE G1 - Table of values for p(j,k)

APPENDIX H: Computer Programs

A number of programs were written to implement the equations described in chapters 5 and 7, and Appendices F and G. The programs are briefly described below, and selected programs are followed by their complete listings.

- RBDKXP     Rectangular geometry; Bi-Domain model; K (frequency) and X (spatial) values computed; output Plotted as equipotential lines. Implements equations 5.3b, 5.7a, 5.10-5.12, 5.16-17, 5.19-5.20, 5.22-24, 5.26-5.27, F5. Input variables: source-type (ITYPE: abrupt, lateral diffuse, lateral and transverse diffuse), NPTS (length of coefficient arrays), AA (source width along x-coordinate), UMSC (lateral border width), BB (height of rectangular zone), PO (extracellular bulk resistivity), PI (intracellular bulk resistivity), PB (bath bulk resistivity), SPACEC (space constant), STEPX (distance between spatial sample points), YBEG (value for y at lower edge of plot), YEND (value of y at upper edge of plot), and STEPY (incremental value for y). Data files: DATAK stores the Fourier cosine expansion coefficients, ISOCON stores the equipotential values. Additional programs needed: subroutine FOUR2, INIPLT, CONPLT, and PLOT.LB package.
- RAXPLT     Rectangular geometry; Axis Plot. Plots output of RBDKXP as equipotential lines. Input variables: XMAX, YMIN, YMAX (axis dimensions), XAXIS, YAXIS (graph dimensions), XORIG, YORIG (graph origin). Data files: DATAK contains the computed sampled spatial distribution. Additional programs needed: plotting package PLOT.LB
- RBDKP       Similar to RBDKXP, but plots output as surface potential distributions [not listed].

- SSAK      Spherical geometry; Solid Angle model; K (frequency) values computed. Implements equations 7.6, 7.10-7.11, 7.17, 7.19.  
Input variables: source-type (ITYPE: subepicardial, subendocardial, or transmural), LASTN (length of Legendre polynomial expansion), THETAA (angular extent of ischemic zone), PO (extracellular bulk resistivity), PI (intracellular bulk resistivity), PB (body bulk resistivity), PC (intraventricular cavity bulk resistivity), RB (epicardial diameter), RC (endocardial diameter), RA (radius of intramural boundary of ischemic zone).  
Data files: similar to RBDKXP  
Additional programs needed: subroutine EKCOST.
- SSAXP     Spherical geometry; Solid Angle model; X (spatial) values computed; output plotted as equipotential lines. Implements the equations 7.1a, 7.3, 7.4a, 7.7-7.9, 7.12-7.16, 7.18, F11.  
Input parameters: NPTS (length of Fourier cosine expansion), RMIN (lowest plotted value for r), RMAX (highest plotted value of r), STEPR (incremental value for r).  
Data files: similar to RBDKXP.  
Additional programs needed: subroutines FCOEFF, SPLT, SCNPLT, and FOUR2
- SAXPLT    Spherical geometry; AXis pLOt. Similar to RAXPLT [not listed].
- SSAKP     Spherical geometry; Solid Angle model; K (frequency values) computed; output plotted. Similar to RBDKP [not listed].
- FOUR2     Fast Fourier Transform, adapted from FOUR1 [Brenner (1967)] for real, even arrays.  
Input variables: FX (input array), NPTS (length of array FK -1), IEXP (forward or inverse transformation).  
Data files: none.  
Additional programs needed: none.
- EKCOST    Array E, coefficient K; the Legendre polynomial expansion of a rectangular function; a function of COSine Theta. Implements equation 7.6.  
Input variables: THETAA (angular extent of ischemic zone), E (output array containing the

values of the Legendre polynomial expansion coefficients), LASTN (length of array E -1), JFLAG (flag for new or old coefficients).  
Data files: ENTA, which stores the computed values of E(k).  
Additional programs needed: function PCOS2.

PCOS2      PN(COSine(theta)), the nth order Legendre polynomial, evaluated at THETA.  
Input variables: N (order of Legendre polynomial), THETA (value at which the polynomial is to be evaluated).  
Data files: none.  
Additional programs needed: none.

FCOEFF      Fourier COEFFicients. Converts a Legendre polynomial expansion into a Fourier cosine expansion. Implements equation G11.  
Input variables: FX (input/output array of coefficients), NPTS (length of Fourier cosine expansion), LASTN (length of Legendre polynomial expansion).  
Data files: GKTAB, which stores an array of factorial-like expressions, given by equation G10.  
Additional programs needed: none.

INIPLT      INItialization for rectangular coordinate PLoT.  
Input/output variables: XAXIS, YAXIS (graph dimensions), XLFT, XRHY, YTOP, YBOT (page coordinates), YMIN, YMAX (upper and lower values for y on axis).  
Data files: none  
Additional programs needed: none.

CONPLT      CONtour PLoT for rectangular geometry. Plots output of RBDKXP.  
Input variables: FX, FXX (input arrays), CON, LENCON (contour values), NEND (length of data array), XLFT, XRHT, YBOT, YTOP (page coordinates), YMIN, YMAX (lower and upper graph values for y), STEPY (incremental step in y), YCURR (current value of y), ISYM (symmetry of plot).  
Data files: none  
Additional programs needed: none.

SPLT      Spherical initialization PLoT; similar to INIPLT [not listed].

SCNPLT      Spherical CONtour PLoT; similar to CONPLT [not listed].

```

C      THIS PROGRAM TABULATES THE COEFFICIENTS OF THE EIGENFUNCTIONS FOR
C      THE POTENTIAL DISTRIBUTION ARISING FROM A RECTANGULAR ISCHEMIC ZONE,
C      USING THE BI-DOMAIN MODEL, STORING THE VALUES IN DATAK.
C      ONE OF THREE SOURCES CAN BE SELECTED FOR UMS:
C          UMS(X) = UO (|X|<AA), 0 (|X|>AA) (1)
C          UMS(X) = [1-EXP(-A/UMSC)COSH(X/UMSC)]/[1-EXP(-A/UMSC)]
C                  = [SINH(A/UMSC)EXP(-|X|/UMSC)]/[1-EXP(-A/UMSC)] (2)
C          UMS(X,Y) = COS(PI*Y/2.*BS) * [UMSC*2] (3)
C      WHERE PO*UO*SPACEC**2 IS NORMALIZED TO 1.
C      THE SPATIAL DISTRIBUTION FOR FX(X) IS FOUND FOR A RANGE OF Y VALUES.
C      THE EQUIPOTENTIAL CONTOURS FOR FX(X,Y) ARE THEN PLOTTED.
C
C      ADDITIONAL SUBROUTINES REQ'D: FOUR2, INIPLT, CONPLT, PLOT.LB
C
C      DIMENSION A(0:256),B(0:256),C(0:256),D(0:256)
C      DIMENSION FX(0:256),FXX(0:256),CON(25)
C      PICON = 3.141592654
C      PISQRT = SQRT(PICON)
C      ACCEPT 'NEW K/X-VALUES (1), OR X-VALUES (2)? ',JFLAG
C      IF (JFLAG.EQ.2) GO TO 200
C      ACCEPT 'SOURCE-TYPE: 1(ABRUPT), 2(LAT.DIFF.),
C      I 3(LAT.TRANS.DIFF.)? ',ITYPE
C
C      THIS PART OF THE PROGRAM COMPUTES THE FOURIER COEFFICIENTS
C
C      GO TO (10,15,20),ITYPE
10  WRITE (10,11)
11  FORMAT(' TYPE IN VALUES FOR NPTS,A,B,PO,PI,PB,SPACEC,STEPX: ')
    READ (11) NPTS,AA,BB,PO,PI,PB,SPACEC,STEPX
    UMSC = 0.
    BS = 99.
    GO TO 25
15  WRITE (10,16)
16  FORMAT(' TYPE IN VALUES FOR NPTS,A,UMSC,B,PO,PI,PB,SPACEC,STEPX: ')
    READ (11) NPTS,AA,UMSC,BB,PO,PI,PB,SPACEC,STEPX
    BS = 99.
    GO TO 25
20  WRITE (10,21)
21  FORMAT(' TYPE IN VALUES FOR NPTS,A,UMSC,B,BS,PO,PI,PB,
    I SPACEC,STEPX: ')
    READ (11) NPTS,AA,UMSC,BB,BS,PO,PI,PB,SPACEC,STEPX
    SINPIB = SIN(PICON*BB/(2.*BS))
    COSPIB = COS(PICON*BB/(2.*BS))
25  PH = PO*PI/(PO+PI)
    CNORM = 1./((STEPX*FLOAT(NPTS)))
    STEPK = PICON*CNORM
C
C      FOURIER COEFFICIENTS ARE STORED IN DATAK
C
C      CALL DFILW('DATAK',IERR)
C      CALL CFILW('DATAK',I,IERR)
C      CALL OPEN(4,'DATAK',2,IERR)

```

```

WRITE (4,40) NPTS,AA,UMSC,BB,BS,PO,PI,PB,SPACEC,STEPX,ITYPE
40  FORMAT(4X,I3,9(2X,F5.2),2X,I1)
    SK = 0.
    FAC2 = 1.
    IF (ITYPE.EQ.3) FAC2 = 1.+PICON*PICON*SPACEC*SPACEC/(4.*BS*BS)
    ENORM = 1.
    IF (ITYPE.NE.1) ENORM = 1./(1.-EXP(-AA/UMSC))
    DO 100 K=0,NPTS
    IF (K.GT.0) GO TO 46

C
C  COMPUTE D-C TERMS
C
    A(0) = -AA*ENORM/FAC2
    B(0) = -A(0)
    C(0) = 0.
    D(0) = 0.
    IF (ITYPE.NE.3) GO TO 85
    FAC4 = PICON*SPACEC*SINPIB/(2.*BS)
    B(0) = (COSP I B+FAC4)*B(0)
    D(0) = -PI*FAC4*A(0)/(PH*SINH(BB/SPACEC))
    GO TO 85

C
C  COMPUTE ALL OTHER FREQUENCIES
C
46  GAMMA = FAC2+SK*SK*SPACEC*SPACEC
    GAMMA2 = 1.+SK*SK*UMSC*UMSC
    A(K) = -ENORM*SIN(SK*AA)/(GAMMA*SK*GAMMA2)
    ALPHA = SK*BB
    HSINA = SINH(ALPHA)
    HCOSA = SQRT(1.+HSINA*HSINA)
    BETA = BB*SQRT(SK*SK+(1./(SPACEC*SPACEC)))
    HSINB = SINH(BETA)
    HTANB = TANH(BETA)
    FAC1 = PO*ALPHA*HSINA/BETA
    DEN = HCOSA+(PB/PH)*HSINA+FAC1/(HTANB*PI)
    B(K) = -A(K)/DEN
    D(K) = 0.
    IF (ITYPE.NE.3) GO TO 80
    FAC3 = PICON*SINPIB*BB/(2.*BETA*BS)
    B(K) = (COSP I B+FAC3/HTANB)*B(K)
    D(K) = -PI*FAC3*A(K)/(PH*HSINB)
80  C(K) = -(PB/PH)*HSINA*B(K)
    D(K) = D(K)-FAC1*B(K)/(HSINB*PH)
85  WRITE (4) A(K),B(K),C(K),D(K)
    SK = SK+STEPK
100  CONTINUE
    GO TO 220
200  CALL OPEN(4,"DATAK",1,IERR)
C
C  COME HERE IF THE FOURIER COEFFICIENTS ARE ALREADY AVAILABLE
C  IN DATAK
C
    READ (4,201) NPTS,AA,UMSC,BB,BS,PO,PI,PB,SPACEC,STEPX,ITYPE

```

```

          RBDKXP
201  FORMAT(3X, I3, 9(2X, F5.2), 2X, I1)
      DO 210 J=0, NPTS
      READ (4, 205) A(J), B(J), C(J), D(J)
205  FORMAT(4(3X, E13.6))
210  CONTINUE
      CNORM = 1./ (STEPX*FLOAT(NPTS))
      STEPK = PICON*CNORM
220  ACCEPT 'SYMMETRICAL (1) OR ASYMMETRICAL (2) PLOT? ', ISYM
      ACCEPT 'AXIS: XMAX? ', XMAX
      ACCEPT 'AXIS: YMIN, YMAX? ', YMIN, YMAX
      NEND = IFIX(XMAX/STEPX)

C
C      WE INCREMENT IN STEPS OF STEPYH UP TO -(BY+STEPYH), THEN IN STEPS
C      OF STEPYL UP TO (BY+STEPYH), THEN BACK TO STEPS OF STEPYH.
C
      ACCEPT 'PLOT: YBEG, YEND, STEPY-LOW, STEPY-HIGH? ', YBEG, YEND,
      ISTEPYL, STEPYH
      BY = BB
      IF (ISYM.EQ.2) BY = BB/2.
      YB2 = BY+STEPYH
      YB1 = -YB2

C
C      THE FILE ISOCON CONTAINS THE EQUIPOTENTIAL VALUES.  THE FIRST
C      ENTRY IS LENCON, THE LENGTH OF THE ARRAY.
C
      CALL OPEN(9, 'ISOCON', 1, IERR)
      READ (9, 224) LENCON
224  FORMAT(3X, I2)
      DO 228 J=1, LENCON
      READ (9, 226) CON(J)
226  FORMAT(3X, F7.5)
228  CONTINUE
      CALL CLOSE(9, IERR)

C
C      INITIALIZE GRAPH
C
      CALL INIPLT(XMAX, YMIN, YMAX, XLFT, XRHT, YTOP, YBOT)

C
C      THIS PART OF THE PROGRAM COMPUTES THE SPATIAL DISTRIBUTIONS
C
      Y = YBEG
      SY = 0.
      IF (ISYM.EQ.2) SY = BY-YBEG
      COSYB = 1.
      IRUN = 1
      IF (ITYPE.EQ.1.OR.ITYPE.EQ.2) GO TO 250
230  COSYB = COS(PICON*SY/(2.*BS))
250  SK = 0.
      DO 260 K=0, NPTS
      IF (SY.GT.BB) GO TO 256
      SKSY = SY*SQRT(SK*SK+(1./(SPACEC*SPACEC)))
      SKY = SK*SY
      HCOSKY = .5*(EXP(SKY)+EXP(-SKY))

```

```

      H COSKSY = .5*(EXP(SKSY)+EXP(-SKSY))
      FX(K) = (COSYB*A(K)-PO*D(K))*H COSKSY/(PO+P I)+B(K)*H COSKSY)*CNORM
      GO TO 258
256  VALUE = ABS(SK*(SY-BB))
      FX(K) = C(K)*EXP(-VALUE)*CNORM
258  SK = SK+STEPK
260  CONTINUE
      C
      C   EVALUATE FOURIER INTEGRAL
      C
      CALL FOUR2(FX,NPTS,1)
      IF (IRUN.EQ.1) GO TO 400
      C
      C   WRITE OUT CONTOUR INTO RBDKXP.SC
      C
      CALL COMPLT(FX,FXX,CON,LENCON,NEND,XLFT,XRHT,YBOT,YTOP,
1YMIN,YMAX,STEPY,Y,ISYM)
400  IRUN = IRUN+1
      TYPE 'Y = ',Y,' ',      SY = ',SY
      STEPY = STEPYH
      IF (Y.GE.YB1.AND.Y.LT.YB2) STEPY = STEPYL
      Y = Y+STEPY
      IF (Y.GT.YEND) GO TO 500
      IF (ISYM.EQ.2) GO TO 420
      SY = SY+STEPY
      GO TO 430
420  SY = SY-STEPY
      C
      C   ARRAY FXX(N) CONTAINS THE VALUES OF FX(N) FOR THE PREVIOUS
      C   VALUE OF Y.  THIS IS TO ENABLE THE EQUIPOTENTIAL PLOT
      C   TO BE DRAWN.
      C
430  DO 450 N=0,NEND
      FXX(N) = FX(N)
450  CONTINUE
      GO TO (250,250,230),ITYPE
500  CALL PLOT(0,,0,,999)
      CALL CLOSE(4,LERR)
      END

```



RAXPLT

C  
C  
C  
C  
C  
C  
C

THIS PROGRAM PLOTS THE AXES FOR RECTANGULAR COORDINATES.  
IT IS USED IN CONJUNCTION WITH RBDKXP.

TWO MODES OF OPERATION ARE POSSIBLE: A SYMMETRICAL PLOT AROUND THE  
X-AXIS, WHERE  $FX(X,Y) = FX(X,-Y)$ , OR AN ASYMMETRICAL PLOT  
AROUND THE X-AXIS, IN WHICH CASE THE UPPER, Y-BOUNDARY  
IS ASSUMED TO BE AGAINST A ZERO CONDUCTIVE MEDIUM.

```

CALL OPEN(4, "DATAK", 1, IERR)
READ (4, 201) NPTS, AA, UMSC, BB, BS, PO, PI, PB, SPACEC, STEPX, ITYPE
201  FORMAT(3X, I3, 9(2X, F5.2), 2X, I1)
CALL CLOSE(4, IERR)
ACCEPT "SYMMETRICAL (1) OR ASYMMETRICAL (2) PLOT? ", ISYM
ACCEPT "AXIS: XMAX? ", XMAX
ACCEPT "AXIS: YMIN, YMAX? ", YMIN, YMAX
ACCEPT "GRAPH DIMENSIONS (X-AXIS, Y-AXIS) IN INCHES? ", XAXIS, YAXIS
ACCEPT "PLOT: XORIG, YORIG? ", XORIG, YORIG
CALL PLOTS(2, "RAXPLT.SC", 7)
CALL ROTATE(90., 0., 0.)
XDEL = XMAX/XAXIS
YDEL = (YMAX-YMIN)/YAXIS
XLFT = XORIG
XRHT = XLFT+XAXIS
YBOT = YORIG+YMIN/YDEL
YTOP = YBOT+YAXIS
CALL AXIS(XORIG, YORIG, "X (CM)", -6, XAXIS, 0., 0., XDEL)
CALL AXIS(XORIG, YBOT, "Y (CM)", 6, YAXIS, 90., YMIN, YDEL)
BY = BB
IF (ISYM.EQ.2) BY = BY/2.
EPIBY = YORIG+BY/YDEL
ENDOBY = YORIG-BY/YDEL
CALL PLOT(XORIG, EPIBY, 3)
CALL PLOT(XRHT, EPIBY, 2)
CALL PLOT(XORIG, ENDOBY, 3)
CALL PLOT(XRHT, ENDOBY, 2)
CALL SYMBOL(5., 6.25, .07, " A = ".0., 5)
CALL NUMBER(999., 999., .07, AA, 0., 1)
CALL SYMBOL(999., 999., .07, "      = ".0., 9)
CALL NUMBER(999., 999., .07, UMSC, 0., 1)
CALL SYMBOL(999., 999., .07, "      B = ".0., 10)
CALL NUMBER(999., 999., .07, BY, 0., 1)
CALL SYMBOL(999., 999., .07, "      BS = ".0., 10)
CALL NUMBER(999., 999., .07, BS, 0., 1)
CALL SYMBOL(5., 6., .07, "PO = ".0., 5)
CALL NUMBER(999., 999., .07, PO, 0., 2)
CALL SYMBOL(999., 999., .07, "      PI = ".0., 9)
CALL NUMBER(999., 999., .07, PI, 0., 2)
CALL SYMBOL(999., 999., .07, "      PB = ".0., 9)
CALL NUMBER(999., 999., .07, PB, 0., 2)
CALL SYMBOL(999., 999., .07, "      = ".0., 9)
CALL NUMBER(999., 999., .07, SPACEC, 0., 1)
CALL PLOT(0., 0., 999)
END

```

## SSAK

```

5 C THIS PROGRAM TABULATES THE COEFFICIENTS OF THE EIGENFUNCTIONS FOR
C THE POTENTIAL DISTRIBUTION ARISING FROM A SPHERICAL ISCHEMIC ZONE,
C USING THE BI-DOMAIN POISSON MODEL, STORING THE VALUES IN
C DATAK.
C ONE OF THREE SOURCES CAN BE SELECTED FOR MS = -(RM/PI)*GRAD(UMS):
C SUBEPI: UMS(R,T) = 1 (RA<R<RB; IT<TA), 0 (OTHERWISE) (1)
C SUBENDO: UMS(R,T) = 1 (RC<R<RA; IT<TA), 0 (OTHERWISE) (2)
C TRANS: UMS(R,T) = 1 (RC<R<RB; IT<TA), 0 (OTHERWISE) (3)
C WHERE PH*(RM/PI)*UO IS NORMALIZED TO 1.
C
C ADDITIONAL SUBROUTINES REQ'D: EKDCOST, PCOS2.
C
C DIMENSION A(0:512),B(0:512),C(0:512),D(0:512),E(0:512),FX(0:512),
C ICON(21),FXX(0:256)
C PICON = 3.141592654
C ACCEPT 'NEW T/K/X-VALUES (1), K/X-VALUES (2)? ',JFLAG
C ACCEPT 'SOURCE-TYPE: 1(SUBEPI.), 2(SUBENDO.), 3(TRANS.)? ',ITYPE
C ENFAC = 1.
C EPFAC = 1.
C
C THE VARIABLES ENFAC AND EPFAC DETERMINE THE TYPE OF ISCHEMIC ZONE
C
C IF (ITYPE.EQ.1) ENFAC = 0.
C IF (ITYPE.EQ.2) EPFAC = 0.
C GO TO (10,20),JFLAG
10 ACCEPT 'LASTN (500)? THETA? ',LASTN,THETA
C
C OBTAIN COEFFICIENTS OF LEGENDRE POLYNOMIAL EXPANSION FOR
C RECTANGULAR FUNCTION
C
20 CALL EKDCOST(THETA,E,LASTN,JFLAG)
C IF (ITYPE.EQ.3) GO TO 30
C ACCEPT 'PO,PI,PB,PC,RB,RC,RA? ',PO,PI,PB,PC,RB,RC,RA
C GO TO 35
30 ACCEPT 'PO,PI,PB,PC,RB,RC? ',PO,PI,PB,PC,RB,RC
C RA = 0.
35 PH = PO*PI/(PO+PI)
C
C STORE CALCULATED COEFFICIENTS OF LEGENDRE POLYNOMIAL EXPANSION
C IN DATAK
C
C CALL DFILW('DATAK',IERR)
C CALL CFILW('DATAK',1,IERR)
C CALL OPEN(4,'DATAK',2,IERR)
40 WRITE (4,40) LASTN,THETA,PO,PI,PB,PC,RB,RC,RA,ITYPE
C FORMAT(4X,I3,3X,F5.2,4(1X,F7.2),3(3X,F5.2),3X,I1)
C RCB = RC/RB
C
C WE INITIALIZE RCBK AND RCBK1 FOR K=1.
C
C RCBK = RCB
C RCBK1 = RCB*RCB

```

## SSAK

```

DO 100 K=0, LASTN
IF (K.GT.0) GO TO 50
C
C
C
COMPUTE D-C TERMS
A(0) = -EPFAC*E(0)
B(0) = 0.
C(0) = 0.
D(0) = (ENFAC-EPFAC)*E(0)
GO TO 85
50 IF (RCBK.LT..00000001) GO TO 70
C
C
C
CALCULATE ALL OTHER FREQUENCIES
PBK = K/PB
PBK1 = PBK+(1./PB)
PHK = K/PH
PHK1 = PHK+(1./PH)
PCK = K/PC
PCK1 = PCK+(1./PC)
FAC1 = PBK1+PHK
FAC2 = PBK1-PHK1
FAC3 = PCK-PHK
FAC4 = PCK+PHK1
RCB2K1 = RCBK*RCBK1
DEN = FAC1*FAC4-FAC2*FAC3*RCB2K1
A(K) = (ENFAC*PCK*FAC2*RCBK1-EPFAC*PBK1*FAC4)*E(K)/DEN
B(K) = (EPFAC*PBK1*FAC3*RCBK-ENFAC*PCK*FAC1)*E(K)/DEN
C(K) = EPFAC*E(K)+A(K)+B(K)*RCBK1
D(K) = ENFAC*E(K)+A(K)*RCBK+B(K)
RCBK = RCBK*RCB
RCBK1 = RCBK1*RCB
GO TO 85
70 A(K) = -EPFAC*PBK1*E(K)/FAC1
B(K) = -ENFAC*PCK*E(K)/FAC4
C(K) = A(K)+EPFAC*E(K)
D(K) = B(K)+ENFAC*E(K)
85 WRITE (4,90) A(K),B(K),C(K),D(K),E(K)
90 FORMAT(1X,5(2X,F9.6))
100 CONTINUE
CALL CLOSE(4,LERR)
END

```

## SSAXP

```

C
C THIS PROGRAM IS USED IN CONJUNCTION WITH SSAK
C
C THE SPATIAL DISTRIBUTION FOR FX(R,T) IS FOUND FOR A RANGE OF R
C VALUES. THE ISOCONTOURS FOR FX(R,T) ARE THEN PLOTTED.
C
C ADDITIONAL SUBROUTINES REQ'D: SPLT, SCNPLT, FCOEFF
C FOUR2, PLOT.LB.
C
C DIMENSION A(0:512),B(0:512),C(0:512),D(0:512),E(0:512),FX(0:512),
1CON(25),FXX(0:256)
C PICON = 3.141592654
C JFLAG = 3
C CALL OPEN(4,"DATAK",1,IERR)
C
C READ STORED VALUES OF COEFFICIENTS FOR LEGENDRE POLYNOMIAL
C EXPANSION
C
C READ (4,201) LASTN,THETAA,PO,PI,PB,PC,RB,RC,RA,ITYPE
201 FORMAT(3X,I3,3X,F5.2,4(1X,F7.2),3(3X,F5.2),3X,I1)
C ENFAC = 1.
C EPFAC = 1.
C
C THE VARIABLES ENFAC AND EPFAC DETERMINE THE TYPE OF ISCHEMIC
C ZONE
C
C IF (ITYPE.EQ.1) ENFAC = 0.
C IF (ITYPE.EQ.2) EPFAC = 0.
C DO 203 J=0,LASTN
202 READ (4,202) A(J),B(J),C(J),D(J),E(J)
203 FORMAT(5(2X,F9.6))
C CONTINUE
C ACCEPT 'NPTS (=100./STEPT)? ',NPTS
C STEPT = 100./FLOAT(NPTS)
C ACCEPT 'RMIN,RMAX,STEPR-LOW,STEPR-HIGH? ',RMIN,RMAX,STEPRL,STEPRH
C
C WE INCREMENT IN STEPS OF STEPRH UP TO RC-STEPRH, THEN IN STEPS OF
C STEPRL UP TO RB+STEPRH, THEN BACK TO STEPS OF STEPRH.
C
C RCSR = RC-STEPRH
C RBSR = RB+STEPRH
C
C THE FILE ISOCON CONTAINS THE EQUIPOTENTIAL VALUES. THE
C FIRST ENTRY IS LENCON, THE LENGTH OF THE ARRAY.
C
C CALL OPEN(9,"ISOCON",1,IERR)
210 READ (9,210) LENCON
C FORMAT(3X,I2)
C DO 220 J=1,LENCON
215 READ (9,215) CON(J)
220 FORMAT(3X,F7.5)
C CONTINUE
C CALL CLOSE(9,IERR)

```

SSAXP

```
C
C   INITIALIZE GRAPH
C
CALL SPLT(RMAX,XLFT,XRHT,YTOP,YBOT,THETA, RB,RC,RA,
IPO,PI,PB,PC, ITYPE)
IRUN = 1
R = RMIN+.0001
230 RRC = R/RC
RRB = R/RB
C
C   THIS PART OF THE PROGRAM COMPUTES THE SPATIAL DISTRIBUTIONS
C
IF (R.GE.RB) GO TO 260
IF (R.GT.RC) GO TO 250
RRCK = 1.
DO 245 K=0, LASTN
FX(K) = D(K)*RRCK
IF (RRCK.LT..00000001) GO TO 245
RRCK = RRCK*RRC
245 CONTINUE
GO TO 200
250 RRBK = 1.
RCRK1 = 1./RRC
C
C   DETERMINE THE LEGENDRE EXPANSION COEFFICIENTS FOR THE
C   PROPER TYPE OF ZONE
C
DO 255 K=0, LASTN
FX(K) = A(K)*RRBK+B(K)*RCRK1
IF (R.LT.RA) FX(K) = FX(K)+ENFAC*E(K)
IF (R.EQ.RA) FX(K) = FX(K)+E(K)
IF (R.GT.RA) FX(K) = FX(K)+EPFAC*E(K)
IF (RRBK.LT..00000001) GO TO 254
RRBK = RRBK*RRB
254 IF (RCRK1.LT..00000001) GO TO 255
RCRK1 = RCRK1/RRC
255 CONTINUE
GO TO 200
260 RBRK1 = 1./RRB
DO 265 K=0, LASTN
FX(K) = C(K)*RBRK1
IF (RBRK1.LT..00000001) GO TO 265
RBRK1 = RBRK1/RRB
265 CONTINUE
C
C   WE CONVERT THE LEGENDRE POLYNOMIAL EXPANSION TO A FOURIER
C   COSINE SERIES EXPANSION.
C
200 CALL FCOEFF(FX,NPTS, LASTN)
C
C   WE NORMALIZE FX(K) IN PREPARATION FOR THE FOURIER TRANSFORM
C
DO 202 K=0, NPTS
```

SSAXP

```
IF (K.EQ.0) GO TO 282
FX(K) = .5*FX(K)
282 CONTINUE
C
C WE EVALUATE THE FOURIER SERIES EXPANSION
C
CALL FOUR2(FX,NPTS,1)
IF (IRUN.EQ.1) GO TO 400
C
C WRITE OUT CONTOUR INTO SSAXP.SC
C
CALL SCNPLT(FX,FXX,CON,LENCON,NPTS,XLFT,XRHT,YBOT,YTOP,
IRMAX,STEPR,R)
400 IRUN = IRUN+1
TYPE 'R = ',R
STEPR = STEPRH
IF (R.GE.RCSR.AND.R.LT.RBSR) STEPR = STEPRL
R = R+STEPR
IF (R.GT.RMAX) GO TO 500
C
C ARRAY FXX(N) CONTAINS THE VALUES OF FX(N) FOR THE PREVIOUS
C VALUE OF Y. THIS IS TO ENABLE THE EQUIPOTENTIAL PLOT
C TO BE DRAWN.
C
DO 450 N=0,NPTS
FXX(N) = FX(N)
450 CONTINUE
GO TO 230
500 CALL CLOSE(4,LERR)
CALL PLOT(0.,0.,999)
END
```

```

C
C
C
C
SUBROUTINE FOUR2(FX,NPTS, IEXP)

THIS PROGRAM COMPUTES THE FAST FOURIER TRANSFORM FOR A
REAL, EVEN ARRAY.

DIMENSION FT(1:2,0:511),FX(0:256)
PI = 3.141592654
NN = 2*NPTS
N = 2*NN
DO 5 I=0,NPTS
FT(1,I) = FX(I)
IF (I.EQ.0.OR.I.EQ.NPTS) GO TO 4
II = NN-I
FT(1,II) = FT(1,I)
FT(2,II) = 0.
4 FT(2,I) = 0.
5 CONTINUE
J = 1
DO 50 I=1,N,2
IF (I-J) 10,20,20
10 TEMPR = FT(J)
TEMPI = FT(J+1)
FT(J) = FT(I)
FT(J+1) = FT(I+1)
FT(I) = TEMPR
FT(I+1) = TEMPI
20 M = N/2
30 IF (J-M) 50,50,40
40 J = J-M
M = M/2
IF (M-2) 50,30,30
50 J = J+M
MMAX = 2
60 IF (MMAX-N) 70,90,90
70 ISTEP = 2*MMAX
DO 80 M=1,MMAX,2
THETA = PI*FLOAT(IEXP*(M-1))/FLOAT(MMAX)
WR = COS(THETA)
WI = SIN(THETA)
DO 80 I=M,N,ISTEP
J = I+MMAX
TEMPR = WR*FT(J)-WI*FT(J+1)
TEMPI = WR*FT(J+1)+WI*FT(J)
FT(J) = FT(I)-TEMPR
FT(J+1) = FT(I+1)-TEMPI
FT(I) = FT(I)+TEMPR
80 FT(I+1) = FT(I+1)+TEMPI
MMAX = ISTEP
GO TO 60
90 DO 100 I=0,NPTS
FX(I) = FT(1,I)
100 CONTINUE
RETURN
END

```

EKCOST

```
C
C   THIS PROGRAM COMPUTES THE FIRST (LASTN+1) COEFFICIENTS OF THE
C   LEGENDRE POLYNOMIAL EXPANSION OF A RECTANGULAR FUNCTION WITH
C   A WIDTH OF 2*THETAA.  IF NEW COEFFICIENTS ARE NOT TO BE
C   COMPUTED.  SET JFLAG =2; OTHERWISE JFLAG = 1.
C
C   ADDITIONAL FILES REQ'D:  ENTA
C
SUBROUTINE EKCOST(THETAA,E, LASTN, JFLAG)
  DIMENSION E(0:512)
  CALL OPEN(7, 'ENTA', 2, KERR)
  IF (JFLAG.EQ.2) GO TO 100
  WRITE (7, 10) THETAA, LASTN
10  FORMAT(4X, F6.3, 3X, I3)
  DO 50 K=0, LASTN
  IF (K.GT.0) GO TO 20
  E(0) = (COS(THETAA)-1.)/2.
  GO TO 50
20  K0 = K-1
  K1 = K+1
  E(K) = (PCOS2(K1, THETAA)-PCOS2(K0, THETAA))/2.
50  CONTINUE
  DO 70 K=0, LASTN
  WRITE (7) E(K)
70  CONTINUE
  CALL CLOSE(7, JERR)
  RETURN
100  READ (7, 110) THETAA, LASTN
110  FORMAT(3X, F6.3, 3X, I3)
  DO 150 K=0, LASTN
  READ (7, 120) E(K)
120  FORMAT(3X, E13.6)
150  CONTINUE
  CALL CLOSE(7, JERR)
  RETURN
  END
```



PCOS2

```
FUNCTION PCOS2(N,THETA)
C
C WE EVALUATE THE NTH ORDER LEGENDRE POLYNOMIAL, PN(COSINE(THETA)).
C
  IF (N.EQ.0) GO TO 90
  SN = FLOAT(N)
  ILAST = IFIX(SN/2.)
  PCOS2 = 0.
  I = 0
  N2 = 2*N
  N3 = N2-1
  FAC1 = 2.
  FAC2 = 1.
  FAC3 = 1.
  DO 20 J=1,N3,2
  FAC2 = FAC2*FLOAT(J)/FLOAT(J+1)
20 CONTINUE
  I2 = 2*I
  IF (I.EQ.0) GO TO 35
  IF (I2.EQ.N) FAC3 = .5
  FAC1 = FAC1*FLOAT(I2-1)/FLOAT(I2)
  FAC2 = FAC2*FLOAT(N2-I2+2)/FLOAT(N2-I2+1)
35 PCOS2 = PCOS2+FAC1*FAC2*FAC3*COS(FLOAT(N-I2)*THETA)
  I = I+1
  IF (I.LE.ILAST) GO TO 30
  RETURN
90 PCOS2 = 1.
  RETURN
END
```

FCEFF

```
C
C   THIS PROGRAM CONVERTS A LEGENDRE POLYNOMIAL EXPANSION INTO A
C   FOURIER COSINE EXPANSION.
C
C   ADDITIONAL FILES REQ'D:  GKTAB
C
C   SUBROUTINE FCEFF(FX,NPTS,LASTN)
C   DIMENSION G(0:512),FC(0:256),FX(0:512)
C   CALL OPEN(8,"GKTAB",1,IERR)
C
C   THE FILE "GKTAB" CONTAINS THE VALUES:
C       G(I) = (2*I-1)(2*I-3)...(1)/[(2*I)(2*I-2)...(2)]
C
C   LASTI = (LASTN+NPTS)/2
C   DO 20 I=0, LASTI
C   READ (8,10) G(I)
10  FORMAT(3X,E13.6)
20  CONTINUE
C   DO 200 J=0, NPTS
C   IF (J.GT.0) GO TO 80
C   FC(0) = FX(0)
C   DO 30 I2=2, LASTN, 2
C   I = I2/2
C   FC(0) = FC(0)+G(I)*G(I)*FX(I2)
30  CONTINUE
C   GO TO 200
80  FC(J) = FX(J)*G(J)
C   LASTI = LASTN-J
C   DO 100 I2=2, LASTI, 2
C   I = I2/2
C   FC(J) = FC(J)+FX(I2+J)*G(I)*G(I+J)
100 CONTINUE
C   FC(J) = 2.*FC(J)
200 CONTINUE
C   DO 300 K=0, NPTS
C   FX(K) = FC(K)
300 CONTINUE
C   CALL CLOSE(8, IERR)
C   RETURN
C   END
```

INIPLT

```
C
C   THIS PROGRAM INITIALIZES THE PLOT FOR RECTANGULAR COORDINATES
C
C   TWO MODES OF OPERATION ARE POSSIBLE: A SYMMETRICAL PLOT AROUND THE
C   X-AXIS, WHERE  $FX(X,Y) = FX(X,-Y)$ , OR AN ASYMMETRICAL PLOT
C   AROUND THE X-AXIS, IN WHICH CASE THE UPPER, Y-BOUNDARY
C   IS ASSUMED TO BE AGAINST A ZERO CONDUCTIVE MEDIUM.
C
SUBROUTINE INIPLT(XMAX, YMIN, YMAX, XLFT, XRHT, YTOP, YBOT)
ACCEPT 'GRAPH DIMENSIONS (X-AXIS, Y-AXIS) IN INCHES? ', XAXIS, YAXIS
CALL PLOTS(2, 'RBDKXP.SC', 7)
CALL ROTATE(90., 8., 0.)
XDEL = XMAX/XAXIS
YDEL = (YMAX-YMIN)/YAXIS
XLFT = 5.-(XAXIS/2.)
C   XORIG = XLFT
XRHT = XLFT+XAXIS
YBOT = 3.5-(YAXIS/2.)
C   YORIG = YBOT-YMIN/YDEL
YTOP = YBOT+YAXIS
RETURN
END
```

## CONPLT

```

C      THIS SUBROUTINE PLOTS ISOCONTOURS ON A GRID WITH DIMENSIONS
C      XAXIS,YAXIS.
C      THE ARRAY FX CONTAINS VALUES AT THE CURRENT VALUE OF SY, WHILE
C      THE ARRAY FXX CONTAINS VALUES AT THE VALUE OF SY-STEPY.
C      THE ARRAY CON (LENGTH CONLEN) CONTAINS THE VALUES FOR THE
C      ISOCONTOURS.
C      THE X-AXIS EXTENDS FROM 0 TO XMAX, WHILE THE Y-AXIS EXTENDS
C      FROM -YMAX TO YMAX.
C      XP,YP ARE THE PLOT DIMENSIONS, IN INCHES.
C
C      SUBROUTINE CONPLT(FX,FXX,CON,LENCON,NEND,XLFT,XRHT,YBOT,YTOP,
C      IYMIN,YMAX,STEPY,YCURR,ISYM)
C      DIMENSION FX(0:256),FXX(0:256),CON(25)
C      XORIG = XLFT
C      YORIG = YBOT-YMIN*((YTOP-YBOT)/(YMAX-YMIN))
C      DELX = (XRHT-XLFT)/FLOAT(NEND)
C      DELY = (YTOP-YBOT)*STEPY/(YMAX-YMIN)
C      Y = YORIG+YCURR*(YTOP-YBOT)/(YMAX-YMIN)
C      X = XORIG+DELX
C      DO 105 I=1,NEND
C      FX1 = FXX(I-1)
C      FX2 = FXX(I)
C      FX3 = FX(I-1)
C      FX4 = FX(I)
C      DO 90 K=1,LENCON
C      FXCON = CON(K)
C      ICASE = 1
C      IF (FXCON.GT.FX1) ICASE = ICASE+1
C      IF (FXCON.GT.FX2) ICASE = ICASE+2
C      IF (FXCON.GT.FX3) ICASE = ICASE+4
C      IF (FXCON.GT.FX4) ICASE = 9-ICASE
C      GO TO (90,10,20,30,40,50,60,70), ICASE
10     X1 = X-DELX*(FX2-FXCON)/(FX2-FX1)
C      Y1 = Y-DELY
C      X2 = X-DELX
C      Y2 = Y-DELY*(FX3-FXCON)/(FX3-FX1)
C      GO TO 80
20     X1 = X-DELX*(FX2-FXCON)/(FX2-FX1)
C      Y1 = Y-DELY
C      X2 = X
C      Y2 = Y-DELY*(FX4-FXCON)/(FX4-FX2)
C      GO TO 80
30     X1 = X-DELX
C      Y1 = Y-DELY*(FX3-FXCON)/(FX3-FX1)
C      X2 = X
C      Y2 = Y-DELY*(FX4-FXCON)/(FX4-FX2)
C      GO TO 80
40     X1 = X-DELX
C      Y1 = Y-DELY*(FX3-FXCON)/(FX3-FX1)
C      X2 = X-DELX*(FX4-FXCON)/(FX4-FX3)
C      Y2 = Y
C      GO TO 80

```

CONPLT

```
50  X1 = X-DELX*(FX2-FXCON)/(FX2-FX1)
    Y1 = Y-DELY
    X2 = X-DELX*(FX4-FXCON)/(FX4-FX3)
    Y2 = Y
    GO TO 80
60  X1 = X-DELX*(FX2-FXCON)/(FX2-FX1)
    Y1 = Y-DELY
    X2 = X-DELX
    Y2 = Y-DELY*(FX3-FXCON)/(FX3-FX1)
    CALL PLOT(X1,Y1,3)
    CALL PLOT(X2,Y2,2)
    IF (ISYM.EQ.2) GO TO 70
    Y3 = 2.*YORIG-Y1
    Y4 = 2.*YORIG-Y2
    CALL PLOT(X1,Y3,3)
    CALL PLOT(X2,Y4,2)
70  X1 = X-DELX*(FX4-FXCON)/(FX4-FX3)
    Y1 = Y
    X2 = X
    Y2 = Y-DELY*(FX4-FXCON)/(FX4-FX2)
80  CALL PLOT(X1,Y1,3)
    CALL PLOT(X2,Y2,2)
    IF (ISYM.EQ.2) GO TO 90
    Y3 = 2.*YORIG-Y1
    Y4 = 2.*YORIG-Y2
    CALL PLOT(X1,Y3,3)
    CALL PLOT(X2,Y4,2)
90  CONTINUE
    X = X+DELX
100 CONTINUE
    RETURN
    END
```

REFERENCES

1. BARR L and BERGER WK (1964): The role of current flow in the propagation of cardiac muscle action potentials. Pfluger's Arch Ges Physiol 279: 192-194.
2. BARR L, DEWEY MM, and BERGER W (1965): Propagation of action potentials and the structure of the nexus in cardiac muscle. J Gen Physiol 48: 797-823.
3. BARR L and JAKOBSSON E (1976): The spread of current in electrical syncytia. In: Physiology of Smooth Muscle (E. Bulbring and M.F. Shuba, eds.), pp. 41-48. New York: Raven Press.
4. BAYLEY RH (1942): An interpretation of the injury and the ischemic effects of myocardial infarction in accordance with the laws which determine the flow of electric currents in homogeneous volume conductors and in accordance with relevant pathologic changes. Am Heart J 24: 514.
5. BAYLEY RH (1958): Biophysical Principles of Electrocardiography. Paul B. Hoeber, Inc., New York. Chaps. 2,9,10.
6. BECKER LC, FERREIRA R, THOMAS M (1973): Mapping of left ventricular blood flow with radioactive microspheres in experimental coronary artery occlusion. Cardiovasc Res 7: 391-400.
7. BERGER WK (1972): Correlation between the ultrastructure and function of intercellular contacts. In: Electrical Phenomena in the Heart (W.C. De Mello, ed.). Chap. 2. New York: Academic Press.
8. BERKINBLIT MB, DOVALEV SA, SMOLYANINOV VS, and CHAILAKHYAN LM (1965): Input resistance of syncytial structures. Biofizika 10: 309-316.
9. BODENHEIMER MM, BANKA VS, LEVITES R, and HELFANT RH (1976): Temporal relation of epicardial electrographic, contractile and biochemical changes after acute coronary occlusion and reperfusion. Am J Cardiol 37: 486-492.
10. BRAUNWALD E and MAROKO PR (1974): Protection of the Ischemic Myocardium. In: The Myocardium: Failure and Infarction (E. Braunwald, ed). New York: HP

Publishing Co., Inc.

11. BRAUNWALD E and MAROKO PR (1976): ST-segment mapping. Realistic and unrealistic expectations. Circ 54: 529-532.
12. BRENNER NM (1967): Three Fortran programs that perform the Cooley-Tukey Fourier transform. MIT Lincoln Lab. Tech. Note 1967-2, Lexington, Mass.
13. BURDON-SANDERSON J and PAGE FJM (1879): On the time-relations of the excitatory process in the ventricle of the heart of the frog. J Physiol 2: 384.
14. CLERC L (1976): Directional differences of impulse spread in trabecular muscle from mammalian heart. J Physiol 255: 335-346.
15. COHEN D and KAUFMAN LA (1975): Magnetic determination of the relationship between the S-T segment shift and the injury current produced by coronary artery occlusion. Circ Res 36: 414-424.
16. DE MELLO WC (1976): Influence of the sodium pump on intracellular communication in heart fibres: effect of intracellular injection of sodium ion on electrical coupling. J Physiol 263: 171:197.
17. DiBONA D and POWELL J (1977): Quantitative correlation between cell swelling and necrosis in myocardial ischemia (abstr). Circ 55,56: III-70.
18. EIFLER WJ and PLONSEY R (1975): A cellular model for the simulation of activation in the ventricular myocardium. J Electrocardiol 8: 117-128.
19. EISENBERG RS and JOHNSON EA (1970): Three-dimensional electric field problems in physiology. Prog Biophys Mol Biol 20: 1-65.
20. EKMEKCI A, TOYOSHIMA H, KWOCZYNSKI JK, NAGAYA T, and PRINZMETAL M (1961): Angina Pectoris IV. Clinical and experimental difference between ischemia with S-T elevation and ischemia with S-T depression. Am J Cardiol 7: 412-426.
21. ENGEL E, BARCILON V, and EISENBERG RS (1972): The interpretation of current-voltage relationships recorded from a spherical cell with a single microelectrode. Biophys J 12: 384-403.

22. FACTOR SM, SONNENBLICK EH, and KIRK ES (1977):  
Histological border zone of acute myocardial  
infarction: islands or peninsulas (abstr)? Circ  
55,56: III-71.
23. FLAHERTY JT (1976): Clinical uses of precordial  
ST-segment mapping and the pathophysiology of  
ST-segment voltage changes. Circ 53(3): I-85-87.
24. FOZZARD HA and DasGUPTA DS (1976): ST-segment  
potentials and mapping. Theory and experiments.  
Circ 54(4): 533-537.
25. GEDDES LA and BAKER LE (1967): The specific resistance  
of biological material - a compendium of data for the  
biomedical engineer and physiologist. Med Biol Eng  
5: 271-293.
26. GEORGE EP (1961): Resistance values in a syncytium.  
Aust J Exp Biol 39: 267-274.
27. GUYTON RA, McCLENATHAN JH, NEWMAN GE, and MICHAELIS LL  
(1977): Significance of subendocardial S-T segment  
elevation caused by coronary stenosis in the dog.  
Am J Cardiol 40: 373-380.
28. HEARSE DJ, OPIE LH, KATZEFF IE, LUBBE WF, VAN DER WERFF  
TJ, PEISACH M, and BOULLE G (1977): Characterization  
of the "border zone" in acute regional ischemia in  
the dog. Am J Cardiol 40: 716-726.
29. HECHT HH (1961): Some observations and theories  
concerning the electrical behavior of heart muscle.  
Am J Med 30: 720-746.
30. HELLERSTEIN D (1968): Passive membrane potentials. A  
generalization of the theory of electrotonus.  
Biophys J 8: 358-379.
31. HELLERSTEIN HK and KATZ LN (1948): The electrical  
effects of injury at various myocardial locations.  
Am Heart J 36: 184-220.
32. HILLIS LD and BRAUNWALD (1977a): Myocardial ischemia I.  
N Engl J Med 296: 971-978.
33. HILLIS LD and BRAUNWALD (1977b): Myocardial ischemia  
II. N Engl J Med 296: 1034-1041.
34. HILLIS LD and BRAUNWALD (1977c): Myocardial ischemia  
III. N Engl J Med 296: 1093-1096.



35. HIRZEL HO, SONNENBLICK EH, and KIRK ES (1977): Absence of a lateral border zone of intermediate creatine phosphokinase depletion surrounding a central infarct 24 hours after acute coronary occlusion in the dog. *Circ Res* 41: 673-683.
36. HODGKIN AL and HUXLEY AF (1952): A quantitative description of membrane current and its application to conduction and excitation in nerve. *J Physiol* 117: 500-544.
37. HODGKIN AL and RUSHTON WAH (1946): The electrical constants of a crustacean nerve fiber. *Proc Royal Soc* 133: 444-479.
38. HOLLAND RP and ARNSDORF MF (1977): Solid angle theory and the electrocardiogram: physiologic and quantitative interpretations. *Prog Cardiovasc Dis* 19(6): 431-457.
39. HOLLAND RP and BROOKS H (1975): Precordial and epicardial surface potentials during myocardial ischemia in the pig. *Circ Res* 37: 471-480.
40. HOLLAND RP and BROOKS H (1977a): TQ-ST segment mapping: critical review and analysis of current concepts. *Am J Cardiol* 40: 110-129.
41. HOLLAND RP and BROOKS H (1977b): Spatial and nonspatial influences on the TQ-ST segment deflection of ischemia. *J Clin Invest* 60: 197-214.
42. IRVIN RG and COBB FR (1977): Relationship between epicardial ST-segment elevation, regional myocardial blood flow, and extent of myocardial infarction in awake dogs. *Circ* 55: 825-832.
43. ISERI LT, ALEXANDER LC, McCAUGHEY RS, BOYLE AJ, and MEYERS GB. (1952): Water and electrolyte content of cardiac and skeletal muscle in heart failure and myocardial ischaemic injury. *Am Heart J* 43: 215-227.
44. JACK JJB, NOBLE D, and TSIEN RW (1975): Electric Current Flow in Excitable Cells. Chap. 5, Current flow in multi-dimensional systems, pp. 83-97. Oxford: Clarendon Press.
45. JANSE MJ, KLEBER AG, VAN CAPELLE FJL, and DURRER D (1977): Time course of TQ- and ST-segment changes after coronary occlusion in the perfused pig heart (abstr). *Circ* 55,56: III-79.

46. JENNINGS RB, KALTENBACH JP, and SOMMERS HM (1965): Cell death: electrolyte alterations in injured and dying myocardial cells. In: Electrolytes and Cardiovascular Disease (E. Bajusz, ed.), Vol. I, pp. 192-203. New York: S. Karger, Basel.
47. JOHNSON EA (1976): First electrocardiographic sign of myocardial ischemia: an electrophysiological conjecture. *Circ* 53(3): I-82-84.
48. JOYNER RW, RAMON F, and MOORE JW (1975): Simulation of action potential propagation in an inhomogeneous sheet of coupled excitable cells. *Circ Res* 36: 654-661.
49. KARDESCH M, HOGANCAMP CE, and BING RJ (1958): The effect of complete ischemia on the intracellular electrical activity of the whole mammalian heart. *Circ Res* 6: 715-720.
50. KARLSSON J, TEMPLETON GH, and WILLERSON JT (1973): Relationship between epicardial S-T segment changes and myocardial metabolism during acute coronary insufficiency. *Circ Res* 32: 725-730.
51. KATCHER AH, PEIRCE MS, AND SAYEN JJ (1960): Effects of experimental regional ischemia and levarterenol on the RS-T segment and baseline of ventricular surface electrocardiograms obtained by direct-coupled amplification. *Circ Res* 8: 29-43.
52. KATO K, FUKUDA H, and KOYAMA S (1968): Depression of the S-T segment in epicardial electrocardiogram associated with experimental major coronary artery constriction. *J Electrocardiol* 1(2): 167-174.
53. KJEKSHUS JK, MAROKO PR, and SOBEL BE (1972): Distribution of myocardial injury and its relation to epicardial ST-segment changes after coronary artery occlusion in the dog. *Cardiovasc Res* 6: 490-499.
54. KOSHLyakOV NS, SMIRNOV MM, and GLINER EB (1964): Differential equations of Mathematical Physics. Chap. 25, The Helmholtz equation, pp. 398-434. Amsterdam: North-Holland Publishing Co.
55. LEAF A (1973): Cell swelling. A factor in ischemic tissue injury. *Circ* 48: 455-458.
56. LEKVEN J, ILEBEKK A, FONSTELIEN E, and KIIL F (1975): Relationship between ST-segment elevation and local

tissue flow during myocardial ischaemia in dogs.  
Cardiovasc Res 9: 627-633.

57. LIEBERMAN M, SAWANOBORI T, KOOTSEY JM, and JOHNSON EA (1975): A synthetic strand of cardiac muscle. J Gen Physiol 65: 527-550.
58. LORENTE DE NO R (1947): A study of nerve physiology. Studies from the Rockefeller Institute for Medical Research 132: part 1, Chap. 9.
59. MADIAS JE and HOOD WB (1974): Prognostic value of ST-elevation. Circ 49: 1262.
60. MAROKO PR, KJEKSHUS JK, SOBEL BE, WATANABE T, COVELL JW, ROSS J, and BRAUNWALD E (1971): Factors influencing infarct size following experimental coronary artery occlusion. Circ 43: 67:82.
61. MAROKO PR, LIBBY P, COVELL JW, SOBEL BE, ROSS J, and BRAUNWALD E (1972): Precordial S-T segment elevation mapping: an atraumatic method for assessing alterations in the extent of myocardial ischemic injury. The effects of pharmacologic and hemodynamic interventions. Am J Cardiol 29: 223-230.
62. McFEE R and RUSH S (1967): Qualitative effects of thoracic resistivity variations on the interpretation of electrocardiograms. The "Brody" effect. Am Heart J 74: 642-651.
63. MULLER JE, MAROKO PR, and BRAUNWALD E (1975): Evaluation of precordial electrocardiographic mapping as a means of assessing changes in myocardial injury. Circ 52: 16-27.
64. MULLER JE, MAROKO PR, and BRAUNWALD E (1977): Preservation of the Ischemic Myocardium. Kalamazoo, Michigan: Upjohn Company.
65. MULLER JE, MAROKO PR, and BRAUNWALD E (1978): Precordial electrocardiographic mapping. A technique to assess the efficacy of interventions designed to limit infarct size. Circ 57: 1-18.
66. NAGATA Y (1970): The influence of the inhomogeneities of electrical conductivity within the torso on the electrocardiogram as evaluated from the view point of the transfer impedance vector. Jap Heart J 11(5): 489-505.

67. NAHUM LH, HAMILTON WF, and HOFF HE (1943): The injury current in the electrocardiogram. *Am J Physiol* 139: 202-207.
68. NETTER FH (1969): The CIBA Collection of Medical Illustrations. Vol. 5, Heart (F.F. Yonkman, ed.). New York: Case Hoyt Corp.
69. NIELSEN BL (1973): ST-segment elevation in acute myocardial infarction. Prognostic importance. *Circ* 48: 338-345.
70. PAGE E (1962): Cat Muscle in Vitro III. The extracellular space. *J Gen Physiol* 46: 201-213.
71. PAGE SG and NIEDERGERKE R (1972): Structures of physiological interest in the frog heart ventricle. *J Cell Sci* 11: 179-203.
72. PARDEE HE (1920): An electrocardiographic sign of coronary artery occlusion. *Arch Int Med* 26: 244-257.
73. PENEFSKY ZJ and HOFFMAN BF (1963): Effects of stretch on mechanical and electrical properties of cardiac muscle. *Am J Physiol* 204: 433-438.
74. PESKOFF A and EISENBERG RS (1973): Interpretation of some microelectrode measurements of electrical properties of cells. *Ann Rev Biophys Bioeng* 2: 65-79.
75. PESKOFF A and EISENBERG RS (1975): The time-dependent potential in a spherical cell using matched asymptotic expansions. *J Math Biol*: 277-300.
76. PESKOFF A, EISENBERG RS, and COLE JD (1976): Matched asymptotic expansions of the Green's function for the electric potential in an infinite cylindrical cell. *J Appl Math* 30: 222-239.
77. PINE MB, CAULFIELD JB, BING OHL, and ABELMANN WH (1977): Absence of cell swelling following metabolic blockade of myocardium (abstr). *Circ* 55,56: III-71.
78. PLONSEY R (1965): An extension of the solid angle potential formulation for an active cell. *Biophys J* 5: 663-667.
79. PLONSEY R (1974): An evaluation of several cardiac activation models. *J Electrocardiol* 7(3): 237-244.
80. POLIMENI PI (1974): Extracellular space and ionic

- distribution in rat ventricle. Am J Physiol 227(3): 676-683.
81. POLIMENI PI and AL-SADIR J (1975): Expansion of extracellular space in the nonischemic zone of the infarcted heart and concomitant changes in tissue electrolyte contents in the rat. Circ Res 37: 725-732.
  82. PRINZMETAL M, EKMEKCI A, TOYOSHIMA H, and KWOCZYNSKI JK (1959): Angina Pectoris III. Demonstration of a chemical origin of ST deviation in classic angina pectoris, its variant form, early myocardial infarction, and some noncardiac conditions. Am J Cardiol 3: 276-293.
  83. PRINZMETAL M, ISHIKAWA K, NAKASHIMA M, OISHI H, OZKAN E, WAKAYAMA J, and BAINES JM (1968): Correlation between intracellular and surface electrograms in acute myocardial ischemia. J Electrocardiol 1(2): 161-166.
  84. PRINZMETAL M, TOYOSHIMA H, EKMEKCI A, MIZUNO Y, and NAGAYA T (1961): Myocardial ischemia. Nature of ischemic electrocardiographic patterns in the mammalian ventricles as determined by intracellular electrographic and metabolic changes. Am J Cardiol 8: 493-593.
  85. PRINZMETAL M, TOYOSHIMA H, EKMEKCI A, and NAGAYA T (1962): Angina Pectoris VI. The nature of ST segment elevation and other ECG changes in acute severe myocardial ischemia. Clin Sci 23: 489-514.
  86. RAKITA L, BORDUAS JL, ROTHMAN S, and PRINZMETAL M (1954): Studies on the mechanism of ventricular activity XII. Early changes in the RS-T segment and QRS complex following acute coronary artery occlusion: experimental study and clinical applications. Am Heart J 48: 351-372.
  87. REES JR and REDDING VJ (1969): Comparison of myocardial blood flow within, near, and distant from the infarct. Circ Res 25: 161-170.
  88. REID PR, TAYLOR DR, KELLY DT, WEISFELDT ML, HUMPHRIES JO'N, ROSS RS, and PITT B (1974): Myocardial-infarct extension detected by precordial ST-segment mapping. N Engl J Med 290: 123.
  89. RICHESON F, AKIYAMA T, and SCHENK E (1977): Spatial

- determinants of the ischemic TQ-ST segment (abstr).  
Circ 55,56: III-17.
90. RUSH S, ABILDSKOV JA, and McFEE R (1963): Resistivity of body tissues at low frequencies. Circ Res 12: 40-50.
  91. SAMSON WE and SCHER AM (1960): Mechanism of S-T segment alteration during acute myocardial injury. Circ Res 8: 780-787.
  92. SAYEN JJ, KATCHER AH, and PEIRCE G (1961): Electrocardiographic effects of changing the nature of the contact between the exposed heart and the body. Circ Res 9: 497-508.
  93. SCHER AM (1962): Excitation of the heart. In: Handbook of Physiology (W.E. Hamilton, ed.), Sec. 2: Circulation, Vol. I, Chap. 12. Washington, D.C.: American Physiological Society.
  94. SCHMITT OH (1969): Biological information processing using the concept of interpenetrating domains. In: Information Processing in the Nervous System (K.N. Leibovic, ed.), pp. 325-331. New York: Springer-Verlag.
  95. SELWYN AP, OGUNRO EA, and SHIFFINGFORD JP (1977): Natural history and evaluation of ST segment changes and MB CK release in acute myocardial infarction. Br Heart J 39: 988-994.
  96. SHIBA H and KANNO Y (1971): Further study of the two-dimensional theory: an electric model for a flat thin association of cells with a directional intercellular communication. Biophysik 7: 295-301.
  97. SMITH FM (1918): The ligation of coronary arteries with electrocardiographic study. Arch Int Med 8-27.
  98. SMITH HJ, SINGH BN, NORRIS RM, JOHN MB, and HURLEY PJ (1975): Changes in myocardial blood flow and S-T segment elevation following coronary artery occlusion in dogs. Circ Res 36: 697-705.
  99. SMOLYANINOV VV (1971): The problem of the electrical properties of syncytia. In: Models of the Structural-Functional Organization of Certain Biological Systems (I.M. Gelfand, V.S. Gurfinkel, S.V. Fomin, and M.S. Tsetlin, eds.), pp. 132-154. Cambridge: MIT Press.

100. SODI-PALLERES D, BISTENI A, MEDRANO GA, DE MICHELI A, PONCE DE LEON J, CALVA E, FISHLEDER BL, TESTELLI MR, and MILLER BL (1966): The polarizing treatment in cardiovascular conditions. In: Electrolytes and Cardiovascular Diseases (E. Bajusz, ed.), Vol. 2, pp. 198-238. New York: S. Karger, Basel.
101. SOLOMON JC and SELVESTER RH (1971): Current dipole moment density of the heart. *Am Heart J* 81: 351-360.
102. SONNENBLICK EH (1974): Myocardial ultrastructure in the normal and failing heart. In: The Myocardium: Failure and Infarction (E. Braunwald, ed.). New York: HP Publishing Co., Inc.
103. SPEAR JF and MOORE EN (1972): Stretch-induced excitation and conduction disturbances in the isolated rat myocardium. *J Electrocardiol* 5(1): 15-24.
104. SPERELAKIS N (1969): Lack of electrical coupling between contiguous myocardial cells in vertebrate hearts. In: Comparative Physiology of the Heart: Current Trends (F.V. McCann, ed.). Basel: Birkhauser-Verlag, pp. 135-165.
105. SURAWICZ B (1977): The disputed S-T segment mapping: is the technique ready for wide application in practice? *Am J Cardiol* 40: 137-140.
106. TANAKA I and SASAKI Y (1966): On the electrotonic spread in cardiac muscle of the mouse. *J Gen Physiol* 49: 1089-1110.
107. THOMAS RC (1972): Electrogenic sodium pump in nerve and muscle cells. *Physiol Rev* 52: 563-594.
108. TOYOSHIMA H, EKMIKCI A, FLAMM E, MIZUNO Y, NAGAYA T, NAKAYAMA R, YAMADA K, and PRINZMETAL M (1964): Angina Pectoris VII. The nature of S-T depression in acute myocardial ischemia. *Am J Cardiol* 13: 498-509.
109. TUNG L (1976): The inadequacy of the solid angle formulation when used to describe cardiac injury potentials (abstr). *Proc 29th ACEMB*: 80.
110. VINCENT GM, ABILDSKOV JA, and BURGESS MJ (1977): Mechanisms of ischemic ST-segment displacement. Evaluation by direct current recordings. *Circ* 56: 559-566.

111. WEIDMANN S (1966): The diffusion of radiopotassium across the intercalated discs of mammalian cardiac muscle. *J Physiol* 187: 323-342.
112. WEIDMANN S (1970): Electrical constants of trabecular muscle from mammalian heart. *J Physiol* 210: 1041-1054.
113. WHALEN DA, HAMILTON DG, GANOTE CE, and JENNINGS RB (1974): Effect of a transient period of ischemia on myocardial cells. *Am J Path* 74(3): 381-397.
114. WILSON FN, MacLOED AG, and BARKER PS (1933): The Distribution of the Currents of Action and of Injury Displayed by Heart Muscle and Other Excitable Tissues. Ann Arbor: University of Michigan Press.
115. WITTIG JH and WILLIAMS EMV (1977): Mechanism of ST elevations during the three phases of ischemia (abstr). *Circ* 55,56: III-48.
116. WOLFERTH CC, BELLET S, LIVEZUV MM, and MURPHY FD (1945): Negative displacement of the RS-T segment in the electrocardiogram and its relationships to positive displacement; an experimental study. *Am Heart J* 29: 220-245.
117. WOODBURY JW and BRADY AJ (1956): Intracellular recording from moving tissues with a flexibly mounted ultramicroelectrode. *Sci* 123: 100-101.
118. WOODBURY JW and CRILL WE (1961): On the problem of impulse conduction in the atrium. In: Nervous Inhibition (E. Florey, ed.), pp. 124-135. New York: Pergamon Press Ltd.
119. WYLIE CR (1966): Advanced Engineering Mathematics. pp. 388-398. New York: McGraw-Hill, Inc.



BIOGRAPHICAL NOTE

The author was born in Ann Arbor, Michigan in 1950. He attended public high school in Rye, New York, where he graduated as class salutatorian.

In 1967 he entered the Massachusetts Institute of Technology. During that time he participated in the industrial cooperative program with RCA Corporation in Hightstown, New Jersey. As a senior, he was a lecturer for an experimental student-taught course. In 1972 he received a combined Master's and Bachelor's degree in the Department of Electrical Engineering for work done at RCA.

He continued his education at MIT, where he was a part-time laboratory teaching assistant for two undergraduate engineering physiology courses. During his education in graduate school, he was primarily supported as a National Institute of Health trainee, and in 1977 he was awarded a Whitaker Health Science Fund fellowship. He is a member of Eta Kappa Nu, Tau Beta Pi, and Sigma Xi.

In 1976 he became married to Sze-Ping Kuo, a former resident of Bayside, New York and also a graduate of MIT.